UNIVERSITY OF CAPE TOWN

DEPARTMENT OF MECHANICAL ENGINEERING

THE PERFORMANCE OF AN INTEGRAL GREENHOUSE SOLAR AIR-HEATER

by

P. J. Bam

October, 1984

Submitted to the University of Cape Town in fulfilment for the degree of Master of Science in Engineering.

ABSTRACT

The Baird-type solar collector is a solar air-heater, utilising black shade-cloth as the absorber, that is incorporated as part of the roof of a greenhouse. It is intended to be used, in conjunction with a heat storage device, to provide greenhouse heating (and cooling), and so to assist in maintaining an optimum greenhouse plant-cultivation environment.

An analysis of a Baird-type integral greenhouse solar collector is presented in this thesis. This has involved designing and building a solar simulator, which was used to test the performance of a model of a greenhouse-integral solar collector. The experimental results thus derived were compared with results generated using a theoretical heat-transfer model of the solar collector and show that, on average, the theoretical model was capable of predicting the model solar collector heat-gain to within six percent of the measured values. Predictions of performance were made for various input conditions, such as high and low values of inlet-air temperature, different ground temperatures, different mass-flowrates and radiation intensities. Although subject to the input conditions, the results indicated an efficiency of solar energy collection of about 35 percent for the model greenhouse solar collector.

The theoretical model was used (with appropriate modifications), to predict the performance of a "life-size" Baird-type greenhouse integral solar collector. Predictions were made for average conditions in the Cape Peninsula for the months of January and June. Assuming zero windspeed, a collector efficiency of approximately 42 percent is anticipated for most of the January day and approximately 33 percent for most of the June day.

ACKNOWLEDGEMENTS

The author wishes to thank:

Associate Professor J. Gryzagoridis, the project supervisor, for his guidance and encouragement;

Professor R. K. Dutkiewicz, for his help and ideas during Assoc. Prof. Gryzagoridis' sabbatical leave;

Dr R. Smart, for advice regarding the solution of simultaneous non-linear equations;

Assoc. Prof. B. Paddon, Dr K. F. Bennet and Mr A. Sass for computational assistance;

Mr L. Watkins, Mr D. Finlayson and Mr H. Tomlinson for assistance given in the construction of the experimental equipment;

Mr V. Appleton for photographic assistance;

the CSIR and subsequently the University of Cape Town for financial assistance;

Thorn Lighting for donating the lights used in the solar simulator.

TABLE OF CONTENTS

Page

APPENDICES

APPENDICES ctd. Page

APPENDICES ctd. Page

LIST OF ILLUSTRATIONS

Page

LIST OF TABLES

Page

LIST OF FIGURES

LIST OF FIGURES ctd. Page

LIST OF FIGURES ctd.

Page

LIST OF PHOTOGRAPHS

NOMENCLATURE

AM	Air Mass number
A	Area
C_p	Specific heat
C	Constant
d, D	Diameter
E	Emissive power
F	Shape-factor
F_r	Collector heat-removal efficiency factor
G	Total (longwave) radiation incident on a surface
Gr	Grashof number
g	Constant for gravitational acceleration
HR	Heat Radiation
h	Heat-transfer coefficient, head
I	Total (shortwave) radiation incident on a surface
J	Radiosity
k	Thermal conductivity
L, ℓ, x	Length
M	Mass
m	Air Mass Number
$\dot{m}$	Mass flowrate
Nu	Nusselt number
PAR	Photosynthetically Active Radiation
Pr	Prandtl number
Q	Heat flow
q	Heat flow per unit area
Re	Reynolds number
r	Radius
T	Temperature
t	Time

U	Overall collector heat-loss coefficient
v	Volume, velocity

Greek symbols:

ρ	Density, reflectance
μ	Dynamic viscosiy
σ	Boundary layer thickness, Stefan-Boltzmann constant
λ	Wavelength
τ	Transmittance
$\bar{\tau}$	Average transmittance
α	Absorptance
ε	Emittance
θ	Angular measure, incidence angle
β	Volume coefficient of expansion
ν	Kinematic viscosity
Δ	Difference, increment
∇	Gradient
η	Efficiency

Subscripts:

a	ambient
b	bottom, blackbody, bulk
c	chrome, cover
cb	bottom cover
ce	edge cover
ct	top cover
conv	natural convection
e	effective
f	film, friction
fs	free stream
g	glue, ground
gout	ground (direct)
gin	ground (indirect)
h	hydraulic
in	inlet : out outlet
ℓ	length
n, nc	black netting cloth
o	time t=o
p	pressure, perimeter, clear-polyethylene, absorber plate
poly	polyethylene
s	sky, superficial
sin	sky (indirect)
sout	sky (direct)
t	top, time t=t
therm	thermopile
u	useful
w	natural convection
x	cross-section

CHAPTER ONE

INTRODUCTION

Greenhouses provide a controlled growing environment because of the protection they offer from insects and pests and from weather extremes. As a result of the greenhouse microclimate it is possible to grow seasonal crops on a year-round basis as well as increase production as much as ten-fold (Kerr (1)).

However, in many instances heating (or cooling) is needed to maintain desired greenhouse temperature levels. The most common methods of greenhouse heating make use of energy sources such as electricity, kerosene, oil and liquid petroleum gas. Greenhouse cooling is achieved by either natural or forced venting.

1.1 THE GREENHOUSE SOLAR AIR-HEATER

Greenhouses derive their daytime energy input from the sun. They can be considered as large solar collectors with zero air flowrate through them - the plants and ground surface acting as the absorber. A greenhouse solar air-heater is proposed as an alternative energy source to those listed above to maintain optimum greenhouse air temperatures. Since the heating demand is greatest at night, the solar air-heater could be coupled with some form of energy storage device. Use of such a system can result in an ideal arrangement where heat stored during the day is used for nighttime heating.

1.2 THE SOLAR-ASSISTED GREENHOUSE

A solar-assisted greenhouse can be defined as one whose heating requirements are either completely or partially satisfied by a solar heater. There are many different types of solar-assisted greenhouses - a review of these is presented in Chapter Two. This thesis investigates the performance of a Baird-type greenhouse solar collector proposed by Baird, Waters and Mears (2).

CHAPTER TWO

LITERATURE SURVEY

2.1 THE SOLAR-ASSISTED GREENHOUSE

The potential benefit resulting from a controlled growing environment appears to be significant. Appendix 1 contains a summary of information regarding temperature levels and insolation requirements for optimum greenhouse crop cultivation. However, it is evident in the literature that very little work is reported concerning greenhouse integral solar heating systems.

Winegarner (3) suggests the use of a selective baffle collector as part of the roof of a greenhouse. It separates the incident solar energy, through the use of a selective coating, into Photosynthetically Active Radiation (wavelength less than seven hundred micrometres) and Heat Radiation. The PAR portion of the light is passed on through the roof to the growing area, whilst the HR portion is absorbed by the baffle. By circulating air across the baffle the HR portion is transferred to a rock storage basin and can then be directed into the growing area when needed.

Damagnez (4) proposes using a double-skinned greenhouse roof through which a solution of water and copper-chloride is passed. This solution acts as a selective absorber - being transparent to the visible wavelengths yet having a strong absorption in the near infrared. Heat collected is stored in a subterranean tank.

Winegarner's (3) and Damagnez's (4) papers are descriptive in nature and do not include any mathematical statements of the heat-transfer processes involved.

Baird, Waters and Mears (2) have built and tested a fullscale solar greenhouse heating system utilising an integral solar collector and a rock-bed thermal storage system.

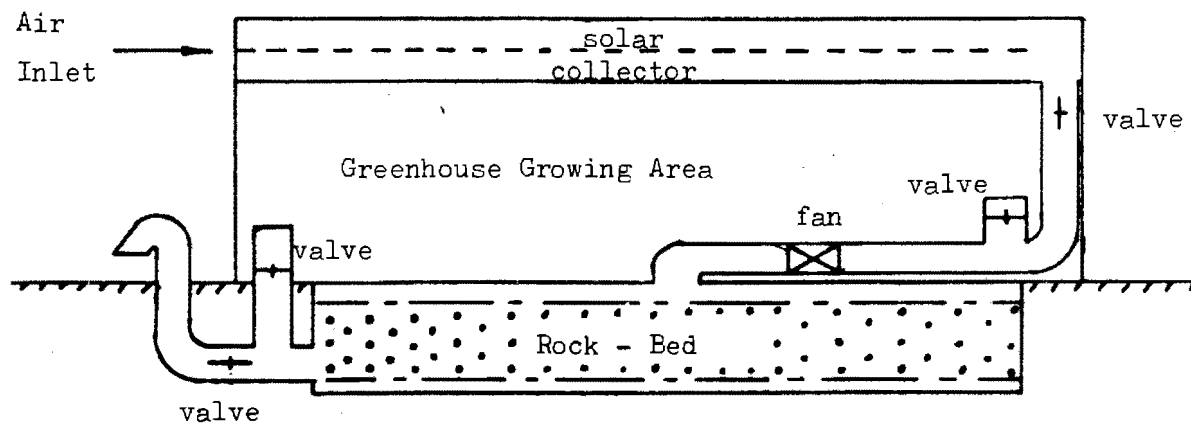

FIGURE 1: Baird, Waters and Mears' solar-assisted greenhouse (2).

The design consists of a solar collector built into the roof of a tunnel-type polyethylene greenhouse. The collector is coupled to a rock-bed heat storage device. Air is blown through the collector and storage medium by means of a fan.

The collector can be thought of as an attic in the greenhouse roof. It is formed by dividing the hot-house into two sections with a sheet of clear-polyethylene. The lower section is the plant cultivation area and the upper section is the solar collector. A woven, high-density,

carbon-black impregnated polyethylene net is suspended in the middle of the collector and behaves as an absorber of incident radiation.

During heat collection air is introduced from the atmosphere and passes through the solar collector where it absorbs heat from the net. From here it is ducted to the rock-bed. When heat is to be added to the greenhouse, ambient greenhouse air is circulated through the rock-bed and returns to the growing area in a heated state.

It is a characteristic of this Baird-type solar collector that daytime insolation on the plants is reduced as a result of absorption by the net and the extra polyethylene cover. However, use of the stored-heat will result in increased nighttime greenhouse ambient-air temperature. The desirability of this varies according to the regional climate and the crop under cultivation. For example, the existence of infrared spectrum in sunlight can lead to excess heat being generated in the greenhouse. This is especially true of hot, arid regions. Sayigh (5) cautions that clear night skies can cause such rapid cooling that plants can die from cold shock. The South African hinterland, comprised to a large extent of semi-desert, is hot by day and cold at night. It is here that the integral greenhouse solar collector could excel. Sayigh (5) confirms this, saying that for tropical and sub-tropical areas a combination of shaded plant with rock-bed storage is applicable. The Baird-type greenhouse solar collector will assist in these functions.

Baird, Waters and Mears (2) measured parameters such as collector air-temperature, rock-bed temperature and collector efficiency. However, their results are all empirically derived and no analytical model for the netting-cloth absorber integral-greenhouse solar air-heater or rock-bed storage system is presented. In fact, there is very little

evidence of any theoretical work related to the performance of greenhouse integral solar-heater systems in the literature. In contrast to the above, a considerable amount of work has been reported on the various aspects of heat-transfer in solar collectors, the simulation of solar radiation and rock-bed heat storage. Some work has been directed towards understanding the thermal behaviour of a greenhouse environment due to what is known as the "greenhouse effect". Examples of energy balance models of this phenomenon can be found in Whittle et al (6), Walker (7), Takakura et al (8), McCormick (9) and Duncan et al (10).

2.2 THE PERFORMANCE AND ANALYSIS OF SOLAR HEATERS

The performance of flat plate collectors is described by the Hottel-Whillier equation (Hottel et al - 11) as:

$$Q_u = A_p.I.(\tau\alpha) - A_p.U_\ell.(T_p-T_a) \quad \ldots\ldots\ldots\ldots\ldots\ldots \quad (1a)$$

The derivation of this equation is based on the solution of the simultaneous energy-balance equations that exist for the collector components and the fluid medium. Although the equation was originally formulated for a sheet and tube water-heater, Whillier (12) and Bliss (13) have shown that the generalised relationships apply to most collector designs.

Beckman et al (14) have rearranged the equation and present it as:

$$q_u = F_r.((\tau\alpha)_e.I - U_\ell.(T_i-T_a)) \quad \ldots\ldots\ldots\ldots\ldots\ldots \quad (1b)$$

Division of this equation by the insolation results in a useful expression that yields the output-to-input energy ratio i.e. the collector efficiency:

$$\eta = q_u/I$$

$$= F_r.((\tau\alpha)_e - U_\ell.((T_i-T_a)/I)) \quad \ldots\ldots\ldots\ldots\ldots\ldots \quad (1c)$$

If the effective transmittance-absorptance product and the overall collector heat-loss coefficient and the collector heat-removal efficiency factor are constant, then the efficiency can be expressed as a straight line function of intercept "$F_r.(\tau\alpha)_e$" and slope "$F_r.U_\ell$" where

the dependent variable is " η " and the independent variable is "$(T_i - T_a)/I$ ". The Bundesverband Solarenergie (BSE) (15) has compiled guidelines for solar collector efficiency testing, which specify the use of this straight line efficiency equation to characterise collector efficiency. In addition to West Germany, the U.S.A., Britain and France have all standardised on the use of the Hottel-Whillier equation (Equation 1) to specify solar collector performance.

It seems that the attempt to categorise performance of the more complex collector configurations with the Hottel-Whillier equation is self-defeating in that the theoretical analysis becomes more complicated than is necessary, for the sake of presenting performance characteristics in a standardised manner. Consideration of the following points serves to reinforce this opinion. The BSE group (15) acknowledges that a shortcoming of the efficiency equation approach is that the effect of different air speeds around the collector is not taken into account and thus specify that different efficiency equations be derived for different windspeeds. Aranovitch and Roumengous (16) point out that the effective transmittance-absorptance product is not constant in that it is influenced by incident radiation angle and that the overall collector heat-loss coefficient depends on thermal processes involving thermal conduction, radiation and natural convection and can only be considered temperature independent as a very first approximation. The collector efficiency factor is not only a function of collector geometry but also depends on the fluid viscosity (which is temperature dependent). Aranovitch et al (16) thus stress that it is difficult to represent the thermal efficiency as a linear function and propose that the collector efficiency be more precisely represented by a polynomial

function such as:

$$\eta = a + b.(T_i-T_a)/I + c.(T_i-T_a)^2/I + \ldots\ldots$$

$$\ldots\ldots + d.(T_i-T_a)^n/I \ldots\ldots \quad (1c)$$

where a, b, c and d are constants

This does not address the true nature of the problem in that a, b, c and d are only approximately constant. For example, the collector heat-removal efficiency factor, which is a component of a, b, c, etc., remains relatively constant for a particular collector over a wide range of flowrates when water is the fluid medium, but there can be significant variation in its value over the range of flowrates used in air-heating collectors as shown by Beckman et al (14). So the values of a, b, and c etc. will vary in practice!

Thus the use of the Hottel-Whillier efficiency equation (Hottel et al - 11) for collector performance presentation is limited in that each efficiency equation, whether a straight line function or a polynomial curve, is strictly speaking only applicable for a specified, constant external windspeed and a specified, constant collector fluid mass-flowrate. The generality of the performance equation is therefore lost if attempts of accurate performance predictions are to be made.

Duffie and Beckman (17) and Parker (18) have derived efficiency and overall loss factors for various types of solar collectors. The derivations of the collector heat-removal factor and the collector overall heat-loss coefficient for the Baird-type of greenhouse solar collector are not included in these analyses and were not found in the literature. It is clear from their results that the derivation of the

collector heat-removal efficiency factor and the overall collector heat-loss coefficient becomes tedious and difficult for more complex collector configurations. Their analyses are for collectors with opaque bottoms and glass covers. This implies that transmission of longwave radiation is ignored and the analyses consequently do not apply to collectors whose covers are semi-transparent to longwave radiation, such as polyethylene. A further disadvantage of the Hottel-Whillier efficiency equation (Hottel et al - 11) type of collector performance presentation is that examination of empirical results does not readily allow performance predictions for collectors of different dimensions.

An alternative approach for the theoretical analysis of complex solar collectors is documented by Selcuk (19). Investigation of his approach reveals that he derives energy balances for all system components and the system fluid. These form a set of simultaneous equations. Instead of manipulating these to yield expressions for the collector heat-removal factor and the overall collector heat-loss coefficient, he chooses to solve the equations numerically so as to provide solutions for the output variables (such as air-outlet temperature, absorber-plate temperature etc.) for a given set of input conditions (such as solar radiation intensity, ambient air temperature etc.).

This thesis makes use of a similar theoretical approach as described above to analyse the performance of the Baird-type greenhouse solar collector.

An advantage of working with the fundamental energy balances is that all the heat-transfer mechanisms can easily be included in the heat-transfer model. (Because of the difficulties that arise if the collector heat-removal factor and the overall collector heat-loss

coefficient are to be evaluated, the heat-transfer processes are often rationalised to include only the most important heat-transfer mechanisms). In addition, it is felt that perhaps more accurate performance predictions can be made by considering finite elements along the length of the collector and evaluating local values of parameters such as heat-transfer coefficients etc. rather than the average collector values as is commonly used in the efficiency equation approach (Hottel et al - 11). However, this numerical approach does not allow collector performance to be presented as conveniently as the Hottel-Whillier equation and requires that a complete analysis be performed for each different set of input conditions in order to predict collector performance.

2.2.1 The Black-Netting Forced-Convection Heat-Transfer Coefficient

The prediction of collector performance has as a prerequisite the knowledge of the absorber convection heat-transfer coefficient. Parker (18) has done sensitivity analyses of collector performance and concludes that the heat-transfer coefficient between the absorber and the transport fluid is of key importance to collector performance. The literature on heat-transfer coefficients is not yet complete and there is a lack of information regarding heat-transfer coefficients for porous media. There is apparently no information available on the convection heat-transfer characteristics for the type of black-netting used in the Baird-type greenhouse solar collector investigated in this thesis. Consequently, an experiment was designed and tests were performed to establish the order-of-magnitude of the black-netting forced-convection heat-transfer coefficient. For more detail, refer to Appendix 2.

2.2.2 Radiation Properties of the Collector Materials

The literature contains frequent reference to the possible use of thin transparent films as covers for solar collectors to replace glass. It is often mentioned that plastic covers, unlike glass covers, are not completely opaque to the longwave radiation emitted by the hot surface of the collector absorber. Whillier (29) and Tabor (30) have investigated the longwave and shortwave radiation transmittance of various plastic films and glasses. The results show that there are substantial variations in the results depending on the type of radiation as well as the type of glass or plastic used. Appendix 3 includes results of tests conducted to evaluate the shortwave and longwave radiation properties of the solar collector materials.

2.3 SOLAR SIMULATORS

For solar energy research the variability of outdoor conditions presents difficulties - thus indoor testing in a controlled environment using solar simulators is desirable. The BSE Working Group (15) has specified some preliminary guidelines for the design of solar simulators. The most important criterion is that the simulator radiation spectral distribution should resemble as closely as possible that of solar radiation for Air Mass numbers 1 to 2, where the Air Mass number is defined as:

$$m = \text{secant}(\beta) \quad \ldots\ldots\ldots\ldots\ldots\ldots\ldots\ldots\ldots\ldots\ldots\ldots \quad (2)$$

An approximation to the Air Mass 2 spectral distribution has also been suggested by Moon (20) and Benning (21) as a reasonable criterion for solar simulator source selection, and this basis has been used by NASA (22) and by Gillett in the Cardiff University simulator (23). Other factors to be considered include:

(a) the uniformity of radiation intensity on the collector plane. Gillett (23) and the BSE group (15) state that a variation of up to ten percent from the mean flux intensity may be considered satisfactory for a simulator source.

(b) it is desirable that collector incident radiation be as parallel as possible. This criterion is most important for testing concentrating devices where, according to Gillett (23), departure from parallelism has a strong effect on the concentration ratio. If the beam divergence is

large, this may also be important for devices using covers whose transmission coefficient is a function of incidence angle.

(c) the simulator should be able to provide radiation over a range of incidence angles. Azimuthal variation can be provided by turning the test surface in the horizontal plane. However, it is not possible to simulate solar altitude variations by changing the tilt of the test surface because mechanisms of heat-transfer within and on the surface of the solar collector often rely on natural convection processes. The simulator radiation sources should therefore be able to move through a ninety degree arc to cover the full range of possible solar altitudes.

The most suitable light for a solar simulator radiation source is the subject of some controversy as seen in Benning (21), Yass et al (22), Pekruhn et al (24), Beeson (25), McMillan et al (26) and Gillett (23 and 27). The most commonly used lights include:

(1) Xenon Arc
(2) Tungsten-Halogen Quartz
(3) Compact Source Iodide Arc

A detailed analysis of these lights and the design of a solar simulator used in the experiments is included in Appendix 4.

2.3.1 Effective "Field-of-View" Temperature

The main radiating surfaces within the collector field-of-view are the walls, ceiling and floor of the test cell. Preferably, these have to be maintained at a known, uniform temperature. The light sources may take

up a significant proportion of the field-of-view of the collector and hence the temperature of the lamps will affect the collector-environment radiation heat exchange. Gillett (23) specifies that the effective field-of-view temperature in a solar simulator is normally taken to be ambient air-temperature, whereas the field-of-view temperature outdoors is specified by Parmelee (28) to be three degrees Kelvin below ambient-air temperature for a completely overcast sky and by Whillier (12) to be six degrees Kelvin below ambient-air temperature for a clear sky.

Thermal radiation from the lamps and lamp housings may be either in the form of a focussed beam or a diffuse emission. If the lamps have open reflectors then the thermal radiation may form part of the beam and in this case Gillett (27) states that the thermal radiation can be very high. If the lamps have a cover glass then this will absorb thermal radiation and re-emit diffusely from its front surface.

2.3.2 Diffuse Irradiation Corrections to Collector Efficiency

According to Gillett (27), the CSI-lamp solar simulator produces a negligible quantity of diffuse short-wave radiation. Consequently collector performance measurements made in the simulator apply for direct radiation only. However, Gillett (27) claims that in steady-state outdoor testing on clear days there is usually between fifteen and twenty five percent diffuse irradiation. He concludes that for single glazed collectors a comparison of simulator and clear-sky outdoors test results will show simulator values about two percent higher than the outdoor results.

In general, it appears that the use of solar simulators for the experimental evaluation of solar system performance is considered acceptable if the simulator is designed with the abovementioned criteria in mind.

CHAPTER THREE

THEORY

Since air is being forced through the solar collector for the purpose of collecting heat from the black-netting, the enthalpy gain of the air can be expressed as:

$$Q_u = \dot{m}.C_p.(T_{out}-T_{in}) \quad \ldots\ldots\ldots\ldots\ldots\ldots\ldots\ldots \quad (3)$$

The evaluation of the collector heat-gain " Q_u" is accomplished in experimental conditions by measurement of the mass-flowrate and the inlet and outlet-air temperatures. The theoretical prediction of the collector heat-gain requires the calculation of the outlet-air temperature for a specified set of input conditions (which includes fluid mass-flowrate and inlet-air temperature). The outlet-air temperature is calculated by considering the energy balances that apply to the collector components and the fluid medium and solving the resultant set of simultaneous equations. In formulating the energy balances some assumptions have been made:

(a) Heat flow by conduction through the edges of the covers and the black-netting is assumed to be negligible. A sample "worst case" calculation is included in Appendix 5, which shows that conduction heat-transfer from cover to cover or black-netting is less than half a percent of the input energy.

(b) longwave radiation reflections between the collector surfaces are not taken into account. The reflected thermal energy is of minor significance, being a second order effect, taking place between surfaces of only slightly different temperatures.

(c) the polyethylene greenhouse side covers are ignored as they are not part of the collector.

(d) the greenhouse ambient-air and ground temperatures are assumed to remain the same as the outside ambient-air and ground temperatures respectively. (The scope of this thesis does not include the prediction of greenhouse climatic environment).

(e) the fluid (in this case air) is assumed to be transparent to both longwave and shortwave radiation. (Holman (41), on the subject of gas radiation, states that air can be regarded as radiation-transparent at low temperatures).

Neither the geometries nor the cross-sectional areas of the top and bottom sections of the model collector are similar. Appendix 6 contains an analysis of the flowrates through the collector, where it is shown that about forty-eight percent of the total mass-flowrate passes through the bottom section and about fifty-two percent passes through the top section of the collector respectively. A consequence of this is that the boundary layer growth of the top and bottom sections does not progress at an equal rate, nor does the onset of fully developed flow occur simultaneously. Appendix 7 contains an investigation of the boundary layer growth for the collector. From this analysis it can be concluded that the range of testing embraced three flow regimes:

(1) undeveloped flow

(2) semi-developed flow

(3) fully developed flow

In this thesis the onset of fully developed flow is defined as taking place when the boundary layer thickness of one plane, for flow between two planes, becomes half the distance between the planes. Conversely, undeveloped flow exists when the boundary layer thickness of a plane is less than half the distance between the planes. In both cases, identical flow patterns are established in the top and bottom collector sections. On the other hand, semi-developed flow occurs in the model when (for a given element) flow is fully developed in the bottom section whilst still developing in the top section. According to Kays (42), if the Prandtl number of the fluid is unity (for air the Prandtl number is approximately unity), then heat and momentum are diffused through the fluid at approximately the same rates. Thus boundary layer thicknesses referred to in this thesis may be derived from hydrodynamic boundary layer theory.

The derivation of the collector longwave radiation electrical-analogy circuit is given in Appendix 8 and the reader is referred to this section for an explanation of the thermal radiation terms that appear in the following heat-transfer equations.

3.1 THE COLLECTOR ENERGY BALANCES - DEVELOPING FLOW

In the derivation of the following heat-transfer equations, the boundary layer thicknesses in both the top and bottom sections are taken to be small enough that flow remains undeveloped. Thus all convection heat-transfer coefficients of the collector internal-surfaces are related to flat-plate heat-transfer theory.

(a) The Energy Balance on the Fluid in the Top Section of the Collector

\+ (1) forced-convection heat-transfer from the black-netting to the fluid

= (2) forced-convection heat-transfer from the fluid to the top cover

\+ (3) fluid heat-gain

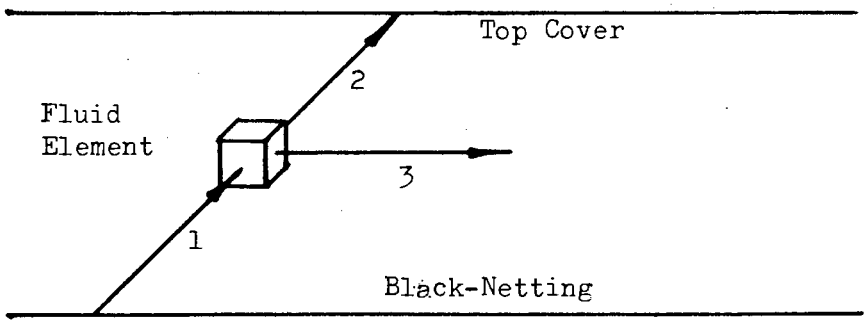

$$h_{nt}.A_n.(T_n-T_{fst})$$

$$= h_{ct}.A_{ct}.(T_{fst}-T_{ct})$$

$$+ \dot{m}_t.C_{pt}.(T_{outt}-T_{int}) \quad \ldots\ldots\ldots\ldots\ldots\ldots\ldots\ldots\ldots\ldots\ldots\ldots \quad (4)$$

(b) Energy Balance on the Fluid in the Bottom Section of the Collector

+ (1) forced-convection heat-transfer from the black-netting to the fluid

= (2) forced-convection heat-transfer from the fluid to the bottom cover

+ (3) forced-convection heat-transfer from the fluid to the edge covers

+ (4) fluid heat-gain

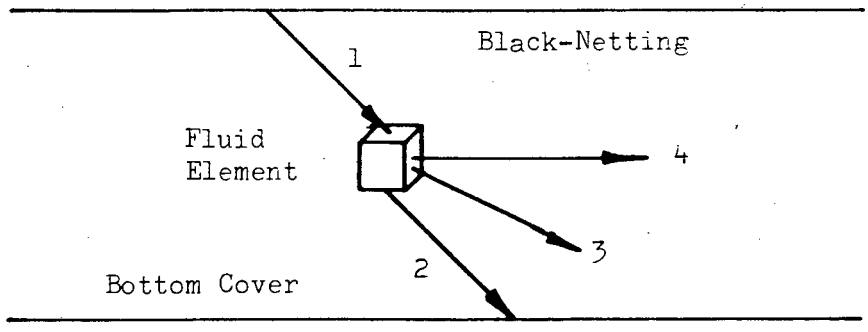

$$h_{nb}.A_n.(T_n-T_{fsb})$$

$$= h_{cb}.A_{cb}.(T_{fsb}-T_{cb})$$

$$+ 2.(h_{ce}.A_{ce}.(T_{fsb}-T_{ce}))$$

$$+ \dot{m}_b.C_{pb}.(T_{outb}-T_{inb}) \quad \ldots\ldots\ldots\ldots\ldots\ldots\ldots\ldots\ldots\ldots (5)$$

(c) Energy Balance on the Top Cover

\+ (1) solar radiation absorbed in the top cover

\+ (2) forced-convection heat-transfer from the fluid into the top cover

\+ (3) heat radiated from netting to top cover

\+ (4) heat radiated from bottom cover to top cover

\+ (5) heat radiated from edge covers to top cover

= (6) heat radiated from the top cover to the sky

\+ (7) heat radiated from the top cover to the ground

\+ (8) heat convected from the top cover to the atmosphere

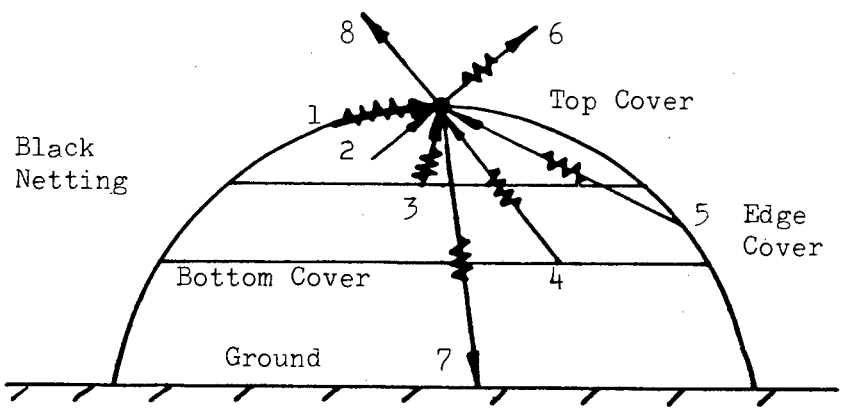

$$
\begin{aligned}
& A_{cts}.I.\alpha_{cte} \\
+\ & h_{ct}.A_{ct}.(T_{fst}-T_{ct}) \\
+\ & A_{n}.F_{n-ct}.\varepsilon_{n}.\varepsilon_{ct}.\sigma.(T^4_{n}-T^4_{ct}) \\
+\ & A_{cb}.F_{cb-ct}.\varepsilon_{cb}.\varepsilon_{ct}.(1-\varepsilon_{n}).\sigma.(T^4_{cb}-T^4_{ct}) \\
+\ & 2.A_{ce}.F_{ce-ct}.\varepsilon_{ce}.\varepsilon_{ct}.(1-\varepsilon_{n}).\sigma.(T^4_{ce}-T^4_{ct}) \\
=\ & A_{ct}.F_{ct-s}.\varepsilon_{ct}.\varepsilon_{s}.\sigma.(T^4_{ct}-T^4_{s}) \\
+\ & (\sigma.(T^4_{ct}-T^4_{g}))/((1/A_{ct}.F_{ct-g}.\varepsilon_{ct}.(1-\varepsilon_{n}).(1-\varepsilon_{cb})) + (1-\varepsilon_{g})/(\varepsilon_{g}.A_{g})) \\
+\ & h_{wct}.A_{ct}.(T_{ct}-T_{a}) \quad \ldots\ldots\ldots\ldots\ldots\ldots\ldots\ldots\ldots\ldots\ldots\ldots \quad (6)
\end{aligned}
$$

(d) Energy Balance on Bottom Cover

+ (1) forced-convection heat-transfer from the fluid to the bottom cover

+ (2) solar radiation absorbed by the bottom cover

+ (3) heat radiated from the netting cloth to the bottom cover

= (4) heat radiated from the bottom cover to the top cover

+ (5) heat radiated from the bottom cover to the sky

+ (6) heat radiated from the bottom cover to the edge covers

+ (7) heat radiated from the bottom cover to the ground

+ (8) heat convected from the lower side of the bottom cover to the greenhouse atmosphere

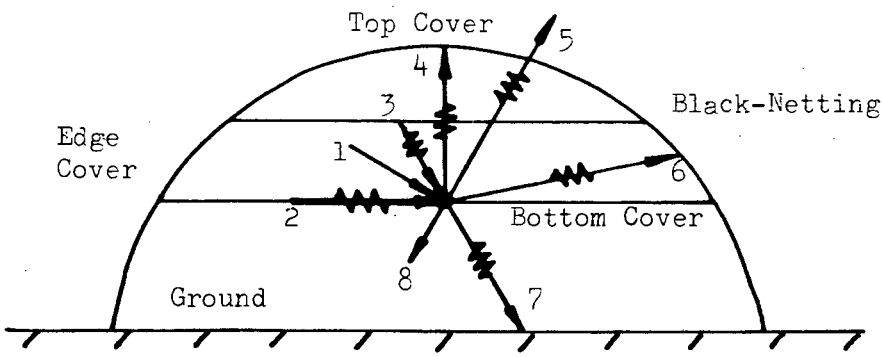

$$h_{cb}.A_{cb}.(T_{fsb}-T_{cb})$$

$$+ \; A_{cb}.I.\alpha_{cbe}$$

$$+ \; A_{n}.F_{n-cb}.\varepsilon_{n}.\varepsilon_{cb}.\sigma.(T_{n}^4-T_{cb}^4)$$

$$= \; A_{cb}.F_{cb-ct}.\varepsilon_{cb}.\varepsilon_{ct}.(1-\varepsilon_{n}).\sigma.(T_{cb}^4-T_{ct}^4)$$

$$+ \; A_{cb}.F_{cb-s}.\varepsilon_{cb}.\varepsilon_{s}.(1-\varepsilon_{ct}).(1-\varepsilon_{n}).\sigma.(T_{cb}^4-T_{s}^4)$$

$$+ \; 2.A_{cb}.F_{cb-ce}.\varepsilon_{cb}.\varepsilon_{ce}.\sigma.(T_{cb}^4-T_{ce}^4)$$

$$+ \; (\sigma.(T_{cb}^4-T_{g}^4))/((1/A_{cb}.F_{cb-g}.\varepsilon_{cb}) + (1-\varepsilon_{g})/(\varepsilon_{g}.A_{g})$$

$$+ \; h_{convcb}.A_{cb}.(T_{cb}-T_{a}) \qquad \ldots\ldots\ldots\ldots\ldots\ldots\ldots\ldots\ldots\ldots \quad (7)$$

(e) Energy Balance on Edge Cover

\+ (1) forced-convection heat-transfer from fluid to the edge cover

\+ (2) solar radiation absorbed by edge cover

\+ (3) heat radiated from netting to edge cover

\+ (4) heat radiated from bottom cover into edge cover

= (5) heat radiated from the edge cover to the ground

\+ (6) heat radiated from the edge cover to the sky

\+ (7) heat radiated from the edge cover to the top cover

\+ (8) heat convected from the outside-surface of the edge cover to the atmosphere

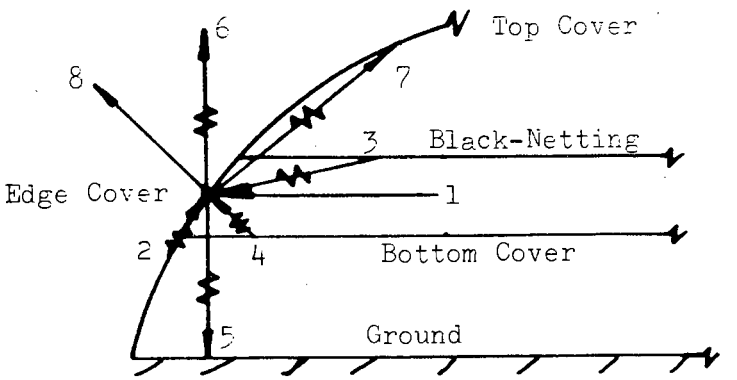

$$\begin{aligned}
& h_{ce}.A_{ce}.(T_{fsb}-T_{ce}) \\
+\ & A_{ces}.I.\alpha_{cee} \\
+\ & A_{n}.F_{n-ce}.\varepsilon_{n}.\varepsilon_{ce}.\sigma.(T^4_{n}-T^4_{ce}) \\
+\ & A_{cb}.F_{cb-ce}.\varepsilon_{cb}.\varepsilon_{ce}.\sigma.(T^4_{cb}-T^4_{ce}) \\
=\ & (\sigma.(T^4_{ce}-T^4_{g}))/((1/A_{ce}.\varepsilon_{ce}.(F_{ce-gout} + F_{ce-gin}.(1-\varepsilon_{cb}))) + (1-\varepsilon_{g})/(\varepsilon_{g}.A_{g})) \\
+\ & \sigma.A_{ce}.\varepsilon_{ce}.\varepsilon_{s}.(F_{ce-sout} + F_{ce-sin}.(1-\varepsilon_{n}).(1-\varepsilon_{ct})).(T^4_{ce}-T^4_{s}) \\
+\ & A_{ce}.F_{ce-ct}.\varepsilon_{ce}.\varepsilon_{ct}.(1-\varepsilon_{n}).\sigma.(T^4_{ce}-T^4_{ct}) \\
+\ & h_{wce}.A_{ce}.(T_{ce}-T_{a}) \qquad \ldots\ldots\ldots\ldots\ldots\ldots\ldots\ldots\ldots\ldots\ldots\ldots \text{(8)}
\end{aligned}$$

(f) Energy balance on Black-Netting

+ (1) solar radiation absorbed by black-netting

= (2) forced-convection heat-transfer from the top side of the netting to the top fluid

+ (3) heat radiated to the top cover from the netting

+ (4) heat radiated to the sky from the netting

+ (5) forced-convection heat-transfer from the bottom side of the netting to the bottom fluid

+ (6) heat radiated into the bottom cover from the netting

+ (7) heat radiated into the ground from the netting

+ (8) heat radiated to the edge covers from the netting

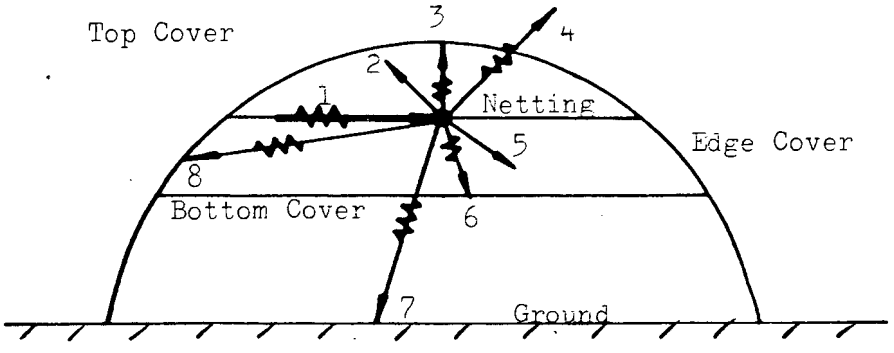

$$A_n.I.\alpha_{ne}$$

$$= h_{nt}.A_n.(T_n-T_{fst})$$

$$+ A_n.F_{n-ct}.\varepsilon_n.\varepsilon_{ct}.\sigma.(T_n^4-T_{ct}^4)$$

$$+ A_n.F_{n-s}.\varepsilon_n.\varepsilon_s.(1-\varepsilon_{ct}).\sigma.(T_n^4-T_s^4)$$

$$+ h_{nb}.A_n.(T_n-T_{fsb})$$

$$+ A_n.F_{n-cb}.\varepsilon_n.\varepsilon_{cb}.\sigma.(T_n^4-T_{cb}^4)$$

$$+ (\sigma.(T_n^4-T_g^4))/((1/A_n.F_{n-g}.\varepsilon_n.(1-\varepsilon_{cb})) + (1-\varepsilon_g)/(\varepsilon_g.A_g))$$

$$+ 2.A_n.F_{n-ce}.\varepsilon_n.\varepsilon_{ce}.\sigma.(T_n^4-T_{ce}^4) \quad \ldots\ldots\ldots\ldots\ldots\ldots\ldots\ldots (9)$$

(g) Energy Balance on the Fluid(s)

\+ (1) heat-gain by top fluid

\+ (2) heat-gain of bottom fluid

= (3) heat-gain of fluid

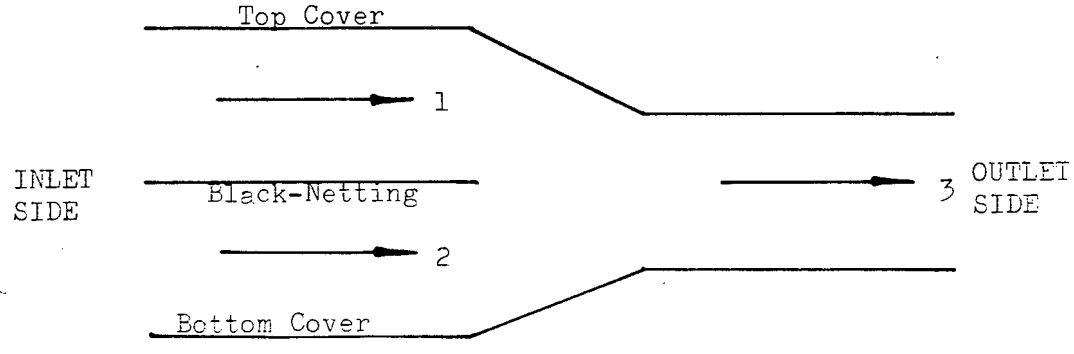

$$\dot{m}_t \cdot C_{pt} \cdot (T_{outt} - T_{int})$$

$$+ \quad \dot{m}_b \cdot C_{pb} \cdot (T_{outb} - T_{inb})$$

$$= \quad \dot{m} \cdot C_p \cdot (T_{out} - T_{in}) \qquad \ldots\ldots\ldots\ldots \qquad (10)$$

3.2 THE COLLECTOR ENERGY BALANCES - SEMI-DEVELOPED FLOW

For a given mass-flowrate, the length from the collector leading edge to the point where fully developed flow occurs is different for the top and bottom sections of the model collector. This is borne out in Appendix 7 where it is shown that with changing mass-flowrate the bottom collector section is the first to become fully developed. In other words, given the correct length from the collector leading edge and a suitable mass-flowrate, the situation will arise where flow in the bottom section will be fully developed whilst flow in the top section will still be developing. To solve such elements an appropriate set of simultaneous equations was developed, where the heat-transfer relationships for the bottom section were based on fully-developed tube-flow relationships, whilst the developing top section was treated as in 3.1 above.

The tube heat-transfer relationships define heat-transfer as taking place between the tube and the fluid, where the fluid temperature is defined as the mean bulk-fluid temperature. The mean bulk-fluid temperature is the average of the bulk inlet-fluid temperature and the bulk outlet-fluid temperature. The equations are written as before, but the free-stream temperatures are replaced with mean bulk-fluid temperatures when considering forced-convection heat-transfer in the bottom section of the collector. Similarly, the surface heat-transfer coefficients in the bottom section are derived from tube rather than flat-plate relationships (see Appendix 20).

3.3 THE COLLECTOR ENERGY BALANCES - FULLY DEVELOPED FLOW

Further changes in the fluid flowrate and a position suitably distant from the collector leading edge results in a situation where the flow regime in both the top and bottom collector elements is fully developed. The solution for this situation is an extension of that discussed in 3.2 above, in that the forced-convection heat-transfer in both the top and bottom collector sections is now based on tube flow theory.

In each of the above cases, the solution consists of a set of seven simultaneous non-linear equations containing seven unknown variables, namely:

(1) The top-cover temperature
(2) The edge-cover temperature
(3) The bottom-cover temperature
(4) The netting temperature
(5) The top outlet-air temperature
(6) The bottom outlet-air temperature
(7) The mixed outlet-air temperature

The solutions are found by using Newton's method to create seven linear equations which are solved using Gauss-Jordan elimination. An analysis of the mathematics involved in solving "N" simultaneous non-linear equations is given in Appendix 9.

The theoretical model considers the collector as consisting of ten elements. Starting at the inlet side, and using specified input values

of inlet-air temperature, ambient-air temperature, ground temperature, windspeed, air mass-flowrate and insolation levels, calculations are made to decide whether the flow is undeveloped, semi-developed or fully developed. Once the applicable set of equations has been selected, the local values of such parameters as heat-transfer coefficients, radiation shape factors etc. are calculated. (The details of the derivations and calculations of the various heat-transfer coefficients and radiation shape factors are given in Appendix 10 and 11 respectively). The initial solution is assumed and Newton's method is used to find values for the seven unknown temperatures. The next element is then analysed, using the previous element's top and bottom outlet-air temperatures as the new element's top and bottom inlet-air temperatures. The procedure is repeated and all the elements are analysed until the outlet end of the collector is reached. At this point the outlet-air temperature is used to calculate a theoretical collector heat-gain, which is compared with empirical results from a similar collector configuration using identical input values.

The prediction of performance for a life-size Baird-type solar collector (specified in Appendix 12) is made using the same theoretical approach. Naturally the actual input values change and consideration has to be given to the effects of different scale on the nature of the flow and the boundary layer growth. Chapter 5 and Appendix 7 contain analyses of the life-size system and show limitations that exist regarding the performance prediction for such a system. The results of the life-size Baird-type solar collector are listed in Appendix 25.

CHAPTER FOUR

EXPERIMENT

An experiment was needed to obtain measured performance data for the Baird-type solar collector for use in a comparison with theoretical performance. A model of the Baird-type integral greenhouse solar collector was therefore constructed, and its performance was evaluated using radiation from a solar simulator.

In order to measure the collector heat-gain, it was necessary to measure the collector air mass-flowrate and the inlet-air and outlet-air temperatures. Use of this information and a knowledge of the incident radiation intensity enabled the calculation of the collector efficiency. A complete specification of collector performance required a knowledge of all the input variables. Besides those mentioned above, this included the ambient-air temperature in the vicinity of the collector, the ground or floor temperature and the windspeed around the collector. Since these parameters were measured for each test, and since the material properties and heat-transfer coefficients of the collector surfaces were known or established, it was possible to predict the outlet-air temperature for each test by solving the set of simultaneous equations using the measured input data. The following sections of Chapter 4 describe the experimental equipment.

4.1 THE SOLAR SIMULATOR

The concept of solar simulation was discussed in Chapter 2 and certain criteria emerged as being relevant to simulator performance. In summary, these included:

(1) the uniformity of radiation intensity on the collector plane.

(2) the parallelism of incident radiation on the collector plane.

(3) the ability to change the angle of incident radiation through movement of source azimuth and altitude.

An important consideration for a simulator radiation source is that it should be capable of producing variable intensities without changing the nature of the spectral distribution or affecting the useful lamp life. Some variation may be achieved by physically moving the radiation source away from the test surface if it has some divergence in its output beam (as is generally the case). However, in order to contain the system in a physically manageable space it is desirable to be able to reduce the radiation output by reducing the input electrical power. Appendix 4 contains a comparison of the relative advantages and disadvantages of the three lamps most frequently used for solar simulators, namely, the Xenon Arc, the Compact Source Iodide Arc and the Tungsten-Halogen Quartz Filament lamp.

A simulator was designed (see Appendix 4) so as to satisfy as many of the above criteria as possible. Two CSI lamps were mounted on a trolley that could move along a semi-circular track. This provided altitude variation. Azimuthal variation was achieved by rotating the collector in the plane of the floor. Radiation intensity was controlled by varying the input voltage to the lights, whilst the input voltage to the system

was made independent of mains supply fluctuations by means of a voltage stabilising device. The simulator is shown in Photograph 1.

Photograph 1: The Solar Simulator

4.2 THE MODEL BAIRD-TYPE GREENHOUSE SOLAR COLLECTOR

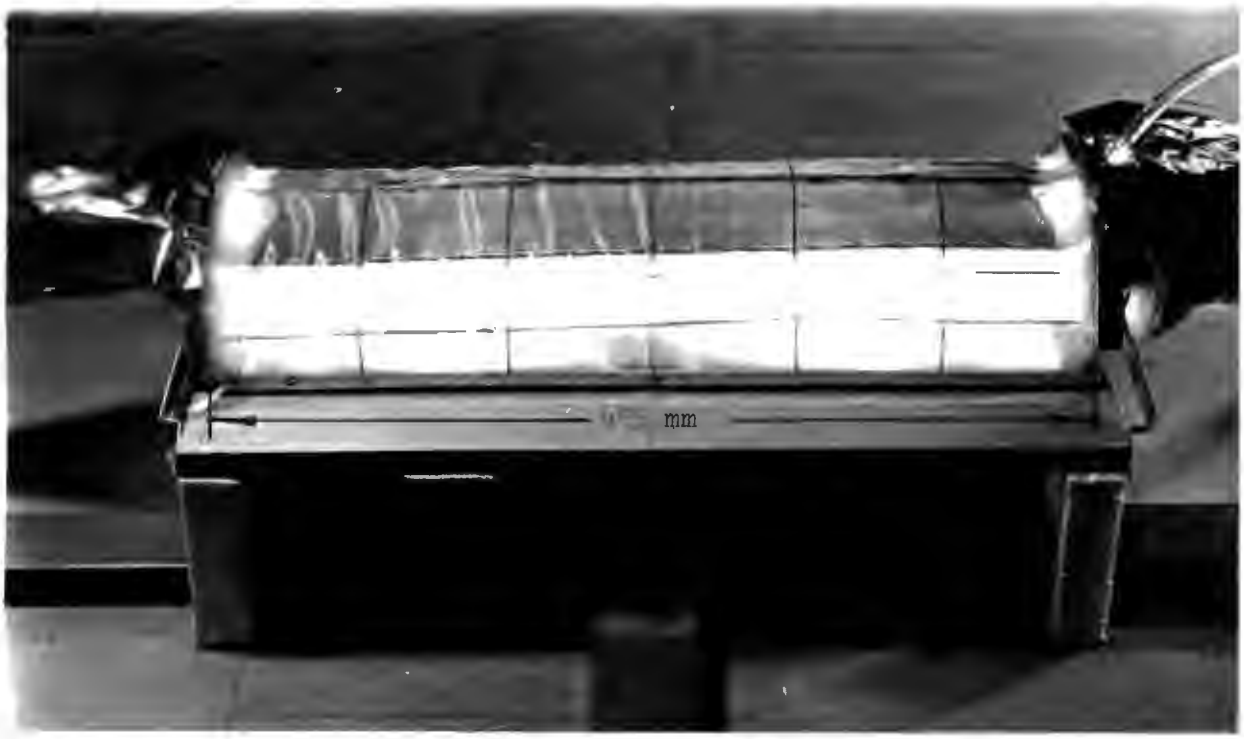

Photograph 2: The Model Baird-Type Greenhouse Solar Collector

The model was built in accordance with the proportions of commercially available greenhouses, however, the solar simulator restricted the model size to approximately 1:66 scale (in order that radiation uniformity was maintained to within 10% of the mean value). The result was a greenhouse 455mm long and 150mm wide (Appendix 13 contains details of the model dimensions and cross-sectional areas). Photograph 2 shows the model with the solar collector built into the greenhouse roof. "Swirling-chambers" can be seen at the inlet and outlet ends of the collector. These are thermally insulated with a 50mm thick layer of glassfibre and covered with a reflective cover of Aluminium-coated celluloid film. They enhance the accuracy of the air-temperature measurements by mixing the air before measurement takes place. In addition, the temperature measuring

device is protected from direct incident radiation and hence erroneous air-temperature measurement. Also visible is the clear plastic hose, which was part of a pressure tapping used to measure the internal pressure in the solar collector (this assisted in calculating the air mass-flowrate through the collector). The model was mounted on a rectangular wooden frame, with center removed, all of which was placed approximately 100mm above the floor level.

4.3 AIR SUPPLY AND FLOW MEASUREMENT

The solar collector heats air that is forced through it, and for this an air supply source was needed. An air compressor was used for this purpose, equipped with a regulating valve for flowrate adjustment and having a maximum delivery rate of approximately 0.0035 kg/s. The velocity of flow was measured by means of a sharp-edged orifice-plate with corner pressure-tappings, designed in accordance with B.S. 1042: Part 1: 1964 (43)

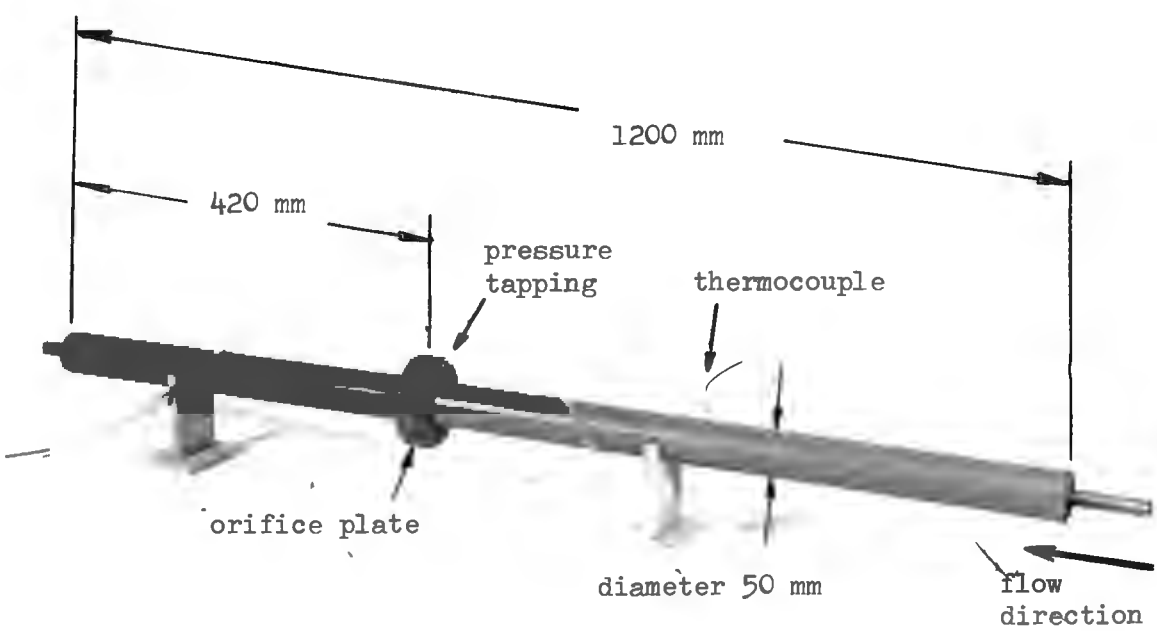

Photograph 3: The Orifice-Plate Apparatus

The orifice-plate was designed to measure air velocities over the range available from the compressor. The unit is shown in Photograph 3. The clear plastic hoses that connected with the pressure-tappings are visible. These connected with an inclined mercury-manometer which was used to measure upstream and downstream orifice-plate fluid pressures. Also visible is the upstream-fluid temperature measuring thermocouple. Details of the orifice-plate design and a sample flowrate calculation are given in Appendix 14.

4.4 TEMPERATURE MEASUREMENT

It was necessary to determine the temperature of the following variables for each test:

(a) collector inlet-air temperature
(b) collector outlet-air temperature
(c) ambient-air temperature
(d) floor/ground temperature
(e) upstream orifice-plate air temperature

Iron-Constantan thermocouples were used to measure these variables, except the ambient-air temperature of the laboratory, for which a shielded mercury-bulb thermometer was used. The thermocouples were connected to a data processing device which converted the thermocouple ouput to a temperature value, calibrated as correct to the nearest 0.1 degree Centigrade (see Appendix 15). Thermocouples were used because they have a much lower thermal-inertia than mercury-bulb thermometers. Also, they have the advantage of being very small, consequently they are easier to install in confined spaces and are less disturbing to flow regimes. Because of their low heat-capacity, they have a very small effect on temperature regimes.

The inlet-air temperature thermocouple was placed at the exit of the inlet "swirl-chamber", and readings from it were compared with values obtained from another thermocouple placed directly upstream of the "swirl-chamber". The two values were always within 0.1 degree Centigrade of each other which confirmed that the inlet-air temperature thermocouple was not severely affected by collector re-radiation. The

outlet-air temperature thermocouple was placed directly downstream of the outlet "swirl-chamber". The ambient-air temperature was measured with a shielded mercury thermometer placed about two metres to the side of the simulator and about one metre above the floor level. Upstream orifice-plate air temperature was measured with a thermocouple as shown in Photograph 3.

4.5 RADIATION INTENSITY MEASUREMENT

Among the types of instruments which are available for measuring radiation intensity, two are shown below in Photograph 4 and are the Thermopile (a) and Solarimeter (b) respectively.

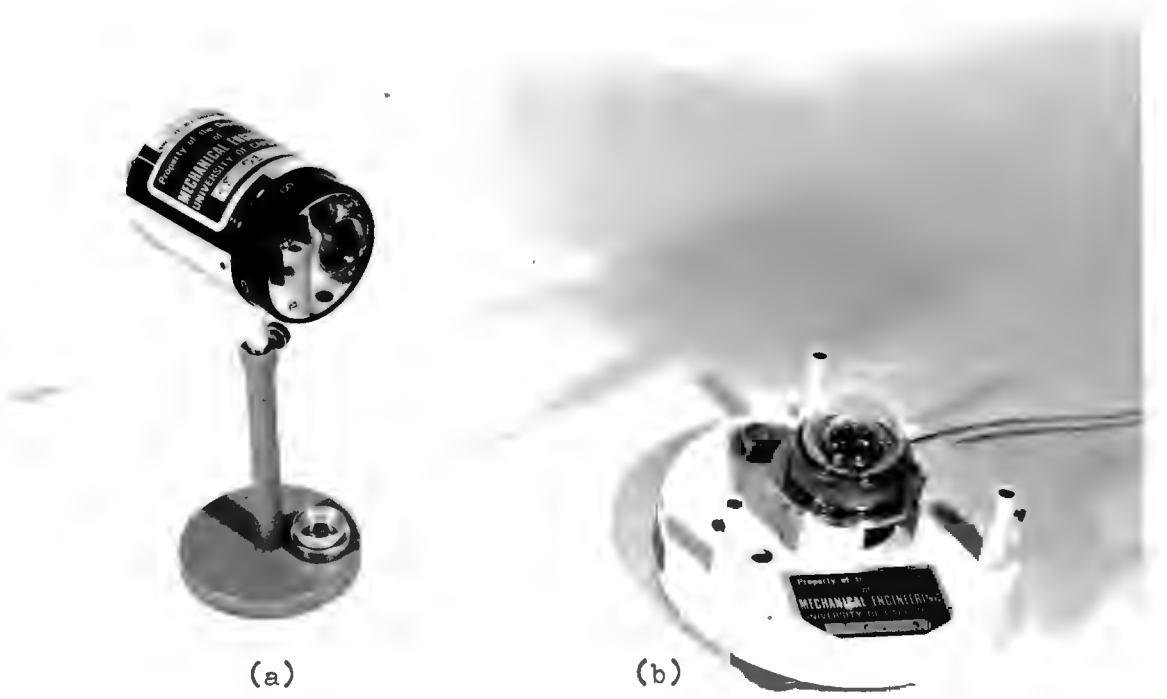

Photograph 4: (a) Thermopile (b) Solarimeter

Each of these instruments was used in combination with a voltmeter. The output voltage was directly proportional to radiation intensity. Although both instruments measure the span of wavelengths pertaining to solar radiation, the thermopile responds to a broader wavelength spectrum. The wavelength response range of each instrument is quoted by

the manufacturers to be between 0.15 and 15 micrometres for the thermopile and between 0.3 and 2.5 micrometres for the solarimeter. The thermopile was designed with a conical entrance configuration that accepts radiation through a total acceptance angle of ten degrees. On the other hand, the solarimeter utilises a clear, hemispherical cover that enables it to view all radiation coming from the hemisphere above the instrument. The simulated solar radiation incident on the model was measured at six equispaced positions along the collector using a solarimeter, and the results were used with Simpson's Rule to yield a mean radiation intensity incident on the model. Appendix 16 contains details of these measurements and calculations.

4.6 THE GENERAL LAYOUT AND EXPERIMENTAL METHOD

Photograph 5 shows the general layout of the experimental apparatus described above. Tests were conducted with the system in the following manner. The simulator lights and the air compressor were switched on and allowed time to reach steady-state. (Temperature measurements indicated that steady state conditions were established approximately two hours after start-up). The radiation intensity was measured, and the temperatures listed in 4.4 were recorded. In addition, the atmospheric pressure, the internal solar collector pressure, and the upstream and downstream orifice-plate pressures were recorded. These were needed to calculate the air mass-flowrate. Also required for this calculation was the relative humidity of the air, which was measured by the use of a wet and dry-bulb thermometer. The tests were repeated for different flowrates and different radiation intensities. A total of forty-three tests were conducted with an irradiation of 852 Watts/square metre and ten tests with an irradiation of 544 Watts/square metre.

These tests yielded experimental results of the collector performance. In order to predict theoretical results, the radiation properties of the polyethylene cover and black-netting for simulated solar and longwave radiation must be known, as well as the black-netting convection heat-transfer coefficient. Unfortunately, this was not initially the case for the materials used and so it was necessary to derive them experimentally. The experimental equipment and methods used to evaluate these properties are listed in Appendices 2 and 3.

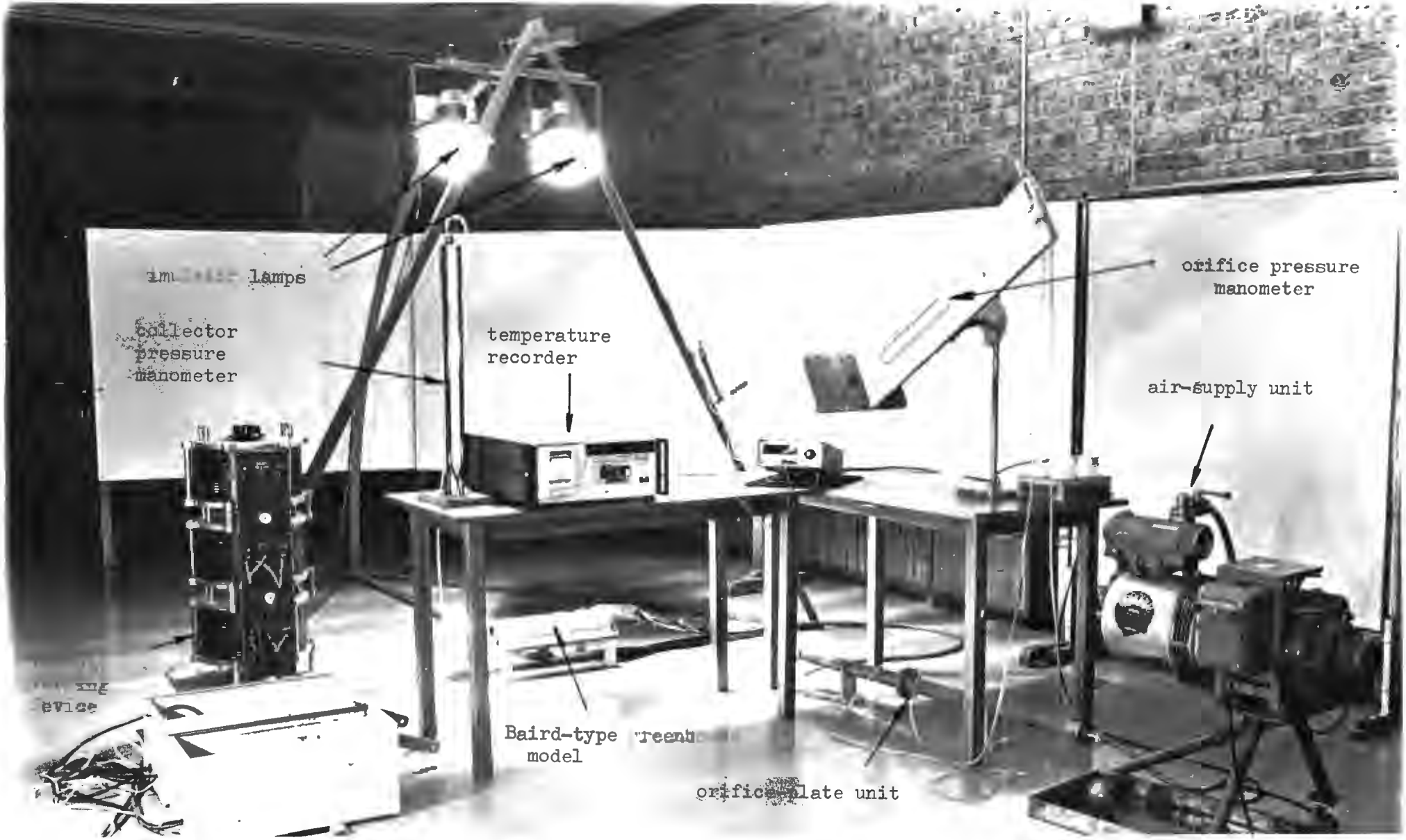
lamps
collector pressure manometer
temperature recorder
orifice pressure manometer
air-supply unit
Baird-type
model
orifice plate unit

CHAPTER FIVE

RESULTS AND DISCUSSION

5.1 EXPERIMENTAL AND THEORETICAL RESULTS OF THE SOLAR COLLECTOR MODEL

Fifty-three tests were conducted on the model Baird-type solar collector. Forty-three of these correspond to an incident radiation intensity of 852 Watts/square metre and ten correspond to an incident radiation intensity of 544 Watts/square metre. These values of incident radiation were used since they are similar to January and June peak values in the Cape Peninsula (see Appendix 17) and represent maximum and minimum intensities attainable in the solar simulator. (Extremes of incident radiation are desirable to help establish how sensitive the collector efficiency is to a change in insolation, and to see how well the theoretical model is able to predict differences in performance as a result of these changes.)

The experiments were conducted in a laboratory whose ambient-air temperature was recorded to vary between 17 and 21 degrees Centigrade. Seventy-five percent of the tests were conducted with an ambient-air temperature between 18 and 19.5 degrees Centigrade (see Appendix 18). However, much greater differences existed in the solar collector inlet-air temperature (see Figures 2 and 3), with lower and upper limits being approximately 21 and 31 degrees Centigrade respectively. The inlet-air temperature varies as a function of air mass-flowrate and is a consequence of the throttling process used for flowrate regulation. The scatter in the inlet-air temperatures shown in Figures 2 and 3 was

FIGURE 2: COLLECTOR INLET AND OUTLET-AIR AND LABORATORY AMBIENT-AIR TEMPERATURES

(Incident Radiation = 852 W/m²)

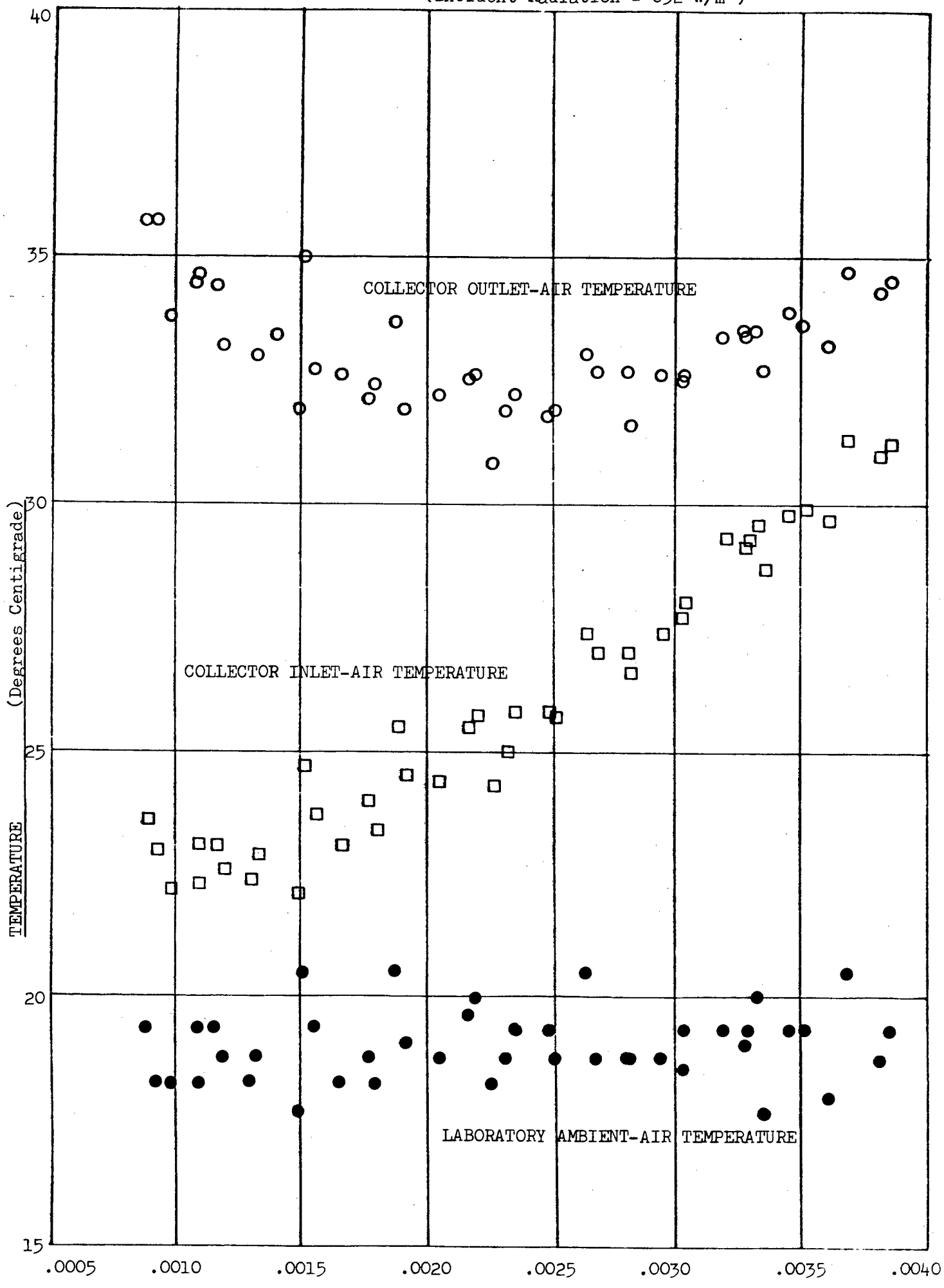

FIGURE 3: COLLECTOR INLET AND OUTLET-AIR AND LABORATORY AMBIENT-AIR TEMPERATURES

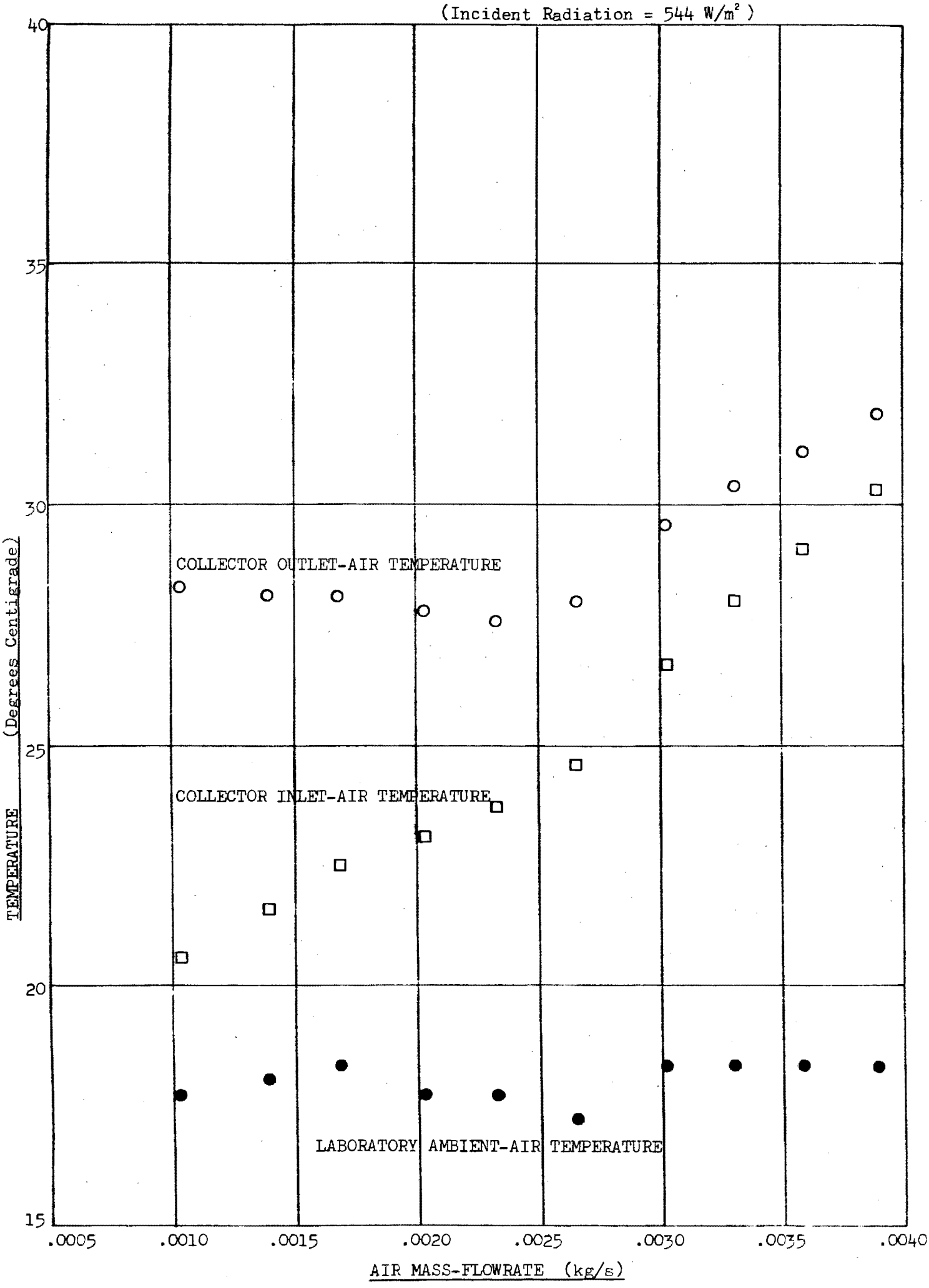

caused by variations in the laboratory ambient-air temperature (since the compressor ingests laboratory air). The Hottel-Whillier equation (Equation 1b, page 7) prescribes that collector efficiency is dependent on the difference between the inlet-air temperature and the ambient-air temperature. The changes in ambient-air and inlet-air temperatures are therefore expected to influence the collector performance.

The experimental and theoretical results are presented graphically with collector efficiency being the dependent variable and air mass-flowrate being the independent variable. The theoretical predictions are generated using two approaches. The first approach assumes that fully developed flow does not occur in either the top or bottom sections of the collector. All internal convection processes are represented using flat-plate heat-transfer considerations. From here on this approach is referred to as "The Flat-Plate Heat-Transfer Model". The second approach makes use of the flat-plate heat-transfer approach until boundary layer theory predicts that flow has become fully developed - from which point onwards the heat-transfer processes are described by tube-type relationships. From here on this approach is referred to as "The Flat-Plate/Tube Heat-Transfer Model". Both of these models consider the collector to be made up of ten elements or segments.

5.1.1 Results of the Flat-Plate Heat-Transfer Model

Results from the experimental data and the theoretical test predictions are shown in Figures 4 and 5 and listed in Appendix 19. Figure 4 shows the results for an incident radiation of 852 Watts/square metre and Figure 5 shows the results for an incident radiation of 544 Watts/square metre respectively. In both cases the collector efficiency is of the order of 35 percent, and shows a trend of decreasing efficiency for

FIGURE 4: MEASURED AND PREDICTED COLLECTOR EFFICIENCIES (Flat-Plate Heat-Transfer Model)

(Ambient-Air Temperature varies)
(Inlet-Air Temperature varies)
(Incident Radiation = 852 W/m²)

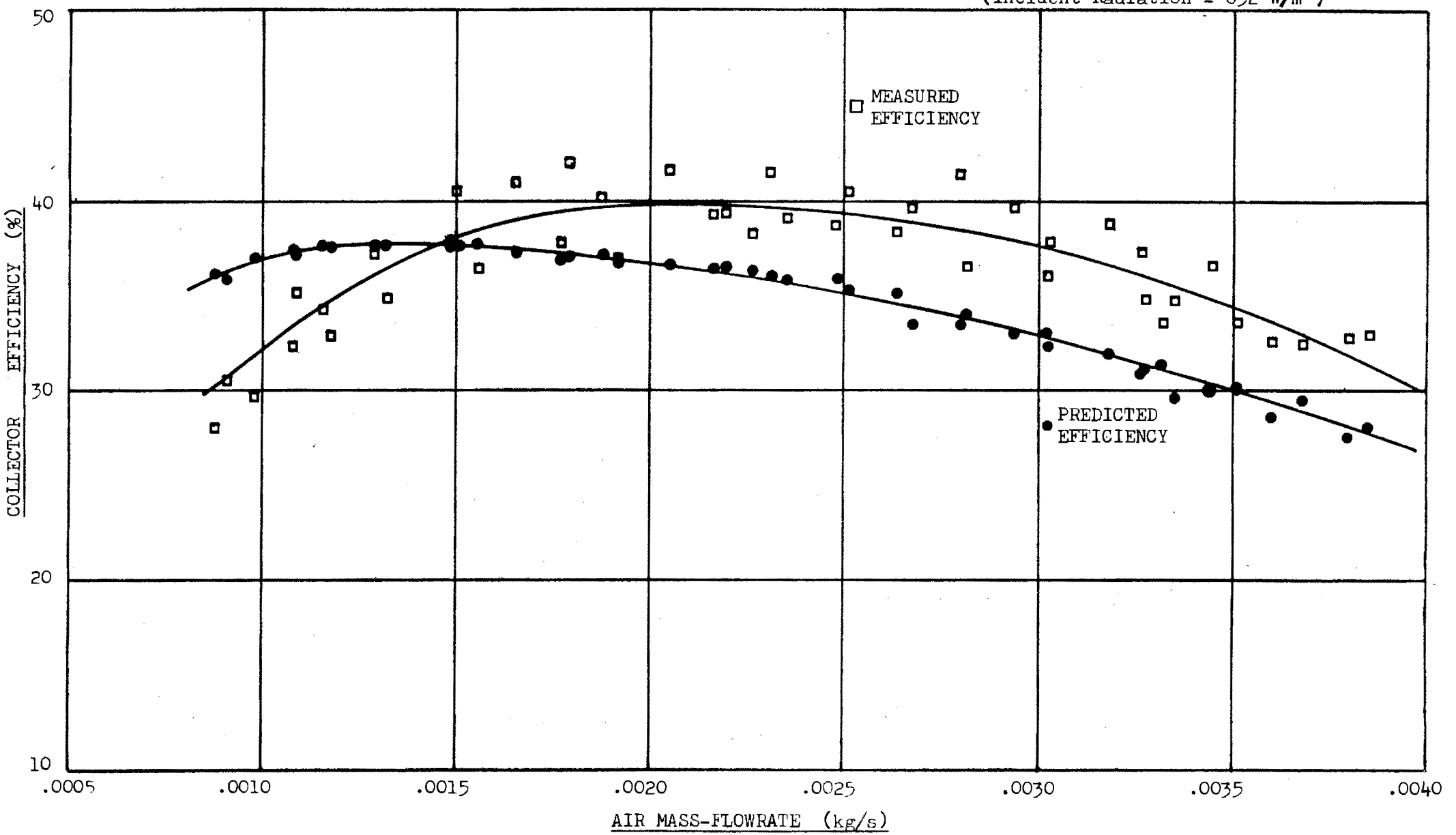

FIGURE 5: (Flat-Plate Heat-Transfer Model)
MEASURED AND PREDICTED COLLECTOR EFFICIENCIES

*(Ambient-Air Temperature varies)
(Inlet-Air Temperature varies)
(Incident Radiation = 544 W/m^2)

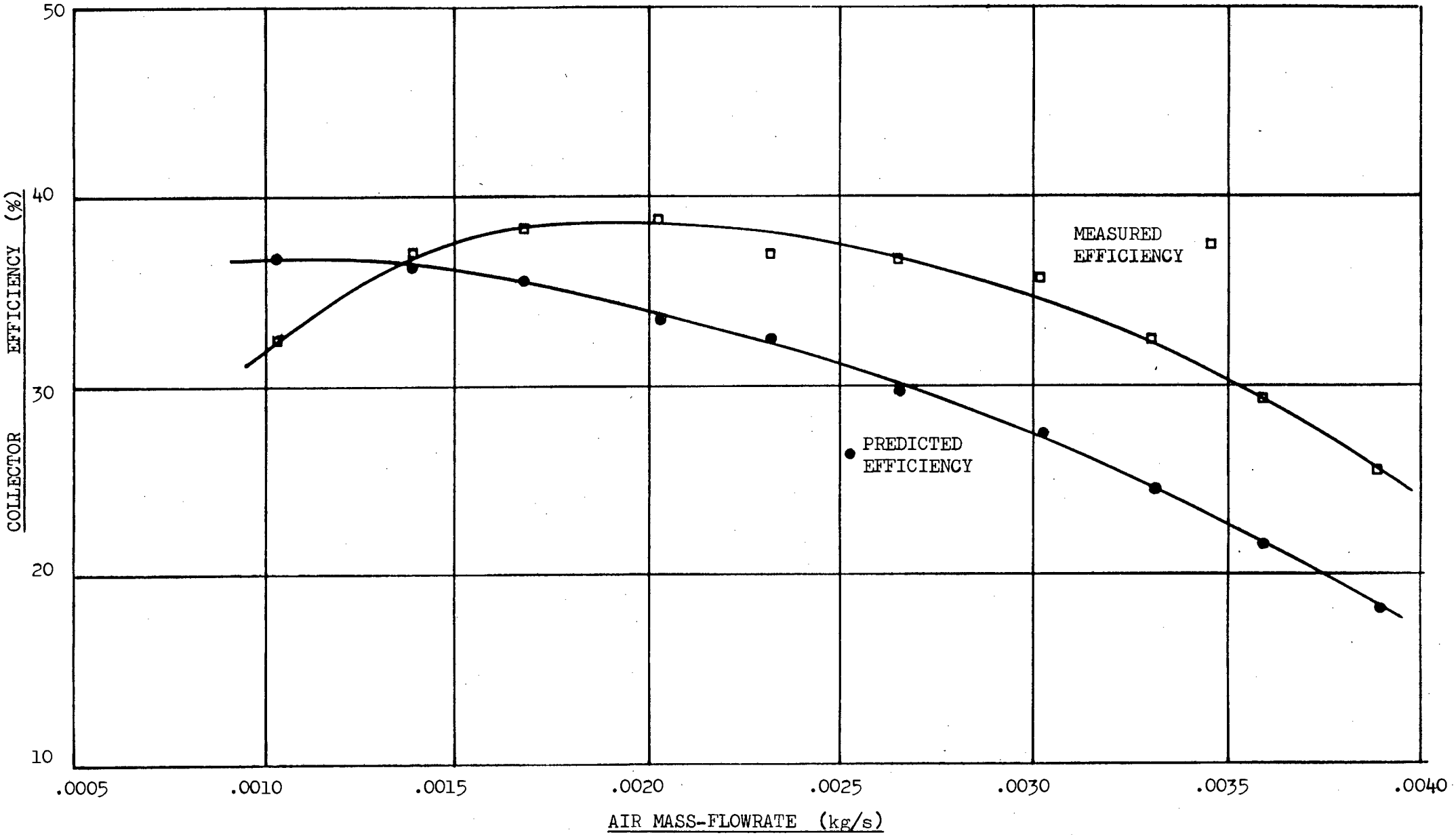

FIGURE 6: HISTOGRAM OF PERCENTAGE PREDICTED HEAT-GAIN ERRORS (Flat-Plate Heat-Transfer Model)

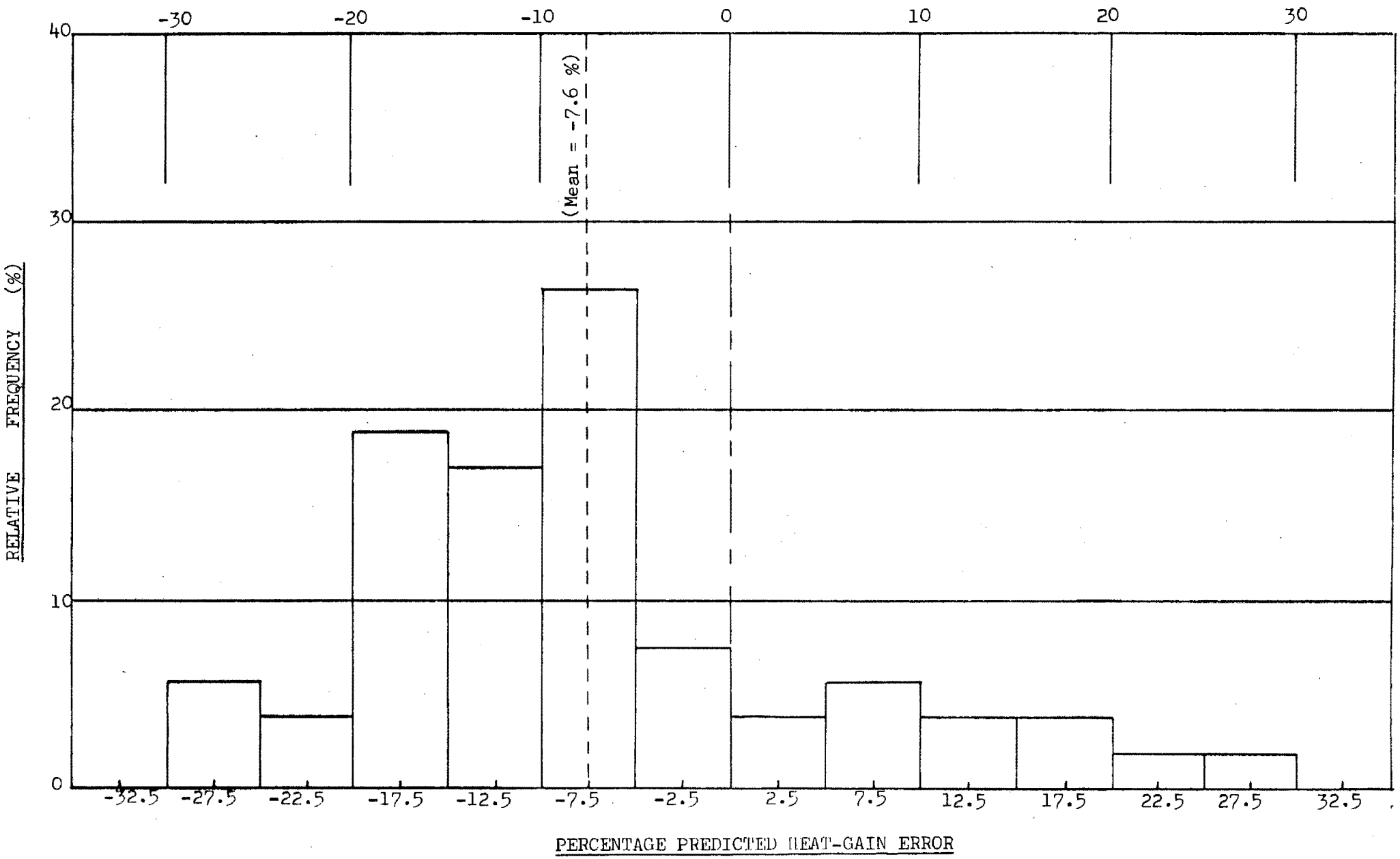

FIGURE 7: PERCENTAGE PREDICTED HEAT-GAIN ERROR (Flat-Plate Model)

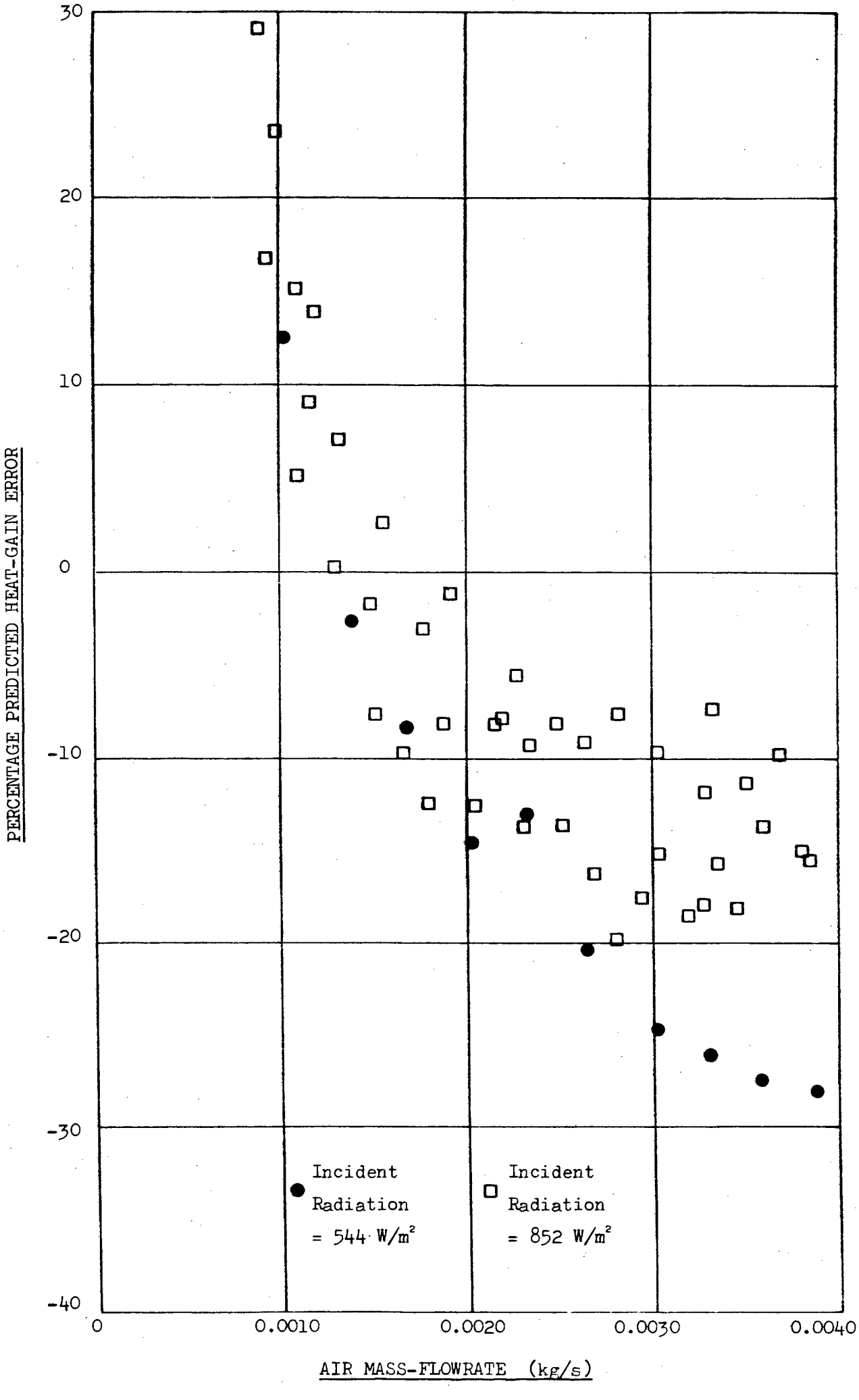

flowrates both higher and lower than about 0.0020 kg/s. The black-netting heat-transfer coefficient increases with increasing flowrate, which indicates that the collector efficiency should increase with increasing flowrate. However, the fact that inlet-air temperature increases with increasing flowrate has significance on the longwave radiation losses from the collector to the environment. The results show that these radiative losses start to outweigh the gains from an increasing black-netting heat-transfer coefficient at flowrates higher than about 0.0020 kg/s.

For both insolation levels, a comparison of empirical and predicted test results shows that the trends of each are similar, although the predicted test results have slightly lower maximum collector efficiencies, occuring at lower flowrates. Figure 6 is a histogram showing the relative frequency distribution of predicted heat-gain errors for the fifty three tests. The mean predicted heat-gain error is an underprediction of 7.6 percent, with a Standard Deviation of 12.4 percent. The underprediction may be partly the result of specifying the ground temperature to have the same value as the laboratory ambient-air temperature. (The ground in the immediate vicinity of the collector model is at a higher temperature than the ground outside the influence of radiation from the solar simulator). Figure 7 represents percentage predicted heat-gain error as a function of air mass-flowrate and shows that overpredictions are made at the lower flowrates whilst underpredictions are made at the higher flowrates. All predictions of collector efficiency are within a band between +29 and -28 percent of the corresponding measured values.

The difficulties involved in maintaining both laboratory ambient-air temperature and collector inlet-air temperature at constant values for

all the tests were insurmountable with the resources available. So all experimental collector performance data is subject to the influence of these changing variables. It is of interest, however, to know what the collector efficiency would be if these variables were held constant. The effect of holding the ambient-air temperature and the inlet-air temperature constant was therefore investigated and the results are shown in Figures 8 and 9. In these predictions the average ambient air-temperature was taken for each group of tests (the first group being those with a radiation intensity of 852 Watts/square metre and the second being those with a radiation intensity of 544 Watts/square metre). On the one hand, the inlet-air temperature was maintained at the highest value recorded in the tests, and on the other hand it was maintained at the lowest value recorded. The results generally show that efficiency increases with increasing mass-flowrate - a consequence of the effect of the increasing black-netting forced-convection heat-transfer coefficient with flowrate. This, combined with the increased flowrate, results in lower collector/environment differential temperatures and therefore reduced longwave radiative losses. Thus the increase of efficiency with increasing flowrate is to be expected.

In addition, it can be seen that a higher inlet-air temperature results in a lower collector efficiency and vice-versa. This is a result of the increased longwave radiative losses that take place between the collector and the environment when the temperature difference between the collector and the environment is greatest.

It is of interest to note that the experimental and predicted test data are bounded above and below by the curves produced as a result of holding the ambient-air temperature constant and the inlet-air temperature constant at maximum and minimum values respectively. In

FIGURE 8: MEASURED AND PREDICTED COLLECTOR EFFICIENCIES (Flat-Plate Model) (Incident Radiation = 852 W/m²)

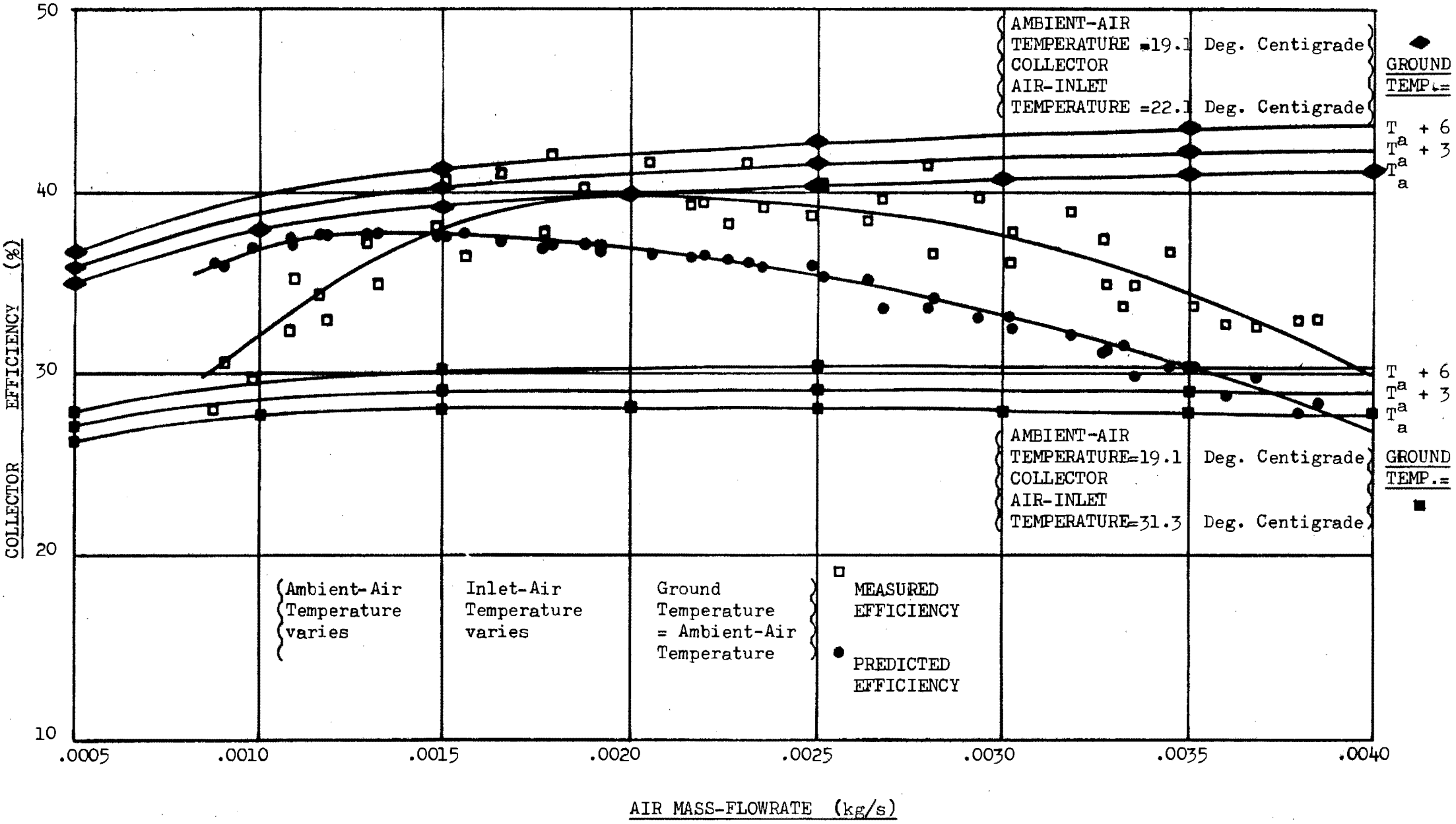

FIGURE 9: MEASURED AND PREDICTED COLLECTOR EFFICIENCIES (Flat-Plate Model) (Incident Radiation = 544 W/m²)

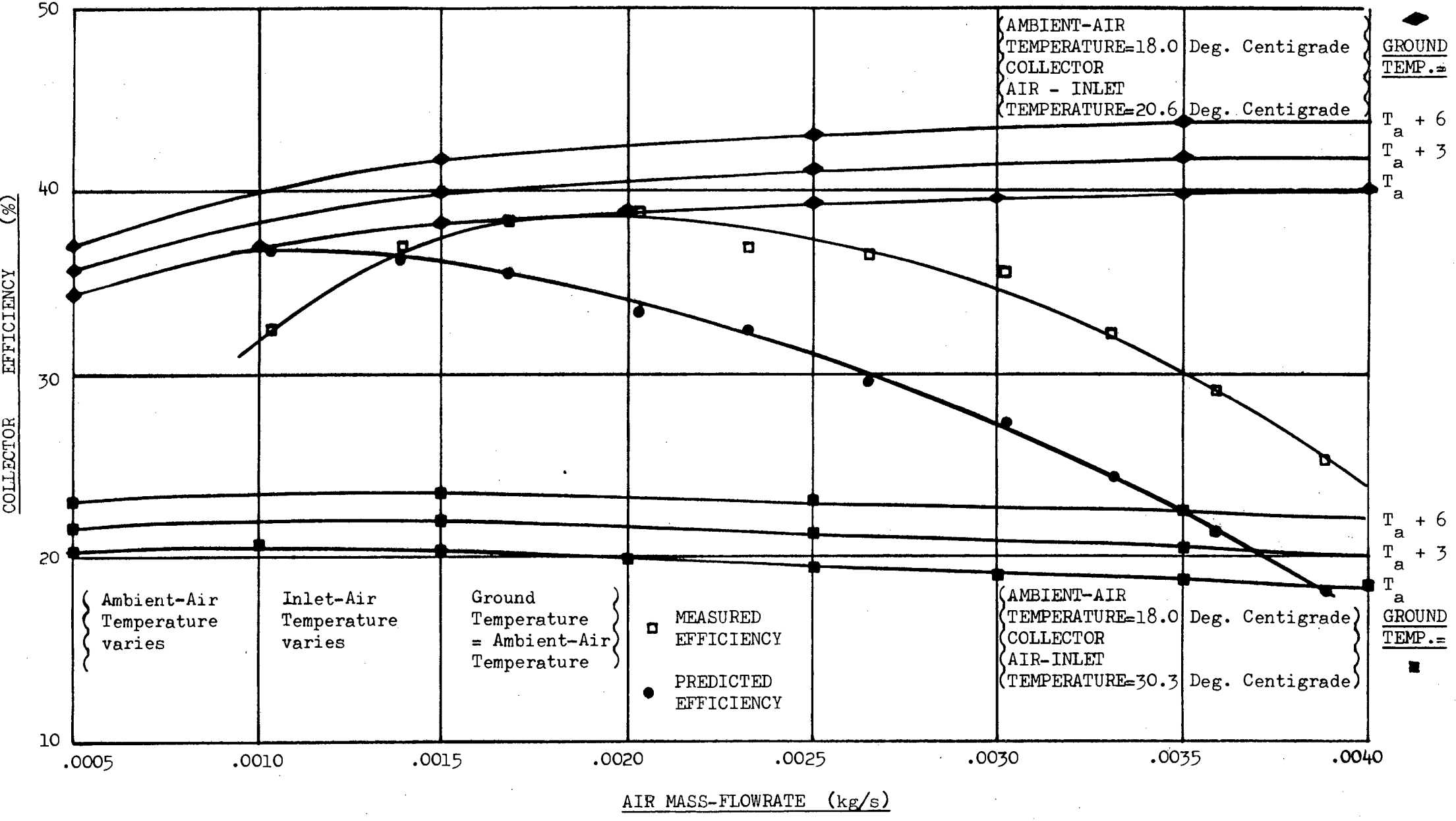

addition, these curves are smooth and do not display the scatter that is evident in the experimental data.

Also shown on Figures 8 and 9 are the results of sensitivity tests to evaluate the effect of ground temperature on collector efficiency. Three ground temperatures were used in the analysis. In the first case, the ground temperature was set equal to ambient-air temperature; in the second and third cases the ground temperature was specified to be three and six degrees Centigrade higher than the ambient-air temperature respectively. The results show that a change of ground temperature by six degrees Centigrade affects the predicted collector efficiency by about two percent when the incident radiation intensity is 852 Watts/square metre and by about four percent when the incident radiation is 544 Watts/square metre. This is to be expected since an increase in ground temperature leads to a smaller ground-collector temperature differential, and hence a smaller collector to ground longwave radiative loss. Also, the 852 Watts/square metre group of tests will have higher collector temperatures than the 544 Watts/square metre group. Thus the raising of the ground temperature will have a smaller overall effect on the system with the greater initial ground-collector temperature differential (i.e. the 852 Watts/square metre group of tests) and vice-versa.

5.1.2 Results of the Flat-Plate/Tube Heat-Transfer Model

This model is considered to be a refinement of the flat-plate model, since it takes account of the boundary layer growth within the collector and changes from a flat-plate type of heat-transfer analysis to a tube-type when theory predicts that flow becomes fully developed. Appendix 20 contains details of the derivation of the tube heat-transfer coefficients. Results from the experimental data and the theoretical test predictions are shown in Figures 10 and 11 and are listed in Appendix 21. Figure 10 shows the results for an incident radiation of 852 Watts/square metre and Figure 11 shows the results for an incident radiation of 544 Watts/square metre respectively. In both cases the measured collector efficiency is of the order of 35 percent, and shows a trend of decreasing efficiency for both higher and lower mass-flowrates than about 0.0020 kg/s. The predicted-efficiency data is similar to that obtained from the flat-plate model, but the values represent a greater underprediction than before. Consideration of the collector heat-transfer coefficients in Appendix 10 shows that the ratio of the netting to cover forced-convection heat-transfer coefficients may be approximated by the following equation:

$$h_{n/h_c} = \ell^{0.58} / \ell^{0.5} = \ell^{0.5} \quad \ldots\ldots\ldots\ldots\ldots\ldots\ldots\ldots \quad (11)$$

Equation 11 implies that the ratio of the netting heat-transfer coefficient to the cover heat-transfer coefficient increases with increasing length from the collector leading edge. However, in the case of the tube analogy, the ratio of the netting to cover heat-transfer coefficient remains constant from the position at which fully developed flow is attained (see Appendix 20), which in turn suggests a smaller

FIGURE 10: MEASURED AND PREDICTED COLLECTOR EFFICIENCIES (Incident Radiation = 852 W/m²) (Flat-Plate/Tube Model)

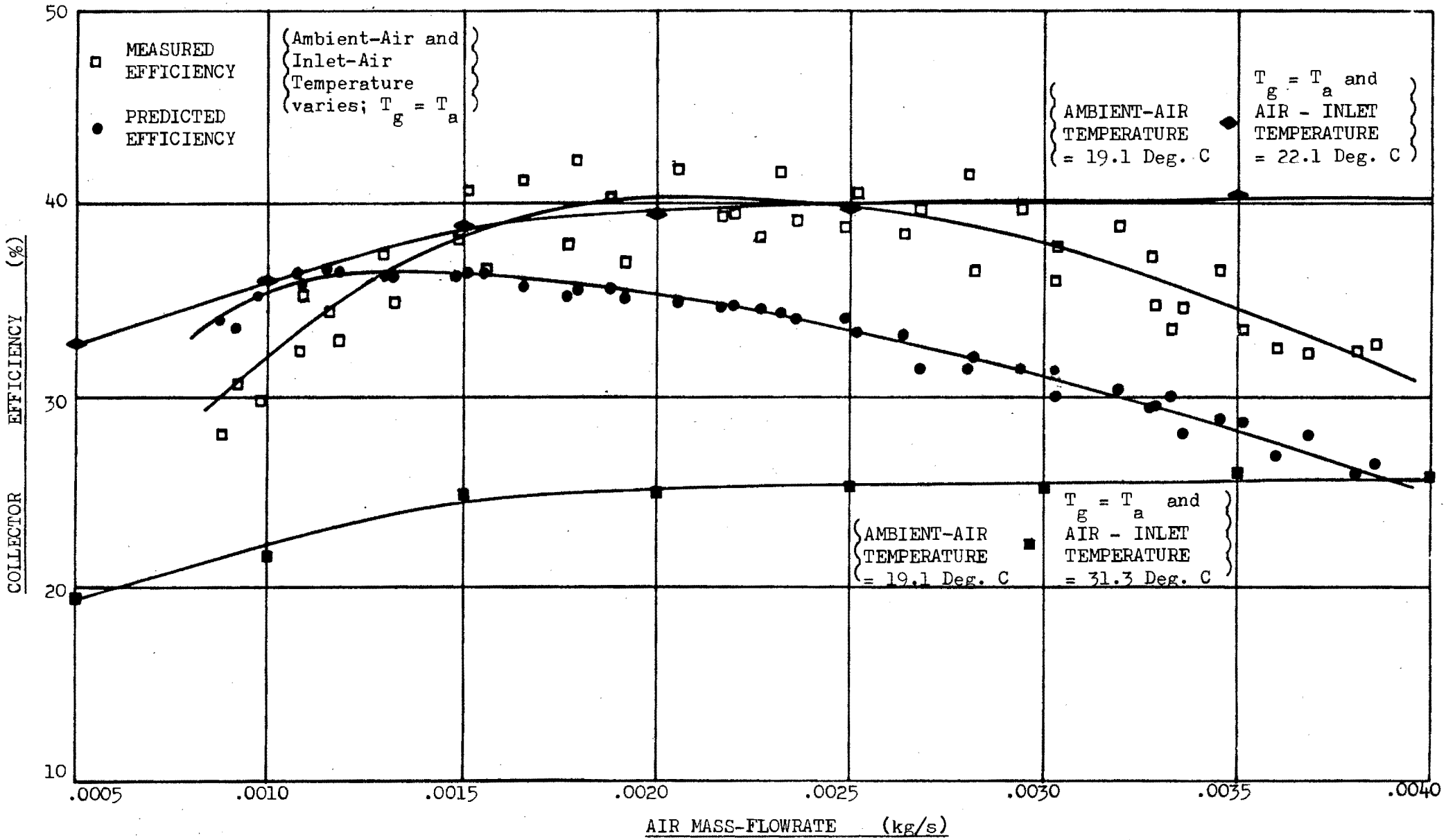

FIGURE 11: MEASURED AND PREDICTED COLLECTOR EFFICIENCIES (Incident Radiation = 544 W/m²)
(Flat-Plate/Tube Heat-Transfer Model)

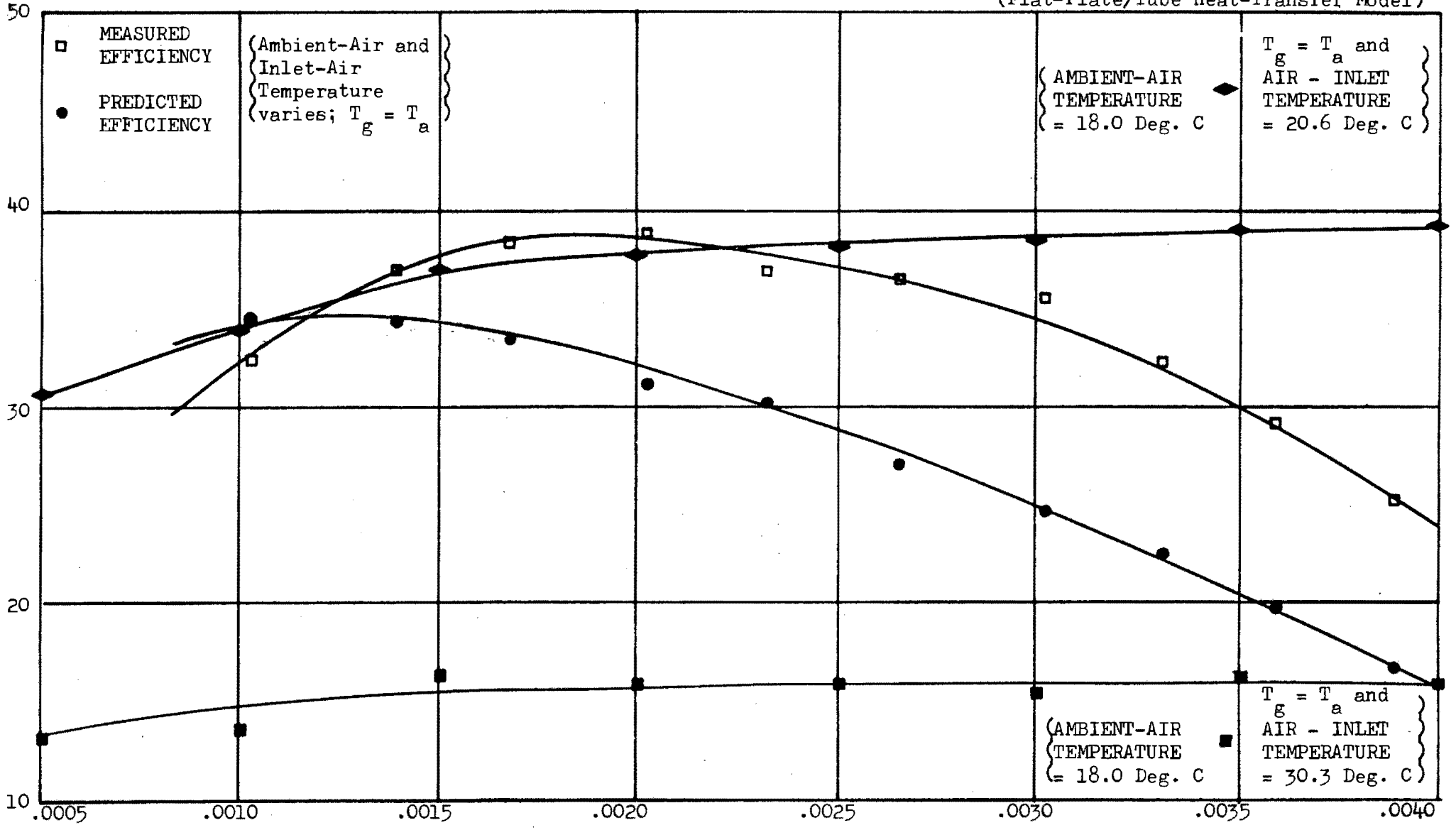

FIGURE 12: HISTOGRAM OF PERCENTAGE PREDICTED HEAT-GAIN ERRORS (Flat-Plate/Tube Heat-Transfer Model)

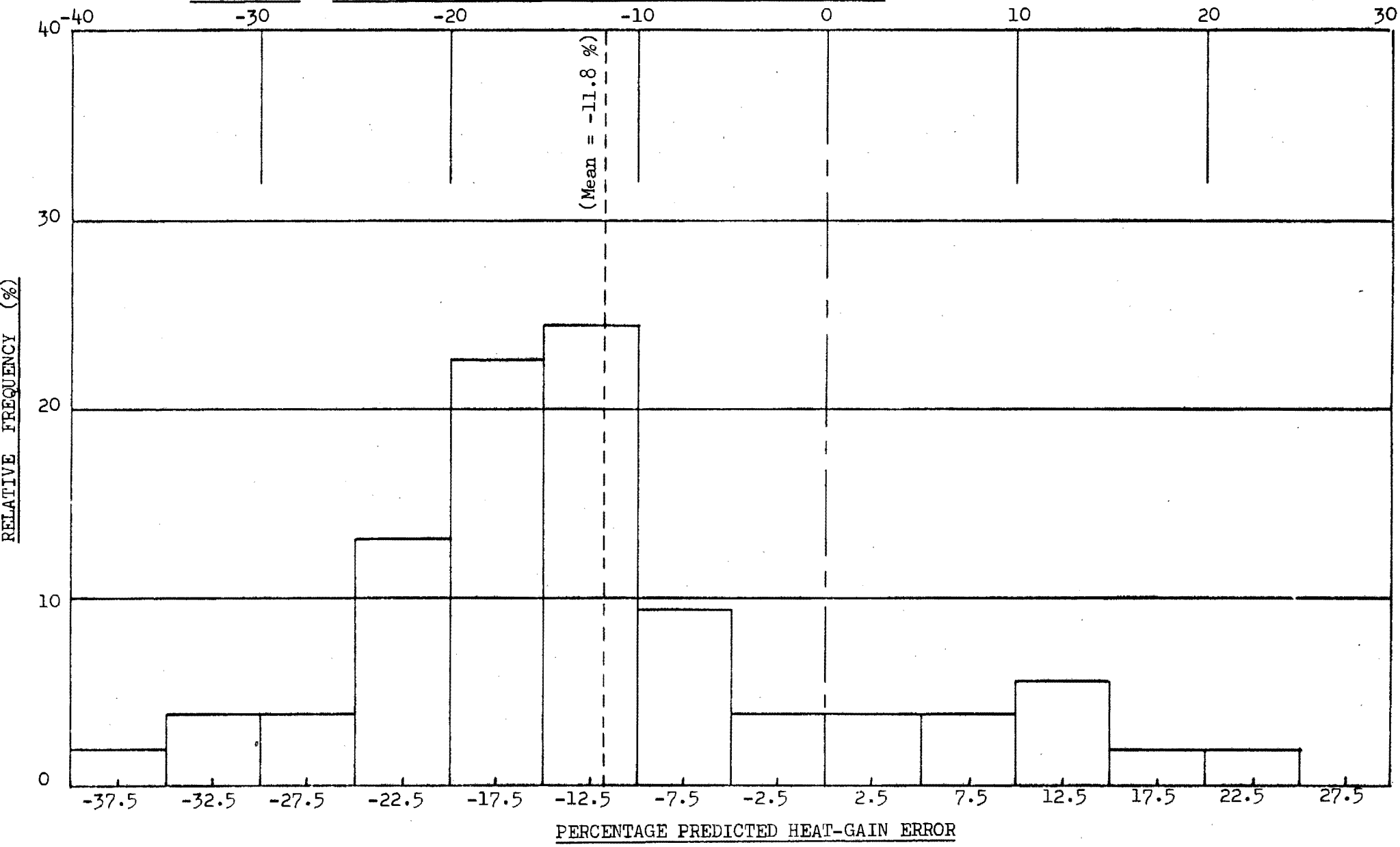

FIGURE 13: PERCENTAGE PREDICTED HEAT-GAIN ERROR (Flat-Plate/Tube Model)

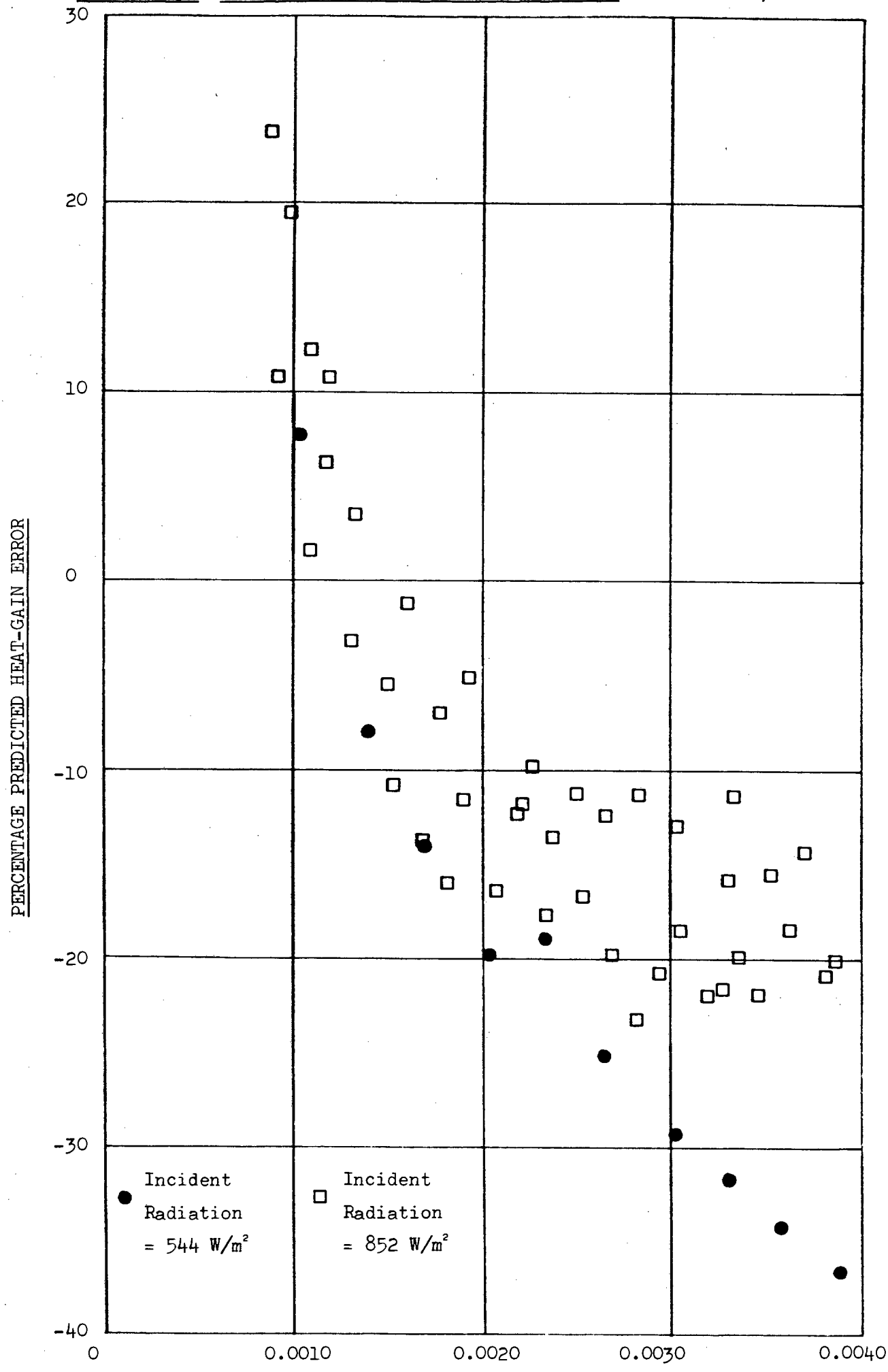

overall heat collection will take place. The fact that this phenomenon explains a larger underprediction of heat collection raises doubt as to whether fully developed flow was actually attained, as theoretically predicted.

Figure 12 is a histogram showing the relative frequency distribution of predicted heat-gain errors for the fifty three tests. The mean predicted heat-gain error is an underprediction of 11.8 percent, with a Standard Deviation of 12.6 percent. As before, the underprediction may be partly the result of specifying the ground temperature to have the same value as the laboratory ambient-air temperature. Figure 13 represents percentage predicted heat-gain error as a function of air mass-flowrate and shows that errors in predictions of heat-gain are within a band between +24 and -36 percent of the corresponding measured heat-gain values (compared with a band-width of +29 to -28 percent for the flat plate model).

As before, the effect of holding the ambient-air temperature and the inlet-air temperature constant was investigated and the results are shown in Figures 10 and 11. The results show that efficiency increases with increasing mass-flowrate (most noticeably at the lower flowrates) and confirm that a higher inlet-air temperature results in a lower collector efficiency (and vice-versa).

The efficiency values predicted by this model are more scattered than those produced by the flat-plate model. This appears to be the result of some instability in the solution process caused by the introduction of an "iteration-within-an-iteration" in order to solve for the black-netting tube forced-convection heat-transfer coefficient.

5.2 LIFE-SIZE BAIRD-TYPE SOLAR COLLECTOR PERFORMANCE PREDICTION

The life-size solar collector has a slightly different geometry from that of the model, as can be seen in Figure 14. For more detail, consult Appendices 12 and 13.

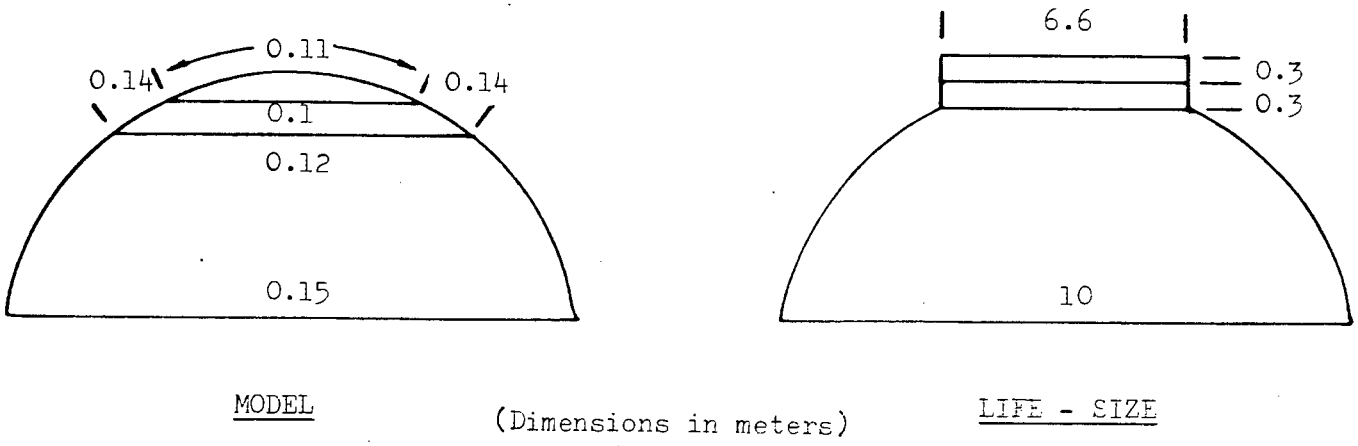

FIGURE 14: THE MODEL AND LIFE-SIZE BAIRD-TYPE SOLAR COLLECTOR GEOMETRIES

There are several reasons for this change. Firstly, some preliminary calculations indicated that a life-size Baird-type collector of the same geometry as the model would require a flowrate in excess of 20 kg/s if a combination of free and forced-convection was to be avoided. (The Grashof-Reynolds criterion is quoted by Holman (41) to be the objective method of evaluating whether a convection heat-transfer process is primarily free or forced-convection in nature. It states that if $Gr/Re^2 < 1$, then forced-convection effects will dominate in the convection heat-transfer process. This criterion was used in this thesis to ensure that the internal convection processes for both the model and life-size collector were forced-convection mode).

Such a high flowrate is also undesirable because it results in a small (i.e. one to two degree Centigrade) collector air temperature rise. Also, this order-of-magnitude of flowrate gives rise to Reynolds numbers larger than those in the range of the tests performed to evaluate the forced-convection black-netting heat-transfer coefficient. This implies that use of the experimentally derived relationship for evaluating the black-netting heat-transfer coefficient involves extrapolating the experimental results listed in Appendix 2 - which is undesirable. Finally, the amount of energy required by a fan to deliver such a high volume of air is considered excessive.

A modified collector geometry was therefore chosen for which the Grashof-Reynolds criterion is less than unity for a flowrate of 10 kg/s on a typical January day and 7 kg/s on a typical June day in the Cape Peninsula (assuming zero windspeed). The flowrate can be smaller in June because the collector temperatures are lower than the collector temperatures in January, leading to smaller buoyancy forces and consequently smaller free-convection effects. The reduced cross-sectional areas of the modified collector allows a smaller flowrate for a given flow velocity, which in turn allows an air temperature rise in the collector of between five and ten degrees Centigrade.

Predictions of collector performance were made using the flat plate model for typical climatic and insolation conditions encountered in the vicinity of the Cape Peninsula for the months January and June. The insolation values used for these predictions are published by the South African Weather Bureau (44) as hourly values of radiation for each month of the year in Cape Town and represent the mean values of data gathered

over the period 1951 to 1962. Appendix 17 lists these values for January and June and includes graphs drawn to yield values of insolation for small time-intervals. In this analysis, a time-interval of 12 minutes was chosen, implying that a full analysis of collector performance was undertaken every twelve minutes. The analysis considers the collector as divided into ten elements (as was done in the analysis of the laboratory-model solar collector).

The ambient-air temperatures used for these predictions are published by the South African Weather Bureau (45) as hourly values for each month of the year and represent the mean values of data gathered over the period 1932 to 1950 at the Wingfield Weather Office. Appendix 22 lists these values for January and June and includes graphs drawn to yield values of ambient-air temperature for twelve-minute time intervals, which are shown in Figures 15 and 17.

The ground temperatures used for these predictions were measured by Malherbe (46) over a two year period in an orchard in Stellenbosch. These values are contained in Appendix 23 and are shown in Figures 15 and 17.

Since these predictions are concerned with performance of a Baird-type solar collector situated in an outdoor environment, the effective sky temperature used in the longwave radiation terms is taken to be six degrees Centigrade below ambient-air temperature (as recommended by Whillier (12)). The collector Reynolds number is calculated at each element and is used to determine whether laminar or turbulent heat-transfer equations are applicable (the equations are listed in Appendix 10).

FIGURE 15: LIFE-SIZE BAIRD-TYPE SOLAR COLLECTOR PERFORMANCE PREDICTION (for a typical January day in the Cape Peninsula)

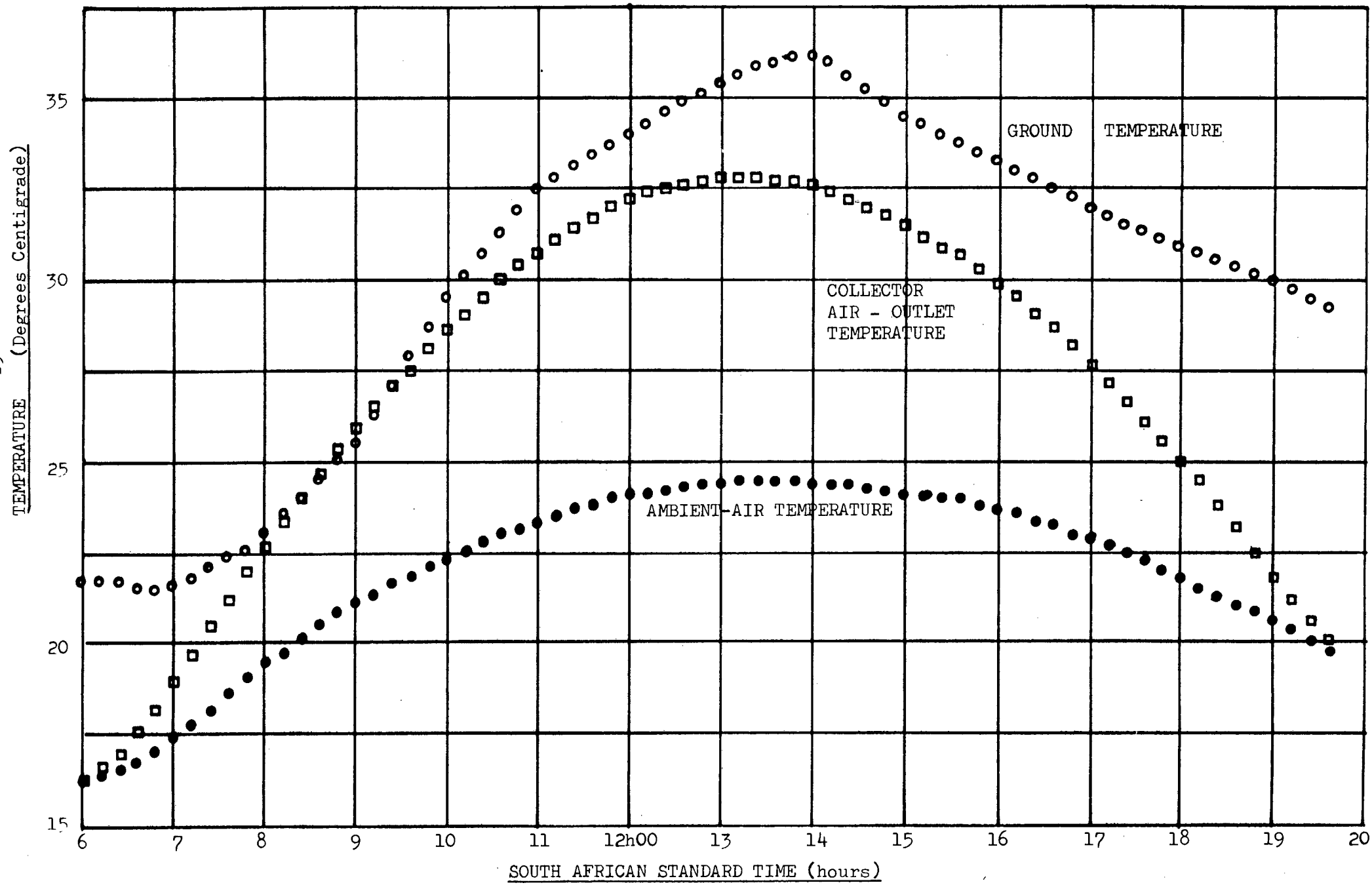

FIGURE 16: LIFE-SIZE BAIRD-TYPE SOLAR COLLECTOR PERFORMANCE PREDICTION (for a typical January day in the Cape Peninsula)

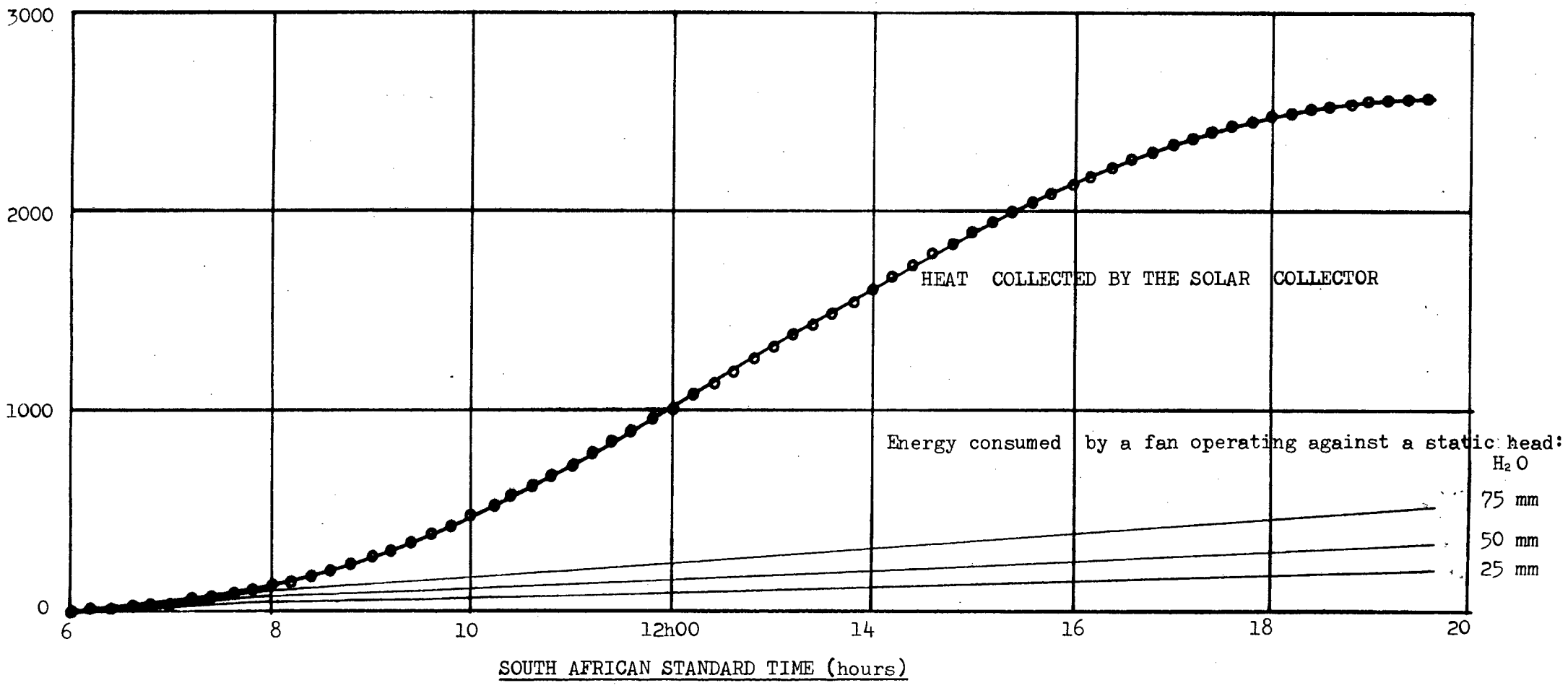

Figure 15 shows the average ambient-air temperature and the average ground temperature as a function of time on a January day, and the values of the predicted outlet-air temperatures are also plotted (these values were calculated on the assumption of zero wind velocity and a collector flowrate of 10 kg/s). Starting at 06h00, the collector heats air to a temperature of 16 degrees Centigrade. The outlet-air temperature peaks at about 33 degrees Centigrade at 13h00, decreasing thereafter, becoming 20 degrees Centigrade (the ambient-air temperature) at 19h30. It is interesting to note that the ground temperature is almost always higher than the collector outlet-air temperature, and that the maximum temperature rise of the collector outlet-air above ambient-air temperature is about 9 degrees Centigrade. Figure 16 shows the collector cumulative heat-gain plotted against time for the January conditions. By the end of the day approximately 2600 MJ will have been collected (over a period of about thirteen hours). Also shown on the figure are the energy requirements for a fan delivering 10 kg/s against static pressure heads of 25, 50 and 75 mm of water respectively. (Appendix 24 contains calculations of pressure-drop across a suitably proportioned rock-bed which predicts a typical pressure-drop of about 5mm of water). In the case of the 75mm head, approximately 500 MJ are consumed by day's end, indicating a net energy gain of about (2600 - 500) = 2100 MJ.

Figure 17 shows the average ambient-air temperature and the average ground temperature as a function of time on a June day, and the values of the predicted outlet-air temperatures are also plotted (these values were calculated on the assumption of zero wind velocity and a collector flowrate of 7 kg/s). Starting at 08h00, the collector heats air to a temperature of 9 degrees Centigrade. The outlet-air temperature peaks at about 21.5 degrees Centigrade at 13h15, decreasing thereafter, becoming

16 degrees Centigrade (the ambient-air temperature) at 17h00. In this case the ground temperature is always lower than both the ambient-air temperature and the collector outlet-air temperature, and the maximum temperature rise of the collector outlet-air above ambient-air temperature is about 4 degrees Centigrade. Figure 18 shows the collector cumulative heat-gain plotted against time for the June conditions. By the end of the day approximately 550 MJ will have been collected. Also shown on the figure are the energy requirements for a fan delivering 7 kg/s against static pressure-heads of 25, 50 and 75 mm of water respectively. In the case of the 75mm head, approximately 230 MJ are consumed by day's end, indicating a net energy gain of about (550 - 230) = 320 MJ. The energy gain of 550 MJ is the solar collector heat gain and is defined as:

$$\text{Solar Collector Heat-Gain} = (\dot{m}.C_p)_{air} \int_{t=o}^{t=t} (T_{out}-T_{ambient})dt \quad ....(12)$$

In practice there is also an ambient heat-gain, which is the ambient heat imparted to the rock-bed (assuming a 100 percent air-to-rock heat transfer) due to the difference between ambient-air temperature and the rock-bed temperature. This can be expressed as:

$$\text{Ambient Heat-Gain} = (\dot{m}.C_p)_{air} \int_{t=o}^{t=t} (T_{ambient}-T_{rock})dt \quad .....(13)$$

The total sensible heat-gain is represented by the sum of equations 12 and 13, and can be evaluated if the rock-bed temperature is known as a function of time. Since this is not the case in this study, the solar collector heat-gain is used above as a guide to evaluate the collector performance.

FIGURE 17: LIFE-SIZE BAIRD-TYPE SOLAR COLLECTOR PERFORMANCE PREDICTION (for a June day in the Cape Peninsula)

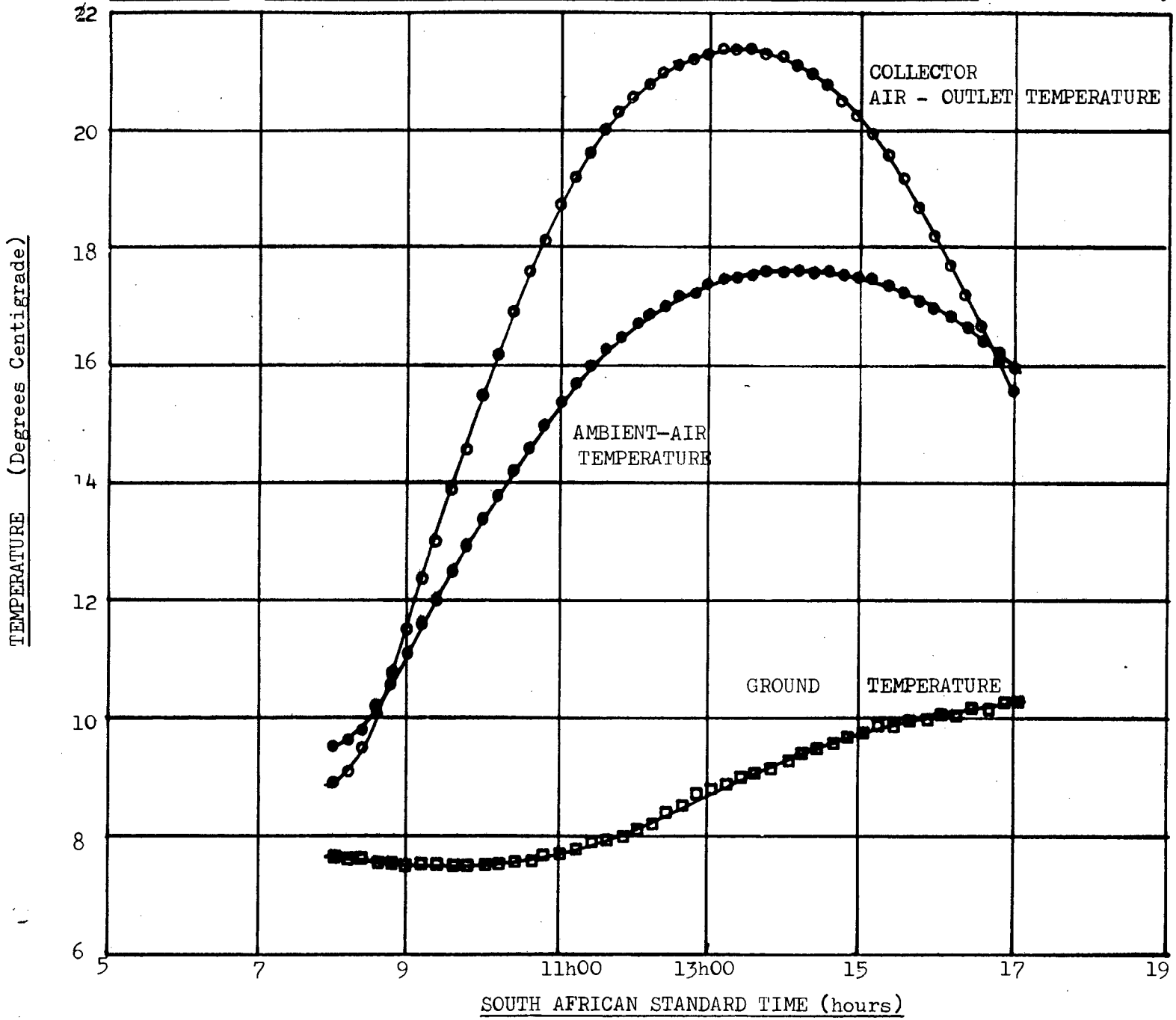

FIGURE 18: LIFE-SIZE BAIRD-TYPE SOLAR COLLECTOR PERFORMANCE PREDICTION (for a typical June day in the Cape Peninsula)

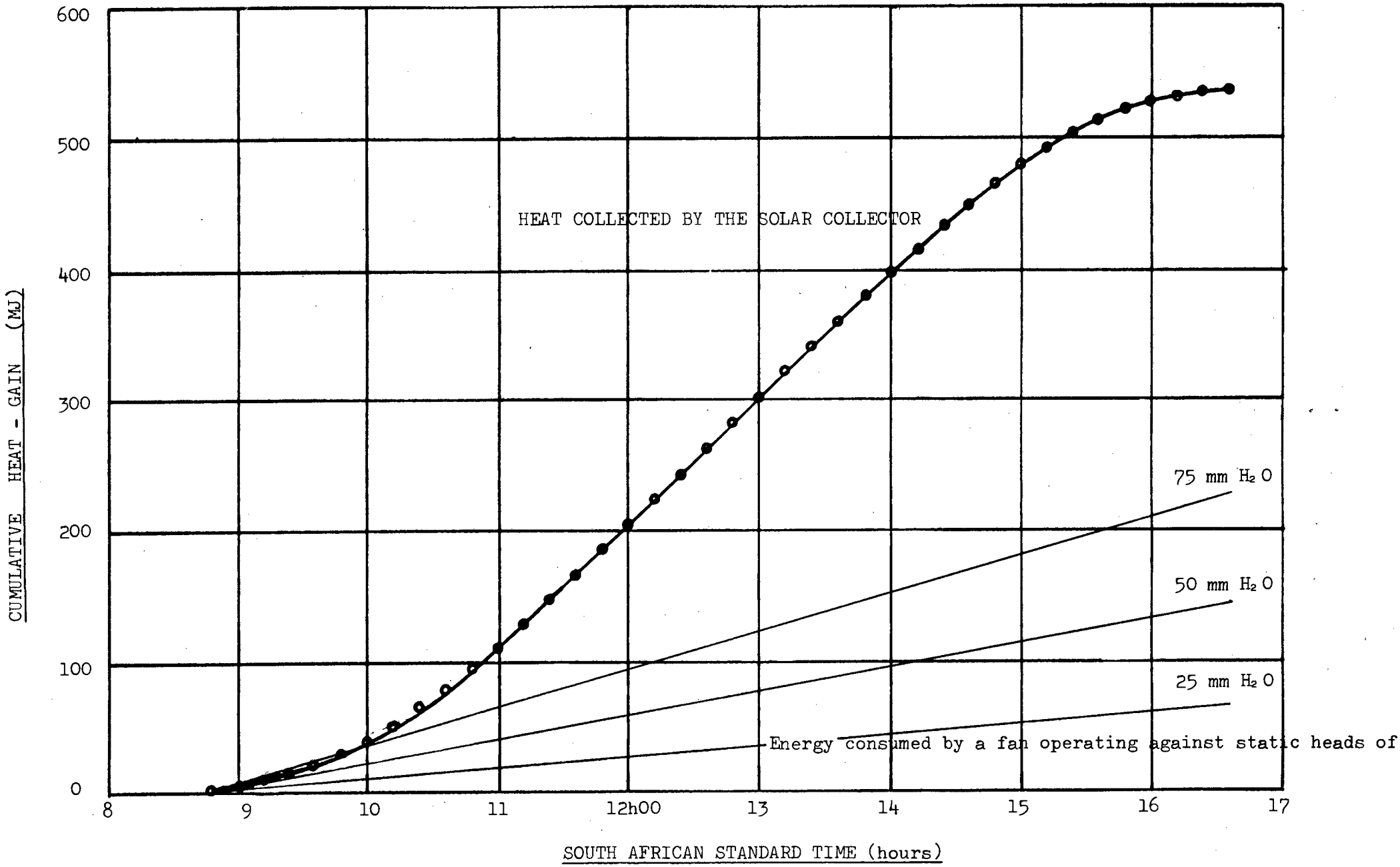

Figure 19 shows "collector efficiency" plotted as a function of "time-of-day" for the January and June-day tests described above. In general, the results show higher values of collector efficiency in January than in June. This is due to the smaller collector-to-ground longwave radiative losses in January, due to the relatively high ground temperature. The efficiency values change through the course of the day, but are relatively constant in an area centered around midday. The midday January collector efficiency is approximately 42 percent and the midday June collector efficiency is approximately 33 percent.

All the results described above are contained in Appendix 25. The nature of the tests done to determine the black-netting heat-transfer coefficient and the collector material radiation properties and the results of the tests are listed in Appendices 2 and 3 respectively. Appendix 27 contains a flowchart of the solution process, whilst Appendix 28 contains a sample calculation and solution verification.

FIGURE 19: SOLAR COLLECTOR EFFICIENCY PREDICTIONS

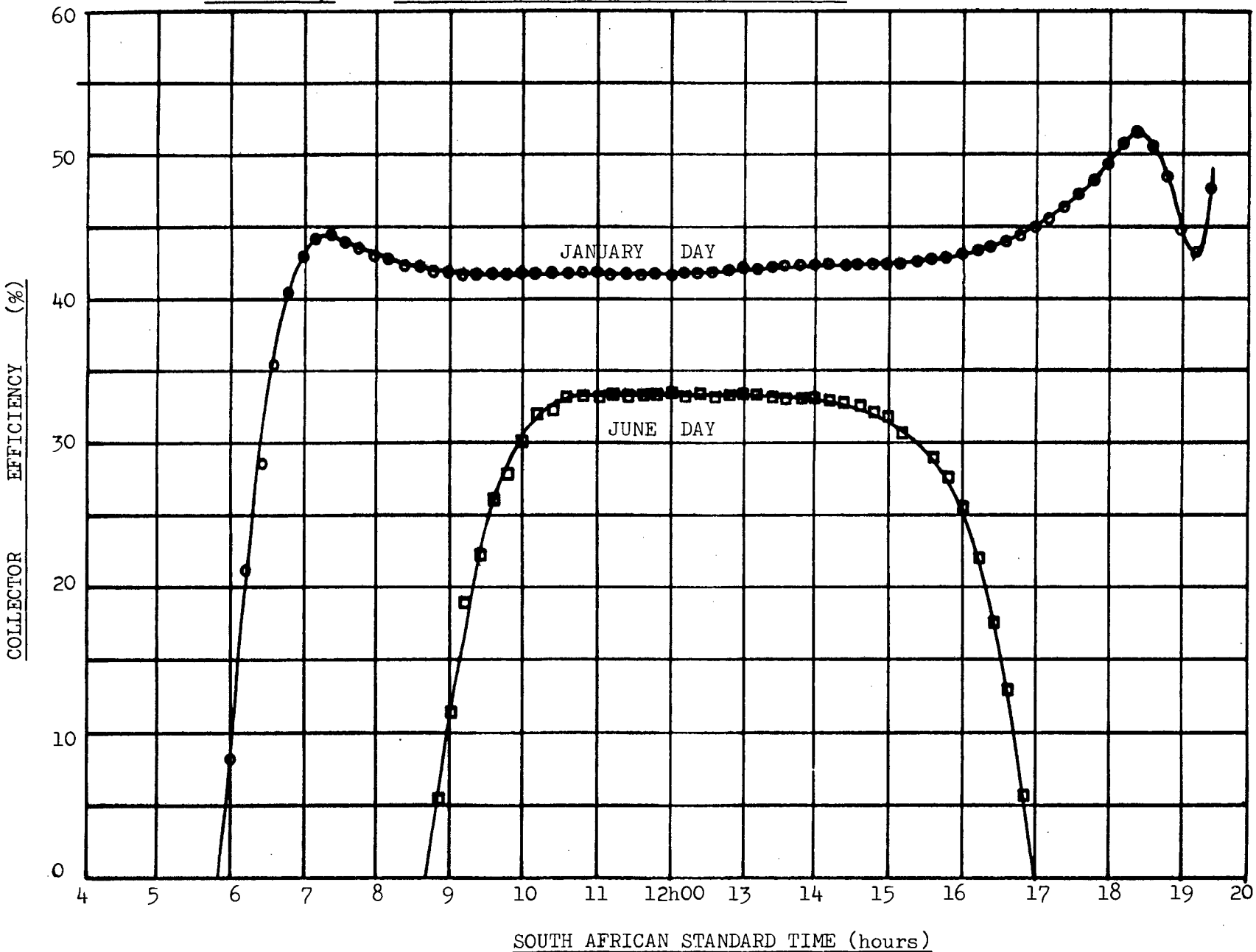

CHAPTER SIX

CONCLUSION

The primary objective of this thesis was the measurement and prediction of performance of a model Baird-type solar collector, with the intention of predicting the performance of a life-size integral-greenhouse solar air-heater. The experimental and theoretical work contained in this thesis shows that an integral-greenhouse solar collector, utilising shade-cloth as the absorber, represents a simple and practical alternative energy source for greenhouse heating.

5.1 EXPERIMENTAL AND THEORETICAL RESULTS OF THE SOLAR COLLECTOR MODEL

The experimental work was performed on a model Baird-type greenhouse approximately sixty-six times smaller than commercially available greenhouses (see Appendix 13), using a specially designed solar simulator as the radiation source (see Appendix 4 for details). The results indicate that as a solar energy collector, the model Baird-type greenhouse is of the order of 35 percent efficient. The collector efficiency depends on the values of the input variables (such as inlet-air temperature, radiation intensity, ambient-air temperature, air mass-flowrate etc.).

It was not feasible to maintain the inlet-air temperatures and laboratory ambient-air temperatures at constant values for the duration of the tests. On the other hand, the theoretical model allowed easy manipulation of input variables in the simulation process.

The theoretical model required verification. The experimental input-data was accordingly used as input-data for the theoretical model and, test by test, the results were compared. Two theoretical approaches were tried, being called the Flat-Plate and the Flat-Plate/Tube models respectively. The Flat-Plate approach underpredicted collector efficiency by an average of 7.6 percent, while the Flat-Plate/Tube approach underpredicted collector efficiency by an average of 11.8 percent. The results of these tests were plotted as "collector air mass-flowrate" versus "collector efficiency" and can be found in Chapter 5.

The theoretical model was used to evaluate the model greenhouse solar collector performance with constant values of ambient-air temperature and inlet-air temperature. It can be concluded from these results that the "peaking" of the model Baird-type solar collector efficiency at about 0.0020 kg/s was the result of an increasing inlet-air temperature with increasing mass-flowrate, and that the scatter of the experimental data was related to the changes of laboratory ambient-air temperature. The theoretical model was also used to study the sensitivity of the greenhouse solar collector to changes in ground temperature, whilst holding the ambient-air and inlet-air temperatures constant as described above. It can be concluded from the results that the collector efficiency was not very sensitive to ground temperature, although it was

more so when subjected to lower radiation intensity levels.

5.2 LIFE-SIZE BAIRD-TYPE SOLAR COLLECTOR PERFORMANCE PREDICTION

The theoretical model should be able to predict the performance of the life-size collector. The accuracy of the prediction is unfortunately unknown, since a life-size Baird-type system was not available for testing. The results generated by the theory should therefore be treated with some caution, although modifications were made wherever necessary to accomodate for the change of scale and geometry.

Predictions of performance for a life-size Baird-type greenhouse solar collector were made for typical January and June days in the Cape Peninsula. The predictions were made ignoring the effects of windspeed other than that which would result from natural convection at the collector external surfaces. The efficiency of solar energy collection is predicted to be approximately 42 percent for most of the January day and approximately 33 percent for most of the June day.

CHAPTER SEVEN

REFERENCES

(1) KERR, W.E., "Seed and cultivars for plastic tunnel production", One Day Symposium - Vegetables Under Plastics, University of Stellenbosch, 31 August 1976.

(2) BAIRD, C.D., WATERS, W.E. AND MEARS, D.R., "Greenhouse solar heating system utilising underbench rock storage", Trans. Am. Soc. agric. Engrs., Paper 77-4012, 1977.

(3) WINEGARNER, R.M., "Greenhouse selective baffle collector", Optical Coating Laboratory Inc., Santa Rosa, California, U.S.A.

(4) DAMAGNEZ, J., "Need and design for a solar greenhouse", National Institute of Agricultural Research, Avignon 84140, Montfavet, France.

(5) SAYIGH, A.A.M., "Greenhouses in Hot Climate", Solar Energy Conversion - An Introductory Course, Pergamon Press, page 1149, 1979.

(6) WHITTLE, R.M. AND LAWRENCE, W.J.C., "The climatology of glasshouses: Part 3 - Air Temperature", J. agric. Engng. Res. 5(2), pp 165 - 178, 1960.

(7) WALKER, J.N., "Predicting temperatures in ventilated greenhouses", Trans. Am. Soc. agric. Engrs., 8(3), pp 445 - 448, 1965.

(8) TAKAKURA, T., JORDAN, K.A. AND BOYD, L.L., "Dynamic simulation of plant growth and environment in the greenhouse", Trans. Am. Soc. agric. Engrs., 14(5), pp 964 - 971, 1971.

(9) McCORMICK, P., "Performance of non-integral solar collector greenhouses", Presentation at Solar Energy Fuel and Food Workshop, Tucson, Arizona, April 4 - 6, 1976.

(10) DUNCAN, G.A., LOEWER, O.J. AND COLLIVER, D.G., "Simulation of solar energy availability, utilisation and storage in greenhouses", Trans. Am. Soc. agric. Engrs., Paper 76 - 4010, 1976.

(11) HOTTEL, H.C. AND WHILLIER, A., "Evaluation of flat-plate solar collector performance", Trans. Conf. on the Use of Solar Energy, 2, Part 1, University of Arizona Press, page 74, 1958.

(12) WHILLIER, A., "Design factors influencing solar collector performance", in Low Temperature Engineering Application of Solar Energy", Chapter 3, Trans. Am. Soc. Heat. Refrig. Air-Condit. Engrs., New York, 1967.

(13) BLISS, R.W., "The derivations of several plate-efficiency factors useful in the design of flat-plate solar heat-collectors", Solar Energy 3(4), Pergamon Press, pp 55 - 64, 1959.

(14) BECKMAN, W.A., KLEIN, S.A. AND DUFFIE, J.A., "Solar Heating Design", John Wiley and Sons, New York, page 19, 1977.

(15) BUNDESVERBAND SOLARENERGIE (BSE), "BSE-Guidelines and Directions for Determining the USABILITY OF SOLAR COLLECTORS A. Solar Collector

Efficiency Test, Revised Edition, Druckerei Wehlmann GmbH & Co KG, Teichstrasse 4, 4300 Essen 1, March 1979.

(16) ARANOVITCH, E. AND ROUMENGOUS, C., "Solar Collector Testing Activities in the European Community", UK-ISES Conference (C22) - Solar Energy Codes of Practice and Test Procedures, London, pp 21 - 45, April 1980.

(17) DUFFIE, J.A. AND BECKMAN, W.A., "Solar Energy Thermal Processes", John Wiley and Sons, New York, pp 164 - 165, 1974.

(18) PARKER, B.F., "Derivation of efficiency and loss factors for solar air-heaters", Solar Energy, Volume 26, Pergamon Press, pp 27 - 32, 1981.

(19) SELCUK, K., "Thermal and Economic Analysis of the Overlapped-Glass Plate Solar Air-Heater", Solar Energy, Volume 13 No 2.B, Pergamon Press, pp 165 - 191, 1971.

(20) MOON, P., "Proposed standard radiation curves for engineering use", J. Franklin Inst., Philadelphia, Vol. 230, pp 583 - 618, 1940.

(21) BENNING, F.N., "Simulation of average sea level sunlight (Air Mass Two)", Solar Energy, Volume 12, Pergamon Press, pp 233 - 242, 1968.

(22) YASS, K. AND CURTIS, H.B., "Low cost, air mass 2 solar simulator", NASA TM-X-3059, June 1974.

(23) GILLETT, W.B., "Solar simulators and indoor testing", UK-ISES Conference (C11) at Royal Institution, London, "Testing of Solar Collectors and Systems", pp 31 - 48, April 1977.

(24) PEKRUHN, W. AND GERMER, R., "Solar simulator", Technical Note, Solar Energy, Pergamon Press, Volume 25, pp 381 - 383, 1980.

(25) BEESON, E.J.G., "The CSI lamp as a source of radiation for solar simulation", Lighting Research and Technology, Volume 10, Nos 3, pp 164 - 166, 1978.

(26) McMILLAN, J.A. AND PETERSON, E.M., "Solar simulation with tungsten-halogen quartz lamps and optical filters", Technical Note, Solar Energy, Pergamon Press, Volume 22, pp 467 - 469, 1979.

(27) GILLETT, W.B., RAWCLIFFE, R.W. AND GREEN, A.A., "Collector testing using solar simulators", UK-ISES Conference (C22), "Solar Energy Codes of Practice and Test Procedures", London, pp 57 - 71, April 1980.

(28) PARMELEE, G.V. AND AUBELE, W.W., Trans. Am. Soc. Heat. Refrig. Air-Condit. Engrs., Volume 58, pp 85 - 106, 1952.

(29) WHILLIER, A., "Plastic covers for solar collectors", Solar Energy, Pergamon Press, Volume 7, No. 3, pp 148 - 151, 1963.

(30) TABOR, H., "Solar collector developments in Israel", Solar Energy 111, Pergamon Press, No. 3, pp 8 - 9, October 1959.

(31) MAREE, P.C.J. AND LAUBSCHER, E.W., "Producing cucumbers in a plastic tunnel during the winter months", Interim Report 4, Dept. of Agronomy, University of Stellenbosch, October 1977.

(32) TAKAHASHI, B., EGUCHI, T. AND YONEDA, K., "Studies on the flower

formation in tomatoes and eggplants IV. Effects of temperature regimes and fertiliser levels on the flower-bud differentiation in tomatoes and eggplants", J. hort. Ass. Japan, 43(3), pp 237 - 246, 1974.

(33) MAREE, P.C.J. AND LAUBSCHER, E.W., "Cultivation of winter tomatoes in a plastic tunnel", Interim Report 1, Department of Agronomy, University of Stellenbosch, October 1977.

(34) U.K. SECTION OF THE INTERNATIONAL ENERGY SOCIETY, "Solar Energy - a U.K. assessment", Chapter 9 - Agricultural and Biological Systems, page 279, UK-ISES, 1976.

(35) DOWNS, R.J. AND HELLMERS, H., "Environment and the experimental control of plant growth", Academic Press Inc., London, U.K., 1975, ISBN 0-12-221450-1.

(36) SCIEZ, G., "Solar radiation for plant growth", J. Appl. Ecol. 11, pp 617 - 636, 1974.

(37) KLAPWIJK, D. AND LINT, P.J.A.L. de, "Growth rates of tomato seedlings and seasonal radiation", Neth. J. Agric. Sci., 23(3), pp 259 - 268, 1975.

(38) RODRIGUEZ, B.P. AND LAMBETH, V.N., "Artificial lighting and spacing as photosynthetic and yield factors in winter greenhouse tomato culture", J. Am. Soc. Hortic. Sci., 100(6), pp 694 - 697, 1975.

(39) MORGAN, J.V. AND CLARKE, E.J., "Influence of temperature, photoperiod and container size on the growth rate and development of tomato plants in growing rooms", Acta Horticulturae No 51, 1975, pp 77 -

87, University College Dublin, Dublin, Irish Republic.

(40) CANHAM, A.E., "Some recent developments in artificial lighting for protected crops", Proceedings of the X1X International Horticultural Congress, 1974, Reading University, Reading, U.K.

(41) HOLMAN, J.P., "Heat transfer", Mcgraw-Hill Kogakusha, Fourth Edition, 1976.

(42) KAYS, W.M., "Convective Heat and Mass Transfer", McGraw-Hill, 1966.

(43) British Standards Institution, B.S. 1042 : Part 1 : 1964, "Methods for the measurement of Fluid Flow in Pipes", British Standards Institution, London.

(44) Weather Bureau of R.S.A., W.B. 32, Department of Transport, "Solar Radiation and Sunshine", Page 25, 1968.

(45) Weather Bureau of R.S.A., W.B. 19, Department of Transport, "Climate of South Africa", Part 1, Climate Statistics, Page 136, 1954.

(46) MALHERBE, I. de V., "Soil Climate with Special Reference to Temperature Fluctuations in an Orchard Soil at Stellenbosch", S.A. Dept. of Agriculture and Forestry, Science Bulletin No. 174 (Stellenbosch-Elsenberg Series No. 30), Government Printer, 1938.

(47) GLANVILLE, A.B., "The Plastic Engineers Data Book", Machinery Publishing, Brighton, 1971.

(48) General Electric Company Heat-Transfer Data Book, edited by R. Hosmer Norris and others, Schenectady, New York, 1970.

(49) WALPOLE, R.E. AND MYERS, R.H., "Probability and Statistics for Engineers and Scientists", 2nd edition, Collier Macmillan International Editions, 1978.

(50) KENNEDY, J.B. AND NEVILLE, A.M., "Basic Statistical Methods for Engineers and Scientists", Harper and Rowe, 2nd edition, 1976.

(51) KINNEY, G.F., "Engineering Properties and Applications of Plastics", Plastics Tables, John Wiley and Sons.

(52) CLOSE, D.J., "Solar Air Heaters for Low and Moderate Temperature Applications", Solar Energy, Pergamon Press, Volume 7, Nos 3, pp 117-124, 1963.

(53) SPIEGEL, M.R., "Mathematical Handbook", McGraw-Hill, 1968.

(54) GERALD, C.F., "Applied Numerical Analysis", Addison-Wesley Publishing Company, 1970.

(55) HENRICI, P., "Elements of Numerical Analysis", John Wiley and Sons, 1964.

(56) Discussion with Dr R. Smart, Department of Applied Mathematics, University of Cape Town.

(57) MASSEY, B.S., "Mechanics of Fluids", 2nd edition, Van Nostrand Reinhold Co., 1972.

(58) LUNDE, P.J., "Solar Thermal Engineering", John Wiley and Sons, New York, 1980.

(59) CLOSE, D.J., "Rock pile thermal storage for comfort air conditioning", Mech. and Chem. Engr. Trans. Engrs., Australia, MC1, 11, 1965.

(60) Discussion with Professor R. Stegen, Department of Mechanical Engineering, University of Cape Town.

(61) Donkin Manufacturing Company, Technical Data Book, Volume 1, Forward Curved Centrifugal Fans.

(62) ECKERT, E. AND DRAKE, R., "Heat and Mass Transfer", 2nd edition, McGraw-Hill Book Company, 1959.

(63) SPARROW AND CESS, "Radiation Heat Transfer", McGraw-Hill, Washington, 1978.

(64) LEEDS AND NORTHRUP CO., "Conversion Tables for Thermocouples", Philadelphia, 007789.

APPENDIX 1

TEMPERATURE LEVELS AND INSOLATION REQUIREMENTS FOR OPTIMUM GREENHOUSE CROP CULTIVATION

The following indicates the order of magnitude of temperature levels for optimum greenhouse crop cultivation. Kerr (1) and Maree et al (31) are of the opinion that the ideal air temperature for cucumber growth is 30-32 degrees Centigrade during the day and 20-23 degrees Centigrade at night. Kerr (1), Takahashi et al (32) and Maree et al (33) state that the ideal day and night temperatures for tomato plant growth are about 25 and 15 degrees Centigrade respectively. It is claimed by the United Kingdom section of the International Energy Society (34) that an increase of greenhouse air temperature from 7 to 12 degrees Centigrade increased tomato yields by 40% to 75%.

According to Winegarner (3), the United Kingdom section of the International Energy Society (34), Sayigh (5) and Downs et al (35), plants can only use radiation in the visible part of the solar spectrum - between 400 and 700 nm - the so-called Photosynthetically Active Radiation (PAR). The major effect of the spectrum from 700 nm upwards, which is the infrared region, is to provide heat. Damagnez (4) and Sciez (36) point out that the infrared region comprises about 50% of total solar radiation.

The following indicates that, except in unusual circumstances, an increase of insolation, either in terms of intensity and/or duration results in an increased crop yield. Kerr (1) reports that high light-intensity can cause tip-burn in lettuce - a factor that in this

special case favours the use of a net for light reduction. Klapwijk and Lint (37) have found that the length of the growing period for tomato seedlings for the attainment of 10g fresh weight per plant in Naaldwijk, Holland, was determined by the amount of radiation in winter only. Rodriguez et al (38) have experimented with supplementary lighting. Plant growth was increased and they could not detect any photosaturation. Morgan and Clarke (39) have shown that extending the photoperiod time from 12 to 16 hours increased growth curves by 43% for tomatoes. Canham (40) used artificial light from low-pressure sodium and mercury halide lamps to supplement winter daylight on young tomato and lettuce plants. Increased growth occurred, the increase being linearly related to the supplementary radiation.

APPENDIX 2

THE BLACK-NETTING FORCED-CONVECTION HEAT-TRANSFER COEFFICIENT

Since the order-of-magnitude of the black-netting forced-convection heat-transfer coefficient was unknown, and since Parker (18) has shown that solar collector efficiency is very sensitive to the absorber surface heat-transfer coefficient, it was decided to devise and conduct an experiment to determine the black-netting heat-transfer coefficient. A magnified view (scale approximately 3.3:1) of the black-netting cloth is shown in Photograph 6.

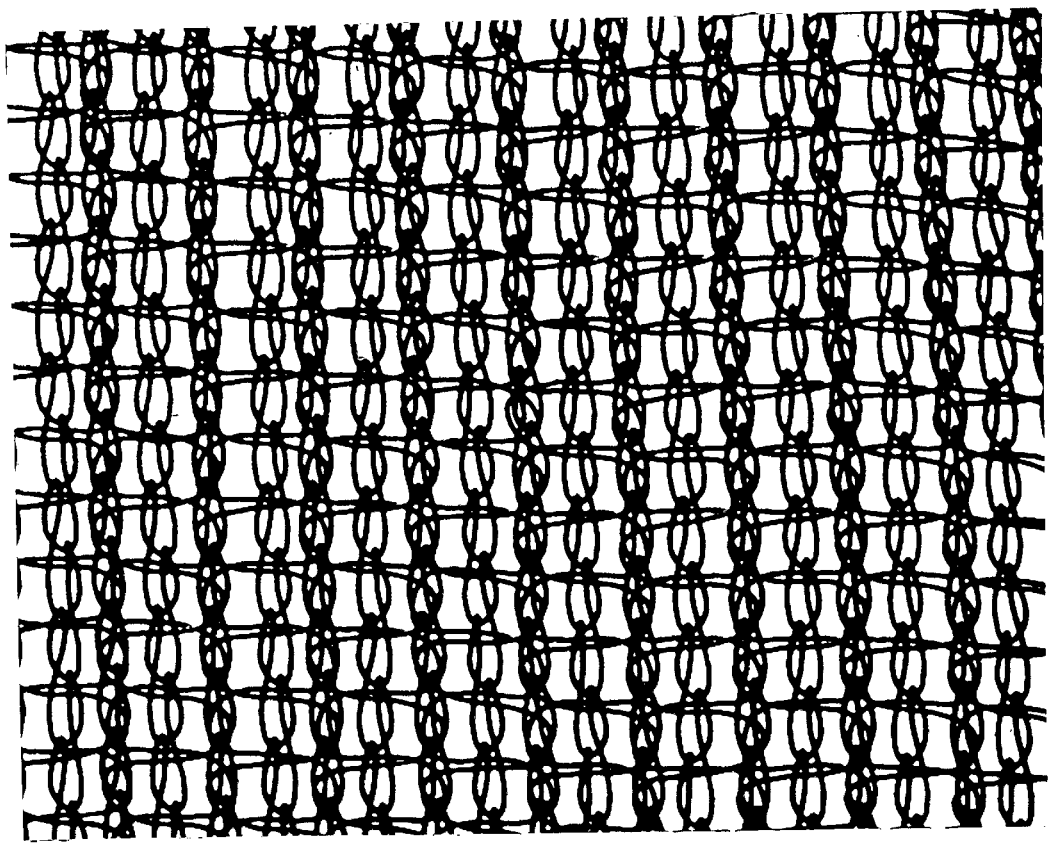

Photograph 6: The Black-Netting Cloth (scale approximately 3.3:1)

2.1 Theoretical derivation

Assuming that the black-netting internal heat resistance is negligible in comparison with the external heat resistance (justified in Appendix 2.5), the netting-cloth can be considered as being uniform in temperature at any cross-section. Consider an element of the netting, for which the heat-transfer is written as:

$$Q = h.A.(T-T_{fs}) = -C_p.\rho.V.\frac{dT}{dt} \quad \ldots\ldots\ldots\ldots\ldots\ldots (1)$$

where 'h' is the surface convection heat transfer coefficient ($W/m^2.^oC$) and 'A' is the surface area of the element (m^2), 'T' is the element temperature (^oC), 'T_{fs}' is the free stream temperature (^oC), 'C_p' is the specific heat of the element ($J/kg.^oC$), 'ρ' is the density of the element (kg/m^3), 'V' is the element volume (m^3) and $\frac{dT}{dt}$ is the rate of change of element temperature (^oC/second).

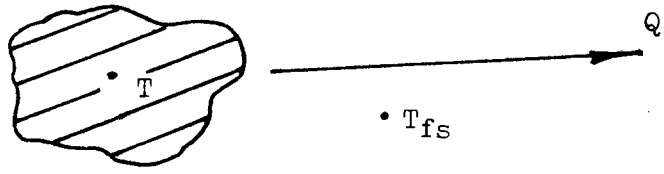

Equation (1) assumes that there are no radiation losses from the element. It is a first order differential equation which can be written in the form:

$$\frac{dy}{dx} + P.y = Q \quad \ldots\ldots\ldots\ldots\ldots\ldots\ldots\ldots\ldots\ldots\ldots\ldots (2)$$

i.e. $$\frac{dT}{dt} + \left[\frac{h.A}{\rho.C_p.V}\right].T = \left[\frac{h.A.T_{fs}}{\rho.C_p.V}\right]$$

where $P = \left[\frac{h.A}{\rho.C_p.V}\right]$ and $Q = \left[\frac{h.A.T_{fs}}{\rho.C_p.V}\right]$

The solution of equation (2) is:

$$y.e^I = \int Q.e^I.dx + C \qquad \text{where C is a constant.}$$

Note that $I = \int P.dx = \int \frac{h.A}{\rho.C_p.V}.dt = \frac{h.A.t}{\rho.C_p.V}$

Substituting the applicable variables results in the following equation:

$$T.e^{\left(\frac{h.A.t}{\rho.C_p.V}\right)} = \int\left(\frac{h.A.T_{fs}}{\rho.C_p.V}\right)e^{\left(\frac{h.A.t}{\rho.C_p.V}\right)}.dt + C$$

$$= T_{fs}.e^{\left(\frac{h.A.t}{\rho.C_p.V}\right)} + C \quad \ldots\ldots\ldots\ldots\ldots\ldots (3)$$

Now t=0 has $T=T_o$ as a boundary condition, hence solving for the constant:

$$T = T_o = T_{fs} + C$$

thus $$C = T_o - T_{fs}$$

Resubstituting this into equation (3) gives:

$$(T - T_{fs}).\ e^{\left(\frac{h.A.t}{\rho.C_p.V}\right)} = (T_o - T_{fs})$$

which is usually written as:

$$\left(\frac{T - T_{fs}}{T_o - T_{fs}}\right) = e^{-\left(\frac{h.A.t}{\rho.C_p.V}\right)} \quad \ldots\ldots\ldots\ldots\ldots\ldots\ldots\ldots (4)$$

The form of this transient heat transfer equation is confirmed by Holman (41) in a discussion on lumped-heat-capacity analysis.

The area of a sample piece of netting 0.52 m wide and 0.90 m long is:

$$(2 \times 0.52 \times 0.90) = 0.936\ m^2 \qquad \text{(top and bottom)}$$

The density of polyethylene is quoted by Glanville (47) to be 950 kg/m^3 and by the General Electric Co. (48) to be 954 kg/m^3. It is thus averaged out as 952 kg/m^3. The sample of netting specified above was massed at 0.06835 kg. This information can be used to find the volume of the netting sample as follows:

$$V = \frac{M}{\rho} = (0.06835/952) = 7.1796 \times 10^{-5}\ m^3$$

Thus the ratio $(A/V)_{netting} = (0.936/7.1796 \times 10^{-5}) = 1.3037 \times 10^4\ m^{-1}$

The specific heat for polyethylene is 2303 $J/kg.^oC$ according to the General Electric Co. (48). This can be used to evaluate

$$(A/\rho.C_p.V) = (1.3037 \times 10^4/(952 \times 2303)) = 5.946 \times 10^{-3}\ m^2.^oC/J$$

This can be substituted into equation (4) and rearranged to give:

$$h = -\left[\log_e\left(\frac{T - T_{fs}}{T_o - T_{fs}}\right) \Big/ t \times 5.946 \times 10^{-3}\right] \quad W/m^2.^oC \ \ldots\ldots (5)$$

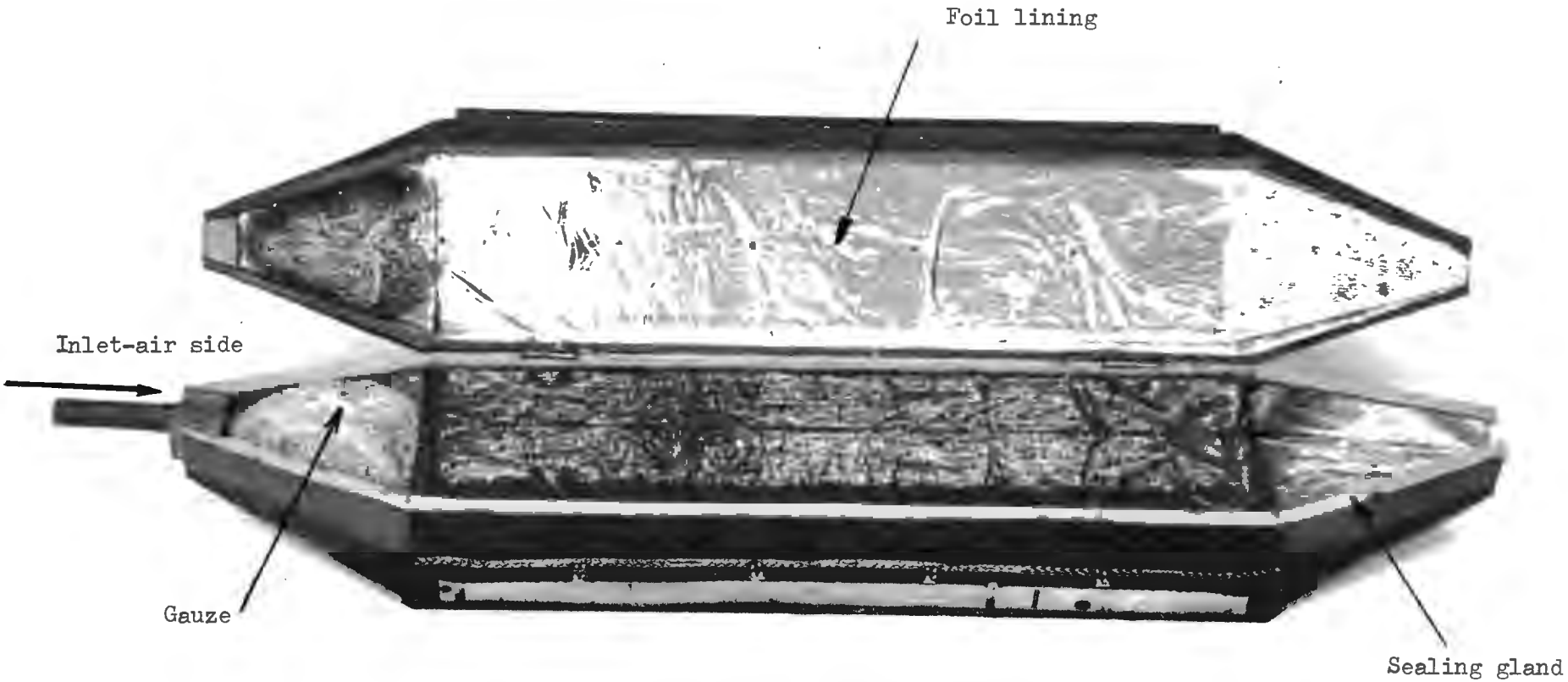

Photograph 7: The Apparatus used for measuring the Black-Netting forced-convection heat-transfer coefficient, shown with the lid in the open position.

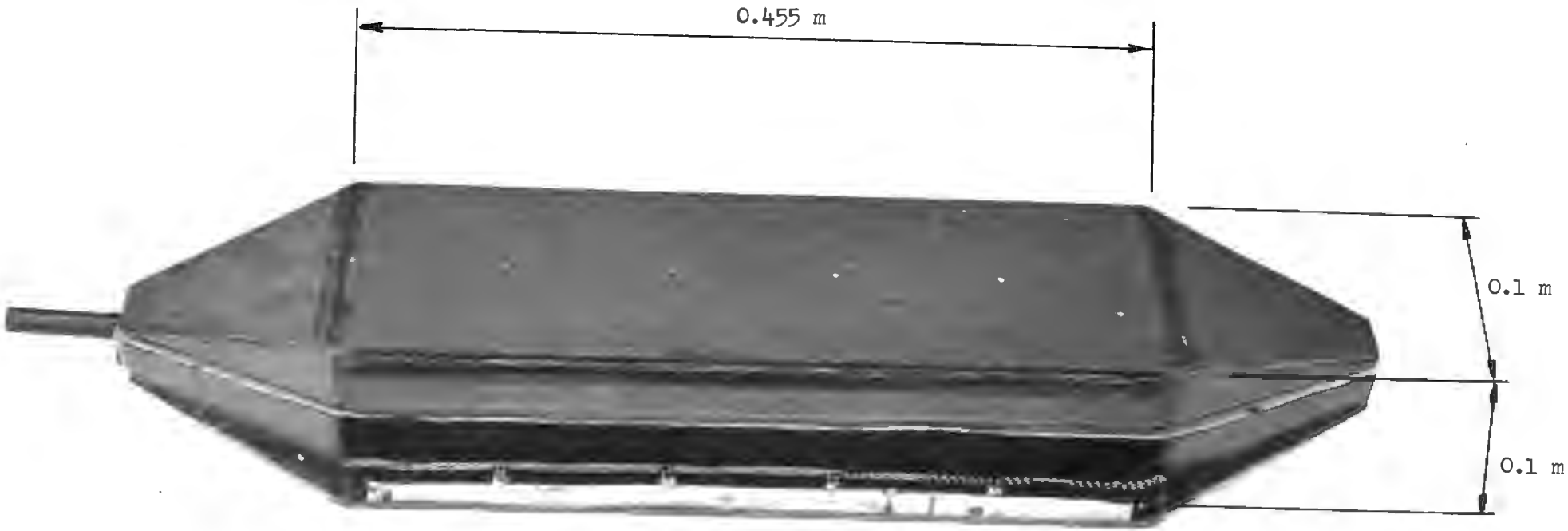

Photograph 8: The Apparatus used for measuring the Black-Netting forced-convection heat-transfer coefficient, shown with the lid in the closed position.

2.2 Experimental Equipment and Method

Photographs 7 and 8 show the device that was built to assist in measuring the temperature decay of the black-netting cloth. Photograph 7 shows the box with the lid open. The interior consists of the black-netting, the foil-lined walls, a sieve at the inlet-end of the box to help distribute incoming air and a sealing gland around the perimeter of the box to make the closed box leak-proof. Photograph 8 shows the box in the closed position. The netting temperature was measured at four equi-spaced locations along the netting by means of Copper-Constantan thermocouples connected to a Philips PM 8000 voltage plotter. (The voltage plotter was calibrated for accurate temperature measurement and the paper feed-rate was checked to ensure accurate time measurement). Free-stream air temperature was measured with a thermocouple placed at the inlet end of the box, directly upstream of the gauze. The air flowrate was measured using the orifice-plate device described in Appendix 14.

The experiments were conducted as follows. The box was placed in the solar simulator and the lid was opened to expose the black-netting to the radiation. During this process the inlet air was diverted to allow the net to heat up. Then the box was quickly closed and the air was allowed to flow through the box. The temperature decay of the netting was represented as a function of time by the trace produced on the voltage plotter.

2.3 Results

A total of forty-one tests were conducted. The results of these tests are tabulated below.

Column A = air mass-flowrate (for kg/s multiply 10^{-6})

Column B = netting temperature at time = 0 (degrees Centigrade)

Column C = netting temperature at time = t (degrees Centigrade)

Column D = free-stream temperature (degrees Centigrade)

Column E = elapsed time between t=0 and t=t (seconds)

Column F = distance from leading edge of plate (metres)

Column G = local heat-transfer coefficient (W/m.m.degree Centigrade)

Column H = Reynolds number

Column I = Nusselt number

TABLE 1: RESULTS OF THE TESTS ON THE BLACK-NETTING

No	A	B	C	D	E	F	G	H	I
1	4385	44.0	23.7	20.4	38.4	0.273	8.6	6036	89.4
2	3387	42.8	23.6	19.5	40.8	0.364	7.1	6237	98.7
3	3387	40.5	23.4	19.5	31.2	0.273	9.1	4693	95.0
4	3387	38.9	22.5	19.5	28.8	0.182	10.9	3138	76.0
5	3387	39.9	20.9	19.6	28.8	0.091	16.2	1570	56.5
6	3735	38.4	21.2	20.4	26.4	0.091	19.5	1730	68.0
7	3733	38.5	22.1	20.4	36.0	0.182	10.9	3455	76.0
8	3732	38.5	23.3	20.5	42.0	0.273	7.5	5171	78.3
9	3732	36.8	22.9	20.5	48.0	0.364	6.7	6913	93.5
10	4116	37.5	24.3	21.1	36.0	0.364	7.6	7593	105.7
11	4108	35.3	22.4	21.7	48.0	0.273	10.4	5705	108.8
12	4122	36.0	22.9	22.4	36.0	0.182	14.8	3804	103.0

No	A	B	C	D	E	F	G	H	I
13	4122	32.0	23.4	23.0	24.0	0.091	20.9	1907	72.8
14	4412	38.2	25.8	24.8	26.4	0.091	16.9	1889	58.4
15	4413	36.1	26.8	25.0	28.8	0.182	10.5	4046	72.6
16	4414	38.3	27.0	25.2	36.0	0.273	9.1	6066	94.2
17	4414	36.5	26.6	25.4	48.0	0.364	7.7	8091	106.4
18	3053	38.5	25.8	23.9	36.0	0.364	9.6	5599	132.8
19	3049	39.4	25.4	24.3	42.0	0.273	10.3	4192	106.7
20	3046	40.3	25.5	24.5	42.0	0.182	11.0	2791	75.9
21	3042	36.8	25.0	24.7	24.0	0.091	26.6	1395	92.0
22	2636	38.7	26.2	24.3	30.0	0.091	11.3	1208	39.0
23	2636	44.8	26.4	24.3	42.0	0.182	9.2	2413	63.3
24	2610	43.2	27.4	24.4	42.0	0.273	7.2	3584	74.3
25	2609	43.0	27.3	24.4	48.0	0.364	6.5	4777	89.5
26	2124	44.0	26.6	24.2	60.0	0.273	5.9	2917	60.9
27	2124	43.5	26.4	24.3	54.0	0.182	6.9	1945	47.5
28	2124	40.0	27.5	24.4	30.0	0.091	9.0	973	31.0
29	1838	41.3	27.1	24.3	36.0	0.091	8.3	842	28.6
30	1838	44.2	27.1	24.3	54.0	0.182	6.0	1682	41.3
31	1507	44.5	28.0	24.4	48.0	0.182	5.9	1379	40.5
32	1507	41.2	26.4	24.3	42.0	0.091	8.4	690	29.0
33	1080	42.1	27.4	24.9	42.0	0.091	7.6	494	26.1
34	4715	34.1	27.1	23.3	21.6	0.364	8.2	8657	113.8
35	4715	36.2	27.5	23.2	21.6	0.273	8.6	6488	89.3
36	4715	35.5	25.9	23.2	24.0	0.182	10.7	4329	74.2
37	4716	33.7	24.0	23.	19.2	0.091	21.1	2176	73.4
38	4984	33.4	24.3	23.0	19.2	0.091	18.5	2299	64.4
39	4982	33.7	25.0	23.0	26.4	0.182	10.4	4591	72.3
40	4979	34.2	26.5	23.0	24.0	0.273	8.1	6866	84.3
41	4978	34.0	25.6	22.9	26.4	0.364	9.0	9167	125.1

These results were processed from the experimental data. An example of the calculations necessary to produce these results is presented below. (Note that the flowrate calculation is omitted since it is presented in Appendix 14).

Sample Calculation - Test 11

Figure 20 shows the output trace recorded by Philips voltage plotter.

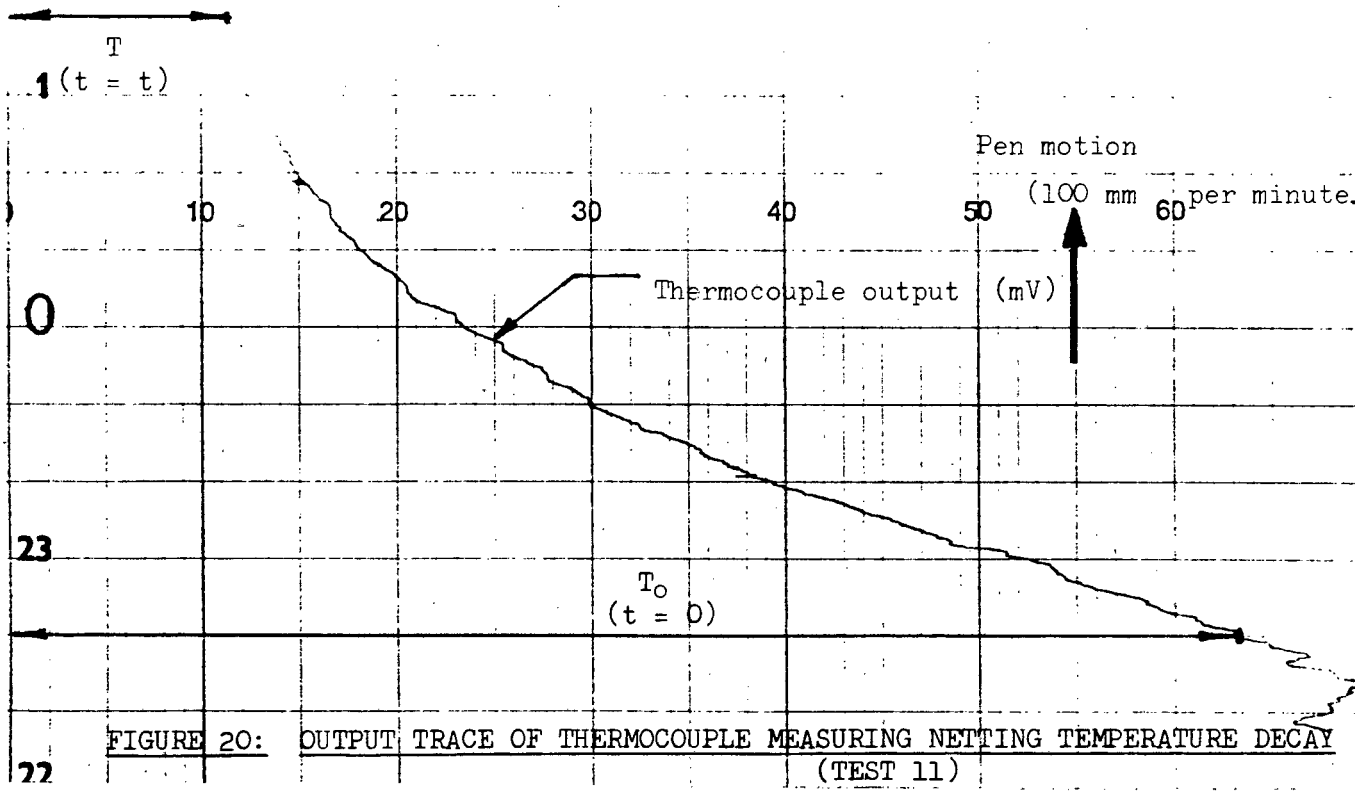

FIGURE 20: OUTPUT TRACE OF THERMOCOUPLE MEASURING NETTING TEMPERATURE DECAY (TEST 11)

Additional data recorded:

Thermocouple reference temperature = 19.6 degrees Centigrade

Free-stream air thermocouple output = 0.079 mV

Paper feed-rate = 100 mm/minute

also recorded, for the purpose of calculating the flowrate, were the wet and dry-bulb air temperatures, the atmospheric pressure, the absolute pressure and the air temperature upstream of the orifice, and the

pressure-drop across the orifice.

Consider Test 11:

The paper has travelled 80mm between t=0 and t=t. Hence elapsed time is (80/100).60 = 48 seconds. The calibration test of the Philips plotter resulted in the following equation to determine voltage output:

$$\text{Voltage} = ((X-1) \times 3.953EE-3) \text{ mV}$$

where 'X' is the distance in mm between the plotting sheet left-hand margin (the zero/datum line) and the trace.Thus the temperature at time t=0 can be worked out from thermocouple tables (Leeds et al - 64) as:

15.7 + Reference temperature

= 15.7 + 19.6

= 35.3 degrees Centigrade

Similarly, the temperature at time t=48 seconds was:

2.8 + 19.6

= 22.4 Degrees Centigrade

The free-stream air temperature was worked out in a similar manner as 21.7 degrees Centigrade.

The local heat-transfer coefficient can now be calculated from equation 5:

$$h = -\left[\log_e \left(\frac{22.4 - 21.7}{35.3 - 21.7}\right) \Big/ 48 \times 5.946 \times 10^{-3}\right] \quad W/m^2.^oC$$

$$= 10.4 \ W/m^2.^oC$$

The calculation of the Reynolds and Nusselt numbers is done with all air properties evaluated at the average film temperature, defined as:

$$\left[\frac{T_s}{2}\right]$$

In this case the average film temperature was 25.3 degrees Centigrade. For this temperature, the air properties were read from tables in Holman (41) at atmospheric pressure as:

$\rho = 1.185$ kg/m^3 $\quad \mu = 1.966 \times 10^{-5}$ kg/m.s $\quad k = 0.0261$ W/m.$^\circ$C

Now $Re_\ell = \left(\frac{\rho.\text{velocity}.\ell}{\mu}\right)$ and velocity $= \left(\frac{\dot{m}}{\rho.A}\right) = \left[\frac{0.004108}{1.185 \times 0.01}\right] = 0.347$ m/s

$$= \left[\frac{1.185 \times 0.347 \times 0.273}{1.96 \times 10^{-5}}\right] = 5709$$

These values differ slightly from Table 1 due to round-off errors.

and $Nu_\ell = \left(\frac{h.\ell}{k}\right) = (10.4 \times 0.273)/0.0261 = 108.8$

In what follows, the dimensionless numbers were assumed to be related as:

(a) $Nu_\ell = C.(Re_\ell)^n$ i.e. one independent variable

(b) $Nu_\ell = C.(\frac{\ell}{L})^m.(Re_\ell)^n$ i.e. two independent variables

If the logarithmic value of equation (a) is written, it is seen to be in the form of a straight line equation i.e.

$$\log_{10}Nu_\ell = n.\log_{10}Re_\ell + \log_{10}C \quad \ldots\ldots\ldots\ldots\ldots\ldots (6)$$

A linear regression analysis of the results produced the following regression table:

SOURCE	SUM OF SQUARES	DEGREES OF FREEDOM	MEAN OF SQUARES
Regression	1.0478467	1	1.0478467
Residual/Error	0.2595836	39	6.65599×10^{-3}
Total	1.3074303	40	

TABLE 2: VARIANCE TABLE FOR ONE DEPENDENT VARIABLE

f-value = 157.43

Coefficient of Determination = 0.801455 ..... (r^2)

Coefficient of Multiple Correlation = 0.895240 ..... (r)

Standard Error of Estimate = 0.081584

The values of 'n' and '$\log_{10}C$' are 0.5012287 and 0.1053667 respectively. On resubstitution into equation (6) and taking anti-logarithms, the following equation results:

$$Nu_\ell = 1.2746\ (Re_\ell)^{0.5} \quad \ldots\ldots\ldots\ldots\ldots\ldots\ldots\ldots\ldots\ldots (7)$$

If logarithms of both sides of equation (b) are taken, the following equation results:

$$\log_{10}Nu_{\ell} = \log_{10}C + m.\log_{10}(\frac{\ell}{L}) + n.\log_{10}(Re_{\ell}) \quad \ldots\ldots\ldots \quad (8)$$

A multiple linear regression analysis of the results produced the following regression table:

SOURCE	SUM OF SQUARES	DEGREES OF FREEDOM	MEAN OF SQUARES
Regression	1.0728844	2	0.5364422
Residual/Error	.2345459	38	0.0061722
Total	1.3074304	40	

TABLE 3: VARIANCE TABLE FOR TWO DEPENDENT VARIABLES

f value = 86.91

Coefficient of Determination = 0.8206 ..... (r^2)

Coefficient of Multiple Correlation = 0.9059 ..... (r)

Standard Error of Estimate = 0.078564

The values of '$\log_{10}C$', 'm' and 'n' are -0.4446, -0.2172 and 0.6351 respectively. Resubstitution of these values into equation (8) and taking anti-logarithms results in the following equation:

$$Nu_{\ell} = 0.3593\,(\frac{\ell}{L})^{-0.22}\,(Re_{\ell})^{0.64} \quad \ldots\ldots\ldots\ldots\ldots \quad (9)$$

The results and the lines produced by equations (7) and (9) are shown on Figure 21, together with the line produced by Kay's equation for a flat plate subjected to Uniform Heat Flux (Kays - Reference 42). In general, it appears that the netting has a laminar forced-convection heat-transfer coefficient about three times larger than that applicable to a flat-plate.

A stepwise comparison and evaluation of the prediction equations using:

(a) one independent variable (b) two independent variables

Case (a):

Computed f = (sum of squares of regression/mean of squares of the error)

= $(1.04784/6.65599 \times 10^{-3})$

= 157.43

Now the f-value from the F chart at the 0.05 level of significance is:

$f_{0.05}(k, n-k-1)$ where 'k' is the number of independent variables

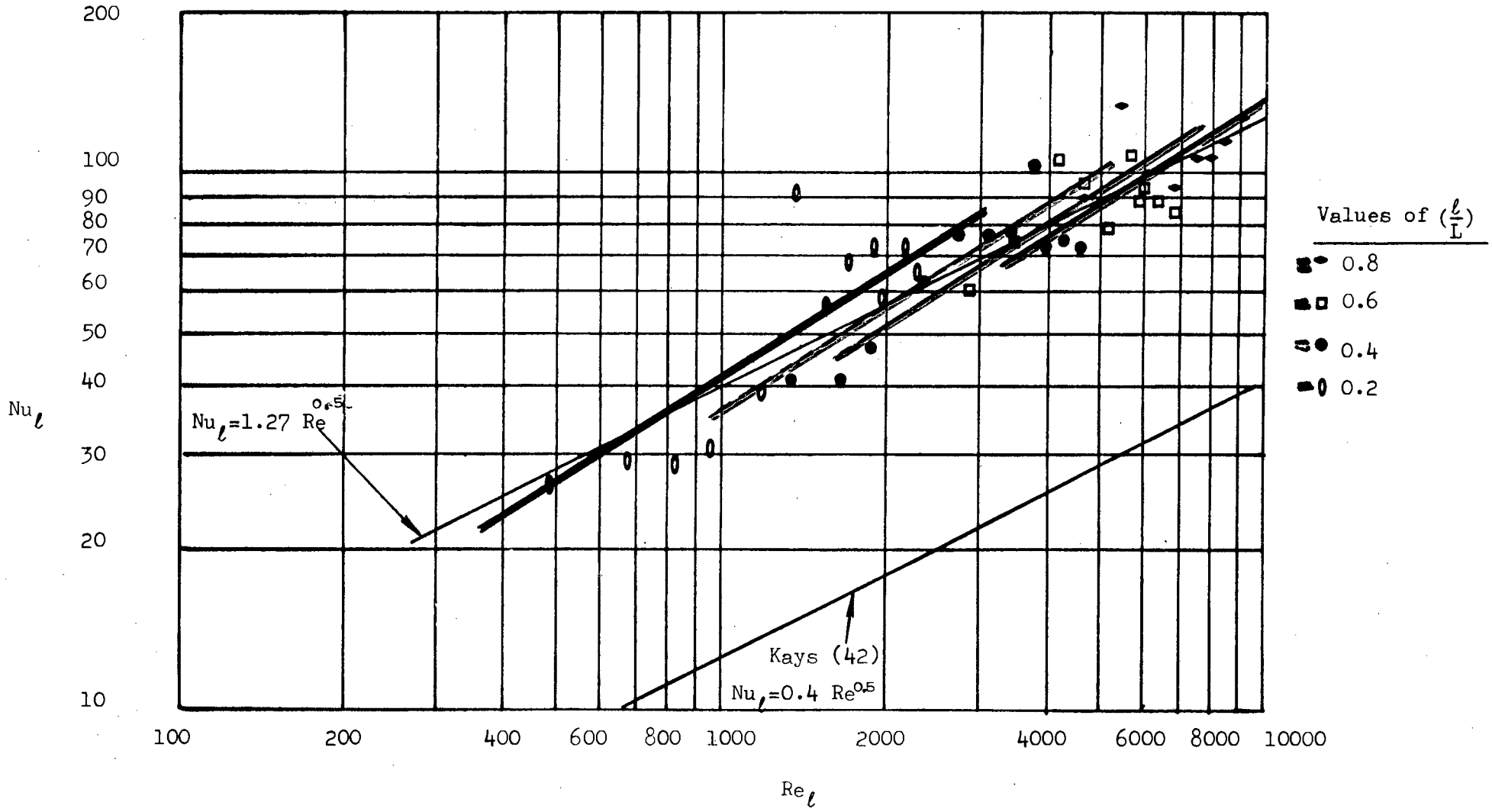

FIGURE 21: THE BLACK NETTING TEST DATA AND PREDICTION EQUATIONS

There are 41 data points and there is one independent variable, hence

$$f_{0.05}(1,39) = 4.08 \text{ from the F chart (see Table 5)}$$

Since the computed f statistic (157) is much larger than the critical value (4.08) at the five percent significance level, it can be concluded that '$\log_{10}Re$' is a highly significant variable, and should be included in the prediction equation. For this model the coefficient of determination is 0.801, which means that 80.1 percent of the variance in '$\log_{10}Nu_{\ell}$' is explained by the prediction equation (equation 7)

Case (b):

The regression sum of squares of the second independent variable i.e. '$\log_{10}(\frac{\ell}{L})$' can be calculated as follows:

$$\text{Regression } (\beta_2/\beta_1) = \text{Regression } (\beta_1, \beta_2) - \text{Regression } (\beta_1)$$

where β_1 is the coefficient 'n' of the variable '$\log_{10}Re_{\ell}$'

and β_2 is the coefficient 'm' of the variable '$\log_{10}(\frac{\ell}{L})$'. In other words, Regression (β_2/β_1) is the regression sum of squares of the restricted regression model using '$m.\log_{10}(\frac{\ell}{L})$' in the presence of '$n.\log_{10}Re_{\ell}$'.

Using values from the regression analysis:

$$\text{Regression } (\beta_2/\beta_1) = 1.0728844 - 1.0478467$$

$$= 0.025037$$

$$\text{Now the computed f-value} = \left[\frac{\text{Regression sum of squares } (\beta_2/\beta_1)}{\text{Mean of squares of the error}}\right]$$

$$= (0.025037/0.0061722) = 4.06$$

The f-value at the 0.05 significance level is:

$$f_{0.05}(1,38) = 4.08$$

Since the computed f-value and the significant f-value are approximately equal, it can be concluded that '$\log_{10}(\frac{\ell}{L})$' is not a significant variable at the five percent level of significance. However, the coefficient of multiple determination for this multiple linear regression model is 0.821, which means that 82.1 percent of the variance of '$\log_{10}Nu_{\ell}$' is explained by the prediction equation. Since the priority is the accurate prediction of 'Nu_{ℓ}' (and by implication, the accurate prediction of the black-netting heat-transfer coefficient), it has been decided to include the variable $(\frac{\ell}{L})$.

TABLE 4 Walpole (49)

Critical
Values of the F Distribution

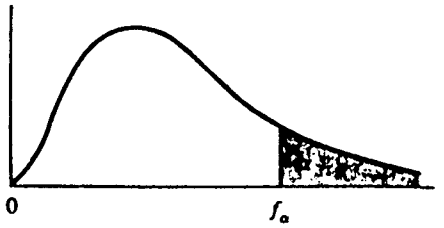

$f_{0.05}(\nu_1, \nu_2)$

ν_2	ν_1								
	1	2	3	4	5	6	7	8	9
1	161.4	199.5	215.7	224.6	230.2	234.0	236.8	238.9	240.5
2	18.51	19.00	19.16	19.25	19.30	19.33	19.35	19.37	19.38
3	10.13	9.55	9.28	9.12	9.01	8.94	8.89	8.85	8.81
4	7.71	6.94	6.59	6.39	6.26	6.16	6.09	6.04	6.00
5	6.61	5.79	5.41	5.19	5.05	4.95	4.88	4.82	4.77
6	5.99	5.14	4.76	4.53	4.39	4.28	4.21	4.15	4.10
7	5.59	4.74	4.35	4.12	3.97	3.87	3.79	3.73	3.68
8	5.32	4.46	4.07	3.84	3.69	3.58	3.50	3.44	3.39
9	5.12	4.26	3.86	3.63	3.48	3.37	3.29	3.23	3.18
10	4.96	4.10	3.71	3.48	3.33	3.22	3.14	3.07	3.02
11	4.84	3.98	3.59	3.36	3.20	3.09	3.01	2.95	2.90
12	4.75	3.89	3.49	3.26	3.11	3.00	2.91	2.85	2.80
13	4.67	3.81	3.41	3.18	3.03	2.92	2.83	2.77	2.71
14	4.60	3.74	3.34	3.11	2.96	2.85	2.76	2.70	2.65
15	4.54	3.68	3.29	3.06	2.90	2.79	2.71	2.64	2.59
16	4.49	3.63	3.24	3.01	2.85	2.74	2.66	2.59	2.54
17	4.45	3.59	3.20	2.96	2.81	2.70	2.61	2.55	2.49
18	4.41	3.55	3.16	2.93	2.77	2.66	2.58	2.51	2.46
19	4.38	3.52	3.13	2.90	2.74	2.63	2.54	2.48	2.42
20	4.35	3.49	3.10	2.87	2.71	2.60	2.51	2.45	2.39
21	4.32	3.47	3.07	2.84	2.68	2.57	2.49	2.42	2.37
22	4.30	3.44	3.05	2.82	2.66	2.55	2.46	2.40	2.34
23	4.28	3.42	3.03	2.80	2.64	2.53	2.44	2.37	2.32
24	4.26	3.40	3.01	2.78	2.62	2.51	2.42	2.36	2.30
25	4.24	3.39	2.99	2.76	2.60	2.49	2.40	2.34	2.28
26	4.23	3.37	2.98	2.74	2.59	2.47	2.39	2.32	2.27
27	4.21	3.35	2.96	2.73	2.57	2.46	2.37	2.31	2.25
28	4.20	3.34	2.95	2.71	2.56	2.45	2.36	2.29	2.24
29	4.18	3.33	2.93	2.70	2.55	2.43	2.35	2.28	2.22
30	4.17	3.32	2.92	2.69	2.53	2.42	2.33	2.27	2.21
40	4.08	3.23	2.84	2.61	2.45	2.34	2.25	2.18	2.12
60	4.00	3.15	2.76	2.53	2.37	2.25	2.17	2.10	2.04
120	3.92	3.07	2.68	2.45	2.29	2.17	2.09	2.02	1.96
∞	3.84	3.00	2.60	2.37	2.21	2.10	2.01	1.94	1.88

TABLE 5

Critical Values of the F Distribution (*continued*)

$f_{0.05}(\nu_1, \nu_2)$

ν_2	ν_1									
	10	12	15	20	24	30	40	60	120	∞
1	241.9	243.9	245.9	248.0	249.1	250.1	251.1	252.2	253.3	254.3
2	19.40	19.41	19.43	19.45	19.45	19.46	19.47	19.48	19.49	19.50
3	8.79	8.74	8.70	8.66	8.64	8.62	8.59	8.57	8.55	8.53
4	5.96	5.91	5.86	5.80	5.77	5.75	5.72	5.69	5.66	5.63
5	4.74	4.68	4.62	4.56	4.53	4.50	4.46	4.43	4.40	4.36
6	4.06	4.00	3.94	3.87	3.84	3.81	3.77	3.74	3.70	3.67
7	3.64	3.57	3.51	3.44	3.41	3.38	3.34	3.30	3.27	3.23
8	3.35	3.28	3.22	3.15	3.12	3.08	3.04	3.01	2.97	2.93
9	3.14	3.07	3.01	2.94	2.90	2.86	2.83	2.79	2.75	2.71
10	2.98	2.91	2.85	2.77	2.74	2.70	2.66	2.62	2.58	2.54
11	2.85	2.79	2.72	2.65	2.61	2.57	2.53	2.49	2.45	2.40
12	2.75	2.69	2.62	2.54	2.51	2.47	2.43	2.38	2.34	2.30
13	2.67	2.60	2.53	2.46	2.42	2.38	2.34	2.30	2.25	2.21
14	2.60	2.53	2.46	2.39	2.35	2.31	2.27	2.22	2.18	2.13
15	2.54	2.48	2.40	2.33	2.29	2.25	2.20	2.16	2.11	2.07
16	2.49	2.42	2.35	2.28	2.24	2.19	2.15	2.11	2.06	2.01
17	2.45	2.38	2.31	2.23	2.19	2.15	2.10	2.06	2.01	1.96
18	2.41	2.34	2.27	2.19	2.15	2.11	2.06	2.02	1.97	1.92
19	2.38	2.31	2.23	2.16	2.11	2.07	2.03	1.98	1.93	1.88
20	2.35	2.28	2.20	2.12	2.08	2.04	1.99	1.95	1.90	1.84
21	2.32	2.25	2.18	2.10	2.05	2.01	1.96	1.92	1.87	1.81
22	2.30	2.23	2.15	2.07	2.03	1.98	1.94	1.89	1.84	1.78
23	2.27	2.20	2.13	2.05	2.01	1.96	1.91	1.86	1.81	1.76
24	2.25	2.18	2.11	2.03	1.98	1.94	1.89	1.84	1.79	1.73
25	2.24	2.16	2.09	2.01	1.96	1.92	1.87	1.82	1.77	1.71
26	2.22	2.15	2.07	1.99	1.95	1.90	1.85	1.80	1.75	1.69
27	2.20	2.13	2.06	1.97	1.93	1.88	1.84	1.79	1.73	1.67
28	2.19	2.12	2.04	1.96	1.91	1.87	1.82	1.77	1.71	1.65
29	2.18	2.10	2.03	1.94	1.90	1.85	1.81	1.75	1.70	1.64
30	2.16	2.09	2.01	1.93	1.89	1.84	1.79	1.74	1.68	1.62
40	2.08	2.00	1.92	1.84	1.79	1.74	1.69	1.64	1.58	1.51
60	1.99	1.92	1.84	1.75	1.70	1.65	1.59	1.53	1.47	1.39
120	1.91	1.83	1.75	1.66	1.61	1.55	1.50	1.43	1.35	1.25
∞	1.83	1.75	1.67	1.57	1.52	1.46	1.39	1.32	1.22	1.00

Hence the dimensionless equation for defining heat-transfer under laminar forced-flow conditions for the black-netting used in this thesis was:

$$Nu_{\ell} = 0.3593 \left(\frac{\ell}{L}\right)^{-0.22} (Re_{\ell})^{0.64} \quad \ldots\ldots\ldots\ldots\ldots (9)$$

The reader is referred to Walpole et al (49) and Kennedy et al (50) for detailed discussion on Linear and Multiple Linear Regression and the optimisation of variables by use of the 'stepwise regression' technique.

2.4 Boundary layer considerations

Figure 22 shows the cross-sectional dimensions of the apparatus used for measuring the black-netting heat transfer coefficient. From this it can be seen that a boundary layer thickness of 25 mm and above will result in fully developed flow. The maximum value of Reynolds number that is likely to be reached using this apparatus is defined by the equation:

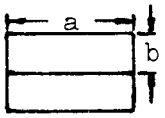

a = 0.1 m
b = 0.05 m

FIGURE 22: BOX CROSS-SECTION

$$Re_{\ell} = \left[\frac{\rho.\ell.\text{Velocity}}{\mu}\right] = \left[\frac{\dot{m}.\ell}{A.\mu}\right] = \left(\frac{0.004 \times 0.455}{0.01 \times 2 \times 10^{-5}}\right)$$

$$= 9100$$

Since this is smaller than 5×10^5, the flow should always be laminar in nature. For laminar flow, Holman (41) quotes the following equation for boundary layer thickness on a flat plate:

$$\sigma = \left[\frac{4.64 \times \ell}{(Re_{\ell})^{0.5}}\right]$$

From this relationship, with the boundary layer thickness 'σ' specified as 0.025 m, the entry length required for fully developed flow to occur can be specified as:

$$\ell = \left(145 \times \dot{m}\right) \text{ metres} \quad \ldots\ldots\ldots\ldots\ldots\ldots\ldots\ldots (10)$$

where '$\dot{m}$' is the air-flowrate in kg/s. This criterion was used to exclude fully developed flow data from the data used to formulate equation (9).

2.5 A comparison of the internal and external black-netting heat resistances

In order that the lumped-heat-capacityanalysis can be applied to determine the black-netting heat transfer coefficient, it was necessary to establish that the internal heat resistance of the netting was much smaller than the external or surface heat resistance. If this was the case then the netting can be considered as being at uniform temperature at any cross-section. Consider the cross-section of netting shown below in Figure 23. The electrical analogy for the heat flow in this

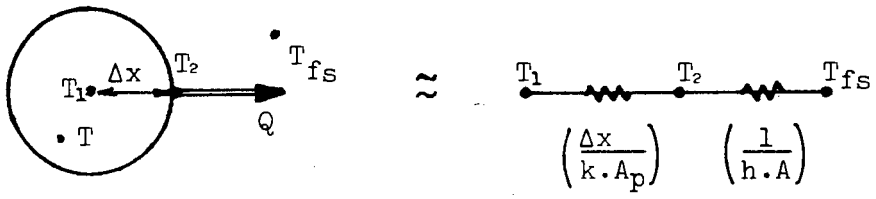

FIGURE 23: THE ELECTRICAL ANALOGY

situation is shown alongside. The symbols have the following meanings:

Δx = strand radius = 0.125×10^{-3} metres

k = thermal conductivity of polyethylene = 0.4 W/m.°C from Kinney (51)

A_p = perimeter area, h = convection heat-transfer coefficient

A = superficial netting cloth area

The ratio $\left[\frac{\text{superficial area strand}}{\text{superficial area netting}}\right]$ is assumed approximately equal to the transmittance of the netting for normal radiation - which is 0.45 from Appendix 3. This can be rewritten as:

$\left(\frac{A_p/\pi}{A}\right) = 0.45$ hence $A = 0.71\ A_p$, but the convection coefficient is based on the total (i.e. top and bottom) area. Thus

$$A = 1.4\ A_p$$

Inspection of the results shows that 'h' varies between 26.6 and 5.9 W/m.°C.

The internal conduction resistance is $\sim\left(0.125 \times 10^{-3}/0.4\right) = 0.0003125$

The external convection resistance is $\sim\left(1/26.6 \times 1.4\right) = 0.02685$

Thus the external resistance is 85 (or more) times larger than the internal resistance.

APPENDIX 3

THE CLEAR-POLYETHYLENE AND BLACK-NETTING RADIATION PROPERTIES

Radiation is electromagnetic in nature and spans wavelengths from 10^{10}-$10^{-8}\mu m$. Figure 24 shows the spectrum of electromagnetic radiation as defined by Beckman et al (17).

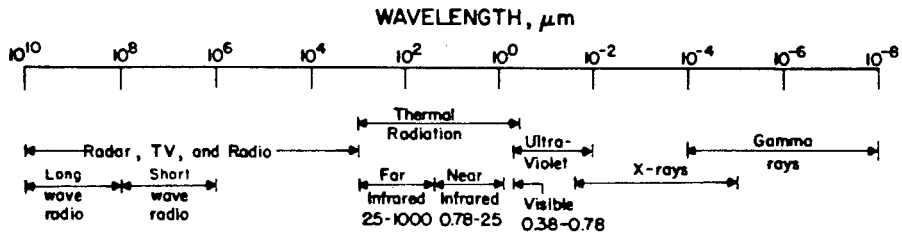

FIGURE 24: SPECTRUM OF ELECTROMAGNETIC RADIATION

Radiation in the region of the electromagnetic spectrum from about 0.2 micrometres to about 100 micrometres is called thermal radiation and is emitted by a surface as a result of its temperature.

The wavelength distribution from a body is a function of its temperature, and Wien has shown (Beckman et al - 17) that the wavelength corresponding to the maximum intensity of blackbody radiation is calculated using the equation:

$$\lambda_{max}.T = 2897.8\ \mu m.^{o}K \quad \ldots\ldots\ldots\ldots\ldots\ldots\ldots\ldots\ (1)$$

This is known as Wien's displacement law and is illustrated in Figure 25, which shows spectral radiation distribution for blackbody radiation from sources at 6000, 1000 and 400 degrees Kelvin.

When radiant energy strikes a material surface, part of it is reflected, part is absorbed and part is transmitted - as shown in Figure 26.

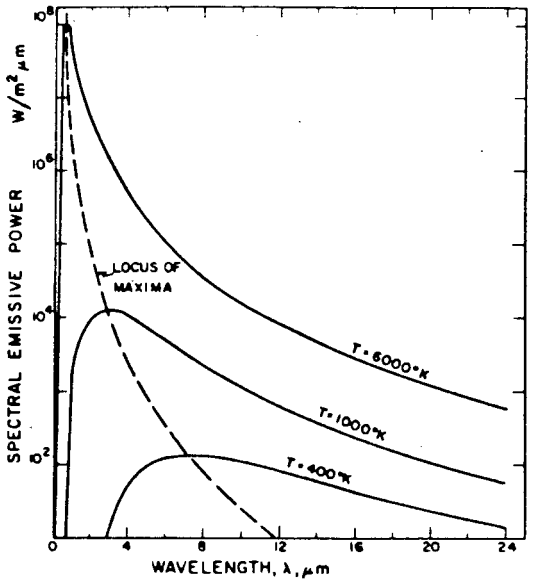

FIGURE 25: THE SPECTRAL DISTRIBUTION OF BLACKBODY RADIATION

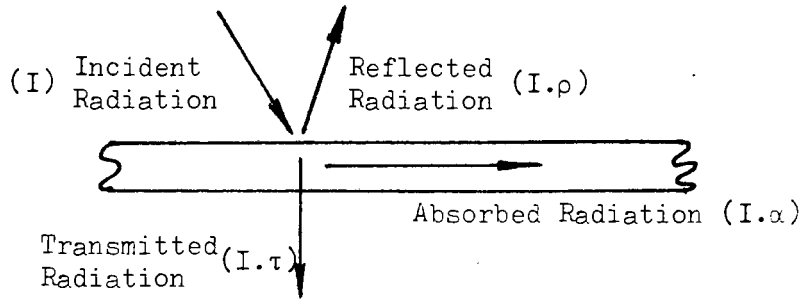

FIGURE 26: THE DISTRIBUTION OF RADIATION ON STRIKING A SURFACE

The reflectance is defined as the fraction of incident radiation reflected, the transmittance is the fraction transmitted and the absorptance is the fraction absorbed. From the law of energy conservation it can be concluded that the sum of these is unity i.e.

$$\rho + \tau + \alpha = 1 \quad \ldots\ldots\ldots\ldots\ldots\ldots\ldots\ldots\ldots\ldots\ldots\ldots\ldots\ldots \quad (2)$$

By definition, a blackbody is a perfect emitter and absorber of radiation. No matter what wavelengths or directions describe the radiation incident on a blackbody, all of that radiation will be absorbed. A blackbody is also a perfect emitter of thermal radiation. The emittance of a surface is defined as the ratio of intensity leaving the surface to that leaving a blackbody at the same temperature. Kirchoff's law (Beckman et al - 17) states that for any body in thermal equilibrium:

$$\alpha = \varepsilon \quad \ldots\ldots\ldots\ldots\ldots\ldots\ldots\ldots\ldots\ldots\ldots\ldots\ldots\ldots\ldots\ldots \quad (3)$$

where 'α' is the absorptance and 'ε' is the emittance of the body.

The absorptance of a material can vary depending on the wavelength characteristics of the radiation. By Kirchoff's law, the same is true of the surface emittance. Wien's law implies that radiation characteristics are source temperature dependent, and so it was suspected that the simulated solar radiation (i.e. shortwave radiation) and low-temperature radiation (i.e. longwave radiation) absorptances of the collector surfaces would be different, and by Kirchoff's law the same would hold for the surface emittances. Thus the radiation properties of the clear-polyethylene and the black-netting were evaluated for both simulated solar radiation and radiation from a low temperature source.

3.1 SIMULATED SOLAR RADIATION

3.1.1 The Clear-Polyethylene

The polyethylene has the tradename "Uvideck" and is manufactured by Gundle Plastics as a greenhouse covering material. Its transmittance was evaluated using the apparatus shown in Photograph 9. Readings of incident radiation were made before and after each test with a thermopile and the polyethylene removed. The transmitted radiation was measured with the polyethylene cover in position at the required angle, and the transmittance was calculated as:

$$\tau(\theta) = \frac{\text{transmitted radiation}}{\text{incident radiation}} \quad \ldots\ldots\ldots\ldots\ldots\ldots \quad (4)$$

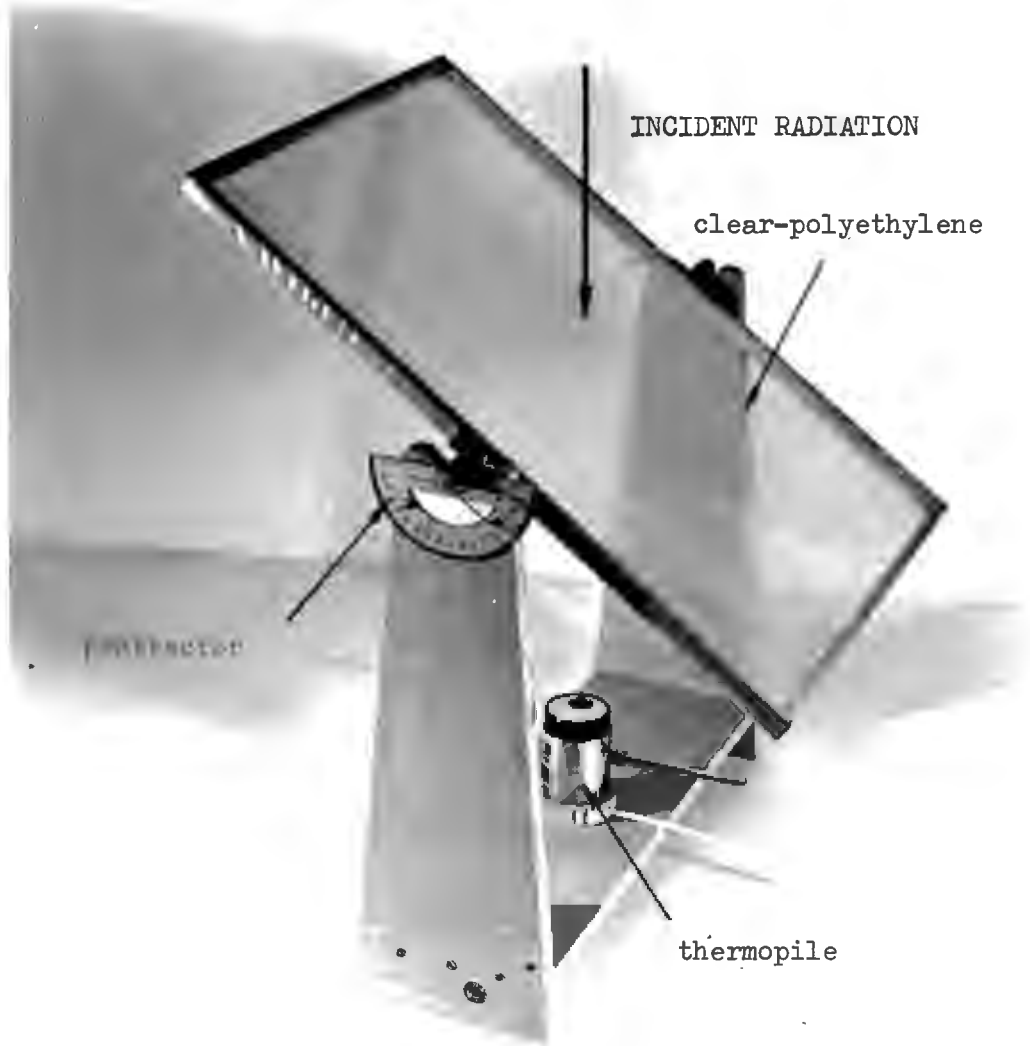

Photograph 9: The Clear-Polyethylene Transmittance Apparatus

Tests were conducted for incident radiation angles between zero and ninety degrees at intervals of five degrees. The tests were repeated four times and an average value of transmittance was calculated. The results are given in Table 6 and are illustrated in Figure 27.

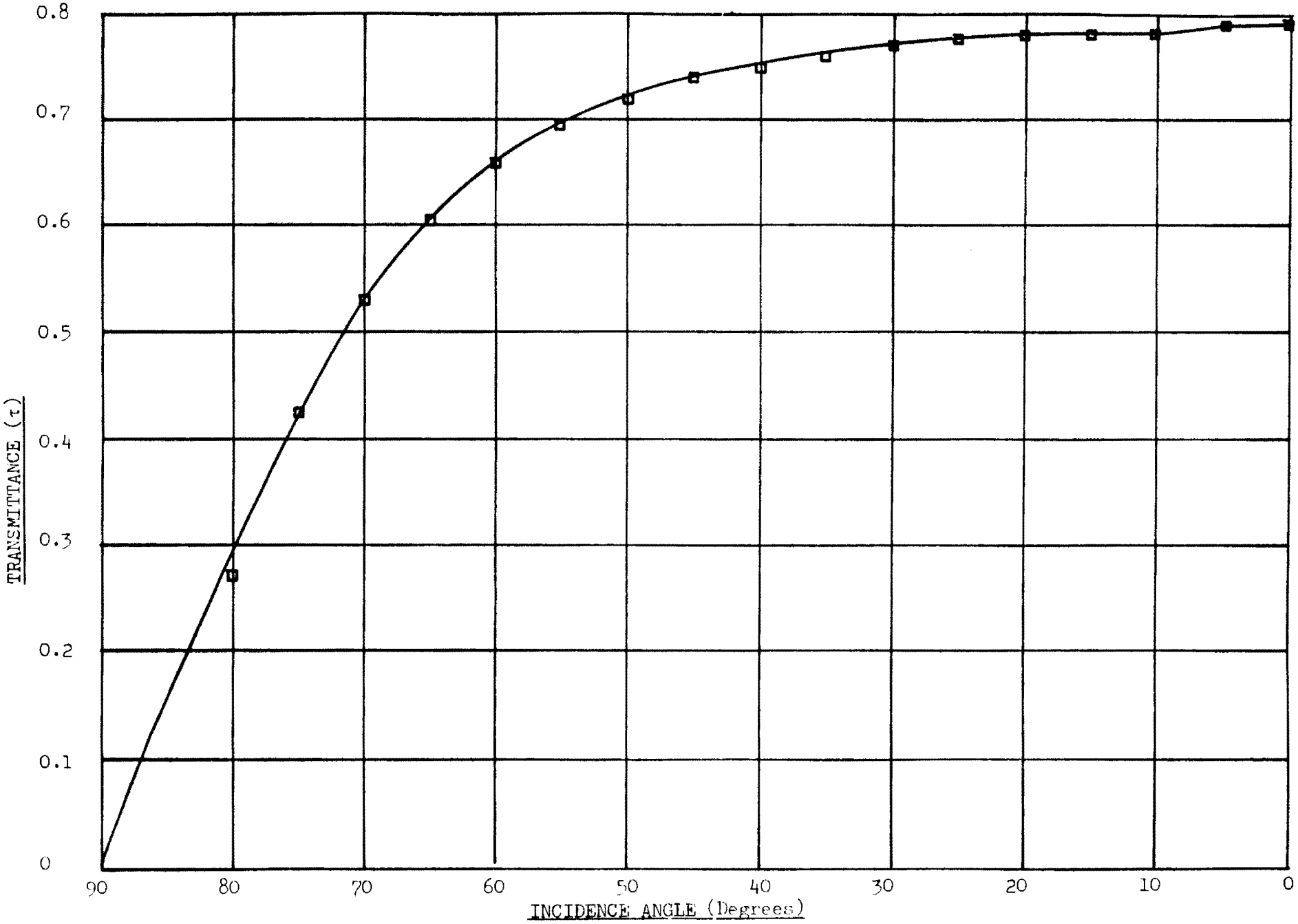

FIGURE 27: THE TRANSMITTANCE OF THE CLEAR-POLYETHYLENE FOR SIMULATED SOLAR RADIATION

Incidence Angle (θ)	τ_1	τ_2	τ_3	τ_4	$\bar{\tau}$
0	0.79	0.79	0.79	0.79	0.79
5	0.79	0.79	0.79	0.79	0.79
10	0.79	0.78	0.78	0.78	0.78
15	0.79	0.78	0.78	0.78	0.78
20	0.78	0.78	0.77	0.78	0.78
25	0.78	0.78	0.77	0.77	0.77
30	0.77	0.77	0.76	0.77	0.77
35	0.76	0.76	0.76	0.76	0.76
40	0.75	0.75	0.75	0.75	0.75
45	0.74	0.74	0.74	0.74	0.74
50	0.72	0.72	0.72	0.72	0.72
55	0.70	0.69	0.70	0.69	0.69
60	0.66	0.65	0.66	0.66	0.66
65	0.60	0.60	0.61	0.61	0.61
70	0.53	0.53	0.53	0.53	0.53
75	0.42	0.42	0.43	0.43	0.43
80	0.26	0.27	0.28	0.27	0.27

TABLE 6: THE CLEAR-POLYETHYLENE TRANSMITTANCE RESULTS

The clear-polyethylene reflectance was evaluated as a function of radiation incidence angle using the apparatus shown in Photograph 10. The thermopile was mounted on a rotatable arm which was used to measure the specular reflection from the polyethylene. This was done by rotating the thermopile so as to receive the reflected radiation at a reflection angle equal to the incidence angle on the polyethylene (Photograph 10).

Photograph 10: The Clear-Polyethylene Reflectance Apparatus

The incident radiation was measured by rotating the thermopile to receive direct radiation from the source. The polyethylene cover was removed during this operation. As before, the tests were conducted for incidence angles between zero and ninety degrees. Each test was repeated four times and an average specular reflectance was calculated for each incidence angle. The specular reflectance was calculated as:

$$\rho_{specular}(\theta) = \frac{\text{reflected specular radiation}}{\text{incident radiation}} \quad \ldots\ldots (5)$$

Beckman et al (17) specify that the diffuse radiation reflectance can be regarded as equal to the specular reflectance at an angle of sixty degrees. Using this relationship, the total reflectance was calculated as:

$$\rho_{total}(\theta) = \rho_{specular}(\theta) + \rho_{specular}(60)^{\circ} \quad \ldots\ldots\ldots (6)$$

The results of these tests are given in Table 7 and are illustrated in Figure 28.

Incidence Angle (θ)	$\rho_{specular}$	ρ_{total}
5	0.07	0.19
10	0.07	0.19
15	0.07	0.19
20	0.07	0.19
25	0.07	0.19
30	0.07	0.19
35	0.07	0.19
40	0.08	0.19
45	0.08	0.20
50	0.08	0.21
55	0.10	0.22
60	0.12	0.24
65	0.16	0.28
70	0.21	0.33
75	0.31	0.43
80	0.47	0.59

TABLE 7: THE CLEAR-POLYETHYLENE REFLECTANCE RESULTS

Beckman et al (17) specify that the diffuse radiation reflectance can be regarded as equal to the specular reflectance at an angle of sixty degrees. Using this relationship, the total reflectance was calculated as:

$$\rho_{total}(\theta) = \rho_{specular}(\theta) + \rho_{specular}(60)^{\circ} \quad \ldots\ldots\ldots (6)$$

The results of these tests are given in Table 7 and are illustrated in Figure 28.

Incidence Angle (θ)	$\rho_{specular}$	ρ_{total}
5	0.07	0.19
10	0.07	0.19
15	0.07	0.19
20	0.07	0.19
25	0.07	0.19
30	0.07	0.19
35	0.07	0.19
40	0.08	0.19
45	0.08	0.20
50	0.08	0.21
55	0.10	0.22
60	0.12	0.24
65	0.16	0.28
70	0.21	0.33
75	0.31	0.43
80	0.47	0.59

TABLE 7: THE CLEAR-POLYETHYLENE REFLECTANCE RESULTS

The clear-polyethylene absorptance was evaluated using the law of conservation of energy (Equation 2) i.e.

$$\alpha = 1 - (\rho_{total} + \tau) \quad \ldots\ldots\ldots\ldots\ldots\ldots\ldots\ldots\ldots\ldots (7)$$

The results are presented in Table 8 and Figure 29.

Incidence Angle (θ)	α
80	0.14
75	0.14
70	0.14
65	0.11
60	0.10
55	0.08
50	0.07
45	0.06
40	0.06
35	0.05
30	0.04
25	0.03
20	0.03
15	0.03
10	0.03
5	0.02

TABLE 8: THE CLEAR-POLYETHYLENE ABSORPTANCE RESULTS

3.1.2 The Black-Netting Properties

The black-netting transmittance was evaluated using the apparatus shown in Photograph 11.

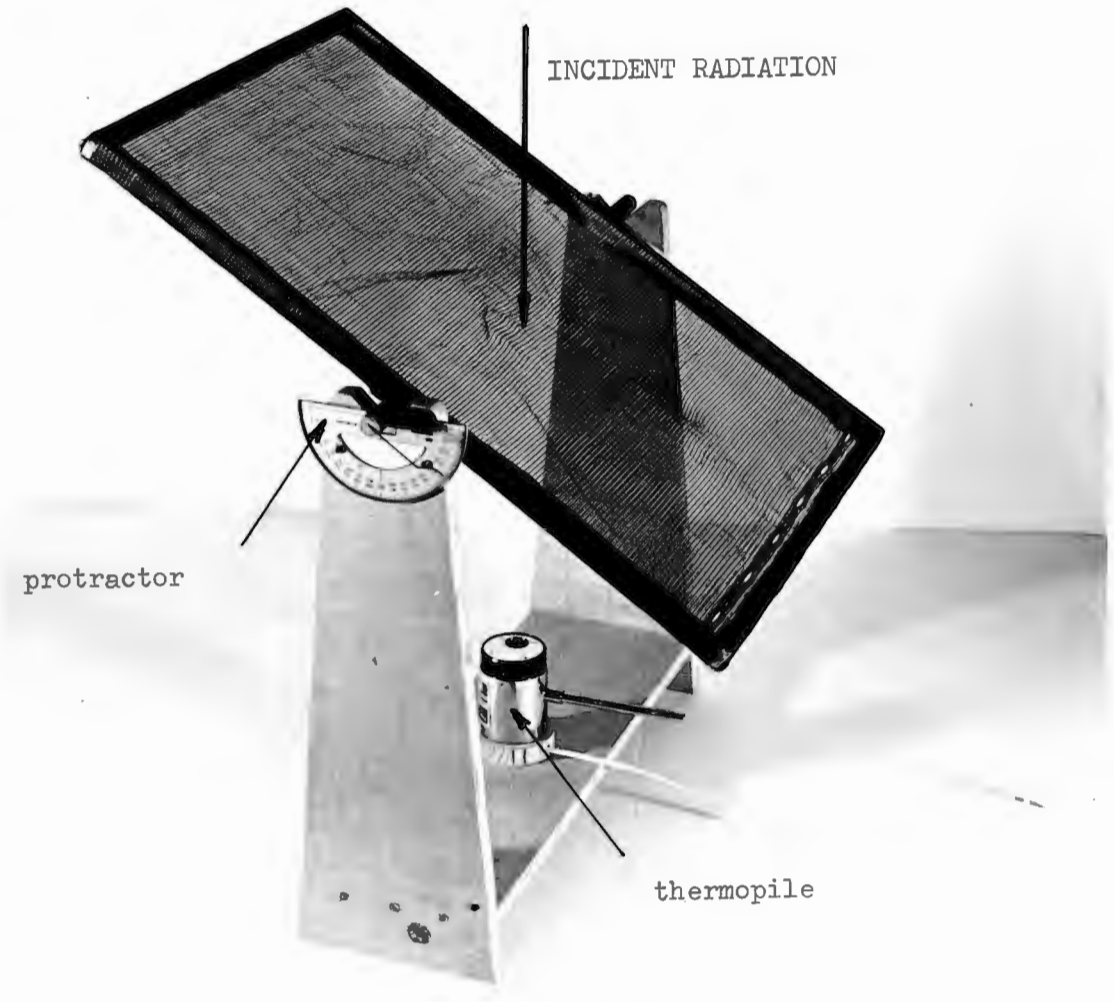

Photograph 11: The Black-Netting Transmittance Apparatus

The procedure is exactly the same as is detailed in Appendix 3.1.1 for the clear-polyethylene. Results of the tests are presented below in Table 9 and are illustrated in Figure 30.

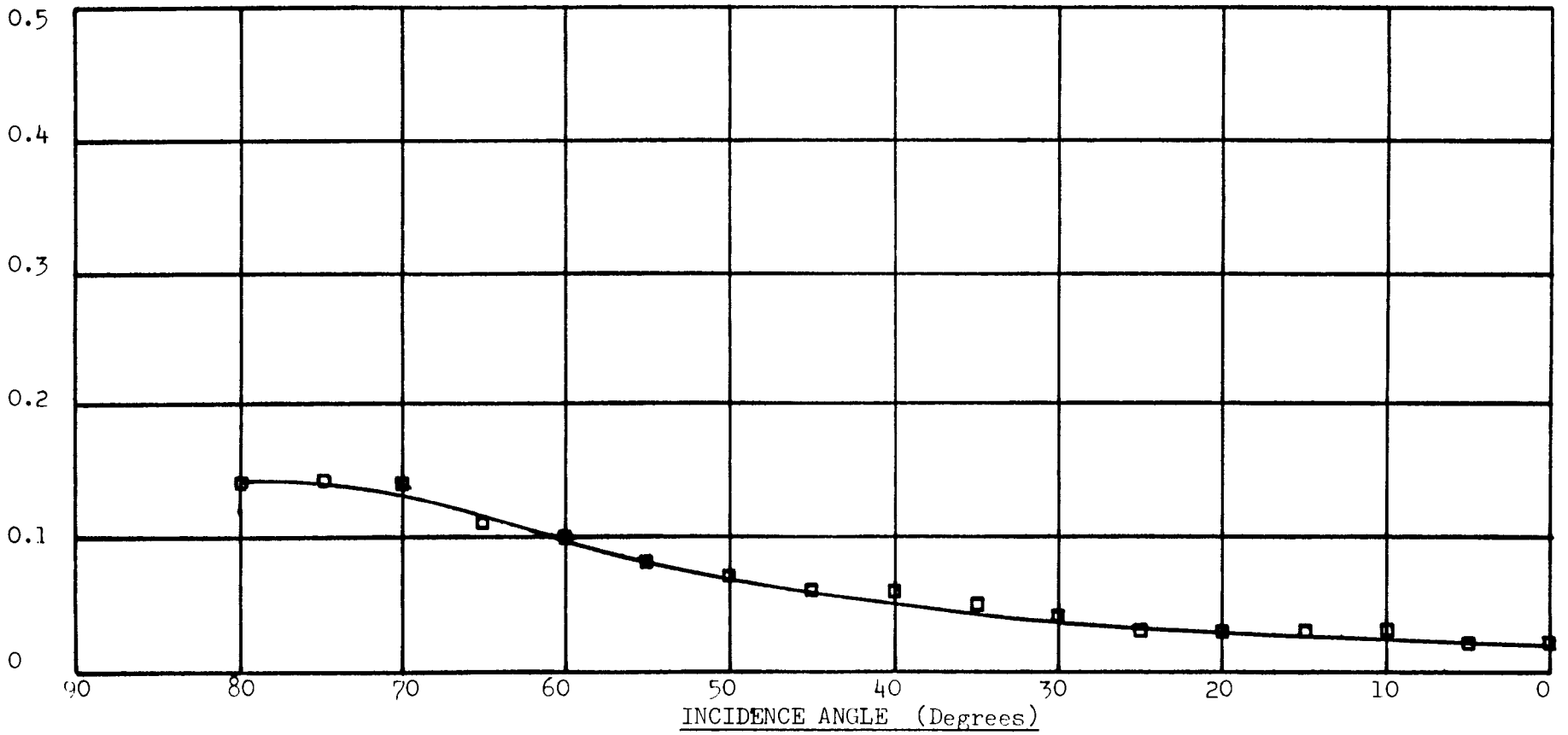

FIGURE 29: THE ABSORPTANCE OF THE CLEAR-POLYETHYLENE FOR SIMULATED SOLAR RADIATION

3.1.2 The Black-Netting Properties

The black-netting transmittance was evaluated using the apparatus shown in Photograph 11.

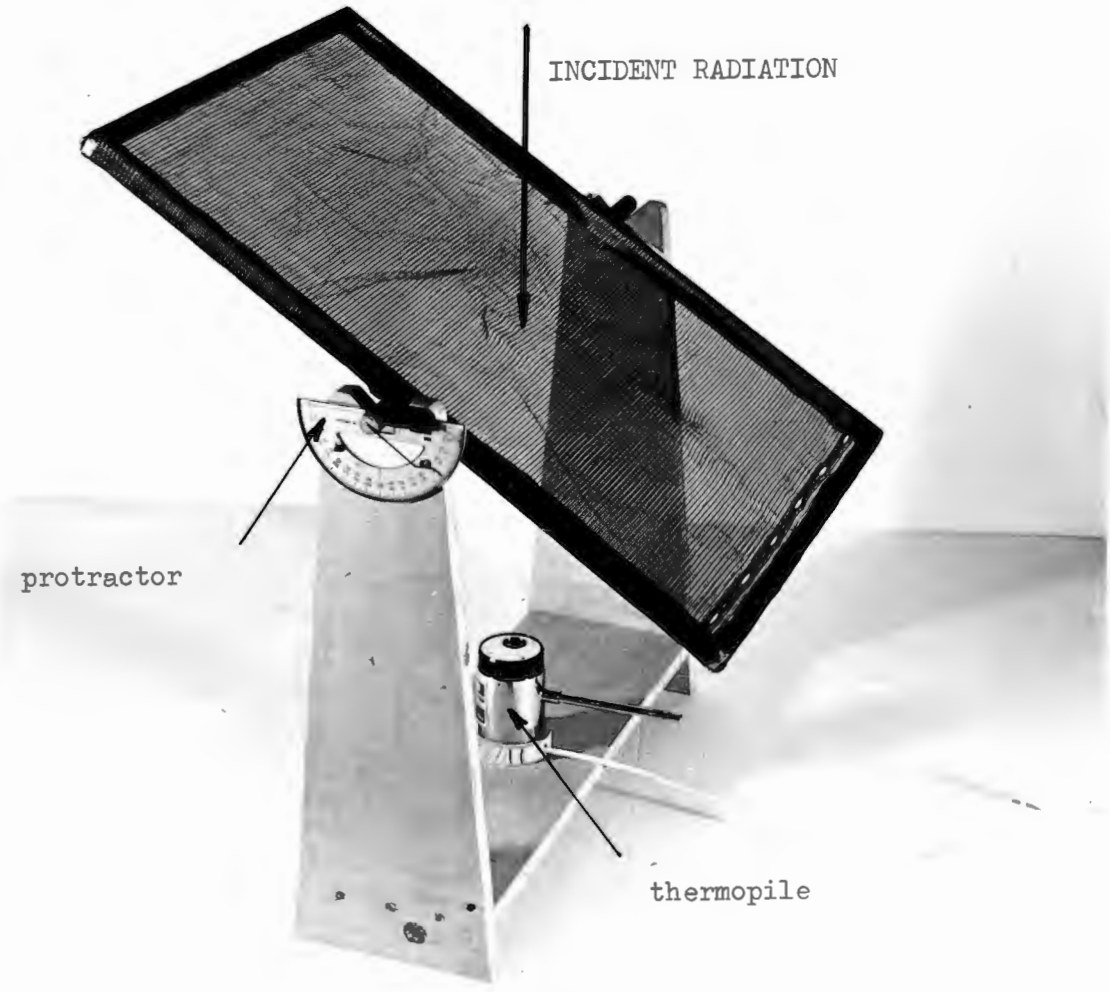

Photograph 11: The Black-Netting Transmittance Apparatus

The procedure is exactly the same as is detailed in Appendix 3.1.1 for the clear-polyethylene. Results of the tests are presented below in Table 9 and are illustrated in Figure 30.

Incidence Angle (θ)	τ_1	τ_2	τ_3	τ_4	τ_5
85	0.01	0.01	0.01	0.01	0.01
80	0.05	0.05	0.03	0.04	0.04
75	0.15	0.15	0.12	0.12	0.14
70	0.22	0.23	0.20	0.20	0.21
65	0.27	0.27	0.25	0.25	0.26
60	0.31	0.31	0.30	0.30	0.31
55	0.34	0.34	0.33	0.34	0.34
50	0.36	0.36	0.36	0.37	0.36
45	0.38	0.38	0.39	0.38	0.38
40	0.39	0.39	0.40	0.40	0.40
35	0.41	0.41	0.42	0.42	0.42
30	0.42	0.42	0.43	0.43	0.43
25	0.43	0.43	0.43	0.43	0.43
20	0.44	0.44	0.44	0.44	0.44
15	0.44	0.45	0.44	0.45	0.45
10	0.44	0.45	0.45	0.45	0.45
5	0.45	0.45	0.45	0.45	0.45
0	0.45	0.45	0.45	0.45	0.45

TABLE 9: THE BLACK-NETTING TRANSMITTANCE RESULTS

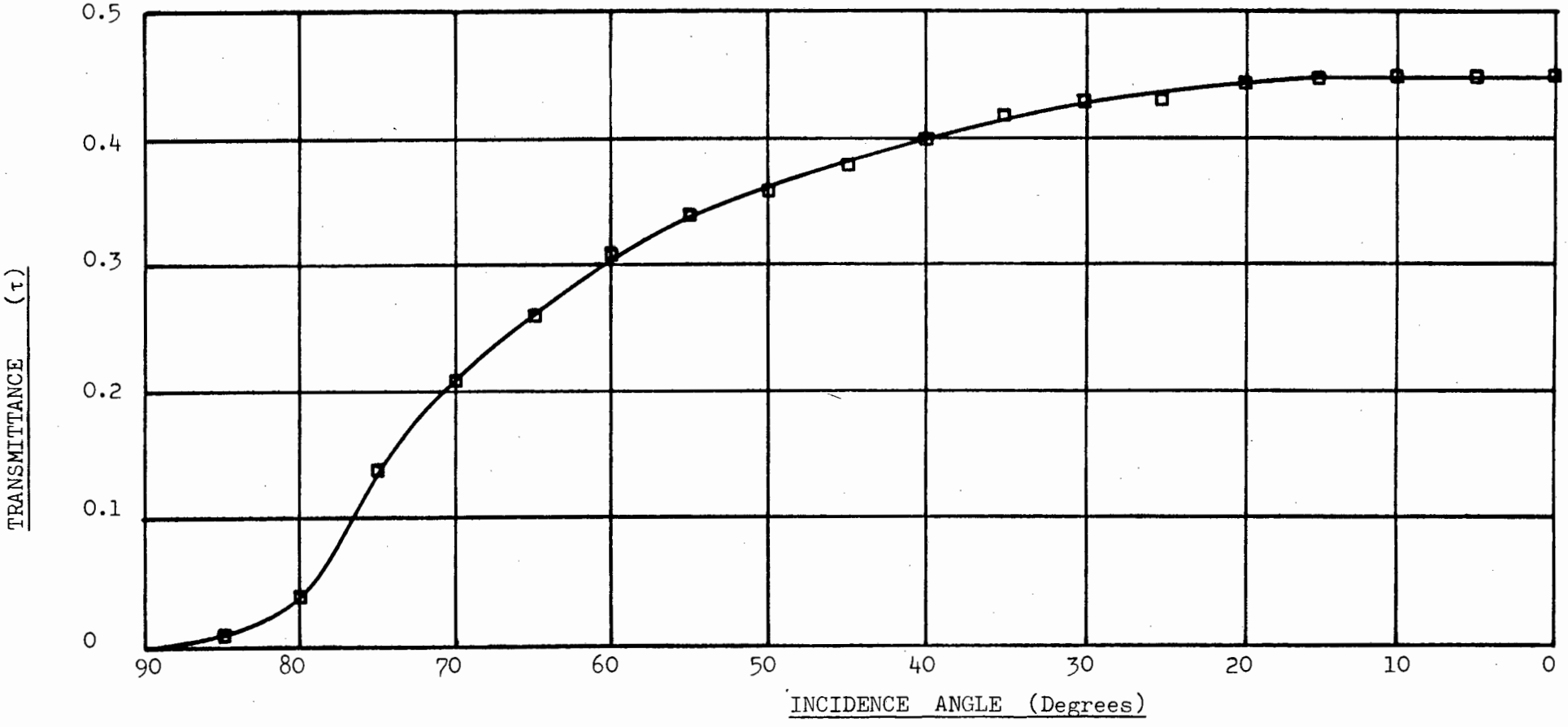

FIGURE 30: THE TRANSMITTANCE OF THE BLACK-NETTING FOR SIMULATED SOLAR RADIATION

The black-netting reflectance was also evaluated as a function of radiation incidence angle, using the apparatus shown in Photograph 12.

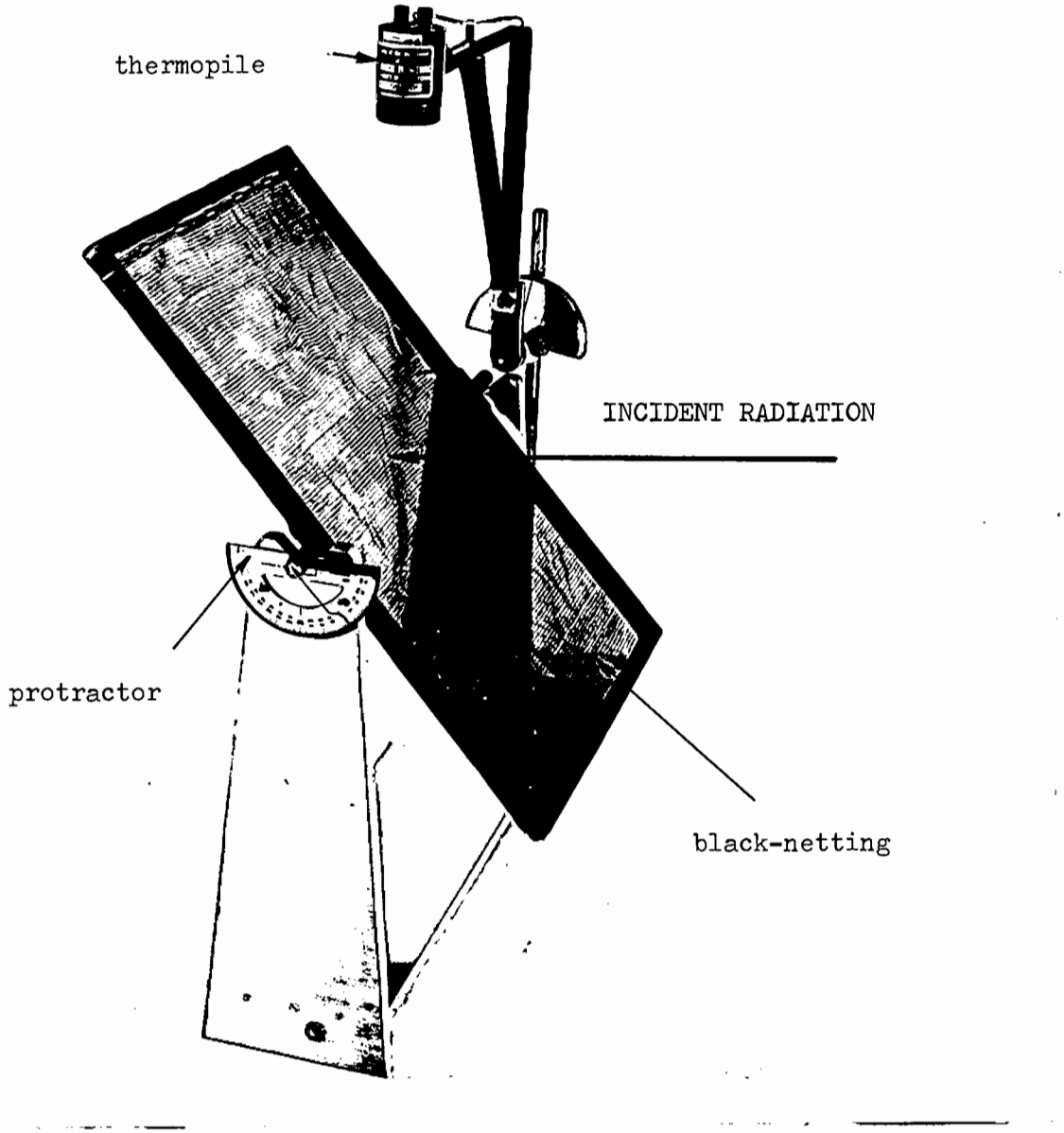

Photograph 12: The Black-Netting Reflectance Apparatus

The procedure is exactly as specified in Appendix 3.1.1 for the clear-polyethylene. The results are listed in Table 10.

Incidence Angle (θ)	ρ
85	0.02
80	0.02
75	0.02
70	0.02
65	0.01
60	0.01
55	0.01
50	0.01
45	0.01
40	0.01
35	0.01
30	0.01
25	0.01
20	0.01
15	0.01
10	0.01
5	0.01
0	0.01

TABLE 10: THE BLACK-NETTING REFLECTANCE RESULTS

The black-netting absorptance for simulated solar radiation was evaluated by using the above data and the law of energy conservation (Equation 2) i.e.

$$\alpha = 1 - (\rho + \tau) \quad \ldots\ldots\ldots\ldots\ldots\ldots\ldots\ldots\ldots\ldots \quad (8)$$

The results are presented in Table 11 and shown graphically in Figure 31.

Incidence Angle (θ)	α
85	0.97
80	0.94
75	0.84
70	0.77
65	0.73
60	0.68
55	0.65
50	0.63
45	0.61
40	0.59
35	0.57
30	0.56
25	0.56
20	0.55
15	0.54
10	0.54
5	0.54
0	0.54

TABLE 11: THE BLACK-NETTING ABSORPTANCE RESULTS

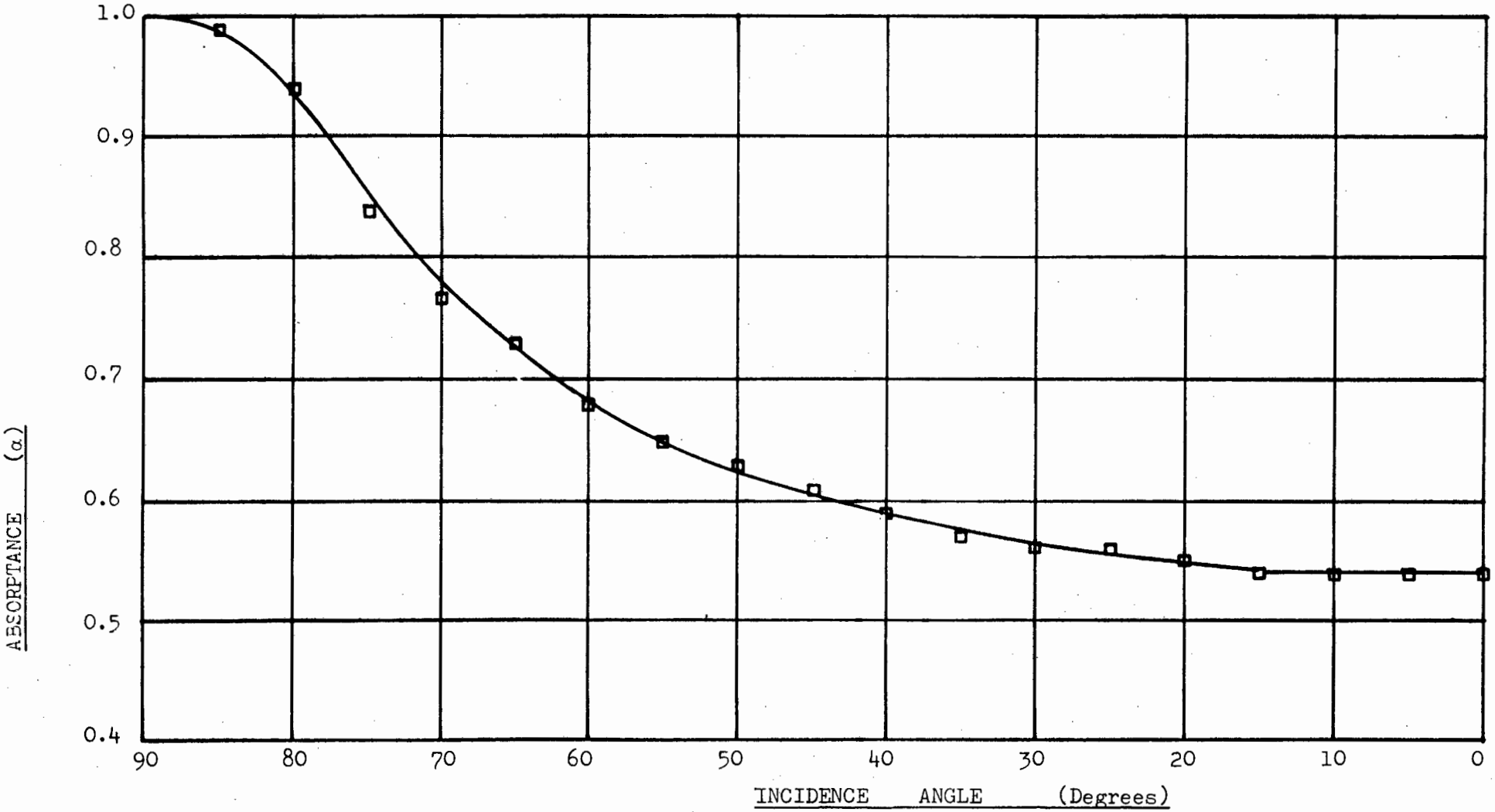

FIGURE 31: THE ABSORPTANCE OF THE BLACK-NETTING FOR SIMULATED SOLAR RADIATION

3.2 RADIATION FROM A LOW-TEMPERATURE SOURCE

3.2.1 The Clear-Polyethylene

The clear-polyethylene transmittance was evaluated as a function of incidence angle for radiation from a source at approximately 100 degrees Centigrade, using the apparatus shown in Photograph 9. The radiation source was a coil heater with a parabolic backing-plate, whose temperature was controlled by a variable-voltage device. The temperature of the coil was monitored during the tests by a mercury-bulb thermometer placed in direct contact with the coil.

The tests were conducted in exactly the same way as detailed in Appendix 3.1.1, the results being listed in Table 12 and presented graphically in Figure 32. It is of interest to compare these figures with the value of 0.4, which is given by Close (52) for the transmittance of plastic film to longwave radiation. For the clear-polyethylene used in these tests, a transmittance of 0.5 is within ten percent of the measured values for angles of incidence between 0 and 65 degrees (see Figure 32).

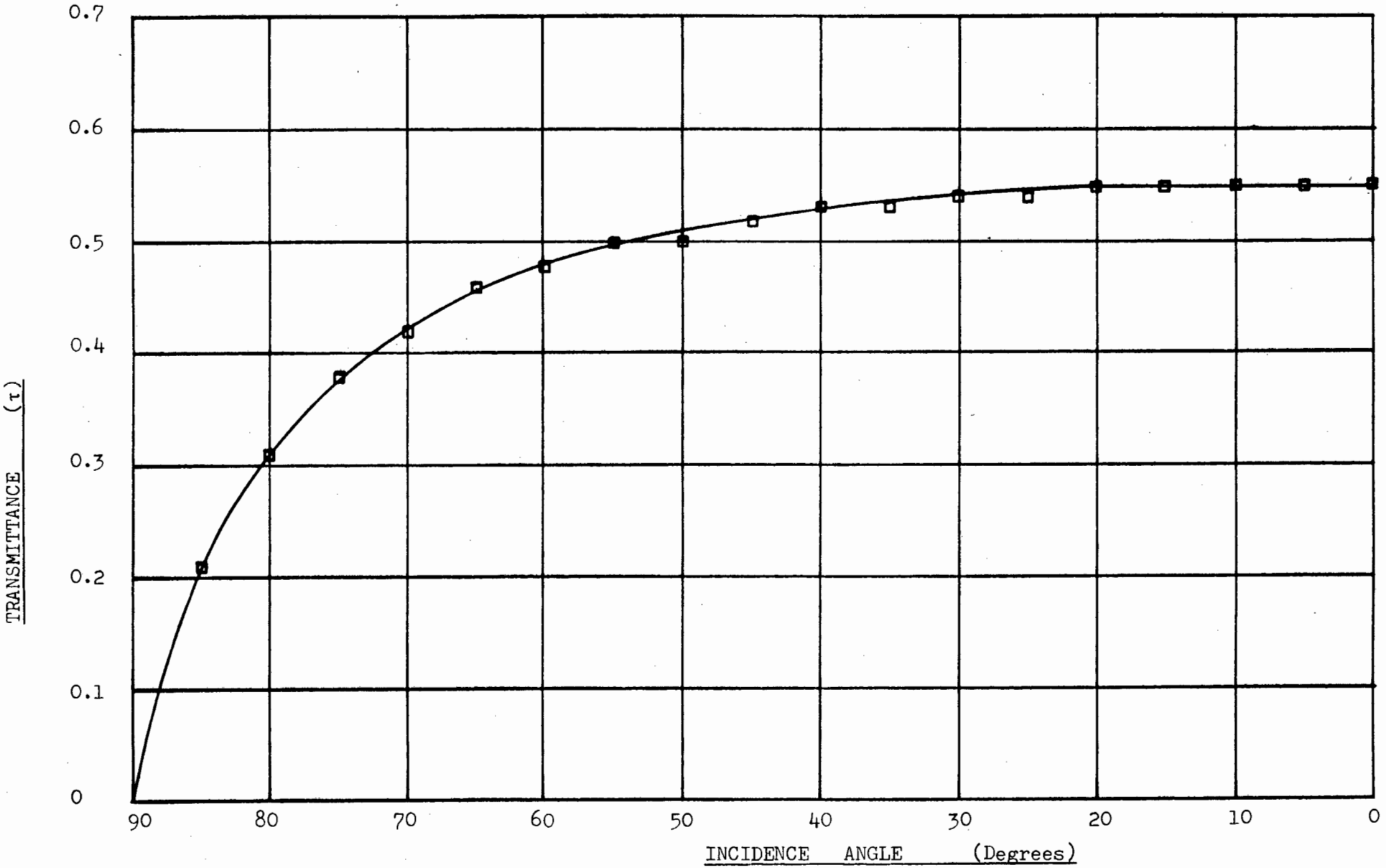

FIGURE 32: THE TRANSMITTANCE OF THE CLEAR-POLYETHYLENE FOR RADIATION FROM A SOURCE AT 100 °C

Incidence Angle (θ)	τ
90	0
85	0.21
80	0.31
75	0.38
70	0.42
65	0.46
60	0.48
55	0.50
50	0.50
45	0.52
40	0.53
35	0.53
30	0.54
25	0.54
20	0.55
15	0.55
10	0.55
5	0.55
0	0.55

TABLE 12: THE CLEAR-POLYETHYLENE TRANSMITTANCE RESULTS

The normal-emittance of the clear-polyethylene was measured using a Leslie-cube (see Photograph 13) and a thermopile. The cube contained boiling water which maintained the faces and the materials glued to them at 100 degrees Centigrade.

Photograph 13: The Leslie-Cube

In order to determine the clear-polyethylene emittance, it was necessary to know the radiation shape-factor between the cube face and the thermopile. The conical entrance of the thermopile makes the use of conventional analytical approaches difficult, so an experiment was conducted to find the shape-factor as a function of distance between the cube and thermopile. A face of the cube was coated with a thick layer of carbon-black from an acetylene torch, having an emittance of 0.99 - according to Beckman et al (17).

The radiation relationship between the two surfaces is defined as:

$$q = \sigma.\varepsilon.F_{cube\text{-}thermopile}.(T^4_{cube} - T^4_{therm}) \quad \ldots\ldots\ldots (9)$$

'T_{cube}' is the absolute temperature of the carbon surface and 'T_{therm}' is the absolute temperature of the thermopile. Obviously, an accurate answer requires an accurate knowledge of the thermopile temperature. The following equation was used to derive the thermopile temperature:

$$q = \sigma.\varepsilon_{therm}.F_{therm\text{-}wall}.(T^4_{therm} - T^4_{wall}) \quad \ldots\ldots\ldots (10)$$

The thermopile was pointed to the room walls (whose temperature was deemed to be the average laboratory ambient-air temperature measured during the course of the tests). The thermopile-to-wall shape-factor was unity and the carbon-black surface of the thermopile has an emittance of 0.99. Equation 10 can therefore be reduced to:

$$T_{therm} = \left[\left(\frac{q}{5.669 \times 10^{-8} \times 0.99}\right) + T^4_{wall}\right]^{0.25} \quad \ldots\ldots (11)$$

Table 13 lists the thermopile temperatures calculated using equation 11 and an average measured ambient-air temperature of 291.7 degrees Kelvin. (The laboratory ambient-air temperature was measured before and after the tests as 18.4 and 18.9 degrees Centigrade respectively).

Test	q in mV	$T_{thermopile}$
1	0.069	292.9
2	0.054	292.6
3	0.042	292.4
4	0.033	292.3
5	0.030	292.2

TABLE 13: THE THERMOPILE TEMPERATURES

Readings were taken three times and averaged for each test. The thermopile output (in mV) was converted to a radiation intensity value by using a conversion factor specified by the manufacturer i.e.

$$10.6 \times 10^{-3} \text{ mV} = 1 \text{ W/m}^2$$

Equation 9 was used to calculate the shape-factor between the thermopile and the face of the Leslie-cube. Three tests were conducted at each of five different distances. The averaged results are listed in Table 14 and are illustrated on Figure 33.

Column A = Test number

Column B = Average thermopile output (mV)

Column C = Distance between thermopile and Leslie-cube (mm)

Column D = Thermopile temperature (degrees Kelvin)

Column E = Cube-to-thermopile shape-factor

A	B	C	D	E
1	0.889	4	292.9	0.1246
2	0.892	6	292.6	0.1246
3	0.891	10	292.4	0.1243
4	0.867	15	292.3	0.1209
5	0.829	20	292.2	0.1155

TABLE 14: THE CUBE-TO-THERMOPILE SHAPE-FACTOR RESULTS

This shape-factor information was utilised to measure the normal-emittance of the clear-polyethylene. The distance between the thermopile and the polyethylene covered cube-face was kept constant at 14.8 mm. The corresponding "cube-to-thermopile" shape-factor was 0.1212

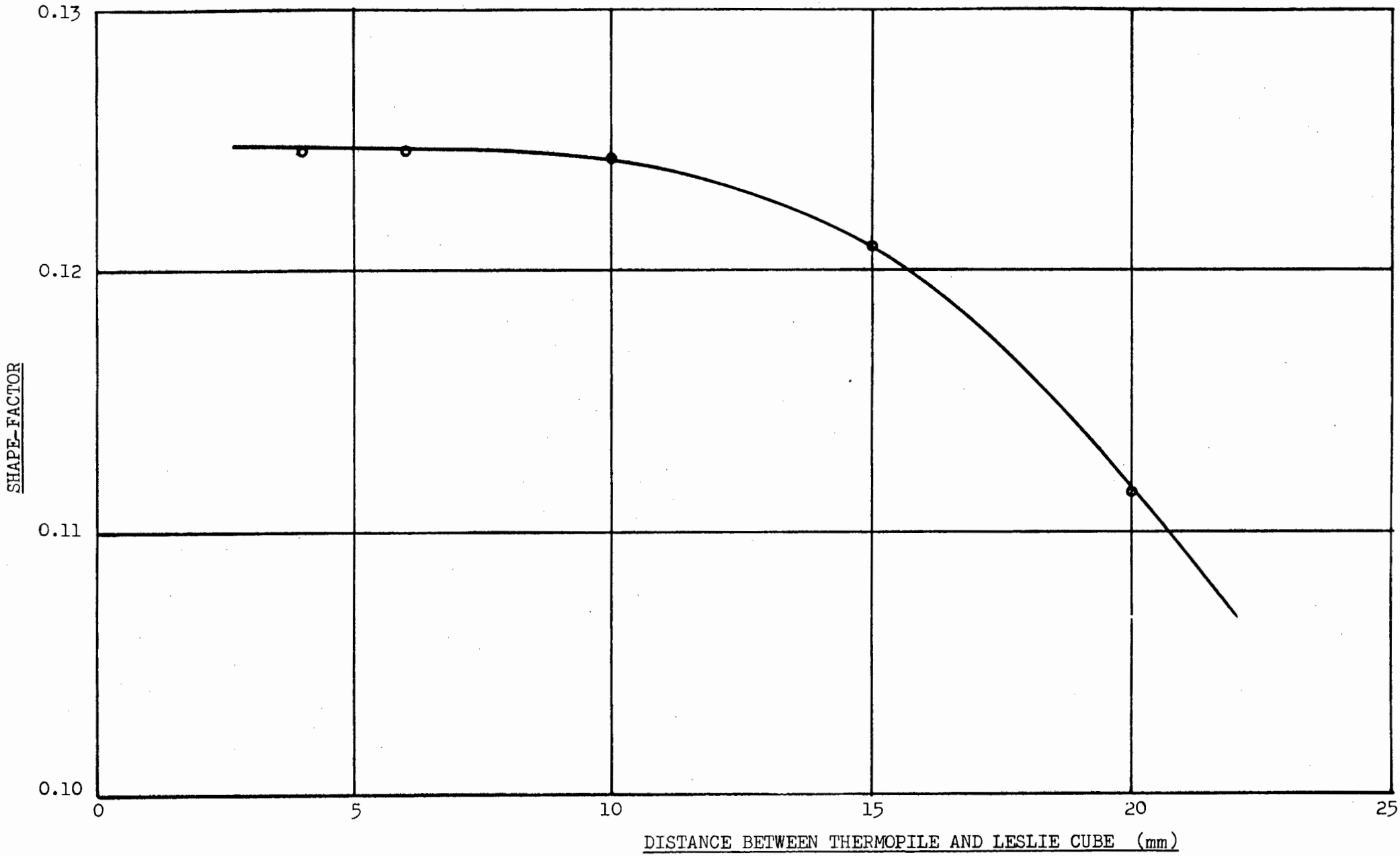

FIGURE 33: LESLIE CUBE - THERMOPILE SHAPE-FACTOR RELATIONSHIP

(see Figure 33). Since the polyethylene transmits 55 percent of the normal, low-temperature source radiation (see Figure 32), the polyethylene emittance was measured using the following equation:

$$q = \sigma.F_{cube\text{-}therm}.\varepsilon_{poly}.(T^4_{cube}-T^4_{thermopile}) + \tau_{poly}.(\sigma.F_{cube\text{-}therm}.\varepsilon_{c+g}.(T^4_{cube}-T^4_{therm})) \quad \ldots\ldots\ldots (12)$$

where 'ε_{c+g}' is the emittance of the cynoacrylate-glue covered chrome face, which had to be determined before the clear-polyethylene emittance could be calculated. To achieve this, one of the chrome faces of the cube was smeared with cynoacrylate-glue, and the following equation was used to calculate the emittance:

$$q = \sigma.F_{cube\text{-}therm}.\varepsilon_{c+g}.(T^4_{cube}-T^4_{thermopile}) \quad \ldots\ldots\ldots\ldots (13)$$

An accurate answer depended on a knowledge of the thermopile temperature. This was established by averaging the results of eight tests to determine the radiation exchange between the thermopile and the laboratory walls, and then using Equation 10 to calculate the thermopile temperature. This was done before each of the eight tests on the "cynoacrylate-glue" face and before each of the eight tests on the "cynoacrylate-glue-polyethylene" face. The averaged results are presented in Table 15. (The laboratory ambient-air temperature was 18.8 and 19.0 degrees Centigrade before and after the tests respectively, hence the average ambient-air temperature was 292 degrees Kelvin.)

A	B	C	D	E
1	0.007	0.742	0.012	0.833
2	0.011	0.735	0.014	0.823
3	0.012	0.728	0.016	0.827
4	0.013	0.727	0.018	0.824
5	0.013	0.731	0.019	0.824
6	0.014	0.741	0.020	0.821
7	0.011	0.739	0.022	0.819
8	0.011	0.743	0.022	0.820
	A v e r a g e	V a l u e s		
	0.012	0.736	0.018	0.824

Column A = Test number

Column B = Thermopile-wall Radiation (mV)

Column C = Chrome+glue-therm Radiation (mV)

Column D = Thermopile-wall Radiation (mV)

Column E = Chrome+glue+poly-therm Radiation (mV)

TABLE 15: RADIATION RESULTS BETWEEN THERMOPILE, WALL, CHROME-AND-GLUE COMBINATION AND CHROME-AND-GLUE-AND-POLYETHYLENE COMBINATION

The thermopile temperature was calculated using equation (10) with the data averaged values in columns B and D in Table 15. The results indicate that the thermopile temperature averaged at 292.2 degrees Kelvin for the chrome-and-glue combination and 292.3 degrees Kelvin for the chrome-and-glue-and-clear-polyethylene combination.

Now, from equation (13), the chrome-and-glue emittance was calculated as:

$$\varepsilon_{c+g} = \frac{0.736 \;/\; 10.6 \times 10^{-3}}{5.669 \times 10^{-8} \times 0.1212 \times (373^4 - 292.2^4)}$$

$$= 0.84$$

Using equation (12) in a similar way with $\tau_{polyethylene} = 0.55$ allowed the polyethylene emittance to be calculated as:

$$\varepsilon_{polyethylene} = 0.48$$

3.2.2 The Black-Netting Properties

The transmittance of the black-netting was evaluated in exactly the same manner as that described in Appendix 3.1.1 for the clear-polyethylene. The results are listed in Table 16 and are shown in Figure 34.

Incidence Angle (θ)	τ_1	τ_2	τ_3	τ_4	$\bar{\tau}$
85	0.17	0.10	0.11	0.11	0.12
80	0.24	0.17	0.19	0.17	0.19
75	0.28	0.25	0.27	0.23	0.26
70	0.33	0.32	0.33	0.30	0.32
65	0.39	0.37	0.38	0.36	0.38
60	0.44	0.41	0.42	0.41	0.42
55	0.46	0.43	0.45	0.45	0.45
50	0.48	0.46	0.45	0.47	0.47
45	0.49	0.48	0.48	0.50	0.49
40	0.51	0.48	0.47	0.49	0.49
35	0.51	0.49	0.50	0.51	0.50
30	0.52	0.51	0.52	0.51	0.52
25	0.53	0.51	0.52	0.52	0.52
20	0.54	0.52	0.53	0.52	0.53
15	0.54	0.52	0.52	0.52	0.53
10	0.54	0.54	0.52	0.52	0.53
5	0.55	0.52	0.52	0.52	0.53
0	0.56	0.52	0.52	0.52	0.53

TABLE 16: THE BLACK-NETTING TRANSMITTANCE FOR RADIATION FROM A LOW-TEMPERATURE SOURCE

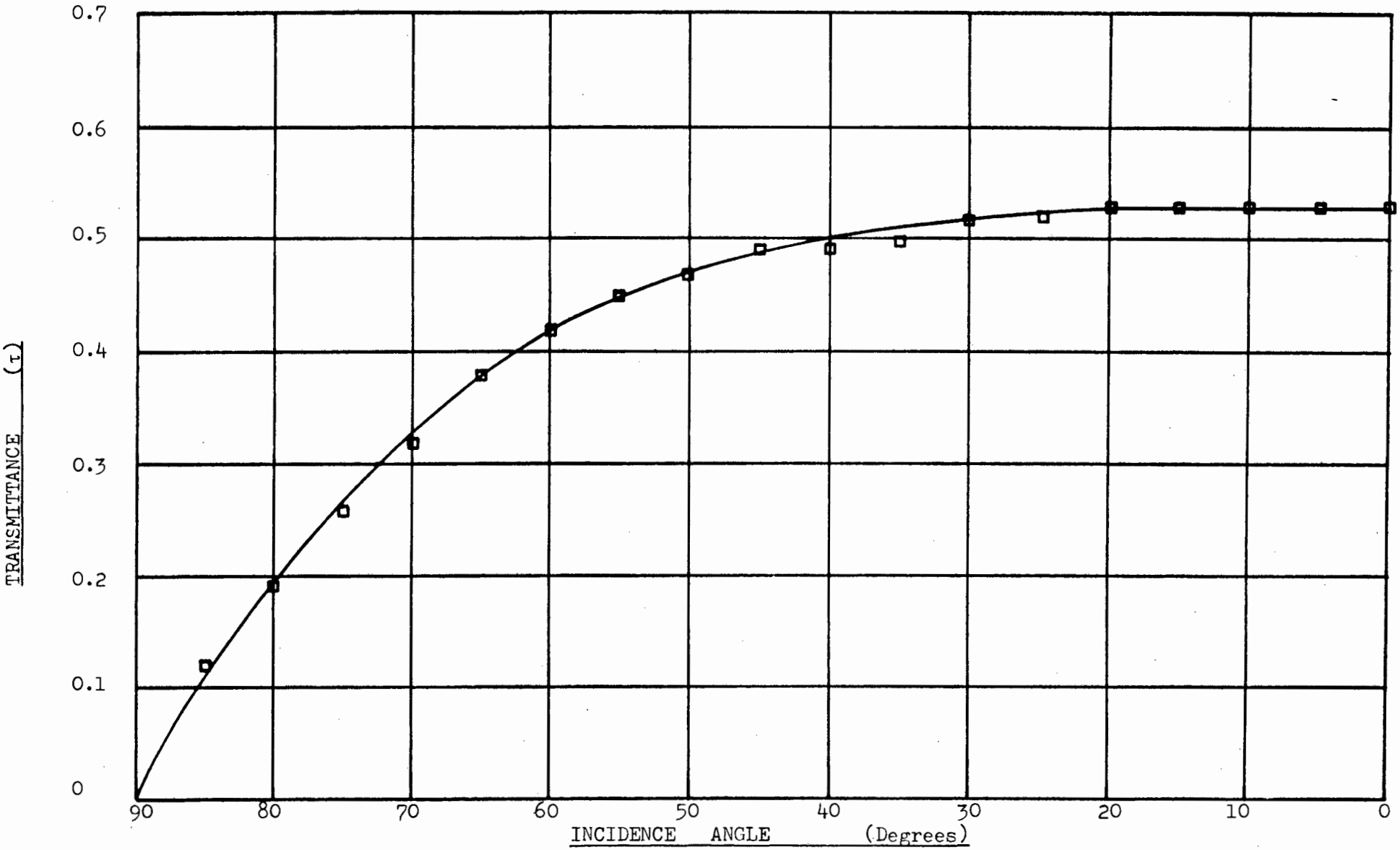

FIGURE 34: THE TRANSMITTANCE OF BLACK-NETTING FOR RADIATION FROM A SOURCE AT 100 °C

The normal-emittance of the black-netting cloth was evaluated in exactly the same way as is detailed in Appendix 3.2.1 for the clear-polyethylene. The average laboratory ambient-air temperature was determined to be 292.6 degrees Kelvin. Six tests were conducted and the results are listed in Table 17.

Column A = Test Number

Column B = Thermopile-wall radiation (mV)

Column C = Average thermopile-wall radiation output (mV)

Column D = Chrome+glue+black-netting - thermopile radiation output (mV)

Column E = Average chrome+glue+black-netting - thermopile radiation output (mV)

A	B	C	D	E
1	0.011	-	0.758	-
2	0.011	-	0.771	-
3	0.012	0.013	0.767	0.764
4	0.014	-	0.763	-
5	0.014	-	0.761	-
6	0.014	-	0.764	-

TABLE 17: RADIATION RESULTS BETWEEN THERMOPILE, WALL AND CHROME-AND-GLUE-AND-BLACK-NETTING

The average thermopile temperature was evaluated using Equation 10 as 292.8 degrees Kelvin. The emittance of the black-netting was derived using the equation:

$$q/A = \sigma.F_{cube-therm}.\varepsilon_n.(T^4_{cube}-T^4_{therm}) + \tau_n.(\sigma.F_{cube-therm}.\varepsilon_{c+g}.(T^4_{cube}-T^4_{therm}) \quad \ldots\ldots (14)$$

The emittance of the "cynoacrylate-glue" surface was evaluated as 0.84 in Appendix 3.2.1, whilst the normal low-temperature radiation transmittance of the black-netting is listed in Table 16 as 0.53. Use of equation 14 allowed the black-netting normal-emittance to be calculated as:

$$\varepsilon_{black-netting} = 0.43$$

The normal-emittance of black-netting at a temperature of about 100 degrees Centigrade (as derived above) applies to the superficial area of the netting.

APPENDIX 4

THE SOLAR SIMULATOR

4.1 The Selection of a Suitable Simulator Radiation Source

The most suitable light for a solar-simulator radiation source is the subject of some controversy. The most commonly used lights include:

(a) Xenon-Arc

The Xenon-Arc has an output spectrum which covers the full solar range (see Figure 35). The peaks that occur around 0.8 micrometres can be filtered out using absorption glass filters. Pekruhn et al (24) have recognised the need for optical filters to produce an acceptable spectrum. This aspect reduces their desirability, since narrow-band optical filters are expensive and diminish the overall radiation intensity on the test plane.

Benning (21) states that Xenon-Arcs are commonly used as radiation sources for the testing of solar cells in Denmark, Germany and France, since they have the merit that variations in power do not cause any appreciable shift in the radiation spectral balance (Beeson - 25). However, the Xenon-Arc is not an efficient converter of electrical to radiative power (Gillett - 23).

(b) Tungsten-Halogen Quartz Filament

McMillan et al (26) have investigated the feasibility of using Tungsten-Filament lights for a solar simulator radiation source. They

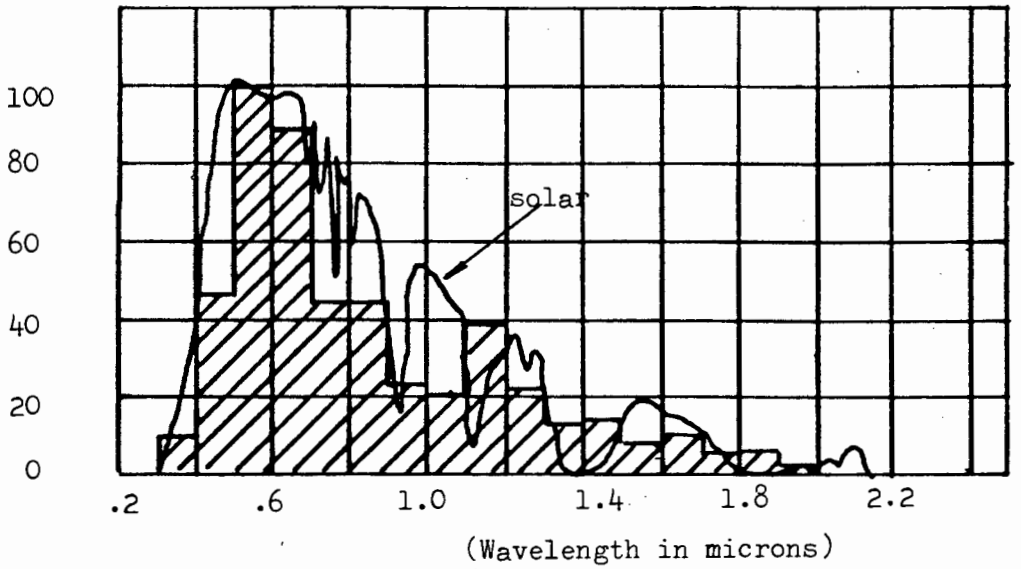

Comparison of CSI spectrum with AM 2 solar spectrum

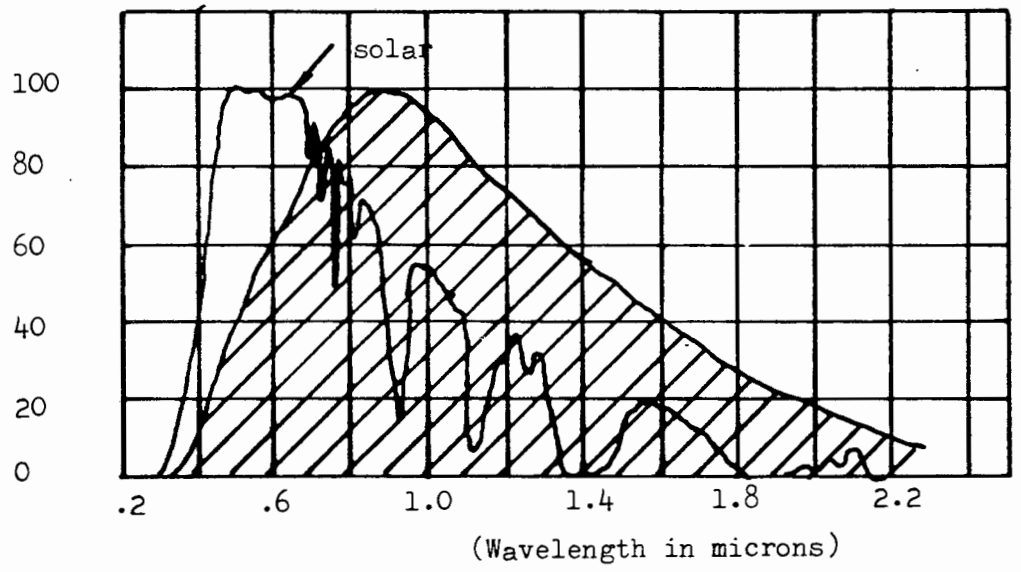

Comparison of Tungsten Halogen spectrum with AM 2 solar spectrum

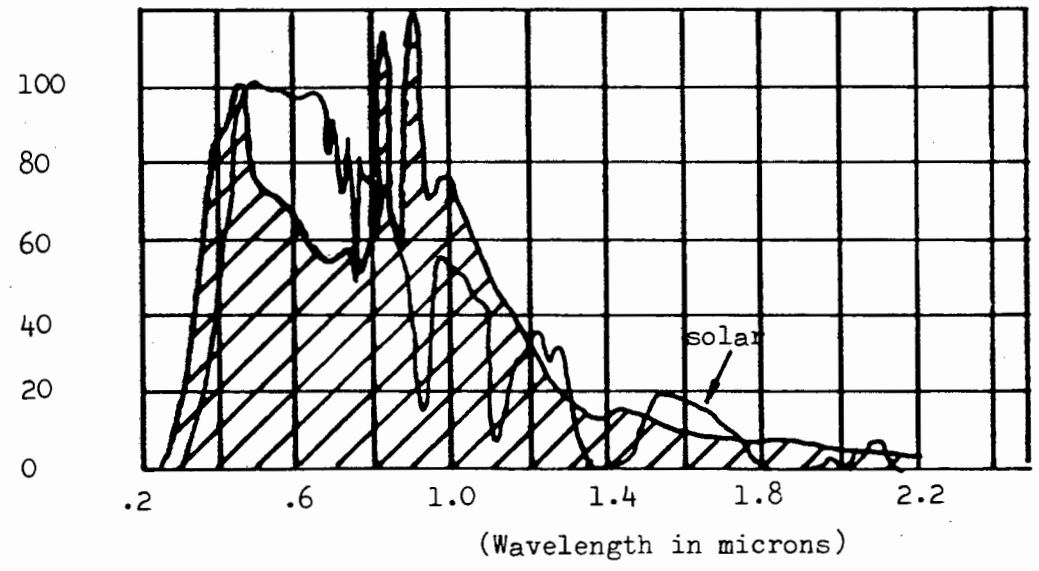

Comparison of Xenon Arc spectrum with AM 2 solar spectrum

FIGURE 35: RADIATION SPECTRA OF COMMERCIALLY AVAILABLE LAMPS (23)

cite lower costs as the major advantage over the Xenon-Arc. The light suffers from a lack of Ultra-Violet (short wavelength) radiation and a surplus of Infra-Red (long wavelength) radiation. This is a result of the maximum-temperature restrictions that exist for the tungsten filament. Gillett (23) mentions that most Tungsten-Filament lights have restrictions regarding their burning position because of the halogen cleansing cycle which is driven by natural convection.

(c) Compact-Source Iodide-Arc

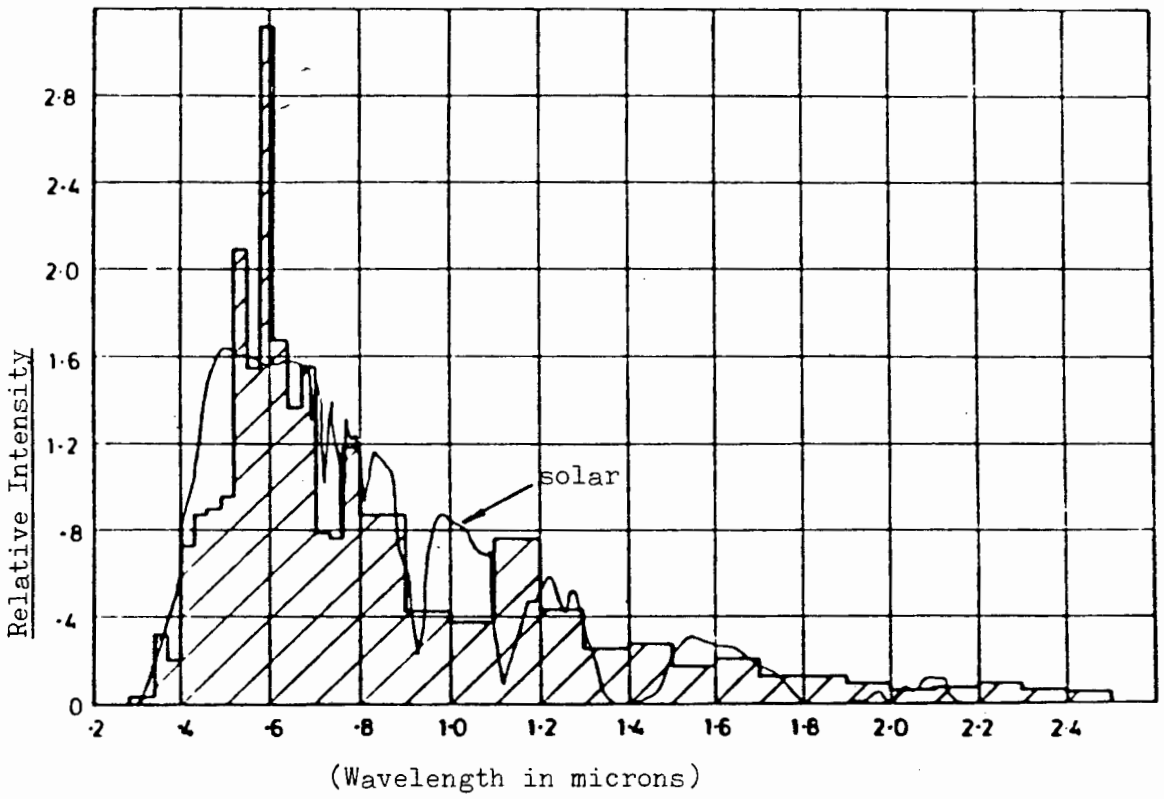

FIGURE 36: THE CSI LAMP SPECTRAL DISTRIBUTION (Gillett - 27)

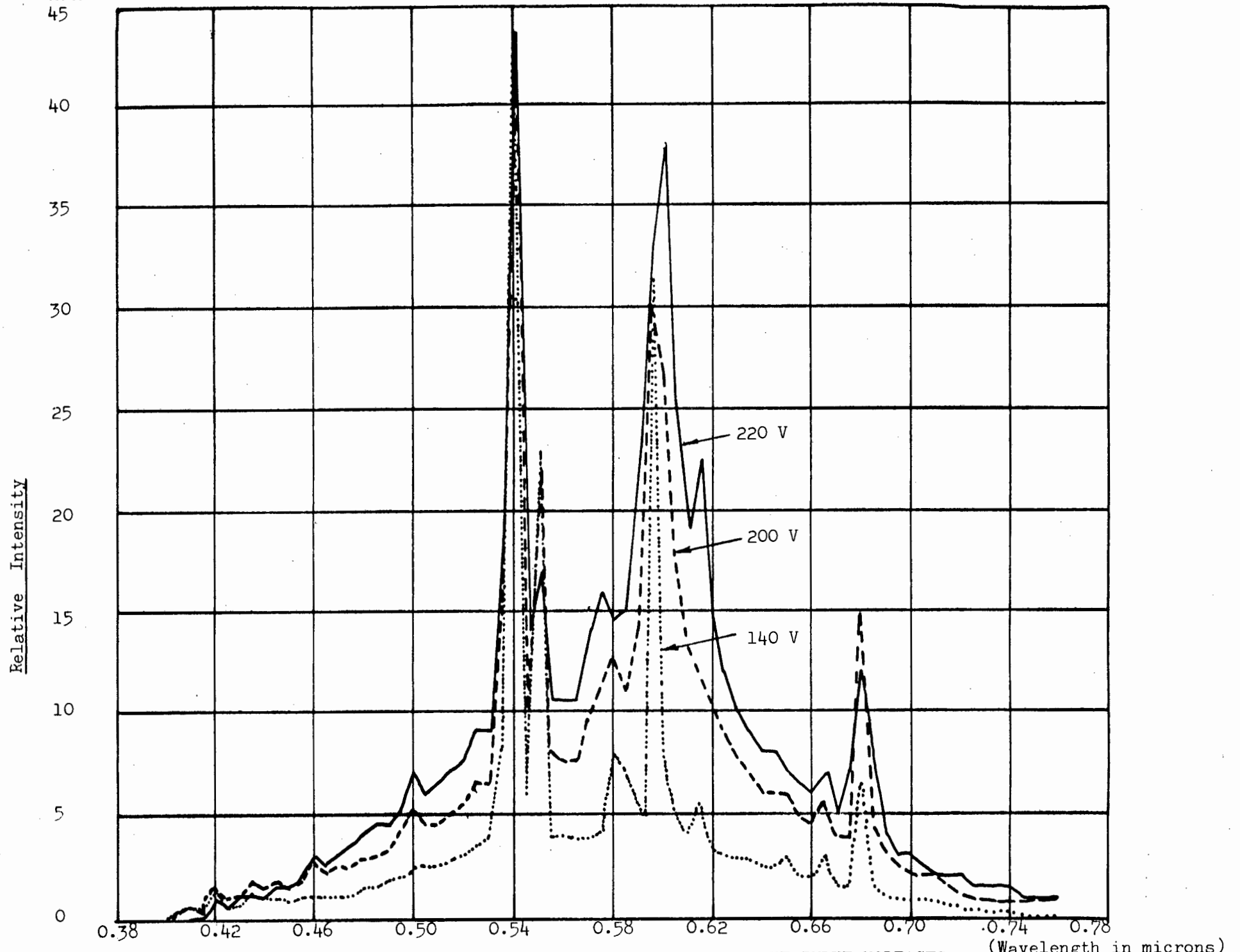

FIGURE 37: THE CSI LAMP SPECTRAL DISTRIBUTION FOR THREE DIFFERENT INPUT VOLTAGES

The CSI light was designed to provide light at football stadia for colour-television filming. The light has good broad-band spectral conformity to that of sunlight (see Figures 35 and 36), and is a more efficient light than the Xenon-Arc. There are two narrow-band high output-power spikes whose presence (plus small spectral shifts that take place at part load) make the light unsuitable for testing photovoltaic devices. This is confirmed in Figure 37, which shows the effect on the CSI lamp spectrum of changing input voltage (investigated by the author with a prism spectrometer). Figure 37 contains plots of radiation intensity as a function of wavelength for input voltages of 140, 200 and 220 volts respectively. Beeson (25) states that the low ultra-violet output makes the light unsuitable for ultra-violet degradation testing. An advantage of the light is that it can operate at any angle.

The CSI lamp has most of the qualities required of a solar simulator radiation source, and was accordingly selected as the radiation source for the solar simulator in this thesis.

4.2 The Solar Simulator Design

The solar simulator was constructed to the specifications shown in Figures 38 and 39. These specifications were drawn up after consulting the BSE guidelines on solar simulator design (15), and Gillett's work (23 and 27) on simulators and indoor testing, and after the completion of optimisation tests described hereunder. Figures 38 and 39 show the simulator frame and the trolley on which the radiation sources were mounted. A winch-and-pulley system was used to raise and lower the

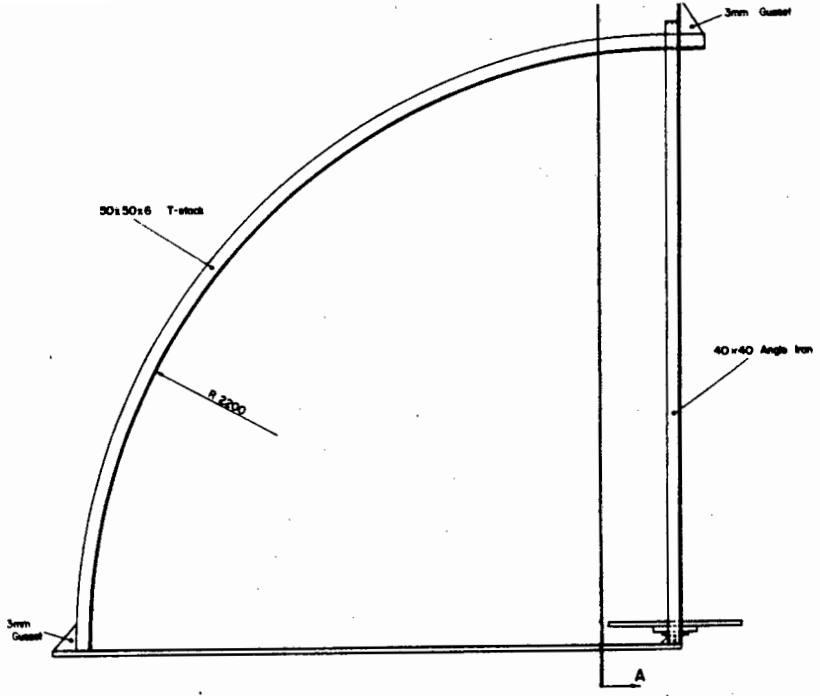

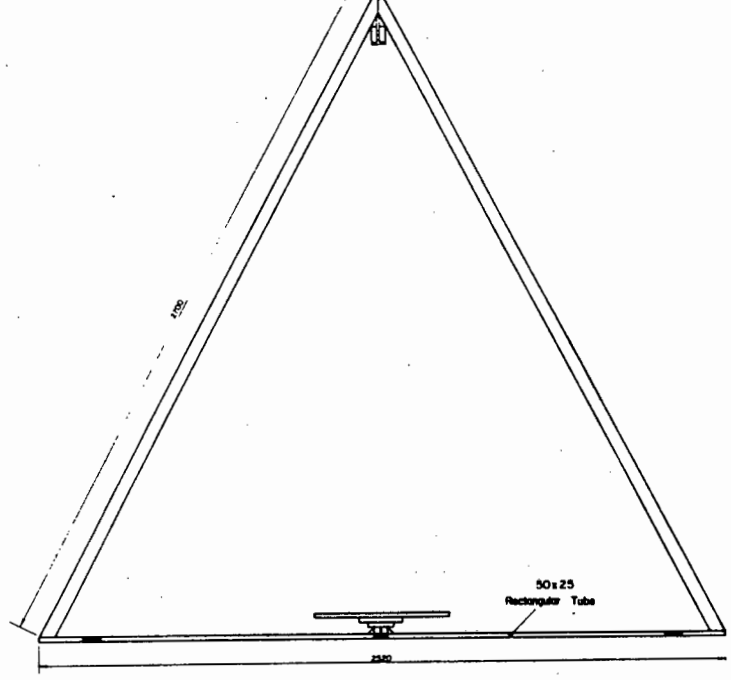

Section AA

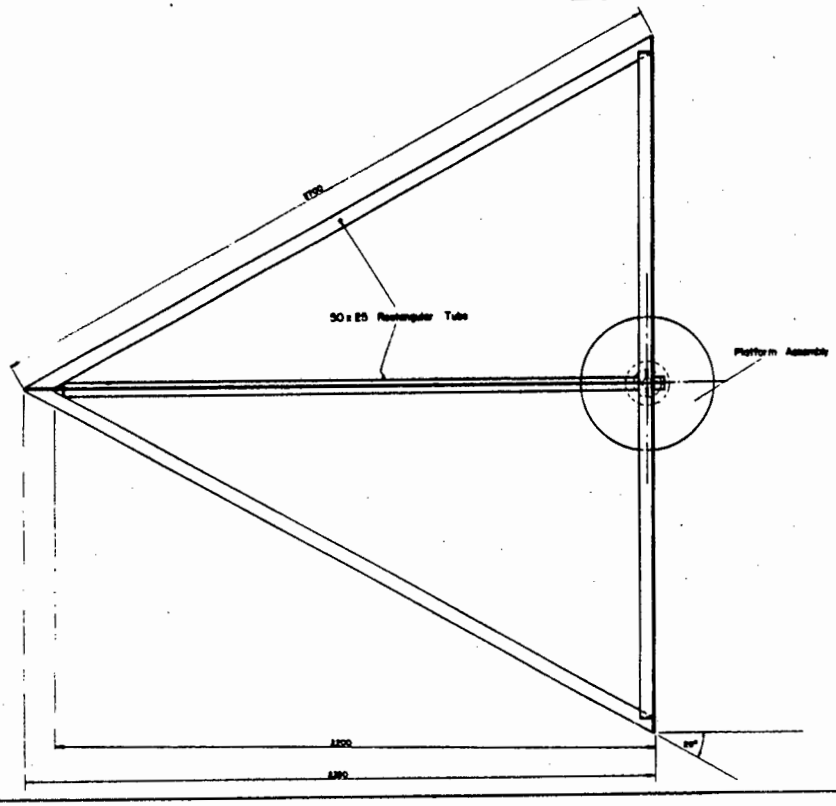

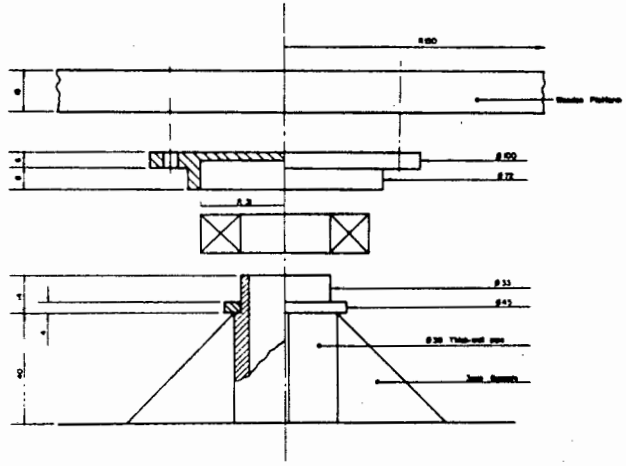

PLATFORM ASSEMBLY
Scale : 1-1

All dimensions in millimetres
Material Mild steel unless otherwise specified
All welded construction

FIGURE 38

UNIVERSITY OF CAPE TOWN DEPARTMENT OF MECHANICAL ENGINEERING	
FRAME FOR SOLAR SIMULATOR	
Scale : 1-10	Date : 17-9-81
Design : P.J. BAM	Drawn :
Checked :	Sheet : 1 of 2

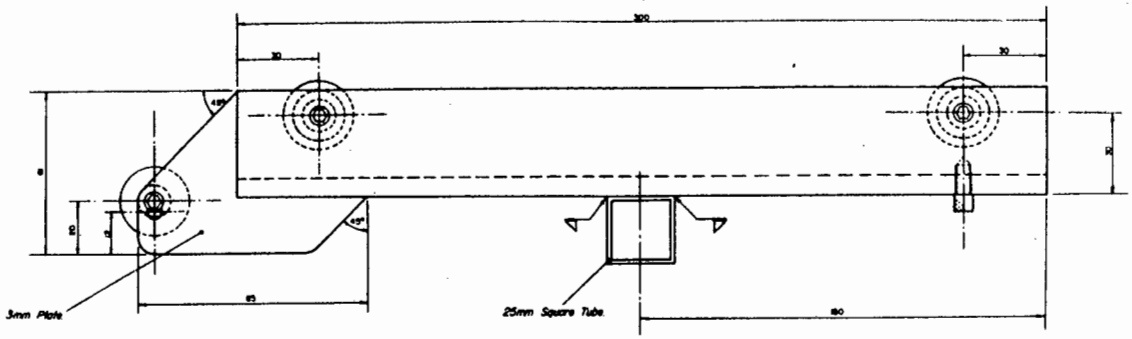

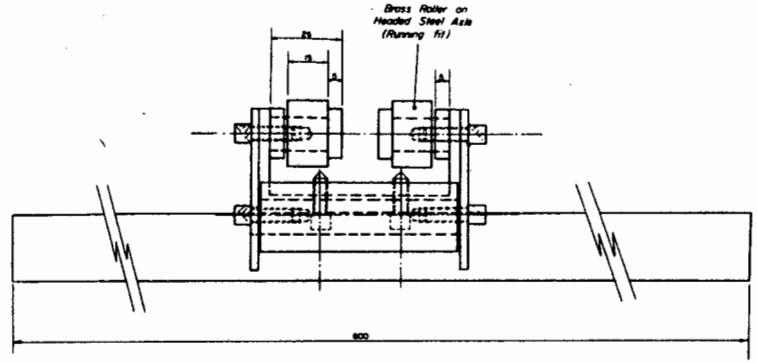

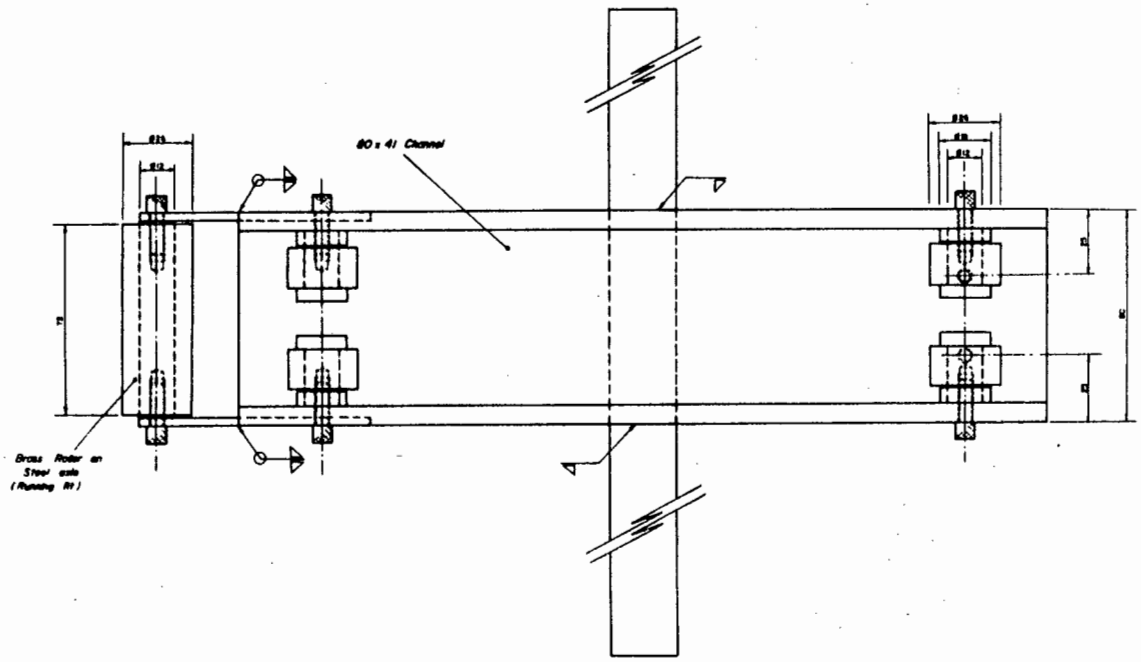

FIGURE 39

All dimensions in millimetres

Material: Mild steel unless otherwise specified

Allen screws used are 5mm thread diameter

Relieve sharp corners

UNIVERSITY OF CAPE TOWN DEPARTMENT OF MECHANICAL ENGINEERING	
TROLLEY FOR SOLAR SIMULATOR	
Scale: 1-1	Date: 17-9-81 A
Design: P.J. BAM	Drawn:
Checked:	Sheet: 2 of 2

Photograph 14: The Solar Simulator

trolley on the curved (50 x 50 x 6)mm T-stock. The simulator is shown in Photograph 14.

In order to optimise the dimensions of the simulator, measurements were made of the radiation intensities of each CSI light. Since the maximum insolation on a January day in the Cape Peninsula is approximately 1000 Watts per square metre (see Appendix 17), it was desirable to choose a distance between the radiation sources themselves, and a distance between the radiation sources and the greenhouse model that would enable the CSI lamps to radiate a maximum of approximately 1000 Watts per square metre on the test surface in as uniform a manner as possible, and over the largest surface area. The radiation intensities were measured on a plane normal to each light source, one light at a time, at a distance of 1.9 metres from the source. The resultant data was plotted as contours of constant radiation intensity, which are shown in Figures 40 and 41 for each of the lamps. Using the principle of linear superposition the most uniform radiation intensity distribution was found to be that shown in Figure 42. This distribution is obtained by mounting the lights about 0.3 metres apart, which results in a maximum greenhouse model dimension of 0.455 metres by 0.15 metres if the variation of the radiation intensity from the mean value is to be kept smaller than 10 percent (BSE-15). The model dimensions are a factor of sixty-six times smaller than a typical commercially available greenhouse.

The simulator design incorporates the ability to change the source altitude angle, azimuth angle and the radiation intensity. The source altitude is varied by raising/lowering the trolley (i.e. the radiation source) on the curved T-stock. The azimuth angle is varied by rotating the test device in the horizontal plane, whilst radiation intensity is

controlled by varying the voltage supplied to the lamps.

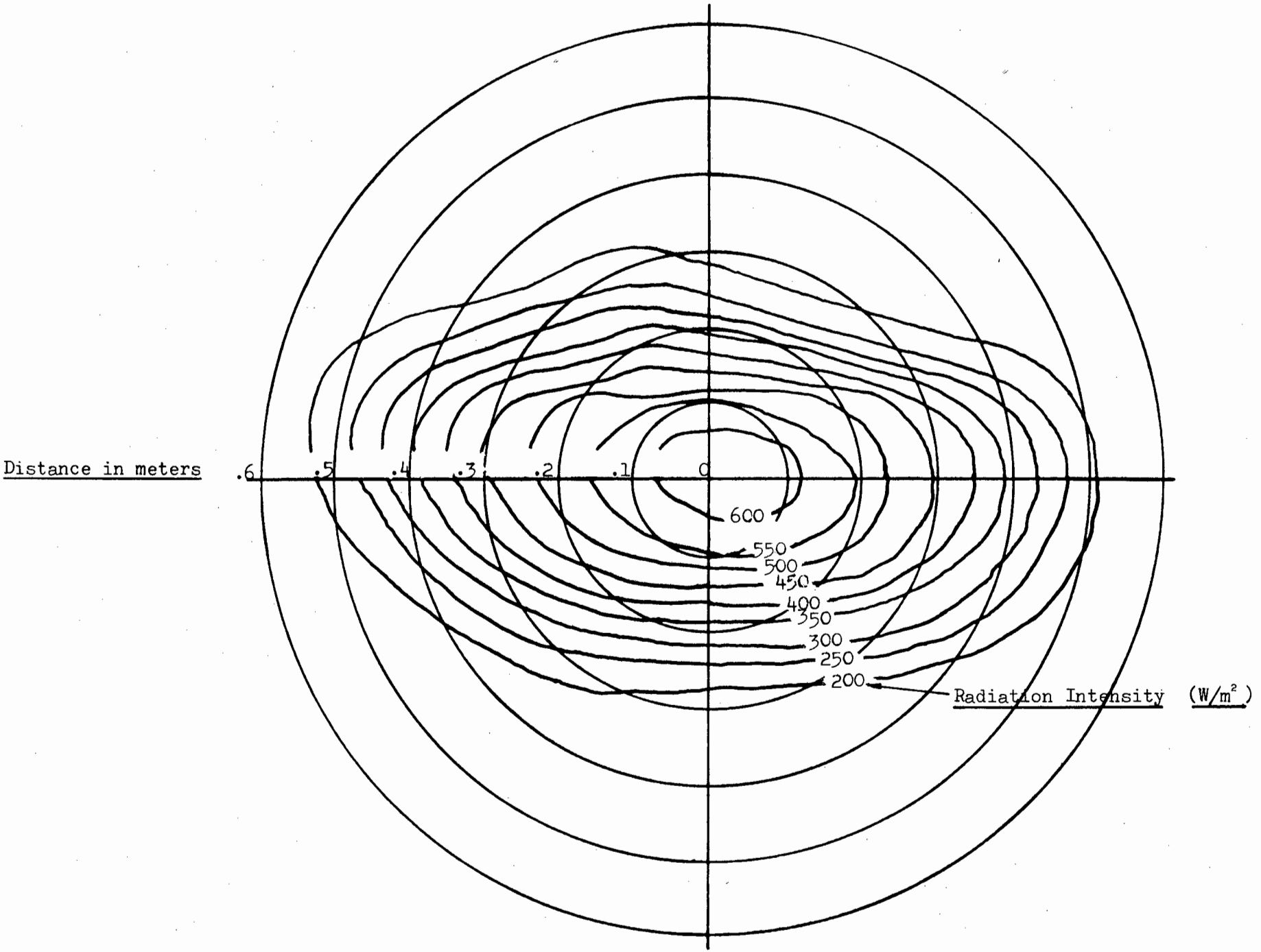

FIGURE 40: CONTOUR LINES OF CONSTANT RADIATION INTENSITY FOR LAMP 1, MEASURED 1.9 METRES FROM THE LAMP

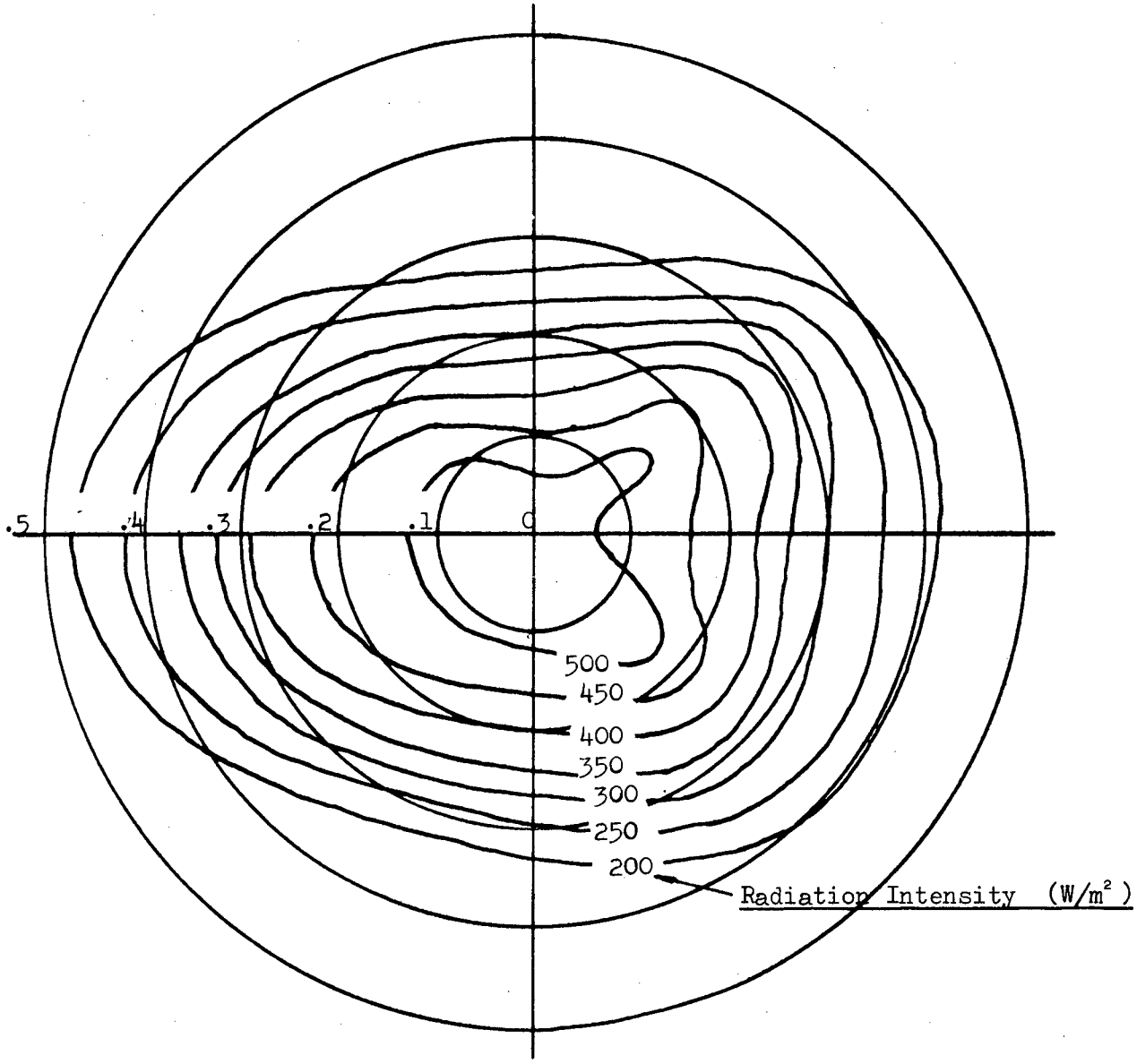

FIGURE 41: CONTOUR LINES OF CONSTANT RADIATION INTENSITY FOR LAMP 2, MEASURED 1.9 METRES FROM THE LAMP

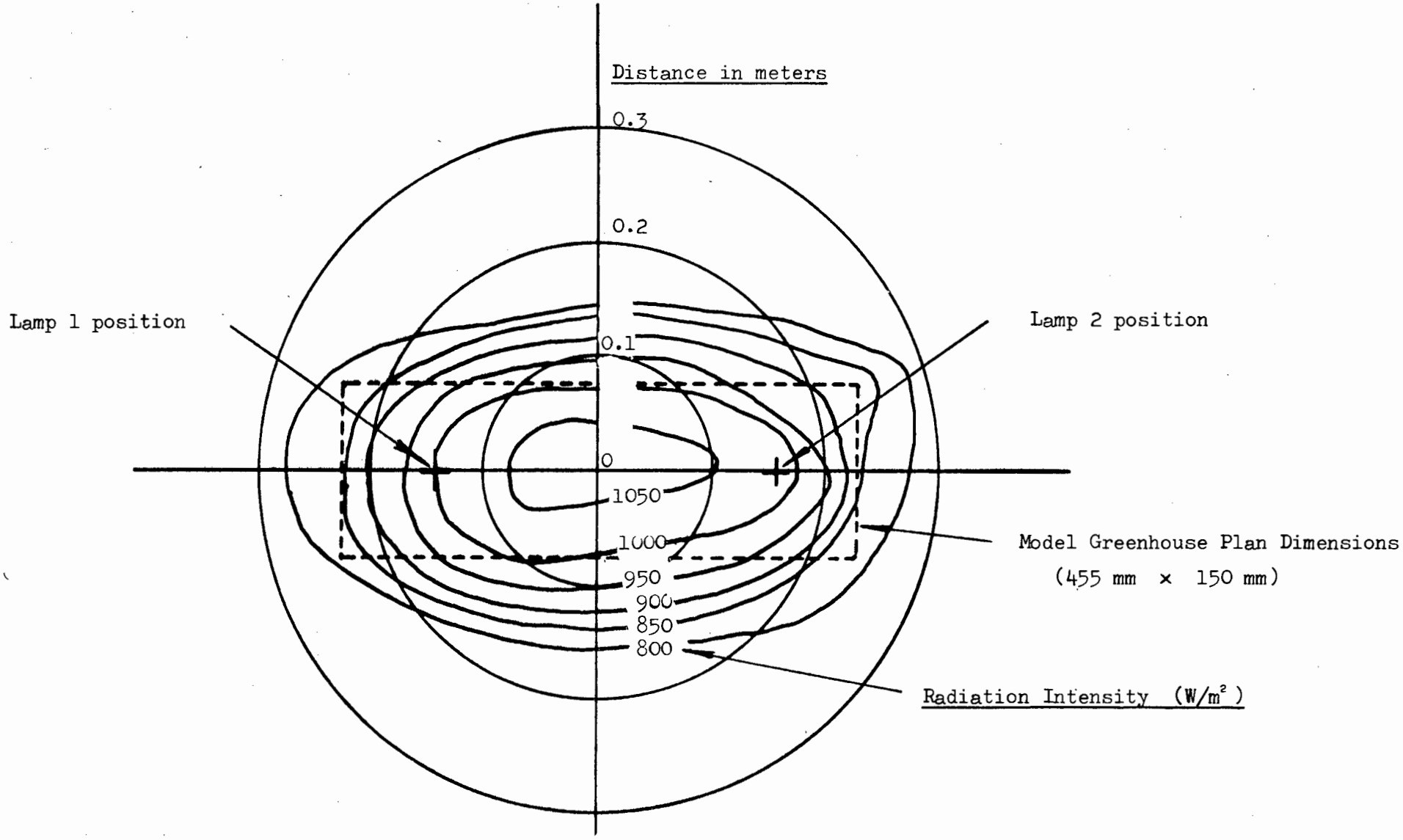

FIGURE 42: CONTOUR LINES OF CONSTANT RADIATION INTENSITY FOR LAMP 1 AND LAMP 2, MEASURED 1.9 METRES FROM THE LAMP

APPENDIX 5

SOLAR COLLECTOR CONDUCTION HEAT TRANSFER CONSIDERATIONS

The flow of heat by conduction through the edges of the covers and the black-netting is assumed in the theoretical analysis to be negligible. The justification for this is appreciated by examining the following worst case calculation, using the equation:

$$Q = -k \times A \times \left(\frac{dT}{dx}\right) \quad \ldots\ldots\ldots\ldots\ldots\ldots\ldots\ldots\ldots\ldots\ldots\ldots \quad (1)$$

Kinney (51) cites a value of 0.4 $W/m^{o}C$ for the thermal conductivity of polyethylene.

(a) The model Baird-type solar collector

The thickness of the polyethylene was measured to be 0.1×10^{-3}m. Examining the potential conduction heat loss from the black-netting to the clear-polyethylene cover:

The contact area will not be larger than twice the collector length multiplied by the polyethlene thickness i.e.

$$A \leq 2 \times 0.455 \times 0.1 \times 10^{-3} = 9.1 \times 10^{-5} \quad m^2$$

Inspection of the results shows that the netting temperature was never more than 25 ^{o}Centigrade higher than the cover temperature. The distance between the centre of the net and the polyethylene cover is 50×10^{-3} m. The worst conduction heat-loss can be estimated to be:

$$Q = 0.4 \times 9.1 \times 10^{-5} \times (25/50 \times 10^{-3})$$

$$= 0.018 \text{ Watts}$$

The input energy to which the collector is subjected is 852 W/m^2, which is 38.8 Watts on the absorber surface. The estimated conduction heat loss is thus considered negligible, being

$$\frac{0.018}{38.8} \times 100 = 0.05\ \% \quad \text{of the energy input.}$$

(b) The life-size Baird-type solar collector

Examining the potential conduction heat-loss from the black-netting to the clear-polyethylene cover in the same manner as in (a):

The contact area will not be larger than twice the collector length multiplied by the polyethylene thickness i.e.

$$A \leq 2 \times 30 \times 0.1 \times 10^{-3} = 6 \times 10^{-3} \text{ m}^2$$

Inspection of the results shows that the netting temperature was never more than 25 degrees Centigrade higher than the cover temperature. The distance between the centre of the net and the polyethylene cover is 3.3 m. The worst conduction heat-loss is thus estimated to be:

$$Q = 0.4 \times 6 \times 10^{-3} \times (25/3.3)$$

$$= 0.018 \text{ Watts}$$

The incident radiation on the absorber surface can be approximated as 500 W/m^2. The input energy to the solar collector is thus:

$$500 \times 30 \times 6.6 = 99 \times 10^3 \text{ Watts}$$

The estimated conduction heat-loss is thus negligible, being

$$\frac{0.018}{99 \times 10^3} \times 100 = 1.8 \times 10^{-5} \text{ \% of the input energy.}$$

APPENDIX 6

CALCULATION OF FLOWRATES THROUGH THE TOP AND BOTTOM COLLECTOR SECTIONS

(a) The model Baird-type solar collector

In the laminar ranges of flowrate, the ratio of flowrate that passed through each collector section was calculated as a direct proportion of the section cross-sectional area to the total collector cross-sectional area. Appendix 13 contains calculations of the cross-sectional areas of the laboratory model. The results of the calculations are:

Area top section = 1309 mm^2

Area bottom section = 1202 mm^2

Thus, Total cross-sectional area = 2511 mm^2

The ratio of the total flow passing through the top section is thus:

$$\dot{m}_t = \left(\frac{1309}{2511}\right) = 0.52 \times \dot{m} \quad \ldots\ldots\ldots\ldots\ldots\ldots\ldots\ldots (1)$$

$$\dot{m}_b = \left(\frac{1202}{2511}\right) = 0.48 \times \dot{m} \quad \ldots\ldots\ldots\ldots\ldots\ldots\ldots\ldots (2)$$

In the turbulent ranges of flowrate, Darcy's equation for head lost due to friction in a pipe may be used to calculate the proportions of flowrate that pass through each of the collector sections.

i.e. $$h_f = \left[\frac{4 \cdot f \cdot \ell \cdot \bar{u}^2}{2 \cdot g \cdot d}\right] \quad \ldots\ldots\ldots\ldots\ldots\ldots\ldots\ldots\ldots\ldots (3)$$

where f = Darcy friction factor, ℓ = pipe length (metres)

d = pipe diameter (metres), $\bar{u}$ = mean fluid velocity (m/s)

g = constant for gravitational acceleration (m/s^2)

h_f = head lost due to friction in a pipe (metres of water)

Darcy's equation is specified by Massey (57). Since both the top and bottom collector sections are connected to common inlet and outlet 'headers', it can be concluded that the head lost due to friction in the top section will equal the head lost due to friction in the bottom section.

The following calculation shows, however, that the range of flowrates tested never entered the turbulent regime, so further analysis using Darcy's equation is not presented.

For laminar flow, $Re_d < 2000$ i.e.

Top section:

$$Re_d = \left[\frac{\dot{m} \times d}{A \times \mu}\right]$$

Since the sections are non-circular, the equivalent hydraulic diameter was used in place of the diameter. The top section hydraulic diameter was calculated in Appendix 13 as:

$$d_{ht} = 0.0249 \text{ metres}$$

thus, for laminar flow:

$$2000 > \left[\frac{\dot{m}_t \times 0.0249}{1309 \times 10^{-6} \times 2 \times 10^{-5}}\right]$$

thus $\dot{m}_t < 0.002102$ kg/s

from which

$\dot{m} < 0.0040$ kg/s using Equation (1)

Bottom section:

$$2000 > \left[\frac{\dot{m}_b \times d_{hb}}{A \times \mu}\right]$$

The bottom section hydraulic diameter was calculated in Appendix 13 as:

$$d_{hb} = 0.0194 \text{ metres}$$

thus, for laminar flow:

$$2000 > \left[\frac{\dot{m}_b \times 0.0194}{1309 \times 10^{-6} \times 2 \times 10^{-5}}\right]$$

thus $\dot{m}_b < 0.002478$ kg/s

from which

$\dot{m} < 0.005163$ kg/s using Eqation (2)

Since the total mass-flowrate was always less than 0.0040 kg/s the flow regime inside the collector was laminar for all the laboratory tests.

(b) The life-size Baird-type collector

From the dimensions given in Appendix 12 it can be seen that the top and bottom cross-sectional areas and shapes were identical. Since this was so, it follows that the flow was equally divided between the top and bottom sections i.e.

$$\dot{m}_t = 0.5 \times \dot{m}$$

$$\dot{m}_b = 0.5 \times \dot{m}$$

APPENDIX 7

CONSIDERATIONS OF BOUNDARY LAYER GROWTH

(a) The model Baird-type solar collector

In the tests, the maximum flowrate was approximately 0.0040 kg/s.

Thus the maximum flowrate in the top section was:

$$\dot{m}_t = (0.004 \times 0.52) = 0.0021 \text{ kg/s} \quad \text{(from Appendix 6)}$$

and $$\dot{m}_b = (0.004 \times 0.48) = 0.0019 \text{ kg/s}$$

This can be used to calculate the maximum Reynolds numbers in the top and bottom sections i.e.

$$Re_{\substack{\text{max top} \\ (\ell=0.455)}} = \left(\frac{\dot{m}_t \cdot \ell}{A_t \cdot \mu}\right)$$

$$= \left(\frac{0.0021 \times 0.455}{1309 \times 10^{-6} \times 2 \times 10^{-5}}\right)$$

$$= 0.37 \times 10^5$$

$$Re_{\substack{\text{max bottom} \\ (\ell=0.455)}} = \left(\frac{\dot{m}_b \cdot \ell}{A_b \cdot \mu}\right)$$

$$= \left(\frac{0.0019 \times 0.455}{1202 \times 10^{-6} \times 2 \times 10^{-5}}\right)$$

$$= 0.36 \times 10^5$$

Since the Reynolds numbers were both below 1.5×10^5, the flow can be considered to have been laminar over the flat-plate.

Considering the top section:

For the purposes of this analysis it is convenient to equate the cross sectional shape of the top section of the collector to the rectangle shown below in Figure 43.

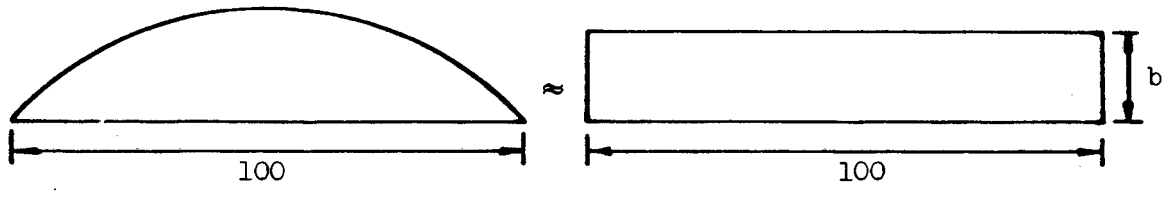

FIGURE 43: THE EQUIVALENT RECTANGLE OF THE TOP COLLECTOR SECTION

Equality of areas defines the equation:

$$\text{Area} = 1309 = 100 \times b$$

Therefore

$$b = 13.1 \text{ mm}$$

So the critical boundary layer thickness can be evaluated as half this thickness i.e.

$$\sigma_{\text{critical top}} = 6.6 \text{ mm (for the onset of fully developed flow)}$$

Since the boundary layer is laminar, the boundary layer thickness is defined for flow over a flat-plate by Holman (41) as:

$$\sigma = \left(\frac{4.64 \times \ell}{(Re_{\ell})^{0.5}}\right) \quad \ldots\ldots\ldots\ldots\ldots\ldots\ldots\ldots\ldots\ldots\ldots\ldots\ldots\ldots (1)$$

$$\text{Now} \quad Re_{\ell} = \left(\frac{\dot{m} \times \ell}{A \times \mu}\right)$$

Substituting this into equation (1) and reworking the subject results in:

$$\ell = \left(\frac{\sigma}{4.64}\right)^2 \times \left(\frac{\dot{m}}{A \times \mu}\right) \quad \ldots\ldots\ldots\ldots\ldots\ldots\ldots\ldots\ldots\ldots\ldots\ldots (2)$$

where 'ℓ' is the distance form the leading edge of the plate for the boundary layer to become 'σ' meters thick for a fluid of dynamic viscosity 'μ' flowing with a flowrate '$\dot{m}$' through a cross-section of area 'A'.

Substituting values for the top section into (2):

$$\ell_t = \left(\frac{0.0066}{4.64}\right)^2 \times \left(\frac{1}{1309 \times 10^{-6} \times 2 \times 10^{-5}}\right) \times \dot{m}_t$$

$$\text{Thus} \quad \ell_t = 77.28 \times \dot{m}_t \quad \text{metres} \quad \ldots\ldots\ldots\ldots\ldots\ldots\ldots\ldots\ldots\ldots (3)$$

Considering the bottom section:

The cross-sectional shape of the bottom section can be equated to the shape of the rectangle shown in Figure 44 .

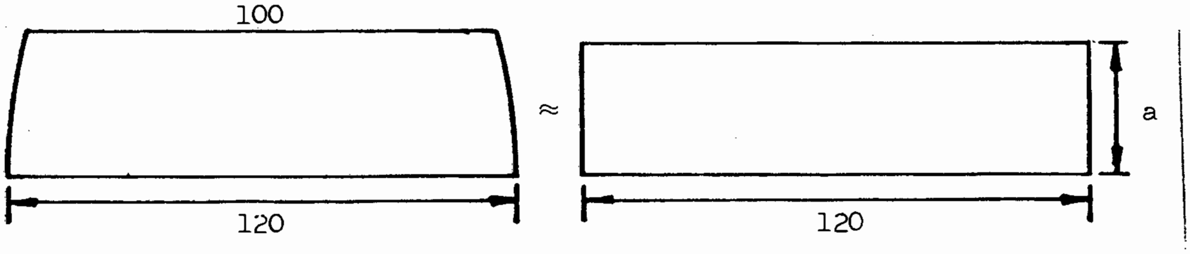

FIGURE 44: THE EQUIVALENT RECTANGLE OF THE BOTTOM COLLECTOR SECTION

Equality of areas defines the equation:

$$\text{Area} = 1202 = 110 \times a$$

Therefore

$$a = 10.9 \text{ mm}$$

Thus

$$\sigma_{\text{critical bottom}} = 10.9 / 2 = 5.45 \text{ mm}$$

Substituting values for the bottom section into (2):

$$\ell_b = \left(\frac{0.0055}{4.64}\right)^2 \times \left(\frac{1}{1202 \times 10^{-6} \times 2 \times 10^{-5}}\right) \times \dot{m}_b$$

Thus $\ell_b = 58.4 \times \dot{m}_b$ metres .....(4)

To appreciate which section is to be the first to attain fully developed flow, consider the following analysis:

$$\ell_t = \left(77.28 \times 0.52 \times \dot{m}\right) \quad \text{from equation (3)}$$

$$= 40.2 \times \dot{m} \quad .....(5)$$

and $$\ell_b = \left(58.4 \times 0.48 \times \dot{m}\right) \quad \text{from equation (4)}$$

$$= 28.0 \times \dot{m} \quad .....(6)$$

Thus it appears that the bottom section is the first to become fully developed for a given flowrate '$\dot{m}$' (at any distance 'x' from the leading edge).

The preceding analysis was based on the consideration of the laminar boundary layer growth for flow over a flat-plate. It is of interest to note what predictions result from a consideration of the flow in the collector cross-sections to be analagous to flow in tubes. In this case the Reynolds numbers can be calculated as:

$$Re_{d\ (\text{max top})} = \left(\frac{d_{ht} \times \dot{m}_t}{\mu \times A_{top}}\right)$$

$$= \left(\frac{0.0249 \times 0.00208}{2 \times 10^{-6} \times 1309 \times 10^{-6}}\right) \approx 1978$$

Similarly, the maximum Reynolds number in the bottom section is:

$$Re_{d\ (max\ bottom)} = \left(\frac{d_{hb} \times \dot{m}_b}{\mu \times A_{bottom}} \right)$$

$$= \left(\frac{0.0194 \times 0.00192}{2 \times 10^{-5} \times 1202 \times 10^{-6}} \right) \approx 1549$$

Thus, if the onset of turbulence is defined to take place at $Re_d = 2000$, it appears that flow in the collector sections never became turbulent during the tests. Thus the concept of hydraulic radius is inapplicable according to Massey (57).

(b) The life-size Baird-type solar collector

The flowrate through the life-size Baird-type collector was of the order of 10 kg/s, and this allows the Reynolds number to be calculated as:

$$Re_{\ell=30} = \left(\frac{m \times \ell}{A_t \times \mu} \right) = \left(\frac{5 \times 30}{0.3 \times 6.6 \times 2 \times 10^{-5}} \right)$$

$$= 3.8 \times 10^6$$

(Collector dimensions come from Appendix 12)

Since this value is larger than 1.5×10^5, it suggests that the flow could result in turbulent conditions.

APPENDIX 8

DERIVATION OF THE COLLECTOR LONGWAVE-RADIATION ELECTRICAL ANALOGY CIRCUIT

Consider the situation shown in Figure 45, which is a representation of the model Baird-type collector media and surroundings that exchange longwave radiation.

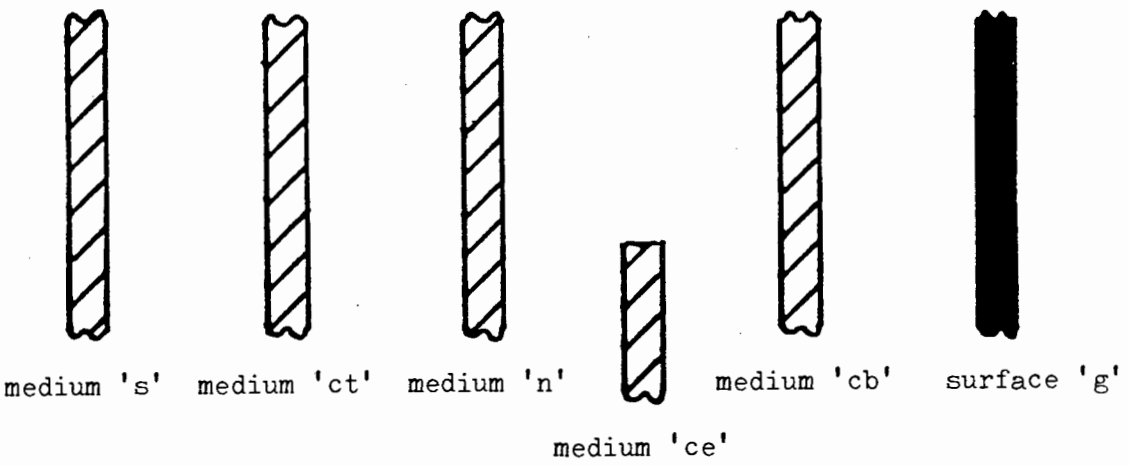

FIGURE 45: THE BAIRD-TYPE GREENHOUSE AND SURROUNDING MEDIA

The following assumptions have been made:

(1) all media were considered to be transmitting, absorbing and non-reflecting to longwave radiation.

(2) the (ground) surface was considered to be absorbing, reflecting and non-transmitting to longwave radiation.

Consider the GROUND-SKY interaction:

Of the energy leaving the surface "g", the amount absorbed by the medium "s" is:

$$\tau_{cb}.\tau_{n}.\tau_{ct}.\alpha_{s}.A_{g}.F_{g-s}.J_{g} = \varepsilon_{s}.A_{g}.F_{g-s}.J_{g}.(1-\varepsilon_{cb}).(1-\varepsilon_{n}).(1-\varepsilon_{ct})$$

(i.e. assuming Kirchoff's identity). "J " is the radiosity of the ground and is the sum of the (longwave) energy emitted and the (longwave) energy reflected, since no energy is transmitted. It can be written as:

$$J_{g} = \varepsilon_{g}.E_{bg} + \rho_{g}.G$$

Of the energy leaving the medium "s", the amount absorbed by the surface "g" is:

$$\tau_{cb}.\tau_{n}.\tau_{ct}.\varepsilon_{s}.E_{bs}.A_{s}.F_{s-g} = \varepsilon_{s}.A_{g}.F_{g-s}.E_{bs}.(1-\varepsilon_{cb}).(1-\varepsilon_{n}).(1-\varepsilon_{ct})$$

Note: (a) '$A_{s}.F_{s-g}=A_{g}.F_{g-s}$' is one of the reciprocity relations for shape factors as defined by Holman (41)

(b) '$\tau=1-\alpha$' is the form of the law of conservation of energy if the reflectance is assumed to be zero.

(c) '$\alpha=\varepsilon$' is the assumption of Kirchoff's identity.

The net energy exchange between surface "g" and medium "s" is:

$$Q_{g-s} = A_g.F_{g-s}.\varepsilon_s.(1-\varepsilon_{cb}).(1-\varepsilon_n).(1-\varepsilon_{ct}).(J_g-E_{bs})$$

$$= \frac{(J_g-E_{bs})}{\frac{1}{A_g.F_{g-s}.\varepsilon_s.(1-\varepsilon_{cb}).(1-\varepsilon_n).(1-\varepsilon_{ct})}}$$

Consider the GROUND-TOP COVER interaction:

Of the energy leaving the surface "g", the amount absorbed by the top cover medium "ct" is:

$$A_g.F_{g-ct}.J_g.\alpha_{ct}.\tau_n.\tau_{cb} = A_g.F_{g-ct}.J_g.\varepsilon_{ct}.(1-\varepsilon_n).(1-\varepsilon_{cb})$$

Of the energy leaving the top cover medium "ct", the amount absorbed by the surface "g" is:

$$A_{ct}.F_{ct-g}.J_{ct}.\tau_n.\tau_{cb} = A_g.F_{g-ct}.\varepsilon_{ct}.E_{bct}.(1-\varepsilon_n).(1-\varepsilon_{cb})$$

The net energy exchange between surface "g" and the medium "ct" is thus:

$$Q_{g-ct} = \frac{J_g - E_{bct}}{\frac{1}{A_g.F_{g-ct}.\varepsilon_{ct}.(1-\varepsilon_n).(1-\varepsilon_{cb})}}$$

In a similar manner to that shown above, the net energy exchange between surface "g" and the netting medium "n" can be calculated as:

$$Q_{g-n} = \frac{J_g - E_{bn}}{\frac{1}{A_g \cdot F_{g-n} \cdot \varepsilon_n \cdot (1-\varepsilon_{cb})}}$$

Likewise, the net energy exchange between the surface "g" and the bottom cover medium "cb" is:

$$Q_{g-cb} = \frac{J_g - E_{bcb}}{\frac{1}{A_g \cdot F_{g-cb} \cdot \varepsilon_{cb}}}$$

Consider the BOTTOM COVER-SKY interaction:

Of the energy leaving the bottom cover medium "cb", the amount which reaches medium "s" is:

$$A_{cb} \cdot F_{cb-s} \cdot J_{cb} \cdot \alpha_s \cdot \tau_{ct} \cdot \tau_n = A_{cb} \cdot F_{cb-s} \cdot \varepsilon_{cb} \cdot E_{bcb} \cdot \varepsilon_s \cdot (1-\varepsilon_{ct}) \cdot (1-\varepsilon_n)$$

Of the energy leaving the sky medium "s", the amount which reaches the bottom cover "cb" is:

$$A_s \cdot F_{s-cb} \cdot J_s \cdot \alpha_{cb} \cdot \tau_{ct} \cdot \tau_n = A_{cb} \cdot F_{cb-s} \cdot \varepsilon_{cb} \cdot \varepsilon_s \cdot E_{bs} \cdot (1-\varepsilon_{ct}) \cdot (1-\varepsilon_n)$$

The net energy exchange between the bottom cover and the sky is:

$$Q_{cb-s} = \frac{E_{bcb} - E_{bs}}{\frac{1}{A_{cb} \cdot F_{cb-s} \cdot \varepsilon_{cb} \cdot \varepsilon_s \cdot (1-\varepsilon_{ct}) \cdot (1-\varepsilon_n)}}$$

Similarly, the net energy exchange between the black-netting medium "n" and the sky "s" is:

$$Q_{n-s} = \frac{E_{bn} - E_{bs}}{\frac{1}{A_n \cdot F_{n-s} \cdot \varepsilon_n \cdot \varepsilon_s \cdot (1-\varepsilon_{ct})}}$$

Likewise, the net energy exchange between the top cover medium "ct" and the sky "s" is:

$$Q_{ct-s} = \frac{E_{bct} - E_{bs}}{\frac{1}{A_{ct} \cdot F_{ct-s} \cdot \varepsilon_{ct} \cdot \varepsilon_s}}$$

Consider the NETTING-TOP COVER interaction:

Of the energy leaving the black-netting medium "n", the amount which is absorbed by the top cover medium "ct" is:

$$A_n \cdot F_{n-ct} \cdot J_n \cdot \alpha_{ct} = A_n \cdot F_{n-ct} \cdot E_{bn} \cdot \varepsilon_n \cdot \varepsilon_{ct}$$

Of the energy leaving the top cover medium "ct", the amount which is absorbed by the netting medium "n" is:

$$A_{ct} \cdot F_{ct-n} \cdot J_{ct} \cdot \alpha_n = A_n \cdot F_{n-ct} \cdot E_{bct} \cdot \varepsilon_{ct} \cdot \varepsilon_n$$

The net energy exchange between the netting medium "n" and the top cover medium "ct" is therefore:

$$Q_{n-ct} = \frac{E_{bn} - E_{bct}}{\frac{1}{A_n \cdot F_{n-ct} \cdot \varepsilon_n \cdot \varepsilon_{ct}}}$$

Similarly, the net energy exchange between the netting "n" and the bottom cover "cb" is:

$$Q_{n-cb} = \frac{E_{bn} - E_{bcb}}{\frac{1}{A_n \cdot F_{n-cb} \cdot \varepsilon_n \cdot \varepsilon_{cb}}}$$

Also, the net energy exchange between the bottom cover "cb" and the top cover "ct" is:

$$Q_{cb-ct} = \frac{E_{bcb} - E_{bct}}{\frac{1}{A_{cb} \cdot F_{cb-ct} \cdot \varepsilon_{cb} \cdot \varepsilon_{ct} \cdot (1-\varepsilon_n)}}$$

Consider the GROUND-EDGE COVER interaction:

Of the energy leaving the ground surface "g", the amount which is directly absorbed by the edge cover medium "ce" is:

$$A_g \cdot F_{gout-ce} \cdot J_g \cdot \alpha_{ce} = A_g \cdot F_{gout-ce} \cdot J_g \cdot \varepsilon_{ce}$$

Of the energy leaving the edge cover "ce", the amount which is directly absorbed by the ground surface "g" is:

$$A_{ce} \cdot F_{ce-gout} \cdot J_{ce} = A_g \cdot F_{gout-ce} \cdot E_{bce} \cdot \varepsilon_{ce}$$

The net, direct energy exchange between the edge cover "ce" and the ground surface "g" is:

$$Q_{gout-ce} = \frac{J_g - E_{bce}}{\frac{1}{A_g \cdot F_{gout-ce} \cdot \varepsilon_{ce}}}$$

Similarly, the net indirect energy exchange (i.e. that which passes through the bottom cover) between the edge cover "ce" and the ground surface "g" is:

$$Q_{gin-ce} = \frac{J_g - E_{bce}}{\frac{1}{A_g . F_{gin-ce} . \varepsilon_{ce} . (1-\varepsilon_{cb})}}$$

Thus the net energy exchange between the edge cover "ce" and the ground surface "g" is the sum of the direct and indirect exchanges i.e.:

$$Q_{g-ce} = Q_{gout-ce} + Q_{gin-ce}$$

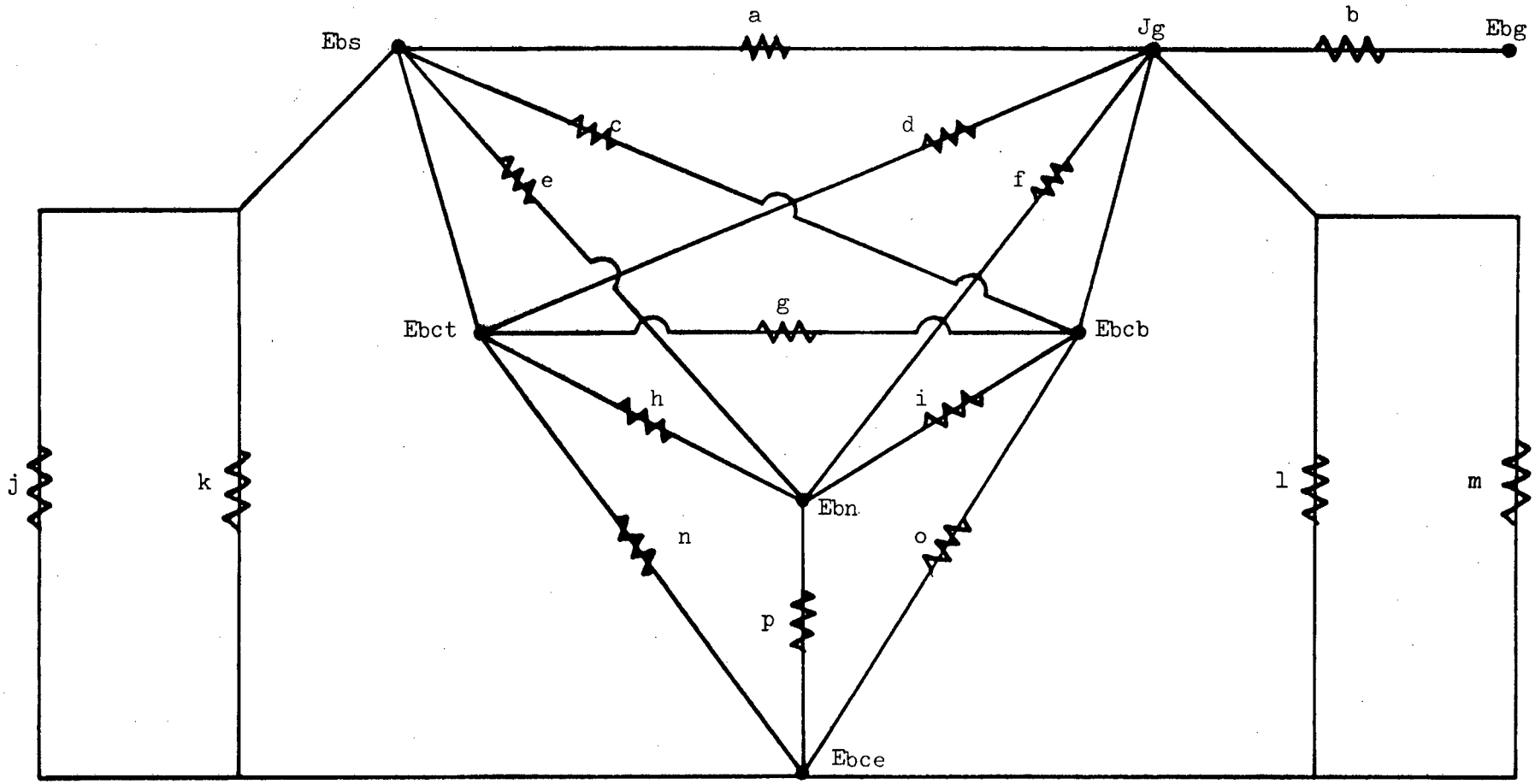

(For explanation of symbols, please turn page)

FIGURE 46 : THE BAIRD-TYPE SOLAR COLLECTOR LONGWAVE-RADIATION ELECTRICAL ANALOGY CIRCUIT

Explanation of Symbols used in Figure 46:

$Ebs = \sigma.(Ts)^4$

$Ebct = \sigma.(Tct)^4$

$Ebce = \sigma.(Tce)^4$

$Ebn = \sigma.(Tn)^4$

$Ebcb = \sigma.(Tcb)^4$

$Ebg = \sigma.(Tg)^4$

$Jg = \varepsilon_g.Ebg + \rho_g.G$

(a) $= 1/(A_g.F_{g-s}.\varepsilon_s.(1-\varepsilon_{cb}).(1-\varepsilon_n).(1-\varepsilon_{ct}))$

(b) $= (1-\varepsilon_g)/(\varepsilon_g.A_g)$

(c) $= 1/(A_{cb}.F_{cb-s}.\varepsilon_{cb}.\varepsilon_s.(1-\varepsilon_{ct}).(1-\varepsilon_n))$

(d) $= 1/(A_g.F_{g-ct}.\varepsilon_{ct}.(1-\varepsilon_n).(1-\varepsilon_{cb}))$

(e) $= 1/(A_n.F_{n-s}.\varepsilon_n.\varepsilon_s.(1-\varepsilon_{ct}))$

(f) $= 1/(A_g.F_{g-n}.\varepsilon_n.(1-\varepsilon_{cb}))$

(g) $= 1/(A_{cb}.F_{cb-ct}.\varepsilon_{cb}.\varepsilon_{ct}.(1-\varepsilon_n))$

(h) $= 1/(A_n.F_{n-ct}.\varepsilon_n.\varepsilon_{ct})$

(i) $= 1/(A_n.F_{n-cb}.\varepsilon_n.\varepsilon_{cb})$

(j) $= 1/(A_{ce}.F_{ce-sin}.\varepsilon_{ce}.\varepsilon_s.(1-\varepsilon_n).(1-\varepsilon_{ct}))$

(k) $= 1/(A_{ce}.F_{ce-sout}.\varepsilon_{ce}.\varepsilon_s)$

(l) $= 1/(A_g.F_{gout-ce}.\varepsilon_{ce})$

(m) $= 1/(A_g.F_{gin-ce}.\varepsilon_{ce}.(1-\varepsilon_{cb}))$

(n) $= 1/(A_{ce}.F_{ce-ct}.\varepsilon_{ce}.\varepsilon_{ct}.(1-\varepsilon_n))$

(o) $= 1/(A_{cb}.F_{cb-ce}.\varepsilon_{cb}.\varepsilon_{ce})$

(p) $= 1/(A_n.F_{n-ce}.\varepsilon_n.\varepsilon_{ce})$

APPENDIX 9

THE SOLUTION OF "N" SIMULTANEOUS, NON-LINEAR EQUATIONS USING NEWTON'S METHOD AND GAUSS-JORDAN ELIMINATION

The solution of a set of 'N' non-linear equations using Newton's method requires that 'N' linearised equations be solved. Gauss-Jordan elimination is used for this purpose.

(a) The solution of a set of linear equations using Gauss-Jordan elimination:

Consider the simple example of three linear equations:

$$3x_1 - x_2 + 2x_3 = 12 \quad \ldots\ldots(1)$$

$$x_1 + 2x_2 + 3x_3 = 11 \quad \ldots\ldots(2)$$

$$2x_1 - 2x_2 - x_3 = 2 \quad \ldots\ldots(3)$$

Multiplying (1) by -1 and (2) by 3 and adding eliminates 'x_1'.

Similarly, multiplying (1) by -2 and (3) by 3 also eliminates 'x_1'.

Thus:

$$3x_1 - x_2 + 2x_3 = 12 \quad \ldots\ldots(4)$$

$$7x_2 + 7x_3 = 21 \quad \ldots\ldots(5)$$

$$-4x_2 - 7x_3 = -18 \quad \ldots\ldots(6)$$

Eliminating 'x_2' by multiplying (5) by -4 and (6) by 7 and adding.

Thus:

$$3x_1 - x_2 + 2x_3 = 12 \quad \ldots\ldots(7)$$

$$7x_2 + 7x_3 = 21 \quad \ldots\ldots(8)$$

$$-21x_3 = -42 \quad \ldots\ldots(9)$$

Obviously $x_3 = 2$ from (9), and back substitution gives $x_2 = 1$, $x_1 = 3$.

Presenting the same problem in matrix notation:

$$\begin{bmatrix} 3 & -1 & 2 \\ 1 & 2 & 3 \\ 2 & -2 & -1 \end{bmatrix} \begin{bmatrix} x_1 \\ x_2 \\ x_3 \end{bmatrix} = \begin{bmatrix} 12 \\ 11 \\ 2 \end{bmatrix}$$

or

$$\underline{A}.\underline{x} = \underline{b}$$

The arithmetic operations affect only the coefficients and the constant terms, so it is only necessary to work with the matrix of coefficients 'augmented' with the '$\underline{b}$' vector i.e.

$$\underline{A}\,|\,\underline{b} = \left[\begin{array}{ccc|c} 3 & -1 & 2 & 12 \\ 1 & 2 & 3 & 11 \\ 2 & -2 & -2 & 2 \end{array}\right]$$

Eliminate the first coefficient in the 'i'th row by adding '$-\frac{a_{i1}}{a_{11}}$' times the first equation to the 'i'th equation.

Similarly, the leading coefficients of successive rows are eliminated by again multiplying by the corresponding negative ratio of coefficients and adding. Thus:

$$\begin{bmatrix} 3 & -1 & 2 & 12 \\ 1 & 2 & 3 & 11 \\ 2 & -2 & -1 & 2 \end{bmatrix} \begin{array}{l} R_2 + (-1/3)R_1 \longrightarrow \\ R_3 + (-2/3)R_1 \longrightarrow \end{array} \begin{bmatrix} 3 & -1 & 2 & 12 \\ 0 & 2.333 & 2.334 & 7.004 \\ 0 & -1.334 & -2.332 & -5.992 \end{bmatrix}$$

and finally

$$R_3 + \left(\frac{1.334}{2.333}\right) R_2 \longrightarrow \begin{bmatrix} 3 & -1 & 2 & 12 \\ 0 & 2.333 & 2.334 & 7.004 \\ 0 & 0 & -1.000 & -1.993 \end{bmatrix}$$

This method is called '<u>Gaussian elimination</u>'. Back substitution gives $x_3 = 1.993$, $x_2 = 1.008$ and $x_1 = 3.007$. The differences of these values from 2, 1 and 3 are due to the effects of round-off.

The 'Gauss-Jordan scheme' eliminates the coefficients in the rows above the working row as well as those below during the same step. This involves more arithmetical operations, but back substitution is then avoided. The effects of round-off errors can be minimised by utilising techniques that involve interchanging rows and columns and is known as 'elimination with a pivoting strategy'. For further information the reader is referred to Gerald (54) and Henrici (55).

(b) The solution of a set of non-linear equations using Newton's method :

This is an iterative method in which convergence is guaranteed provided that the initial 'solution-guess' is near enough the solution. Each iteration involves solving a set of linear equations. The method is as follows:

Arrange the equations as $f_i(x_1, x_2, \ldots, x_n) = 0 \qquad 1 \leq i \leq n$

Form all the partial derivatives $\left(\frac{\partial f_i}{\partial x_j}\right) \qquad 1 \leq j \leq n$

The partial derivatives are the coefficients 'a_{ij}' in the matrix '$\underline{A}$' (they are still functions of $x_1, \ldots, x_n$).

Make the initial solution guess:

$$\underline{x}^o = \underline{x}_1^o, \underline{x}_2^o, \ldots\ldots, \underline{x}_n^o$$

Evaluate '$\underline{b}^o$' where $b_i^o = f_i(\underline{x}^o)$

(i.e. the 'i'th function value calculated using the values $x_1^o, x_2^o, \ldots, x_n^o$

Presumably '$\underline{b}^o$' is smallish but not zero)

Evaluate '$\underline{A}^o$' where $A_{ij}^o = \left(\frac{\partial f_i}{\partial x_j}\right)$ evaluated at '$\underline{x}^o$'.

Solve $\underline{A}^o . \underline{z} = \underline{b}^o$

$$\begin{bmatrix} \frac{\partial f_1}{\partial x_1} & \frac{\partial f_1}{\partial x_2} & \cdots\cdots & \frac{\partial f_1}{\partial x_n} \\ \vdots & & & \vdots \\ \frac{\partial f_n}{\partial x_1} & \cdots\cdots\cdots\cdots & & \frac{\partial f_n}{\partial x_n} \end{bmatrix} \begin{bmatrix} z_1 \\ \vdots \\ z_n \end{bmatrix} = \begin{bmatrix} f_1(\underline{x}^o) \\ \vdots \\ f_n(\underline{x}^o) \end{bmatrix}$$

The solution for '$\underline{z}$' is obtained using Gauss-Jordan elimination performed on the 'n' linear equations above. The next solution approximation is '$\underline{x}^1$' and is calculated as:

$$\underline{x}^1 = \underline{x}^o - \underline{z}$$

The procedure is iterated using '$\underline{x}^1$' which in turn genrates an improved approximation '$\underline{x}^2$'. This is repeated until a satisfactorily accurate solution has been obtained.

Proof for convergence of Newton's method in 'n' dimensions (Smart - 56):

Suppose '$\underline{x}^*$' is the exact root i.e.

$$f_i(\underline{x}^*) = 0 \qquad \text{for } 1 \leq i \leq n$$

and suppose '$\underline{x}^o$' is a fairly good approximation i.e.

$$\underline{x}^o = \underline{x}^* - \underline{h}^o \qquad \text{where } \underline{h}^o \text{ is small}$$

then define

$$\underline{x}^1 = \underline{x}^o - \underline{z} \qquad \text{where } \underline{z}.\nabla f_i = f_i(\underline{x}^o) \text{ for } 1 \leq i \leq n$$

and let $\underline{x}^1 = \underline{x}^* - \underline{h}^1$

Convergence will be proved if it can be shown that '$\underline{h}^1$' is smaller than '$\underline{h}^o$'.

So:
$$\begin{aligned} \underline{h}^1 &= \underline{x}^* - \underline{x}^1 \\ &= \underline{x}^* - \underline{x}^o + \underline{z} \\ &= \underline{h}^o + \underline{z} \end{aligned}$$

Therefore $\underline{h}^1.\nabla f_i = \underline{h}^o.\nabla f_i + \underline{z}.\nabla f_i = f_i^o + \underline{h}^o.\nabla f_i$

but $0 = f_i(\underline{x}^*) = f_i(\underline{x}^o + \underline{h}^o)$

$= f_i^o + \underline{h}^o.\nabla f_i^o$ + 2nd order terms (Taylor Series expansion - 53)

Therefore

$\underline{h}^1$ = squares of $\underline{h}^o$ elements.

For conditions guaranteeing convergence and more detailed explanations of Newton's method, the reader is referred to Gerald (54) and Henrici (56).

Example:

Solve for 'x' and 'y' such that:

$$x^2 + y^2 = 2$$

$$x^2 - y^2 = 1$$

These are two non-linear equations. The solution represents the intersection of the hyperbolas generated by $x^2 - y^2 = 1$ and the circle generated by $x^2 + y^2 = 2$.

$$f_1(x,y) = x^2 + y^2 - 2$$

$$f_2(x,y) = x^2 - y^2 - 1$$

$$\underline{A} = \begin{bmatrix} \frac{\partial f_1}{\partial x} & \frac{\partial f_1}{\partial y} \\ \frac{\partial f_2}{\partial x} & \frac{\partial f_2}{\partial y} \end{bmatrix} = \begin{bmatrix} 2x & 2y \\ 2x & -2y \end{bmatrix}$$

Guess: $\underline{x}^o = (1,1)$ thus $\underline{b}_1{}^o = 0$ and $\underline{b}_2{}^o = -1$

$$\underline{A}^o = \begin{bmatrix} 2 & 2 \\ 2 & -2 \end{bmatrix}$$

Solving $\underline{A}^o . \underline{z} = \underline{b}$

$$\begin{bmatrix} 2 & 2 \\ 2 & -2 \end{bmatrix} \begin{bmatrix} z_1 \\ z_2 \end{bmatrix} = \begin{bmatrix} 0 \\ -1 \end{bmatrix}$$

from which $\underline{z} = (z_1, z_2) = (-0.25, 0.25)$

Hence $\underline{x}^1 = \underline{x}^o - \underline{z} = (1, 1) - (-0.25, 0.25)$

$= (1.25, 0.75)$

The process is now repeated until a satisfactorily accurate answer is obtained. A computer program for solving linear equations using Gauss-Jordan elimination was modified and tested with the above example. After five iterations the solution offered was x = 1.224 and y = 0.707 Resubstitution into the equations at the top of the page validates the program, although the accuracy is limited by the number of iterations. The other points of intersection can be calculated by choosing initial solution values close to the actual solution.

APPENDIX 10

THE COLLECTOR HEAT-TRANSFER COEFFICIENTS

(a) The model Baird-type solar collector internal surfaces

The heat-transfer coefficient on all the internal collector surfaces (other than the black-netting) was deduced from the following equation presented by Kays (42) for a flat plate subjected to uniform heat flux:

$$Nu_{\ell} = 0.453 \times (Pr)^{\frac{1}{3}} \times (Re_{\ell})^{\frac{1}{2}} \quad \ldots\ldots\ldots\ldots\ldots\ldots\ldots\ldots (1)$$

The heat-transfer coefficient for the black-netting was derived experimentally by the author. Details are given in Appendix 2. All the fluid properties in the above equations are evaluated at the film temperature, where the film temperature is defined as:

$$T_{film} = (T_{wall} + T_{free\ stream})/2$$

In the case of the flat-plate/tube theoretical prediction, the tube heat-transfer coefficient is evaluated using the equation derived in Appendix 20.

(b) The life-size Baird-type solar collector internal surfaces

Calculations in Appendix 7 have shown that both laminar and turbulent flow conditions may arise on the internal surfaces of the life-size collector. Thus the heat-transfer coefficient on all the internal surfaces (other than the black-netting) with laminar flow was evaluated using equation (1). After the onset of turbulent flow the heat-transfer coefficient was calculated using the following equation presented

by Eckert and Drake (62) for turbulent flow over a flat plate with varying wall temperature:

$$Nu_{\ell} = 0.0289 \times (Pr)^{\frac{1}{3}} \times (Re)_{\ell}^{0.8} \quad \ldots\ldots\ldots\ldots\ldots\ldots\ldots\ldots(2)$$

All fluid properties in equation (2) are evaluated at the fluid film temperature. The heat-transfer coefficient for the black-netting was derived from the related equation presented in Appendix 2.

(c) The Baird-type solar collector external surfaces

The external surfaces of the collector are subject to natural convection heat-transfer. Simplified equations for the heat-transfer coefficient from various surfaces to air at atmospheric pressure and moderate temperatures are given by Holman (41). The following table contains relevant extracts from these equations.

Surface	Laminar i.e.	Turbulent i.e.
	$10^4 < Gr_f.Pr_f < 10^9$	$Gr_f.Pr_f > 10^9$
Natural convection from edge covers	$h = 1.42 \times (\frac{\Delta T}{\ell})^{0.25}$	$h = 0.95 \times (\Delta T)^{\frac{1}{3}}$
Natural convection from top covers	$h = 1.32 \times (\frac{\Delta T}{\ell})^{0.25}$	$h = 1.43 \times (\frac{\Delta T}{\ell})^{\frac{1}{3}}$
Natural convection from the bottom cover	$h = 0.61 \times (\frac{\Delta T}{\ell^2})^{0.2}$	

In these tables:

h = heat-transfer coefficient $(W/m^2.^oC)$

$\Delta T = (T_{wall} - T_{free\ stream})$ (^oC)

ℓ = mean of the two dimensions for a rectangular surface (metres)

Pr_f = Prandtl number of the fluid (evaluated at the film temperature)

Gr_f = Grashof number evaluated at the film temperature and is defined as:

$$Gr_f = \frac{g \times \beta_f \times (T_{wall} - T_{free\ stream}) \times \ell^3}{\nu_f^2} \quad \text{.....(3)}$$

where g = gravitational acceleration constant (m/s^2)

β_f = volume coefficient of expansion - for ideal gases, $\beta_f = (1/T_f)$ where 'T_f' is the absolute film temperature of the gas in degrees Kelvin

ν_f = kinematic viscosity of the fluid at the film temperature (m^2/s)

APPENDIX 11

THE COLLECTOR LONGWAVE-RADIATION SHAPE-FACTORS

(a) The model Baird-type collector

The prediction of collector performance was made for a model collector subdivided into ten elements. Each element was independently solved and the radiation effects of surrounding collector surfaces outside an element were ignored. Holman (41) contains data for radiation shape factors between parallel rectangles and between perpendicular rectangles with a common edge. A specimen calculation of the shape-factor between the bottom cover and the top cover is included here.

The bottom cover - top cover shape factor:

Consider the bottom and top covers to be two parallel rectangles. The distance between them is calculated in Appendix 7 and is 24 mm. The width of the bottom cover is 120 mm and that of the top cover is 100mm. Let an average width be defined as 110 mm. Figure 47 is a graphical description of the shape-factor between two parallel and equal rectangles.

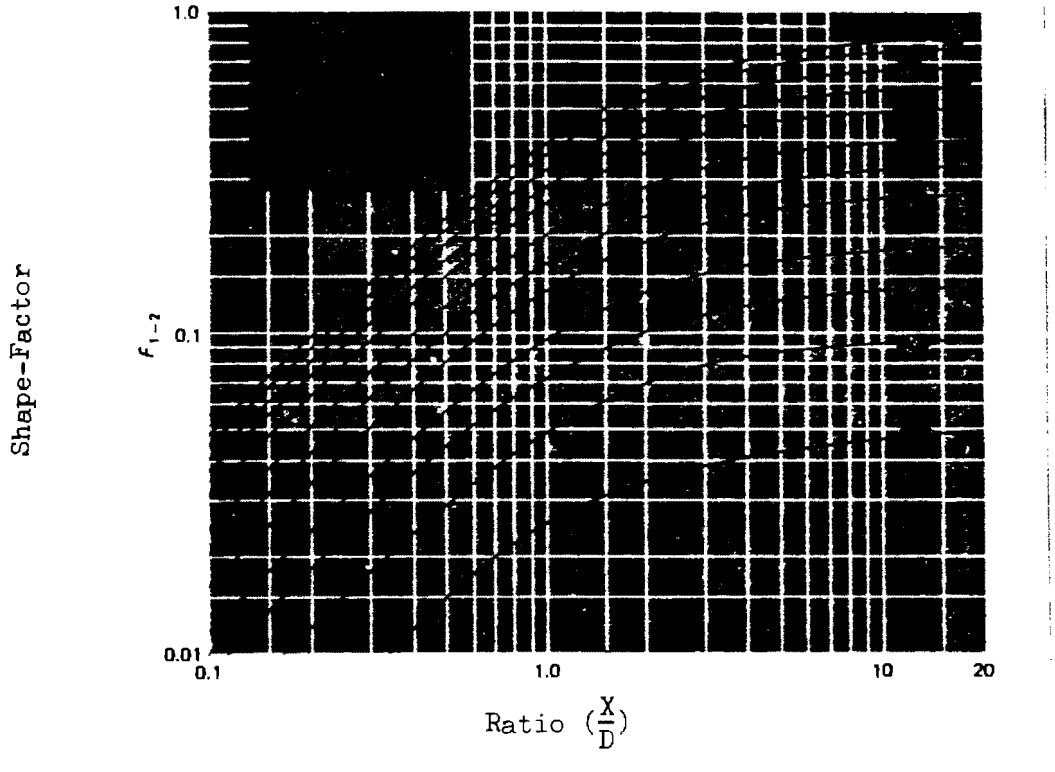

FIGURE 47 : RADIATION SHAPE-FACTOR BETWEEN PARALLEL RECTANGLES (Holman - 41)

Since the collector is divided into ten elements, each element is of length:

$$Y = (455 / 10) = 45.5 \text{ mm}$$

Hence the following ratios can be calculated:

$$(\frac{Y}{D}) = (110/24) = 4.6$$

$$(\frac{X}{D}) = (45.5/24) = 1.9$$

These ratios, in conjunction with Figure 47, allow the shape-factor between the bottom and the top covers to be worked out as:

$$F_{cb-ct} = 0.5$$

The following shape-factors were calculated in the same manner:

$$F_{n-ct} = 0.65$$

$$F_{n-cb} = 0.75$$

Use of Holman's information on perpendicular rectangles with a common edge (Reference 41) allows the following shape-factors to be calculated:

$$F_{n-ce} = 0.05$$

$$F_{cb-ce} = 0.05$$

In the case of the edge and top covers, the surfaces can be regarded as perpendicular rectangles whose edges are now no longer common but instead lie some distance apart. Sparrow and Cess (63) present the shape-factor relationship for this situation, which allows the calculation to be made. The result is:

$$F_{ce-ct} = 0.24$$

In the following cases, the interaction of the surface is with either the sky or the ground. Since these are very large in area, the shape factors are all unity i.e.

$$F_{ct-s} = F_{ct-g} = F_{cb-s} = F_{cb-g} = F_{n-s} = F_{n-g} = 1$$

Since the edge covers are completely surrounded by either sky or ground, it is assumed that the shape-factor for each is:

$$F_{ce\text{-}gout} = 0.25$$

$$F_{ce\text{-}gin} = 0.75$$

$$F_{ce\text{-}sout} = 0.75$$

$$F_{ce\text{-}sin} = 0.25$$

(b) The life-size Baird-type collector

The same techniques were used to calculate the life-size collector shape-factors. The results are listed below:

$$F_{cb\text{-}ct} = 0.9$$

$$F_{n\text{-}ct} = 0.9 = F_{n\text{-}cb}$$

$$F_{n\text{-}ce} = 0.04 = F_{cb\text{-}ce}$$

$$F_{ce\text{-}ct} = 0.36$$

$$F_{n\text{-}g} = F_{ct\text{-}s} = F_{ct\text{-}g} = F_{cb\text{-}s} = F_{cb\text{-}g} = F_{n\text{-}s} = 1$$

Since the edge covers are now vertical, the proportion of sky and ground 'viewed' is identical i.e.

$$F_{ce\text{-}gout} = F_{ce\text{-}gin} = F_{ce\text{-}sout} = F_{ce\text{-}sin} = 1$$

APPENDIX 12

THE LIFE-SIZE BAIRD-TYPE INTEGRAL-GREENHOUSE SOLAR COLLECTOR

The predictions of performance for the life-size solar collector made using the dimensions and geometry shown below in Figure 48. The length of this collector is thirty metres.

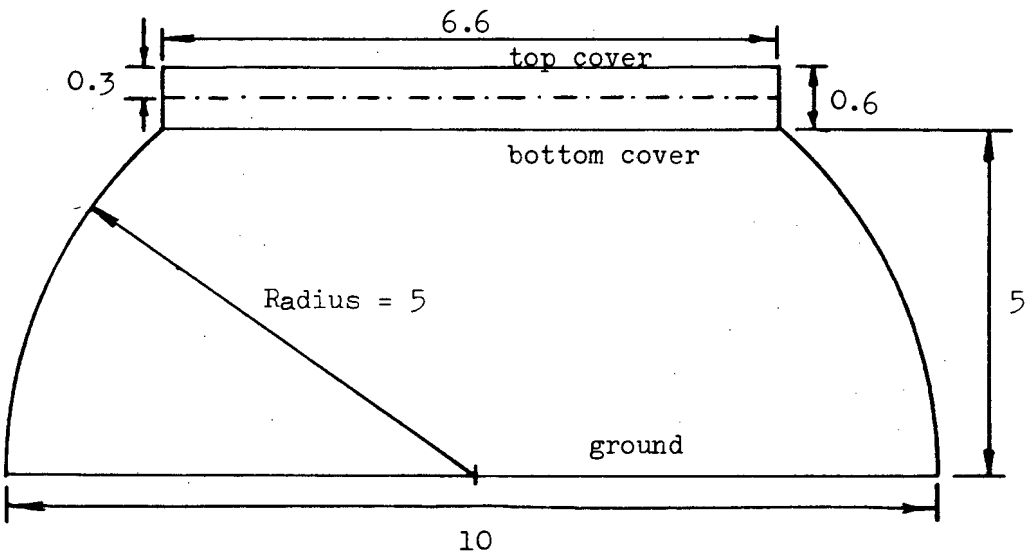

(All dimensions in metres, scale approximately 1:120)

FIGURE 48 : THE LIFE-SIZE BAIRD-TYPE SOLAR COLLECTOR

APPENDIX 13

THE MODEL BAIRD-TYPE INTEGRAL-GREENHOUSE SOLAR COLLECTOR

The dimensions of the model greenhouse cum solar collector are shown in Figure 49.

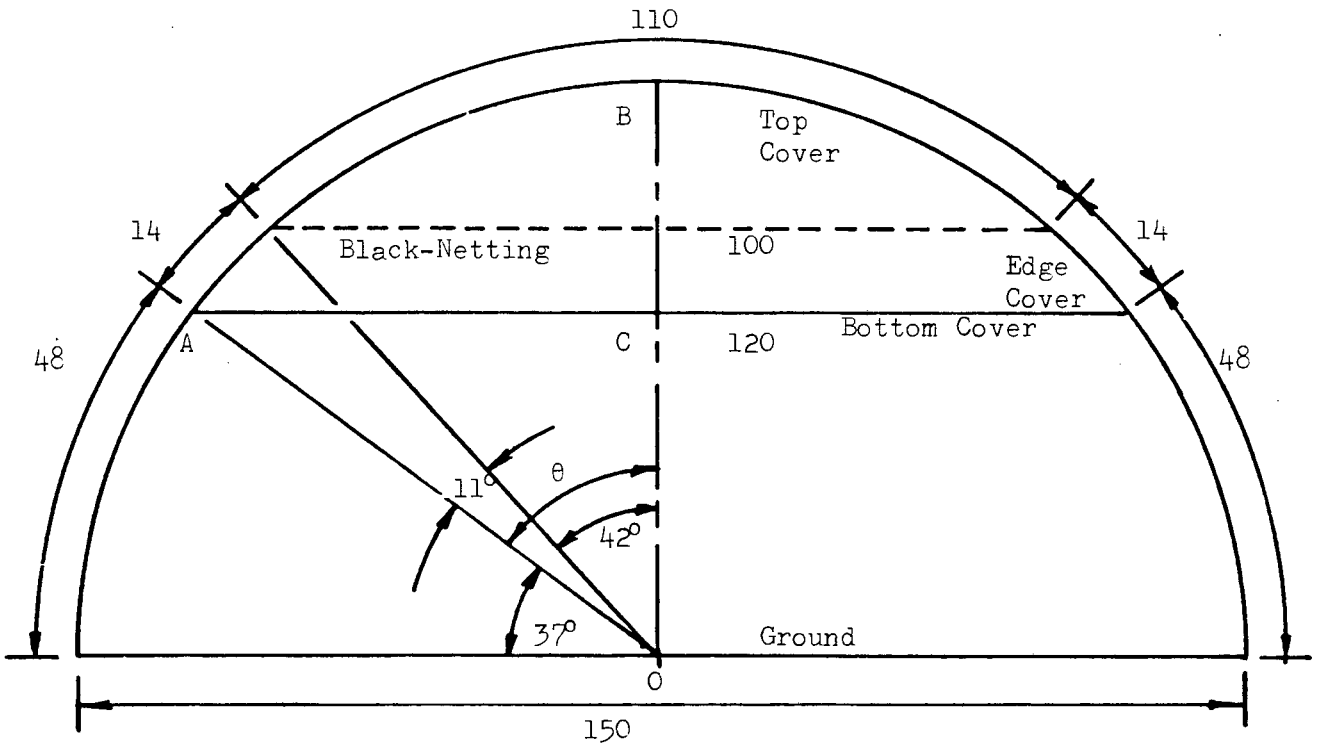

(All dimensions in mm)

(Length = 455 mm)

FIGURE 49: DIMENSIONS OF THE MODEL BAIRD-TYPE SOLAR COLLECTOR

The collector cross-sectional areas were calculated as follows. The area to the left of the line BC is made up of the triangle ABC and the segment of the circle above line AB.

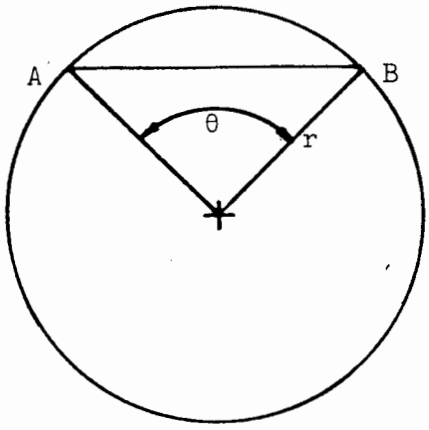

FIGURE 50: SEGMENT OF CIRCLE OF RADIUS "r"

The area of the shaded segment in Figure 50 is defined by Spiegel (53) as:

$$\text{Area segment} = 0.5 \times r^2 \times (\theta - \text{sine}(\theta))$$

where "θ" is the angle subtended by the chord AB at the centre of the circle and is expressed in radians. Since the area of a triangle is half the base times the perpendicular height, the total collector cross-sectional area in Figure 49 may be expressed as:

$$\text{Area} = 2 \times (0.5 \times AC \times BC + 0.5 \times AO^2 \times (\theta - \text{sine}(\theta)))$$

Inserting the appropriate dimensions enabled the total collector cross-sectional area to be calculated as 2511 square millimetres.

The area of the collector cross-section above the black-netting was calculated in a similar manner as 1309 square millimetres. By subtraction the collector cross-sectional area below the black-netting was found to be 1202 square millimetres.

The hydraulic diameter of the top section was calculated as:

$$d_{ht} = \left(\frac{4 \times \text{top section cross-sectional area}}{\text{wetted perimeter}}\right)$$

$$= \left(\frac{4 \times 1309}{110\ 100}\right)$$

$$= 24.9 \text{ mm}$$

Similarly, the hydraulic diameter of the bottom section was calculated as:

$$d_{hb} = \left(\frac{4 \times 1202}{100 + 28 + 120}\right)$$

$$= 19.4 \text{ mm}$$

APPENDIX 14

THE ORIFICE-PLATE FLOWRATE MEASURING APPARATUS

The air flowrate through the model Baird-type solar collector was deduced from pressure measurements made using an orifice-plate with corner tappings, designed in accordance with British Standards specifications (43). This type of orifice-plate was chosen because it is suitable for use in low flowrate work, and in particular, for use in the range of flowrates that were anticipated from the air-supply source.

The following equations were used for design and measurement purposes:

$$W = (0.01252).C.Z.e.E.(d)^2.\sqrt{(h.\rho)} \quad \ldots\ldots (1)$$

$$Rd = ((3.54).W)/(\mu.D.\sqrt{(m)}) \quad \ldots\ldots (2)$$

$$m = (d/D)^2$$

$$E = 1/\sqrt{(1-m^2)}$$

where W = fluid mass-flowrate (kg/hr)

C = basic discharge coefficient

Z = $Zd.Zr$

Zd = pipe size correction factor

Zr = Reynolds number correction factor

e = expansibility factor

E = velocity of approach factor

d = orifice or throat diameter (mm)

h = pressure difference across orifice (mm H_2O)

ρ = fluid density (kg/m^3)

Rd = Reynolds number of orifice

μ = dynamic viscosity of fluid (poise or g/cms)

m = area-ratio

D = pipe internal diameter (mm)

The fluid density is evaluated using:

$$\rho = 43.25 \times \left(\frac{\delta}{K.T} . (P - P_v) + 0.62 \times \frac{P_v}{T} \right) \quad kg/m^3$$

where δ = the specific gravity of the dry gas

P = absolute pressure at the upstream tapping (lbf/in^2)

T = absolute temperature at the upstream tapping (degrees Rankine)

P_v = partial pressure of water vapour (lbf/in^2)

K = gas law deviation coefficient at the temperature "T" and pressure "P"

The orifice was designed so that:

D = 45.72 mm and d = 6.35 mm

therefore

$m = (d/D)^2 = 0.0193$

(Many of the factors listed above are dependent on the area-ratio. The variability of these factors decreases with decreasing area-ratio values, making a small area-ratio value desirable.)

Hence $E = 1/ (1-m^2) = 1.0002$

from the tables

C = 0.596

Zd = ((1 + 1.002)/2) = 1.001 for a plastic pipe of P.T.O.

diameter D = 2 inches

Zr = function of "Rd" and is obtained from a table

e = function of "h/P" and is obtained from a table

Note: Units of "h/P" are as follows:

"h" is expressed in (inches H_2O)

"P" is expressed in ($lbf/inch^2$)

Substituting these values into the equation for mass-flowrate (Equation 1) produces the following simplified equation:

$$W = (0.3012).Zr.e.\sqrt{(h.\rho)}$$

For the measurement of air at atmospheric pressure and temperature, the values of "δ" and "K" are unity. An upper flow measurement limit exists for the measurement of compressible fluids, and is avoided if:

$$(h/P) < 5.5$$

where "h" is in (inches H_2O) and "P" is in (lbf/in^2).

A sample flowrate calculation:

This example is based on the results of test 39.

Measured values from the test include:

Laboratory dry-bulb temperature = 66 degrees Fahrenheit

Laboratory wet-bulb temperature = 60 degrees Fahrenheit

The relative humidity of the air (φ) can be worked out from a psychrometric chart or a hygrometer as 0.71.

Atmospheric pressure = 754.85 mm Hg

Gauge pressure (upstream tapping) = 14 mm Hg

Gauge pressure (across orifice) = 12 mm Hg

Temperature of air at upstream tapping = 24.9 $^{\circ}C$

Calculations:

h = 12 mm Hg

= (12 x 0.53524) = 6.42 inches H_2O

= (12 x 13.5951) = 163.14 mm H_2O

P = (754.85 + 14) = 768.85 mm Hg

= (768.85 x 0.0193368) = 14.867 lbf/in^2

T = 24.9 degrees Centigrade

= ((1.8 x 24.9) + 32) = 76.8 degrees Fahrenheit

= (459.67 + 76.8) = 536.5 degrees Rankine

All the conversion factors used above come from the British Standard (43). From tables, at 76.8 degrees Fahrenheit:

$$P_{vs} = 0.456 \text{ lbf/in}^2$$

and $$P = (\varphi \times P_{vs}) = (0.71 \times 0.456) = 0.324 \text{ lbf/in}^2$$

The air density is calculated as:

$$\rho = 43.25 \times \left(\frac{(14.867 - 0.324)}{536.5} + \frac{(0.62 \times 0.324)}{536.5} \right)$$

$$= 1.189 \text{ kg/m}^3$$

Also (h/P) = (6.42/14.867) = 0.432, which is less than 5.5, so the upper flowrate criterion is satisfied. Using tables, the expansibility factor is obtained using "(h/P)", "m" and "γ". 'γ' is the specific heat ratio, which is 1.4 for air.

Hence e = 0.995

An initial estimate of flowrate is made by assuming Zr =1:

$$W = 0.3012 \times 1 \times 0.995 \times \sqrt{(163.14 \times 1.189)}$$

$$= 4.174 \text{ kg/hr}$$

The Reynolds number can be calculated using equation 2, after evaluating the viscosity of the air at the upstream temperature (i.e. 24.9 degrees Centigrade). From tables:

$$\mu = 0.000183 \text{ g/cms}$$

Thus

$$Rd = ((3.54 \times 4.174)/(0.000183 \times 45.72 \times \sqrt{0.0193})$$

$$= 12712$$

From tables, Zr = 1.024

Hence

$$W = (4.174 \times 1.024)$$

$$= 4.274 \text{ kg/hr}$$

$$= 0.001187 \text{ kg/s}$$

A computer program was written to assist in these calculations. Results showed that the value of "(h/P)" was never greater than 5.5 and the Reynolds number never dropped below 10,000. All the tables referred to are contained in the British Standards (43).

APPENDIX 15

THE CALIBRATION OF THE THERMOCOUPLE TEMPERATURE MEASURING INSTRUMENT

A Fluke Datalogger was used to measure the thermocouple output voltages. The machine has a built-in reference junction and a dedicated microprocessor that enables it to display the thermocouple temperature.

The instrument was calibrated using an insulated flask, filled with water, whose temperature was measured with an accurate thermometer, calibrated by the British Standards Institution (Number 84916 BST 72). The water was measured at a temperature of 19.0 degrees Centigrade, whilst the converted Iron-Constantan thermocouple output displayed by the Datalogger was 18.7 degrees Centigrade. This means that the instrument underread temperatures measured with Iron-Constantan thermocouples by about 0.3 degrees Centigrade for temperatures in the vicinity of 20 degrees Centigrade. To correct for this, all the temperatures measured using this machine (and Iron-Constantan thermocouples) were adjusted upwards by 0.3 degrees Centigrade.

APPENDIX 16

THE MEASUREMENT OF RADIATION INTENSITY IN THE LABORATORY

The measurement of the radiation intensity incident on the absorber area of the model Baird-type solar collector was done in the following manner. The radiation intensity was measured with a solarimeter at six equispaced positions along the central, longitudinal axis of the model collector at the height of the black-netting cloth. This procedure was performed at the beginning and the end of each group of tests.

(a) Determination of the Radiation Intensity for the group of 10 tests:

Figures 51 and 52 show the output values of the solarimeter placed at the six equispaced points along the absorber. Simpson's rule (Spiegel - 53) states that the area under a curve may be expressed as follows:

$$\text{Area} = \frac{\Delta x}{3} \left(y_0 + y_n + \sum_{i=1}^{n-1} y_i.(3 + (-1)^{i+1}) \right)$$

where 'Δx' is an increment length and 'n' is an even number of increments.

This general form of the rule may be simplified and stated as:

$$\text{Area} = \frac{\Delta x}{3} \times ((y_0 + y_6) + 4.(y_1 + y_3 + y_5) + 2.(y_2 + y_4))$$

Inserting actual values for y_0, y_1 to y_6 obtained from Figure 51, allows the area under the curve to be calculated as:

Area = 40.1 = width x mean irradiation

= 6 x mean irradiation

Thus: Mean Irradiation (before tests) = 6.68 mV

The same procedure was followed using data from Figure 51, and the area under the curve was calculated as:

Area = 40.15 = width x mean irradiation

= 6 x mean irradiation

Thus

Mean Irradiation (after tests) = 6.69 mV

The solarimeter conversion factor is specified by the manufacturer as:

1 W/m = 0.0123 mV

Thus the radiation intensities before and after the tests were calculated as 543.1 and 543.9 Watts per square metre respectively. It was decided to use a value of 544 Watts per square metre as the average incident radiation value in calculations relating to the group of 10 tests.

(b) Determination of the Radiation Intensity for the group of 43 tests:

The radiation intensity for the group of 43 tests was measured and calculated in exactly the same manner as is outlined in Appendix 16(a). Data were obtained from Figure 52, and calculations show that radiation intensity before the tests was 853 Watts per square metre and after the tests was 851 Watts per square metre. The average value of 852 Watts per square metre was therefore used as the incident radiation value in all calculations relating to the group of 43 tests.

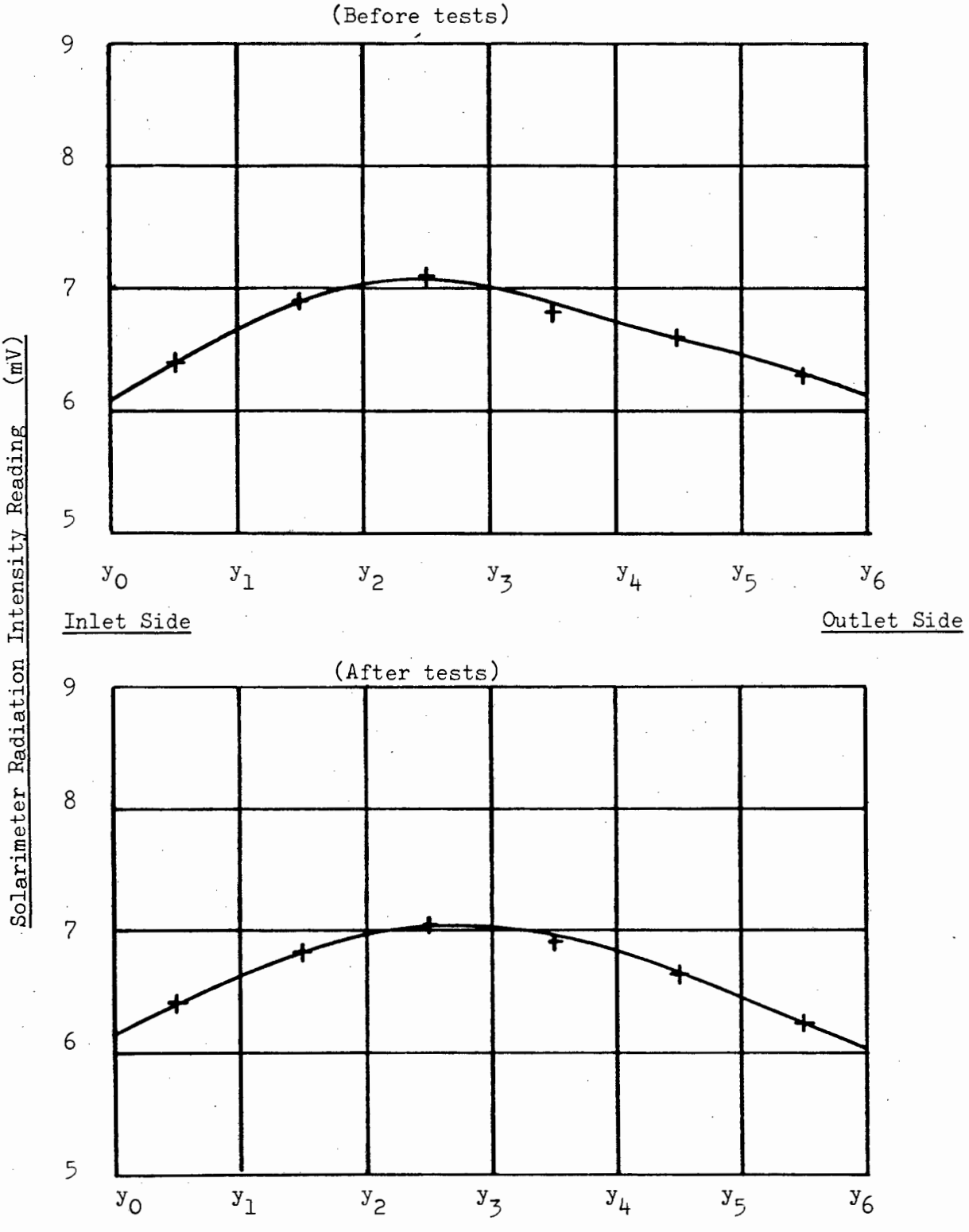

FIGURE 51 : THE RADIATION INTENSITY ON THE MODEL BAIRD-TYPE SOLAR COLLECTOR

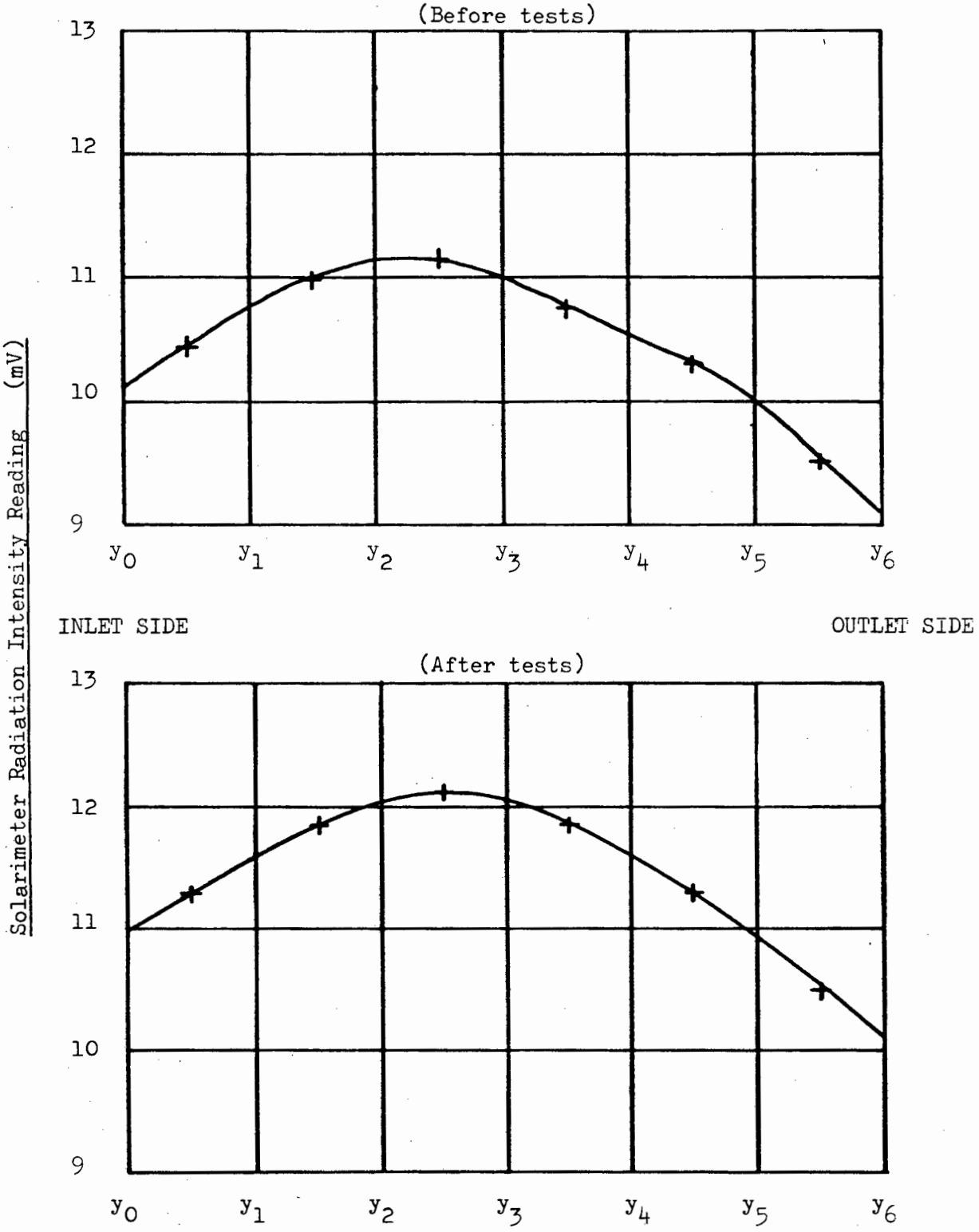

FIGURE 52 : THE RADIATION INTENSITY ON THE MODEL BAIRD-TYPE SOLAR COLLECTOR

APPENDIX 17

JANUARY AND JUNE AVERAGE SOLAR RADIATION DATA FOR CAPE TOWN

The solar radiation data used in this thesis to represent typical solar insolation values for January and June days in the Cape Peninsula were derived from South African Weather Bureau Data, collected over 11 years (circa 1956) at the Wingfield weather station. They are listed as Mean Hourly Values in the Weather Bureau publication (44), and were used to construct the graphs shown in Figures 53 and 54, from which the solar radiation data listed in Appendix 25 was obtained.

The time base in Figures 53 and 54 is Local Mean Time. To convert from Local Mean Time to South African Standard Time at Cape Town, consider the following calculation:

South African Standard Time is based on Longitude 30 degrees East.
Longitude at Cape Town is 18.5 degrees East.
The difference between these two Longitudes = 11.5 degrees.
Since the earth moves through 15 degrees of Longitude per hour, the time difference between the Longitudes is:

$(11.5/15) = 0.77$ hours

$= 46$ minutes

So, if the Local Mean Time at Cape Town is "X" hours, the South African Standard Time is "X + 0.77" hours.

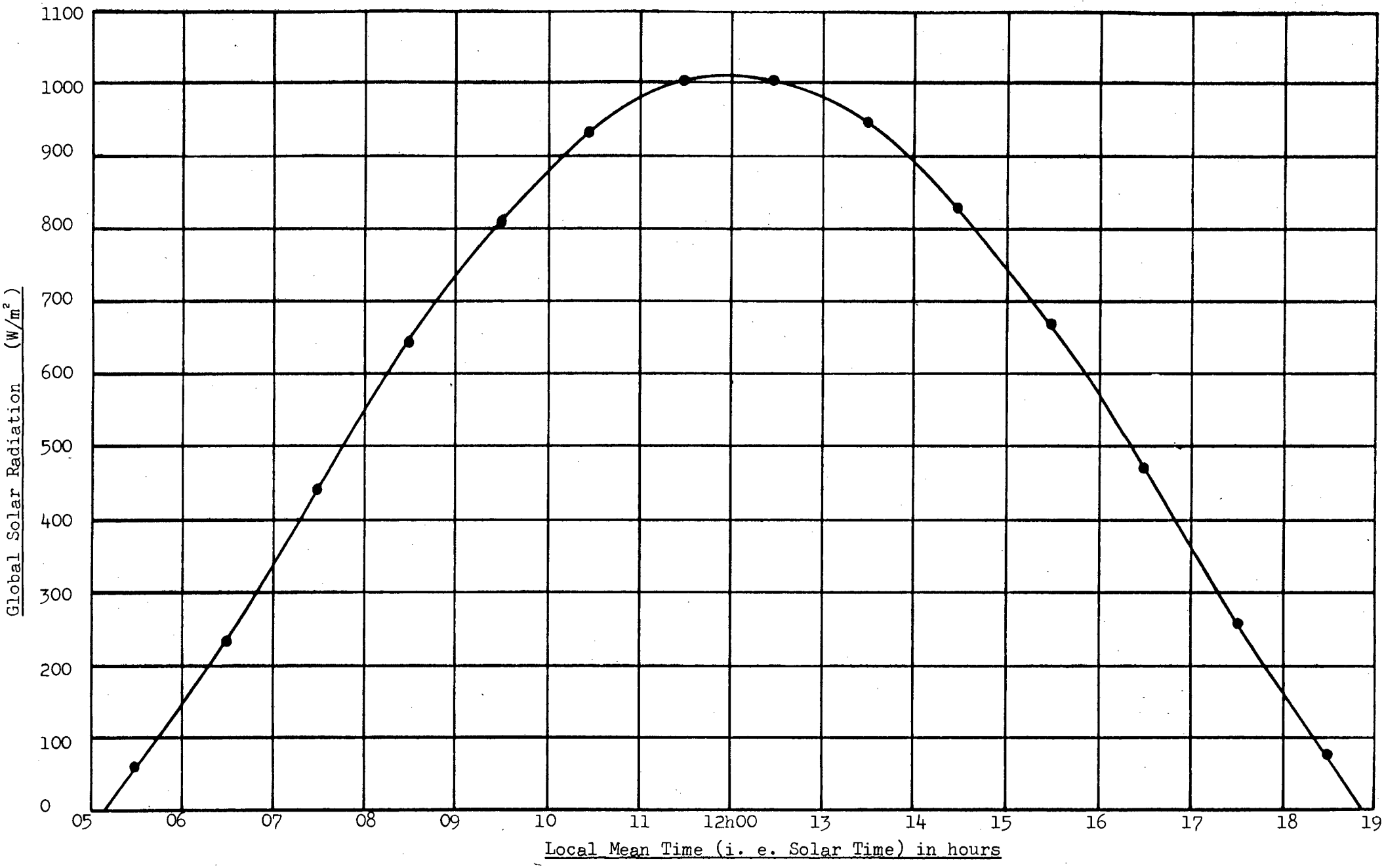

FIGURE 53 : GLOBAL SOLAR RADIATION DATA FOR A TYPICAL JANUARY DAY IN CAPE TOWN (South African Weather Bureau - 44)

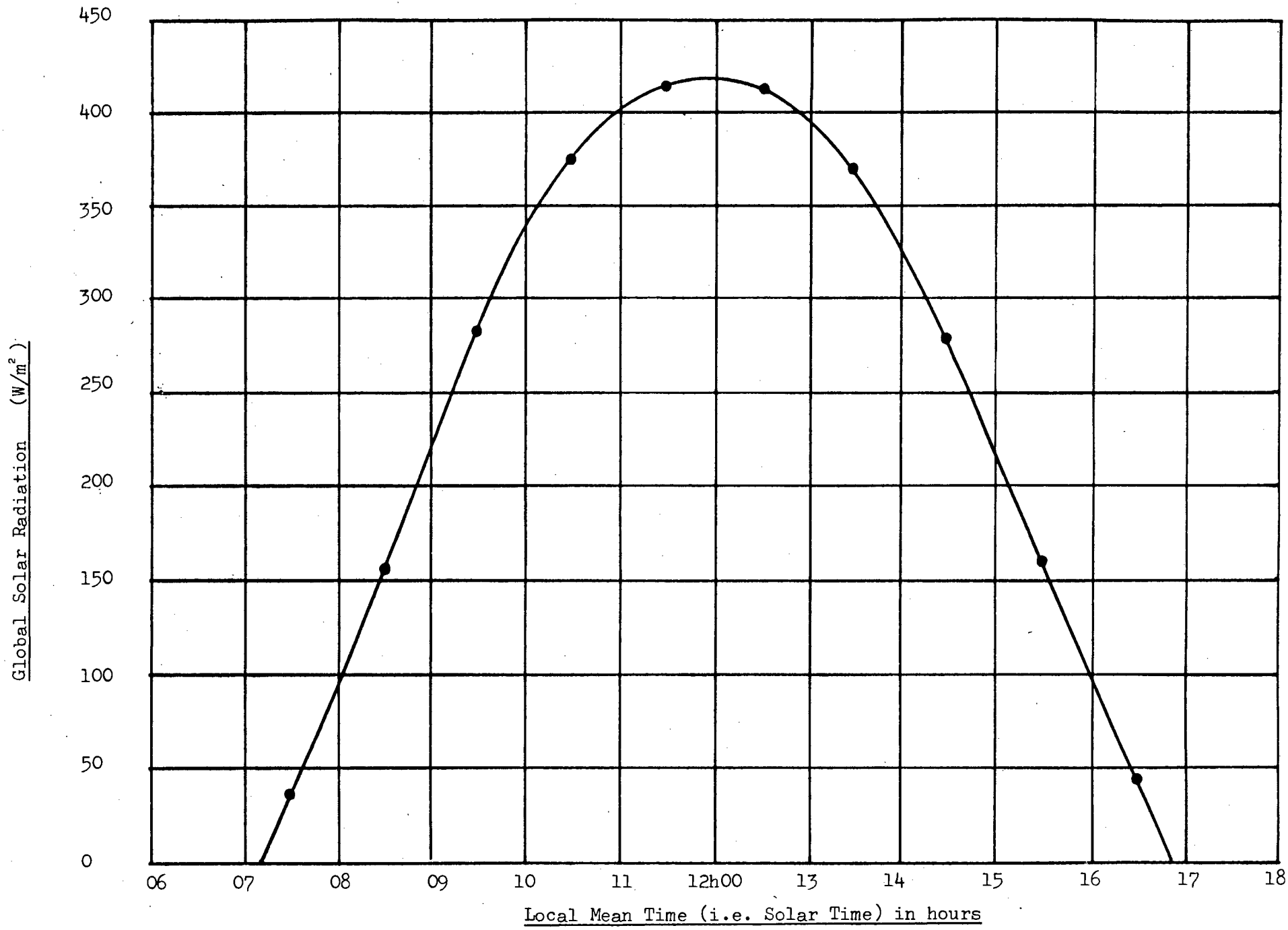

FIGURE 54 : GLOBAL SOLAR RADIATION DATA FOR A TYPICAL JUNE DAY IN CAPE TOWN (South African Weather Bureau - 44)

APPENDIX 18

THE VARIATION OF THE LABORATORY AMBIENT-AIR TEMPERATURE

The numerical values of the laboratory ambient-air temperature are listed with the experimental results in Appendix 19 and Appendix 21, and are shown in Chapter 5 in Figures 2 and 3.

From this data, the mean laboratory ambient-air temperature for the tests conducted with a radiation intensity of 852 Watts per square metre was calculated as 19.1 degrees Centigrade. The mean laboratory ambient-air temperature for the tests conducted with a radiation intensity of 544 Watts per square metre was 18.0 degrees Centigrade.

The following temperature frequency distribution table was constructed from this data:

Column A = Temperature band (degrees Centigrade)

Column B = The frequency or number of tests

Column C = Relative frequency (%)

Column D = The frequency or number of tests

Column E = Relative frequency (%)

A	B	C	D	E
	I = 852		I = 544	
17.0 - 17.5	-	-	1	10
17.5 - 18.0	2	4.7	3	30
18.0 - 18.5	8	18.6	6	60
18.5 - 19.0	12	27.9	-	-
19.0 - 19.5	14	32.6	-	-
19.5 - 20.0	1	2.3	-	-
20.0 - 20.5	2	4.7	-	-
20.5 - 21.0	4	9.3	-	-

An analysis of these results shows that 75 percent of the tests were conducted with a laboratory ambient-air temperature between 18.0 and 19.5 degrees Centigrade. Figures 55 and 56 show the above data graphically.

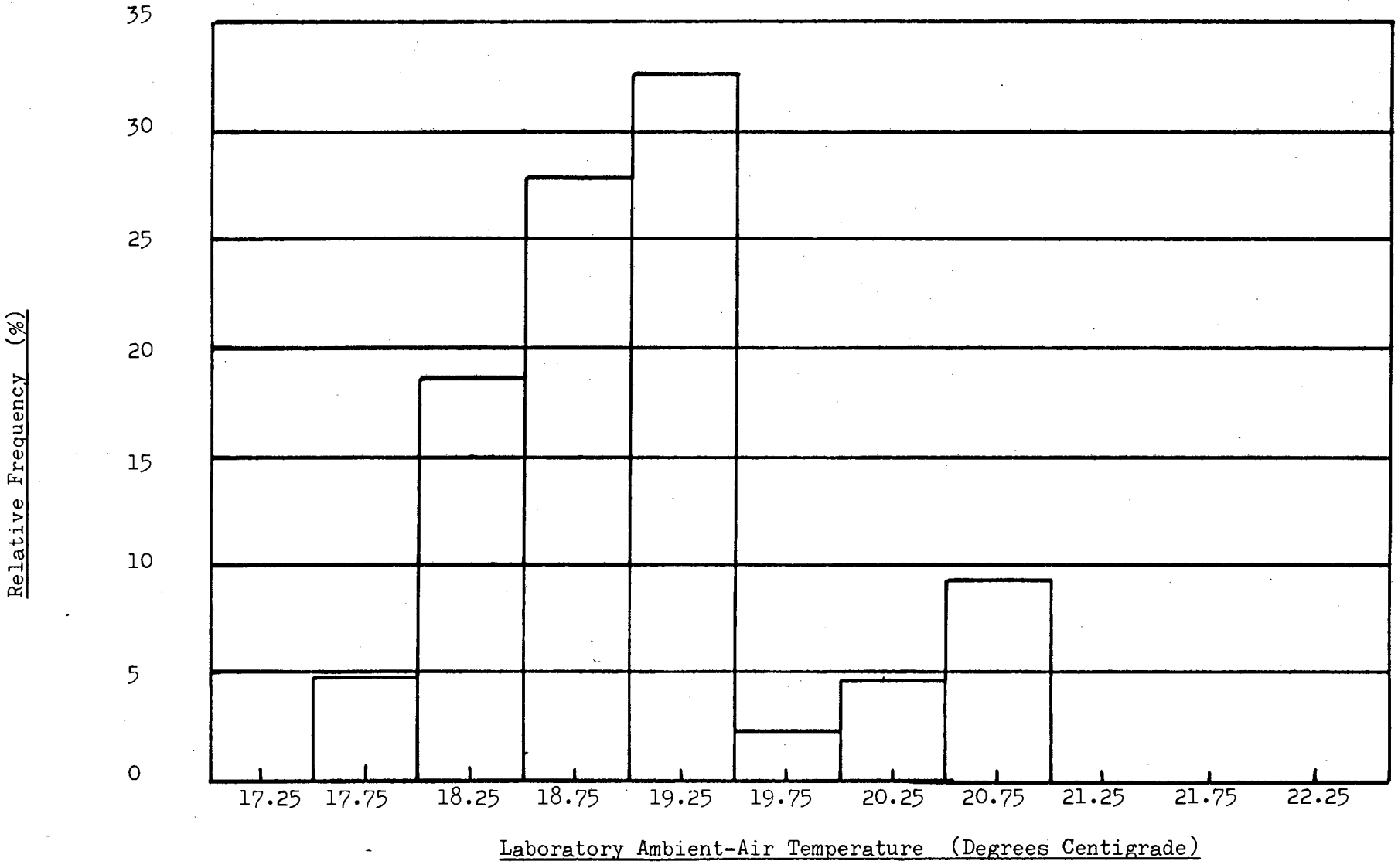

FIGURE 55: LABORATORY AMBIENT-AIR TEMPERATURE FREQUENCY DISTRIBUTION FOR THE TESTS WITH $I = 852\ W/m^2$

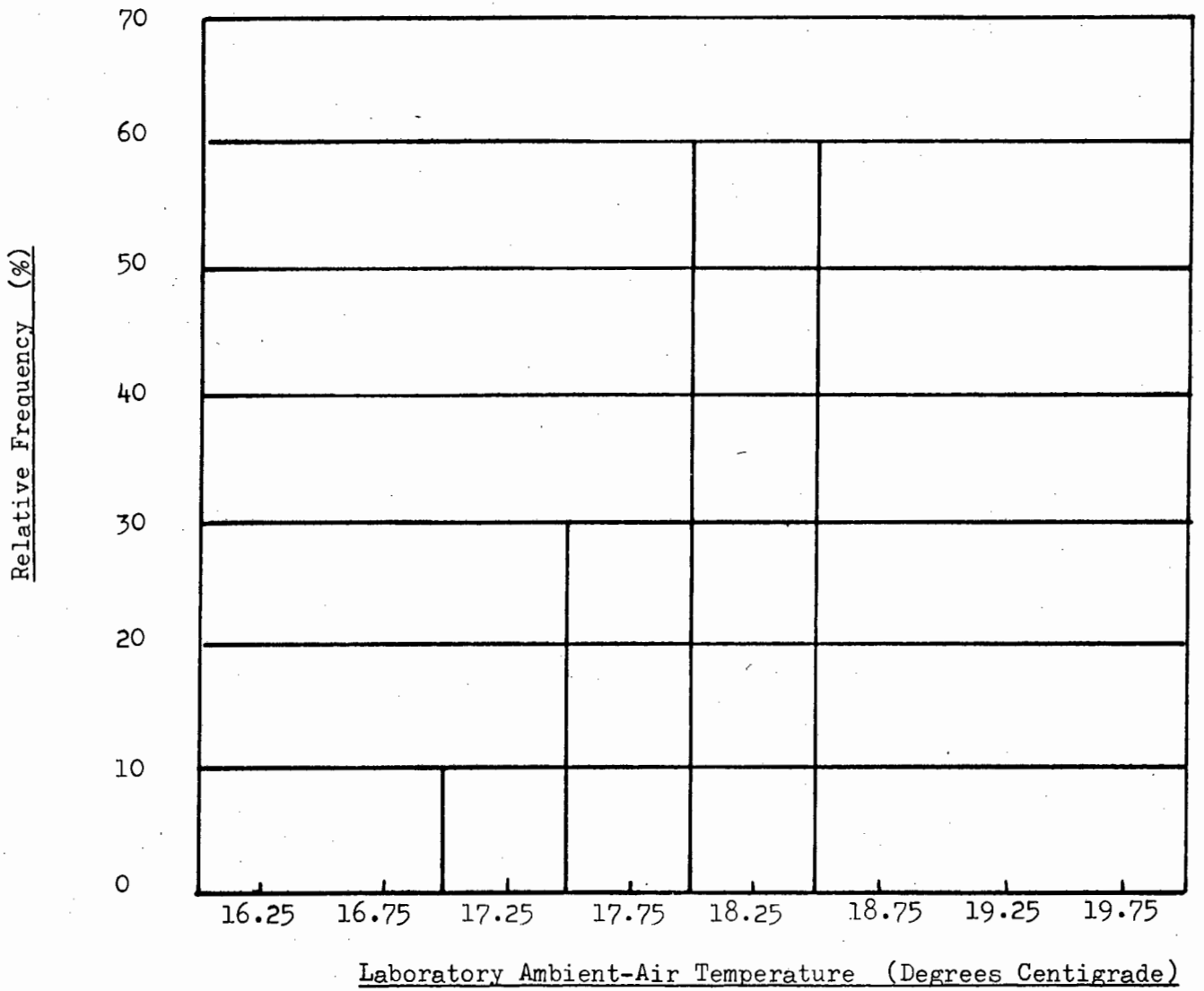

FIGURE 56 : LABORATORY AMBIENT-AIR TEMPERATURE FREQUENCY DISTRIBUTION FOR THE TESTS WITH I = 544 W/m^2

APPENDIX 19

THE FLAT-PLATE MODEL PREDICTED AND EXPERIMENTAL TEST DATA

The mean "predicted heat-gain error" of all the tests listed below was -7.6% with a corresponding standard deviation of 12.4%

19.1 The Results of Tests conducted at a Radiation Intensity of 852 Watts per square metre

Column A = Test Number

Column B = Air flowrate through the collector (for kg/s multiply 10^{-6})

Column C = Ambient-air temperature (degrees Centigrade)

Column D = Inlet-air temperature (degrees Centigrade)

Column E = Measured outlet-air temperature (degrees Centigrade)

Column F = Predicted outlet-air temperature (degrees Centigrade)

Column G = Error in predicted heat-gain (%)

Column H = Measured efficiency (%)

Column I = Predicted efficiency (%)

Column J = The Grashof-Reynolds free convection criterion

A	B	C	D	E	F	G	H	I	J
1	1299	18.3	22.4	33.4	33.4	0.3	37.1	37.2	0.0274
2	1798	18.3	23.4	32.4	31.3	-12.4	42.0	36.8	0.0132
3	2055	18.8	24.4	32.2	31.2	-12.5	41.6	36.4	0.0096

A	B	C	D	E	F	G	H	I	J
4	2515	18.8	25.7	31.9	31.1	-13.6	40.5	34.9	0.0059
5	3031	18.6	27.7	32.5	31.8	-15.2	37.8	32.0	0.0037
6	3604	18.0	29.7	33.2	32.7	-13.8	32.7	28.2	0.0024
7	3356	17.7	28.7	32.7	32.1	-15.8	34.8	29.3	0.0029
8	1489	17.7	22.1	31.9	31.7	-1.6	37.9	37.3	0.0204
9	1660	18.3	23.1	32.6	31.7	-9.6	40.9	37.0	0.0158
10	2317	18.8	25.0	31.9	31.0	-13.7	41.5	35.8	0.0072
11	2804	18.8	27.0	32.7	31.6	-19.8	41.5	33.2	0.0045
12	3451	19.4	29.8	33.9	33.2	-18.2	36.7	30.0	0.0027
13	0920	18.3	23.0	35.7	37.8	16.9	30.3	35.4	0.0564
14	3806	18.8	31.0	34.3	33.8	-16.2	32.6	27.3	0.0021
15	1095	18.3	22.3	34.6	35.2	5.3	35.0	36.8	0.0395
16	2942	18.8	27.4	32.6	31.7	-17.6	39.7	32.7	0.0040
17	3276	19.1	29.1	33.5	32.7	-18.0	37.4	30.7	0.0030
18	3192	19.4	28.7	33.4	32.5	-18.6	38.9	31.7	0.0033
19	2682	18.8	27.0	32.7	31.8	-16.3	39.7	33.2	0.0050
20	2199	20.0	25.7	32.6	32.1	-7.8	39.4	36.3	0.0081
21	1883	20.5	25.5	33.7	33.0	-8.0	40.1	36.9	0.0115
22	1510	20.5	24.7	35.0	34.2	-7.5	40.4	37.4	0.0190
23	1163	19.4	23.1	34.4	35.4	9.2	34.1	37.2	0.0343
24	3854	19.4	31.2	34.5	34.0	-15.6	33.0	27.9	0.0020
25	2262	18.3	24.3	30.8	30.4	-5.5	38.2	36.1	0.0077
26	3027	19.4	28.0	32.6	32.2	-9.6	36.1	32.7	0.0037
27	3513	19.4	29.9	33.6	33.2	-11.4	33.7	29.9	0.0026
28	1559	19.4	23.7	32.7	32.9	2.7	36.4	37.4	0.0180
29	1921	19.1	24.5	31.9	31.8	-1.1	36.9	36.5	0.0112
30	0981	18.3	22.2	33.8	36.5	23.7	29.5	36.5	0.0497
31	1325	18.8	22.9	33.0	33.7	7.2	34.7	37.2	0.0260
32	1774	18.8	24.0	32.2	32.0	-3.0	37.7	36.6	0.0135

A	B	C	D	E	F	G	H	I	J
33	2820	18.8	26.6	31.6	31.2	-7.6	36.6	33.8	0.0045
34	2487	19.4	25.8	31.8	31.3	-8.1	38.7	35.6	0.0061
35	3328	20.0	29.6	33.5	33.2	-7.4	33.7	31.2	0.0029
36	3684	20.5	31.3	34.7	34.4	-9.8	32.5	29.3	0.0022
37	2640	20.5	27.4	33.0	32.5	-9.1	38.4	34.9	0.0052
38	0881	19.4	23.6	35.7	39.2	29.2	27.7	35.7	0.0608
39	1187	18.8	22.6	33.2	34.7	14.0	32.7	37.2	0.0331
40	1085	19.4	23.1	34.5	36.2	15.3	32.1	37.0	0.0397
41	2166	19.7	25.5	32.5	31.9	-8.1	39.3	36.1	0.0084
42	3284	19.4	29.3	33.4	32.9	-11.9	34.9	30.8	0.0030
43	2353	19.4	25.8	32.2	31.6	-9.2	39.1	35.5	0.0069

In the following series of tests, the inlet-air temperature was held at 22.1 degrees Centigrade, the ambient-air temperature was held constant at 19.1 degrees Centigrade and :

Column A = Test Number

Column B = Air flowrate through the collector (for kg/s multiply 10^{-6})

Column C = Ambient-air temperature (degrees Centigrade)

Column D = Inlet-air temperature (degrees Centigrade)

Column E = Predicted outlet-air temperature (degrees Centigrade)

Column F = Predicted efficiency (%)

Column G = The Grashof-Reynolds free convection criterion

(a) Tg = Ta

A	B	C	D	E	F	G
1	.0500	19.1	22.1	48.8	34.6	0.1333
2	1000	19.1	22.1	36.6	37.7	0.0342
3	1500	19.1	22.1	32.1	39.0	0.0141
4	2000	19.1	22.1	29.8	39.8	0.0073
5	2500	19.1	22.1	28.3	40.3	0.0044
6	3000	19.1	22.1	27.3	40.7	0.0028
7	3500	19.1	22.1	26.6	41.0	0.0020
8	4000	19.1	22.1	26.1	41.2	0.0014

(b) Tg = Ta + 3

A	B	C	D	E	F	G
1	0500	19.1	22.1	49.5	35.5	0.1338
2	1500	19.1	22.1	32.4	40.1	0.0142
3	2500	19.1	22.1	28.5	41.5	0.0044
4	3500	19.1	22.1	26.7	42.2	0.0020

(c) Tg = Ta + 6

A	B	C	D	E	F	G
1	0500	19.1	22.1	50.1	36.4	0.1343
2	1500	19.1	22.1	32.7	41.2	0.0143
3	2500	19.1	22.1	28.7	42.7	0.0044
4	3500	19.1	22.1	26.9	43.5	0.0020

In the following series of tests, the inlet-air temperature was held at 31.3 degrees Centigrade, the ambient-air temperature was held constant at 19.1 degrees Centigrade and :

(a) Tg = Ta

A	B	C	D	E	F	G
1	0500	19.1	31.3	51.3	26.0	0.1291
2	1000	19.1	31.3	41.9	27.5	0.0313

A	B	C	D	E	F	G
3	1500	19.1	31.3	38.5	27.9	0.0127
4	2000	19.1	31.3	36.7	28.1	0.0065
5	2500	19.1	31.3	35.6	28.1	0.0039
6	3000	19.1	31.3	34.9	28.0	0.0025
7	3500	19.1	31.3	34.4	27.9	0.0017
8	4000	19.1	31.3	34.0	27.8	0.0013

(b) Tg = Ta + 3

A	B	C	D	E	F	G
1	0500	19.1	31.3	51.9	26.8	0.1295
2	1500	19.1	31.3	38.7	29.0	0.0128
3	2500	19.1	31.3	35.8	29.2	0.0039
4	3500	19.1	31.3	34.5	29.1	0.0018

(c) Tg = Ta + 6

A	B	C	D	E	F	G
1	0500	19.1	31.3	52.6	27.6	0.1299
2	1500	19.1	31.3	39.0	30.1	0.0129
3	2500	19.1	31.3	36.0	30.4	0.0039
4	3500	19.1	31.3	34.6	30.4	0.0018

19.2 The Results of Tests conducted at a Radiation Intensity of 544 Watts per square metre

Column A = Test Number

Column B = Air flowrate through the collector (for kg/s multiply 10^{-6})

Column C = Ambient-air temperature (degrees Centigrade)

Column D = Inlet-air temperature (degrees Centigrade)

Column E = Measured outlet-air temperature (degrees Centigrade)

Column F = Predicted outlet-air temperature (degrees Centigrade)

Column G = Error in predicted heat-gain (%)

Column H = Measured efficiency (%)

Column I = Predicted efficiency (%)

Column J = The Grashof-Reynolds free convection criterion

A	B	C	D	E	F	G	H	I	J
1	1032	17.7	20.6	28.3	29.3	12.6	32.3	36.4	0.0304
2	1396	18.0	21.6	28.1	27.9	-2.6	36.9	35.9	0.0157
3	1683	18.3	22.5	28.1	27.6	-8.2	38.3	35.2	0.0102
4	2030	17.7	23.1	27.8	27.1	-14.5	38.8	33.2	0.0066
5	2325	17.7	23.7	27.6	27.1	-13.0	36.9	32.1	0.0048
6	2651	17.2	24.6	28.0	27.3	-20.3	36.6	29.2	0.0035
7	3023	18.3	26.7	29.6	28.9	-24.6	35.6	26.9	0.0025
8	3307	18.3	28.0	30.4	29.8	-26.0	32.3	23.9	0.0020
9	3588	18.3	29.1	31.1	30.6	-27.4	29.2	21.2	0.0016
10	3887	18.3	30.3	31.9	31.4	-28.1	25.3	18.2	0.0013

In the following series of tests, the inlet-air temperature was held at 20.6 degrees Centigrade, the ambient-air temperature was held constant at 18.0 degrees Centigrade and :

Column A = Test Number

Column B = Air flowrate through the collector (for kg/s multiply 10^{-6})

Column C = Ambient-air temperature (degrees Centigrade)

Column D = Inlet-air temperature (degrees Centigrade)

Column E = Predicted outlet-air temperature (degrees Centigrade)

Column F = Predicted efficiency (%)

Column G = The Grashof-Reynolds free convection criterion

(a) Tg = Ta

A	B	C	D	E	F	G
1	0500	18.0	20.6	37.4	34.2	0.0939
2	1000	18.0	20.6	29.7	36.9	0.0233
3	1500	18.0	20.6	26.9	38.1	0.0095
4	2000	18.0	20.6	25.4	38.8	0.0049
5	2500	18.0	20.6	24.5	39.3	0.0029
6	3000	18.0	20.6	23.8	39.6	0.0019
7	3500	18.0	20.6	23.4	39.8	0.0013
8	4000	18.0	20.6	23.1	40.0	0.0009

(b) Tg = Ta + 3

A	B	C	D	E	F	G
1	0500	18.0	20.6	38.1	35.5	0.0945
2	1500	18.0	20.6	27.1	39.8	0.0096
3	2500	18.0	20.6	24.6	41.1	0.0029
4	3500	18.0	20.6	23.5	41.8	0.0013

(c) Tg = Ta + 6

A	B	C	D	E	F	G
1	0500	18.0	20.6	38.7	36.9	0.0952
2	1500	18.0	20.6	27.4	41.6	0.0097
3	2500	18.0	20.6	24.8	43.0	0.0030
4	3500	18.0	20.6	23.7	43.8	0.0013

In the following series of tests, the inlet-air temperature was held at 30.3 degrees Centigrade, the ambient-air temperature was held constant at 18.0 degrees Centigrade and :

(a) Tg = Ta

A	B	C	D	E	F	G
1	0500	18.0	30.3	40.2	20.2	0.0951
2	1000	18.0	30.3	35.3	20.5	0.0216

A	B	C	D	E	F	G
3	1500	18.0	30.3	33.6	20.2	0.0086
4	2000	18.0	30.3	32.7	19.8	0.0044
5	2500	18.0	30.3	32.2	19.4	0.0026
6	3000	18.0	30.3	31.9	19.0	0.0017
7	3500	18.0	30.3	31.6	18.7	0.0011
8	4000	18.0	30.3	31.4	18.3	0.0008

(b) $T_g = T_a + 3$

A	B	C	D	E	F	G
1	0500	18.0	30.3	40.9	21.5	0.0957
2	1500	18.0	30.3	33.9	21.9	0.0087
3	2500	18.0	30.3	32.4	21.2	0.0026
4	3500	18.0	30.3	31.7	20.5	0.0012

(c) $T_g = T_a + 6$

A	B	C	D	E	F	G
1	0500	18.0	30.3	41.5	22.8	0.0962
2	1500	18.0	30.3	34.2	23.5	0.0088
3	2500	18.0	30.3	32.6	23.0	0.0026
4	3500	18.0	30.3	31.9	22.5	0.0012

APPENDIX 20

DERIVATION OF THE COLLECTOR TUBE HEAT-TRANSFER COEFFICIENT

For fully developed flow in a tube subjected to a constant heat rate (i.e. uniform heat flux), the temperature versus length relationship of the fluid and wall can be illustrated as shown in Figure 57 (Kays - 42).

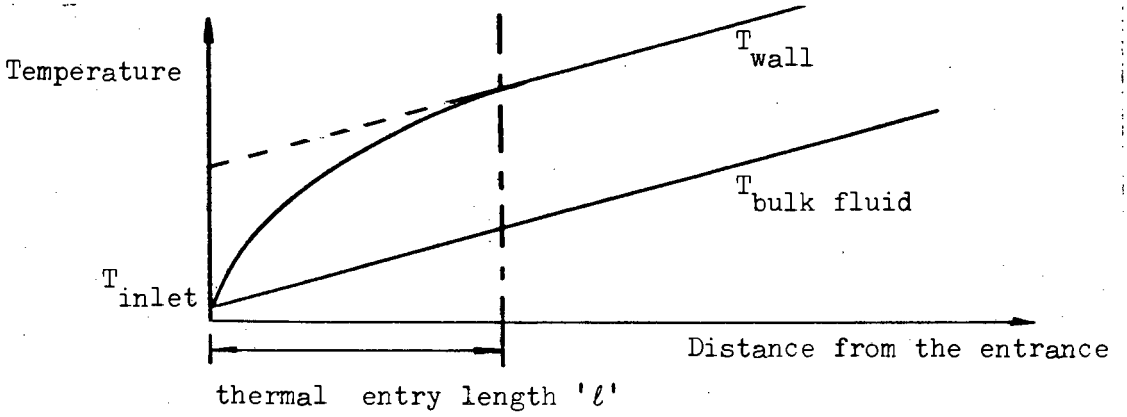

FIGURE 57 : TEMPERATURE VARIATIONS IN THE THERMAL ENTRY REGION OF A TUBE WITH CONSTANT HEAT-RATE PER UNIT OF TUBE LENGTH

For laminar, fully developed flow in a tube, the Nusselt number is constant, and for turbulent, fully developed tube flow the Nusselt number is a function of the Reynolds and the Prandtl numbers. In the case of laminar flow, if the heat rate from the wall to the fluid is constant and the wall temperature minus the bulk fluid temperature is constant, then the tube heat-transfer coefficient must be constant. In the case of turbulent flow, with air as the fluid, then over a small temperature range the Prandtl number can be regarded as constant. Thus for a given Reynolds number (which is constant for a constant mass-flowrate), the tube heat-transfer coefficient will remain constant since the difference of the wall and the bulk fluid temperature remains constant.

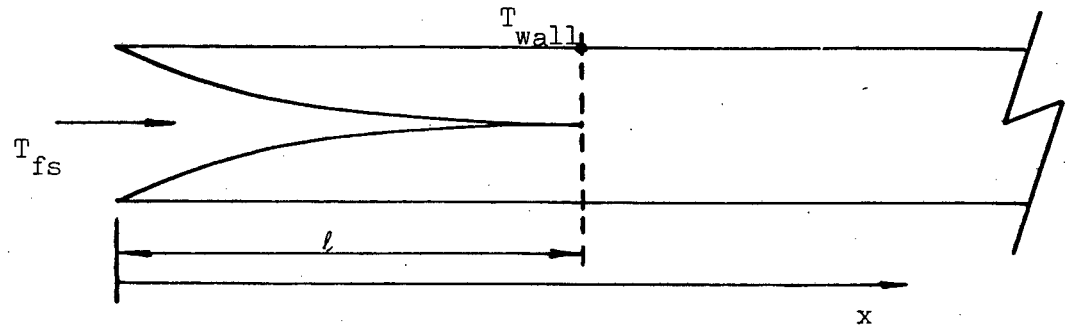

FIGURE 58: THE TRANSITION FROM DEVELOPING TO DEVELOPED FLOW

In the region where 'x' is less than 'ℓ', the flow in the section is developing. Let this be the area in which heat transfer considerations are based on the flat plate analogy. The flow of heat can be written as:

$$Q = h_{\text{flat plate}} \times \text{Area} \times (T_{\text{wall}} - T_{\text{free stream}}) \quad \ldots\ldots\ldots(1)$$

In the region where 'x' is more than 'ℓ', the flow in the section is developed. Let this be the area in which heat transfer considerations are based on tube flow. The flow of heat can be written as:

$$Q = h_{\text{tube}} \times \text{Area} \times (T_{\text{wall}} - T_{\text{bulk fluid}}) \quad \ldots\ldots\ldots\ldots\ldots(2)$$

Now at $x = \ell$ the heat flows are equal. Hence equation (1) and (2) can be equated and rearranged to form the following:

$$h_{\text{tube}} = h_{\substack{\text{flat plate} \\ (\text{at } x = \ell)}} \times \left[\frac{T_{\text{wall}} - T_{\text{free stream}}}{T_{\text{wall}} - T_{\text{bulk fluid}}} \right]_{x = \ell} \quad \ldots\ldots\ldots(3)$$

The value of the tube heat-transfer coefficient can therefore be worked out and remains constant for all 'x' larger than 'ℓ' by the reasoning discussed on the previous page.

APPENDIX 21

THE FLAT-PLATE/TUBE MODEL PREDICTED AND EXPERIMENTAL TEST DATA

The mean "predicted heat-gain error" of all the tests listed below was -11.8% with a corresponding standard deviation of 12.6%

21.1 The Results of Tests conducted at a Radiation Intensity of 852 Watts per square metre

Column A = Test Number

Column B = Air flowrate through the collector (for kg/s multiply 10^{-6})

Column C = Ambient-air temperature (degrees Centigrade)

Column D = Inlet-air temperature (degrees Centigrade)

Column E = Measured outlet-air temperature (degrees Centigrade)

Column F = Predicted outlet-air temperature (degrees Centigrade)

Column G = Error in predicted heat-gain (%)

Column H = Measured efficiency (%)

Column I = Predicted efficiency (%)

Column J = The Grashof-Reynolds free convection criterion

A	B	C	D	E	F	G	H	I	J
1	1299	18.3	22.4	33.4	33.1	-3.2	37.1	35.9	0.0209
2	1798	18.3	23.4	32.4	31.0	-15.9	42.0	35.3	0.0103
3	2055	18.8	24.4	32.2	30.9	-16.3	41.6	34.8	0.0074

A	B	C	D	E	F	G	H	I	J
4	2515	18.8	25.7	31.9	30.9	-16.7	40.5	33.7	0.0047
5	3031	18.6	27.7	32.5	31.6	-18.6	37.8	30.7	0.0031
6	3604	18.0	29.7	33.2	32.6	-18.5	32.7	26.7	0.0019
7	3356	17.7	28.7	32.7	31.9	-20.0	34.8	27.9	0.0024
8	1489	17.7	22.1	31.9	31.4	-5.5	37.9	35.8	0.0151
9	1660	18.3	23.1	32.6	31.3	-13.6	40.9	35.4	0.0115
10	2317	18.8	25.0	31.9	30.7	-17.7	41.5	34.1	0.0055
11	2804	18.8	27.0	32.7	31.4	-23.3	41.5	31.8	0.0036
12	3451	19.4	29.8	33.9	33.0	-22.0	36.7	28.6	0.0022
13	0920	18.3	23.0	35.7	37.1	10.8	30.3	33.6	0.0478
14	3806	18.8	31.0	34.3	33.6	-21.0	32.6	25.7	0.0017
15	1095	18.3	22.3	34.6	34.8	1.6	35.0	35.5	0.0315
16	2942	18.8	27.4	32.6	31.5	-20.8	39.7	31.5	0.0033
17	3276	19.1	29.1	33.5	32.5	-21.7	37.4	29.3	0.0025
18	3192	19.4	28.7	33.4	32.4	-22.0	38.9	30.4	0.0027
19	2682	18.8	27.0	32.7	31.6	-19.9	39.7	31.8	0.0040
20	2199	20.0	25.7	32.6	31.8	-11.8	39.4	34.7	0.0062
21	1883	20.5	25.5	33.7	32.8	-11.5	40.1	35.5	0.0090
22	1510	20.5	24.7	35.0	33.9	-10.8	40.4	36.0	0.0141
23	1163	19.4	23.1	34.4	35.1	6.3	34.1	36.3	0.0269
24	3854	19.4	31.2	34.5	33.8	-20.2	33.0	26.3	0.0016
25	2262	18.3	24.3	30.8	30.2	-9.8	38.2	34.4	0.0058
26	3027	19.4	28.0	32.6	32.0	-13.0	36.1	31.4	0.0031
27	3513	19.4	29.9	33.6	33.0	-15.6	33.7	28.5	0.0021
28	1559	19.4	23.7	32.7	32.6	-1.2	36.4	36.0	0.0132
29	1921	19.1	24.5	31.9	31.5	-5.2	36.9	35.0	0.0087
30	0981	18.3	22.2	33.8	36.1	19.6	29.5	35.3	0.0410
31	1325	18.8	22.9	33.0	33.3	3.5	34.7	35.9	0.0198
32	1774	18.8	24.0	32.2	31.6	-7.0	37.7	35.1	0.0106

A	B	C	D	E	F	G	H	I	J
33	2820	18.8	26.6	31.6	31.0	-11.3	36.6	32.4	0.0035
34	2487	19.4	25.8	31.8	31.1	-11.2	38.7	34.4	0.0049
35	3328	20.0	29.6	33.5	33.1	-11.4	33.7	29.8	0.0024
36	3684	20.5	31.3	34.7	34.2	-14.3	32.5	27.9	0.0018
37	2640	20.5	27.4	33.0	32.3	-12.3	38.4	33.6	0.0041
38	0881	19.4	23.6	35.7	38.6	23.8	27.7	34.2	0.0523
39	1187	18.8	22.6	33.2	34.3	10.8	32.7	36.2	0.0258
40	1085	19.4	23.1	34.5	35.9	12.2	32.1	36.0	0.0318
41	2166	19.7	25.5	32.5	31.6	-12.2	39.3	34.6	0.0064
42	3284	19.4	29.3	33.4	32.8	-15.8	34.9	29.4	0.0025
43	2353	19.4	25.8	32.2	31.3	-13.5	39.1	33.8	0.0052

In the following series of tests, the inlet-air temperature was held at 22.1 degrees Centigrade, the ambient-air temperature was held constant at 19.1 degrees Centigrade and :

Column A = Test Number

Column B = Air flowrate through the collector (for kg/s multiply 10^{-6})

Column C = Ambient-air temperature (degrees Centigrade)

Column D = Inlet-air temperature (degrees Centigrade)

Column E = Predicted outlet-air temperature (degrees Centigrade)

Column F = Predicted efficiency (%)

Column G = The Grashof-Reynolds free convection criterion

(a) Tg = Ta

A	B	C	D	E	F	G
1	0500	19.1	22.1	47.0	32.3	0.1271
2	1000	19.1	22.1	35.9	35.7	0.0245
3	1500	19.1	22.1	32.0	38.6	0.0114
4	2000	19.1	22.1	29.7	39.3	0.0057
5	2500	19.1	22.1	28.2	39.7	0.0035
6	3500	19.1	22.1	26.6	40.6	0.0017

In the following series of tests, the inlet-air temperature was held at 31.3 degrees Centigrade, the ambient-air temperature was held constant at 19.1 degrees Centigrade and:

(a) Tg = Ta

A	B	C	D	E	F	G
1	0500	19.1	31.3	45.9	19.0	0.1148
2	1000	19.1	31.3	39.5	21.4	0.0213
3	1500	19.1	31.3	37.6	24.7	0.0099
4	2000	19.1	31.3	36.1	24.9	0.0049
5	2500	19.1	31.3	35.2	25.3	0.0030
6	3000	19.1	31.3	34.5	25.3	0.0019
7	3500	19.1	31.3	34.2	26.2	0.0015
8	4000	19.1	31.3	33.8	26.1	0.0010

21.2 The Results of Tests conducted at a Radiation Intensity of 544 Watts per square metre

Column A = Test Number

Column B = Air flowrate through the collector (for kg/s multiply 10^{-6})

Column C = Ambient-air temperature (degrees Centigrade)

Column D = Inlet-air temperature (degrees Centigrade)

Column E = Measured outlet-air temperature (degrees Centigrade)

Column F = Predicted outlet-air temperature (degrees Centigrade)

Column G = Error in predicted heat-gain (%)

Column H = Measured efficiency (%)

Column I = Predicted efficiency (%)

Column J = The Grashof-Reynolds free convection criterion

A	B	C	D	E	F	G	H	I	J
1	1032	17.7	20.6	28.3	28.9	7.8	32.3	34.8	0.0243
2	1396	18.0	21.6	28.1	27.6	-8.0	36.9	33.9	0.0116
3	1683	18.3	22.5	28.1	27.3	-13.8	38.3	33.0	0.0072
4	2030	17.7	23.1	27.8	26.9	-19.9	38.8	31.0	0.0050
5	2325	17.7	23.7	27.6	26.9	-19.0	36.9	29.9	0.0035
6	2651	17.2	24.6	28.0	27.1	-25.2	36.6	27.4	0.0027
7	3023	18.3	26.7	29.6	28.8	-29.3	35.6	25.2	0.0020
8	3307	18.3	28.0	30.4	29.6	-31.7	32.3	22.0	0.0016
9	3588	18.3	29.1	31.1	30.4	-34.2	29.2	19.2	0.0013
10	3887	18.3	30.3	31.9	31.3	-36.7	25.3	16.0	0.0010

In the following series of tests, the inlet-air temperature was held at 20.6 degrees Centigrade, the ambient-air temperature was held constant at 18.0 degrees Centigrade and :

Column A = Test Number

Column B = Air flowrate through the collector (for kg/s multiply 10^{-6})

Column C = Ambient-air temperature (degrees Centigrade)

Column D = Inlet-air temperature (degrees Centigrade)

Column E = Predicted outlet-air temperature (degrees Centigrade)

Column F = Predicted efficiency (%)

Column G = The Grashof-Reynolds free convection criterion

(a) Tg = Ta

A	B	C	D	E	F	G
1	0500	18.0	20.6	35.6	30.4	0.0868
2	1000	18.0	20.6	28.9	33.8	0.0164
3	1500	18.0	20.6	26.7	37.0	0.0076
4	2000	18.0	20.6	25.2	37.7	0.0038
5	2500	18.0	20.6	24.4	38.2	0.0023
6	3000	18.0	20.6	23.8	38.5	0.0015
7	3500	18.0	20.6	23.4	39.2	0.0011
8	4000	18.0	20.6	23.0	39.4	0.0008

In the following series of tests, the inlet-air temperature was held at 30.3 degrees Centigrade, the ambient-air temperature was held constant at 18.0 degrees Centigrade and :

(a) Tg = Ta

A	B	C	D	E	F	G
1	0500	18.0	30.3	36.6	12.9	0.0735
2	1000	18.0	30.3	33.6	13.4	0.0133
3	1500	18.0	30.3	33.0	16.2	0.0063
4	2000	18.0	30.3	32.2	15.8	0.0031
5	2500	18.0	30.3	31.9	15.8	0.0019
6	3000	18.0	30.3	31.6	15.4	0.0012
7	3500	18.0	30.3	31.4	16.3	0.0009
8	4000	18.0	30.3	31.3	15.9	0.0007

APPENDIX 22

JANUARY AND JUNE AVERAGE AMBIENT-AIR TEMPERATURES IN CAPE TOWN

The ambient-air temperatures used in this thesis to represent typical temperatures for January and June days in the Cape Peninsula are derived from South African Weather Bureau Data, collected over 17 years (circa 1940) at the Wingfield weather station. They are listed as Mean Hourly Values in the Weather Bureau publication (45). These values were used to construct the graphs shown in Figures 59 and 60, from which the ambient-air temperature data listed in Appendix 25 was obtained.

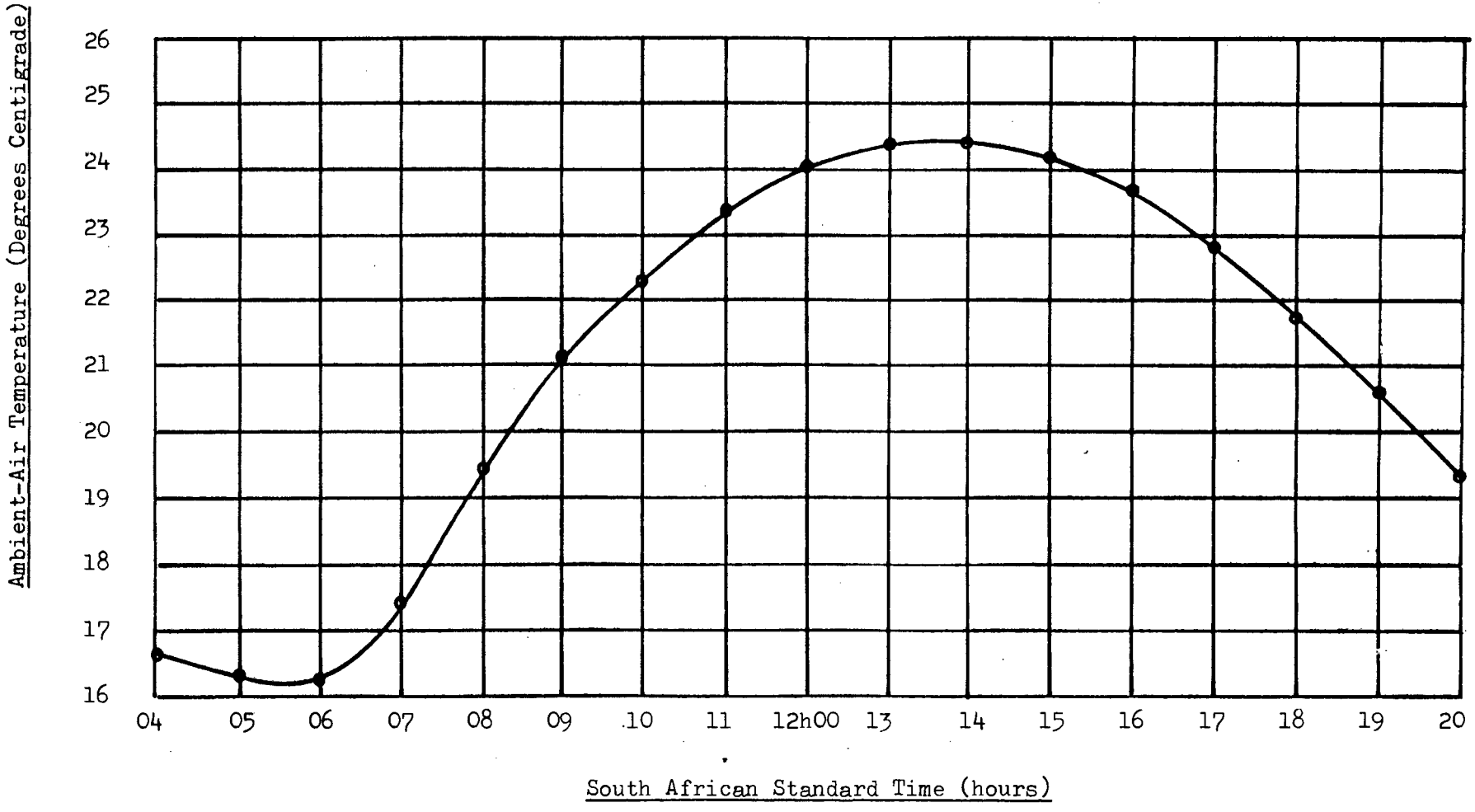

FIGURE 59 : AVERAGE AMBIENT-AIR TEMPERATURE DATA FOR A TYPICAL JANUARY DAY IN CAPE TOWN (S. A. Weather Bureau - 45)

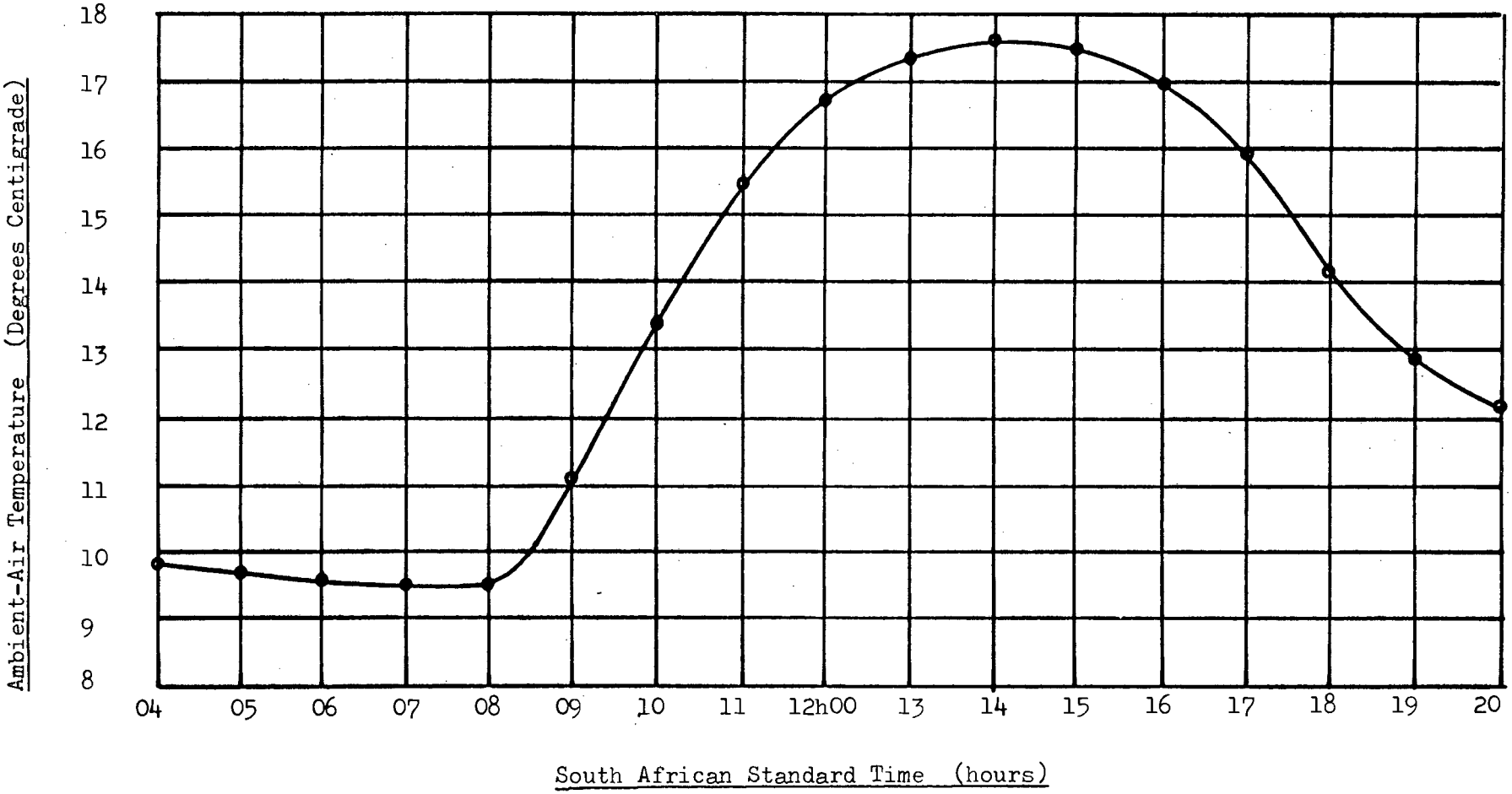

FIGURE 60 : AVERAGE AMBIENT-AIR TEMPERATURE DATA FOR A TYPICAL JUNE DAY IN CAPE TOWN (S. A. Weather Bureau - 45)

APPENDIX 23

JANUARY AND JUNE AVERAGE GROUND TEMPERATURES IN STELLENBOSCH

The ground temperature data used in this thesis comes from a study on the ground temperatures in a Stellenbosch orchard, conducted by Malherbe (46). The observations were done over a two year period circa 1930. Temperatures were only measured for the months January and July. Since no other ground temperature data were available, the July values were used to approximate the June values required for the predictions in this thesis. The average ground temperatures are shown in Figure 61, and are listed in Appendix 25.

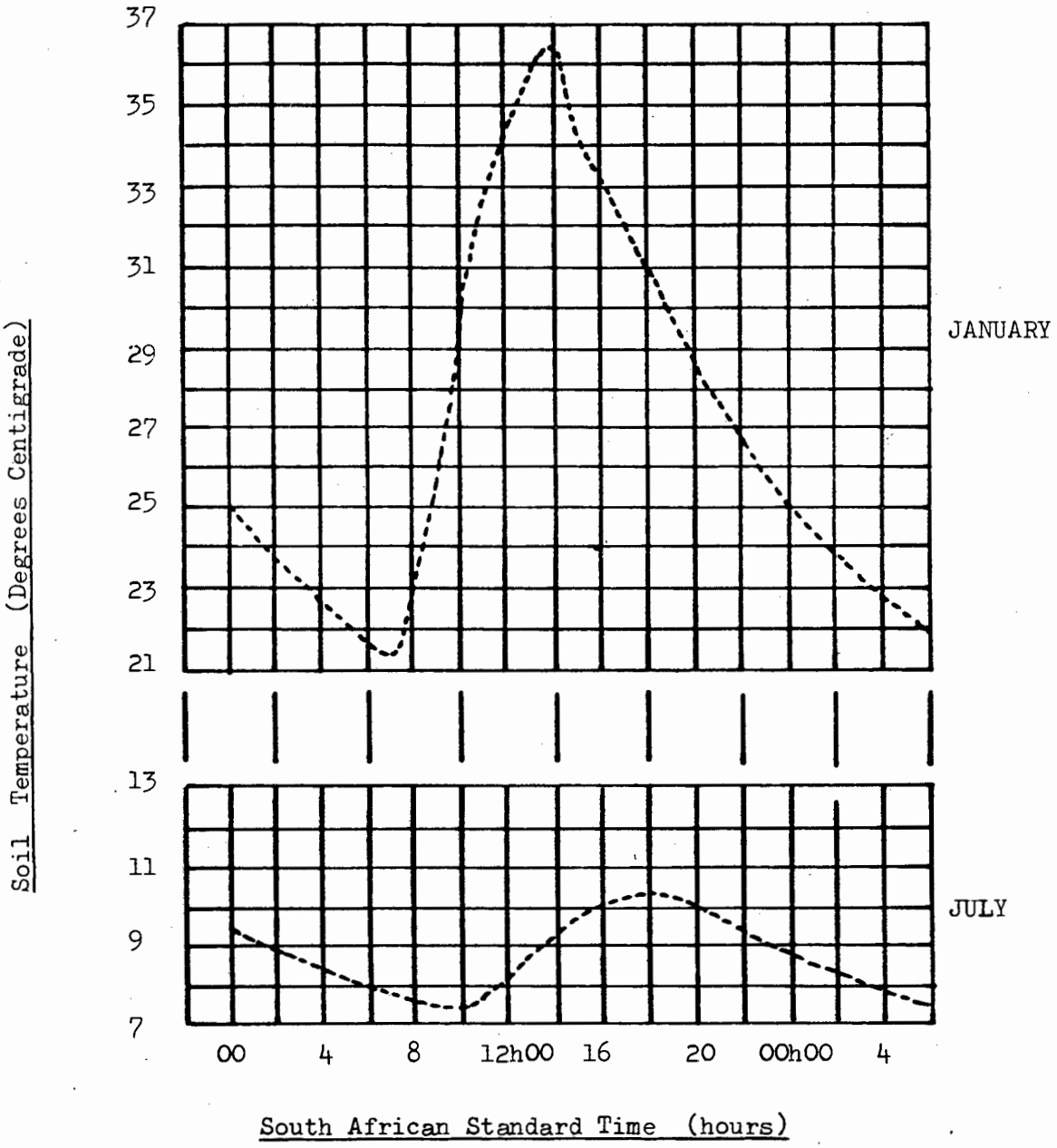

FIGURE 61: THE AVERAGE SOIL TEMPERATURE AT A DEPTH OF 75mm IN AN ORCHARD IN STELLENBOSCH (Malherbe - 46)

APPENDIX 24

THE CALCULATION OF PRESSURE-DROP ACROSS A ROCK-BED

The following calculation serves as a guide to establish the power requirements for a fan that is capable of driving the air at the prescribed flowrate through the collector cum rock-bed system. Only the pressure drop across the rock bed is considered.

An approximate rock-bed dimension needs to be defined. Working on a January cumulative heat gain of 2600 MJ, and assuming a hundred percent air-to-rock heat transfer it is possible to calculate the mass of rock required for a rock-bed temperature rise of 8 degrees Centigrade using the following equation:

$$Q = M_{rock} . C_p . \Delta T \quad \ldots\ldots\ldots\ldots\ldots\ldots\ldots\ldots\ldots\ldots (1)$$

Lunde (58) contains the following values for rock:

$C_p = 837$ J/kg . °C

$\rho = 1600$ kg/m^3 (this is an effective density for rocks of diameter equal to 0.01 metres)

Inserting the relevant values in (1):

$$M_{rock} = \frac{2600 \times 10^6}{837 \times 8} \approx 310\,000 \text{ kg}$$

Thus the volume of rock is:

Volume = 310 000 / 1600 $\approx$ 200m^3 $\approx$ 7000ft^3

A possible rock-bed configuration is thus (30 × 90 ×2.5) ft.

The flowrate is 10 kg/s ≈18000 cubic feet per minute. Duffie and Beckman (17) recommend that the bed be charged by blowing the air downwards, in which case the superficial velocity is:

Superficial velocity = 18000 / (90 × 30) ≈ 6.7cfm/ft^2

Close (59) contains figures that indicate that these conditions will result in a pressure drop of ≈ 5 mm of water across the rock-bed.

After a discussion with Professor Stegen (60), it was decided that the choice of a forward curved centrifugal fan would most closely match the low pressure, high volume requirement. The performance of a forward curved centrifugal fan manufactured by the Donkin company (61) is shown in Figure 62 . It was used to deduce the fan power requirements listed below:

JANUARY		JUNE	
10 kg/s ≈ 17660 cfm		7 kg/s ≈ 12362 cfm	
Static Pressure head (inches of water)	Power (Watts)	Static Pressure head (inches of water)	Power (Watts)
1	4100	1	2421
2	6700	2	5215
3	10450	3	8195

This data was used to evaluate the fan power requirements that are shown in Chapter 5 in Figures 16 and 18.

Forward Curved Centrifugal fan

SIZE No. 39/1·0 SINGLE INLET

Maximum Speed:-

Discharge Area 9·70 ft.²

Class I 490 r.p.m.

Impeller Circumference 10·2 ft.

Air Density 0·075 lb/ft.³

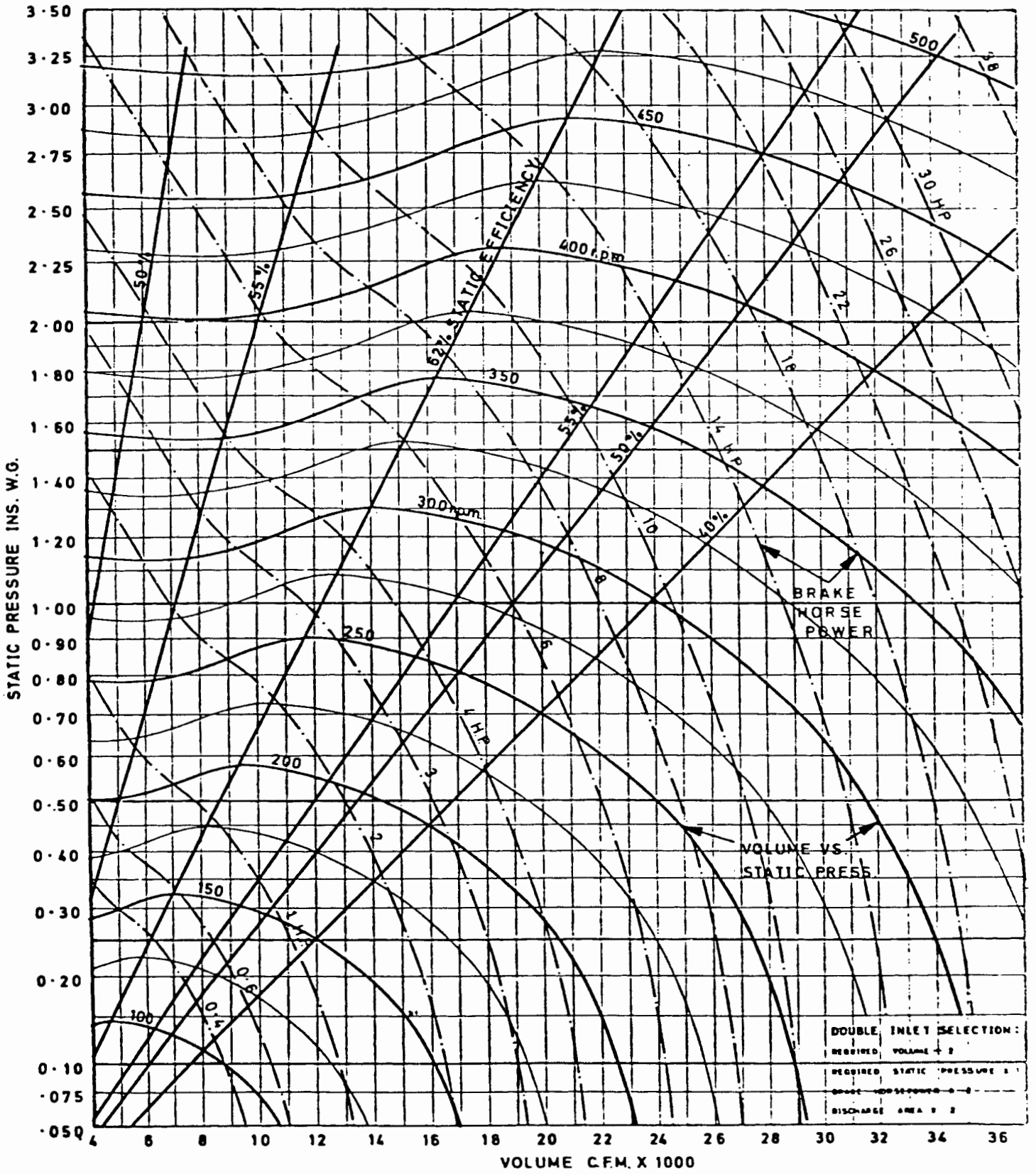

FIGURE 62: THE PERFORMANCE OF A FORWARD CURVED CENTRIFUGAL FAN

APPENDIX 25

THE LIFE-SIZE BAIRD-TYPE SOLAR COLLECTOR PERFORMANCE PREDICTIONS

These results are calculated for a Baird-type solar collector of dimensions as indicated in Appendix 12. In both 25.1 and 25.2 it has been assumed that there is zero windspeed.

Column A = Test Start Time (South African Standard Time in hours)

Column B = Incident Radiation (Watts per square metre)

Column C = Ground temperature (degrees Centigrade)

Column D = Inlet-air temperature (degrees Centigrade)

Column E = Predicted outlet-air temperature (degrees Centigrade)

Column F = Predicted efficiency (percent)

Column G = Cumulative total heat-gain (MJ)

Column H = The Grashof-Reynolds free convection criterion

25.1 The Results of Predictions of Collector Performance for a typical January day in the Cape Peninsula

The air flowrate through the collector was held constant at 10 kg/s.

A	B	C	D	E	F	G	H
6.0	7	21.6	16.2	16.2	8.1	0.08	0.0073
6.2	44	21.6	16.3	16.5	21.1	1.41	0.0186
6.4	75	21.6	16.5	16.9	28.6	4.47	0.0403
6.6	110	21.4	16.7	17.5	35.5	10.03	0.0752
6.8	143	21.4	17.0	18.1	40.4	18.27	0.1157
7.0	176	21.5	17.4	18.9	42.9	29.04	0.1542
7.2	214	21.7	17.7	19.6	44.2	42.52	0.1938
7.4	254	22.0	18.1	20.4	44.4	58.58	0.2329
7.6	294	22.3	18.6	21.1	43.8	76.96	0.2668
7.8	335	22.5	19.0	21.9	43.5	97.73	0.3005
8.0	376	23.0	19.4	22.6	42.9	120.72	0.3353
8.2	417	23.5	19.7	23.3	42.8	146.15	0.3690
8.4	458	24.0	20.1	23.9	42.3	173.80	0.4026
8.6	500	24.5	20.5	24.6	42.1	203.81	0.4353
8.8	540	25.0	20.8	25.3	41.9	236.05	0.4663
9.0	579	25.5	21.1	25.9	41.7	270.47	0.4960
9.2	628	26.3	21.3	26.5	41.7	307.79	0.5343
9.4	657	27.1	21.6	27.0	41.7	346.85	0.5556
9.6	696	27.9	21.8	27.5	41.8	388.33	0.5848
9.8	733	28.7	22.1	28.1	41.7	431.95	0.6114

A	B	C	D	E	F	G	H
10.0	764	29.5	22.3	28.6	41.9	477.55	0.6337
10.2	795	30.1	22.5	29.0	41.8	524.97	0.6553
10.4	822	30.7	22.8	29.5	41.8	573.92	0.6734
10.6	851	31.3	23.0	30.0	41.9	624.70	0.6928
10.8	875	31.9	23.1	30.4	41.9	677.00	0.7084
11.0	901	32.4	23.3	30.7	41.9	730.76	0.7262
11.2	924	32.8	23.5	31.1	41.7	785.73	0.7404
11.4	944	33.1	23.7	31.4	41.7	841.86	0.7520
11.6	962	33.4	23.8	31.7	41.7	899.06	0.7634
11.8	977	33.7	24.0	32.0	41.7	957.16	0.7721
12.0	991	34.0	24.1	32.2	41.7	1016.11	0.7800
12.2	1000	34.3	24.1	32.4	41.8	1075.69	0.7859
12.4	1006	34.6	24.2	32.5	41.9	1135.73	0.7899
12.6	1012	34.9	24.3	32.6	41.9	1196.16	0.7931
12.8	1013	35.2	24.4	32.7	42.0	1256.80	0.7939
13.0	1012	35.5	24.4	32.8	42.1	1317.51	0.7933
13.2	1007	35.7	24.5	32.8	42.1	1378.01	0.7899
13.4	1003	35.9	24.5	32.8	42.2	1438.39	0.7878
13.6	994	36.0	24.5	32.7	42.3	1498.32	0.7822
13.8	986	36.2	24.5	32.7	42.4	1557.90	0.7775
14.0	975	36.4	24.4	32.6	42.5	1617.04	0.7715
14.2	961	36.0	24.4	32.4	42.5	1675.25	0.7612
14.4	944	35.6	24.4	32.2	42.4	1732.33	0.7497
14.6	925	35.3	24.3	32.0	42.5	1788.42	0.7365
14.8	903	34.9	24.2	31.8	42.6	1843.20	0.7215
15.0	878	34.5	24.2	31.5	42.5	1896.40	0.7043
15.2	850	34.3	24.1	31.2	42.6	1947.97	0.6861
15.4	823	34.0	24.0	30.9	42.8	1998.23	0.6673

A	B	C	D	E	F	G	H
15.6	794	33.8	24.0	30.7	42.9	2046.79	0.6474
15.8	763	33.5	23.8	30.3	43.1	2093.67	0.6263
16.0	730	33.3	23.7	29.9	43.3	2138.73	0.6032
16.2	695	33.0	23.6	29.6	43.7	2181.99	0.5780
16.4	660	32.8	23.4	29.1	43.9	2223.33	0.5540
16.6	622	32.5	23.3	28.7	44.2	2262.53	0.5265
16.8	584	32.3	23.0	28.2	44.7	2299.75	0.4992
17.0	544	32.0	22.9	27.7	45.2	2334.79	0.4690
17.2	501	31.8	22.7	27.2	45.8	2367.50	0.4368
17.4	460	31.6	22.5	26.7	46.6	2398.03	0.4055
17.6	417	31.4	22.3	26.1	47.5	2426.28	0.3722
17.8	376	31.2	22.0	25.6	48.5	2452.27	0.3399
18.0	332	31.0	21.8	25.0	49.5	2475.72	0.3041
18.2	291	30.8	21.5	24.5	50.9	2496.82	0.2704
18.4	245	30.6	21.3	23.8	51.7	2514.87	0.2274
18.6	206	30.4	21.1	23.2	50.7	2529.75	0.1837
18.8	167	30.2	20.9	22.5	48.6	2541.32	0.1369
19.0	131	30.0	20.6	21.8	45.0	2549.72	0.0918
19.2	94	29.8	20.4	21.2	43.4	2555.54	0.0586
19.4	54	29.5	20.1	20.6	47.9	2559.23	0.0334
19.6	16	29.3	19.8	20.1	92.2	2561.33	0.0202

25.2 The Results of Predictions of Collector Performance for a typical June day in the Cape Peninsula

The air flowrate through the collector was held constant at 7 kg/s.

A	B	C	D	E	F	G	H
8.8	93	7.5	10.6	10.8	5.3	0.71	0.0838
9.0	117	7.5	11.1	11.5	11.3	2.59	0.1244
9.2	143	7.5	11.6	12.4	18.9	6.45	0.2016
9.4	166	7.5	12.0	13.0	22.2	11.71	0.2545
9.6	192	7.5	12.5	13.9	25.9	18.81	0.3255
9.8	220	7.5	12.9	14.6	27.9	27.55	0.3864
10.0	247	7.5	13.4	15.5	30.1	38.16	0.4577
10.2	272	7.5	13.8	16.2	32.0	50.57	0.5304
10.4	294	7.6	14.2	16.9	32.3	64.10	0.5724
10.6	316	7.6	14.6	17.6	33.3	79.08	0.6278
10.8	335	7.7	15.0	18.1	33.3	95.00	0.6633
11.0	352	7.7	15.4	18.7	33.2	111.67	0.6935
11.2	368	7.8	15.7	19.2	33.4	129.22	0.7224
11.4	380	7.9	16.0	19.6	33.3	147.28	0.7438
11.6	392	7.9	16.3	20.0	33.4	165.93	0.7634
11.8	400	8.0	16.5	20.3	33.4	185.00	0.7770
12.0	407	8.1	16.7	20.5	33.5	204.44	0.7884
12.2	412	8.2	16.9	20.8	33.3	224.00	0.7968
12.4	416	8.4	17.0	21.0	33.4	243.80	0.8035
12.6	418	8.5	17.2	21.1	33.2	263.55	0.8067

A	B	C	D	E	F	G	H
12.8	418	8.7	17.2	21.2	33.4	283.44	0.8063
13.0	417	8.8	17.4	21.3	33.4	303.28	0.8031
13.2	416	8.9	17.5	21.4	33.6	323.21	0.7989
13.4	412	9.0	17.5	21.4	33.3	342.76	0.7920
13.6	407	9.1	17.5	21.4	33.2	362.05	0.7817
13.8	400	9.2	17.6	21.3	33.3	381.06	0.7666
14.0	392	9.3	17.6	21.3	33.2	399.62	0.7514
14.2	380	9.4	17.6	21.1	33.0	417.49	0.7281
14.4	366	9.5	17.6	21.0	32.9	434.67	0.6998
14.6	348	9.6	17.6	20.8	32.7	450.90	0.6634
14.8	330	9.7	17.5	20.5	32.3	381.06	0.6285
15.0	312	9.8	17.5	20.3	32.0	480.31	0.5924
15.2	292	9.9	17.5	20.0	30.8	493.12	0.5391
15.4	270	9.9	17.4	19.6	29.3	504.40	0.4831
15.6	247	10.0	17.2	19.2	27.8	514.17	0.4275
15.8	223	10.0	17.1	18.7	25.8	522.37	0.3713
16.0	198	10.1	17.0	18.2	22.1	528.61	0.2960
16.2	174	10.1	16.9	17.7	17.6	532.98	0.2289
16.4	150	10.2	16.6	17.2	13.0	535.75	0.1687
16.6	126	10.2	16.5	16.7	5.7	536.77	0.1090

APPENDIX 26

CONSIDERATIONS OF THE INTERNAL COLLECTOR RADIATION TRANSMISSIONS, ABSORPTIONS AND REFLECTIONS

The input of energy to the collector covers and black-netting as a result of incident radiation was evaluated for a succession of six reflections. These six inputs are shown in Figures 63, 64 and 65. The results obtained from these are listed below and allow the evaluation of the fractions of the incident radiation that were absorbed by the various collector surfaces.

Energy absorbed by the bottom cover:

$$Q_{\text{bottom cover}} = I.Acb.(\tau_p.\tau_{nc}.\alpha_p + \tau_p.\tau_{nc}.\rho_p.\rho_{nc}.\alpha_p + \tau_p.\rho_{nc}.\rho_p.\tau_{nc}.\alpha_p + \tau_p.\tau^3_{nc}.\rho^2_p.\alpha_p + \tau_p.\tau_{nc}.\rho^2_p.\rho^2_{nc}.\alpha_p + \tau_p.\rho^2_{nc}.\rho^2_p.\tau_{nc}.\alpha_p + \tau_p.\rho^2_{nc}.\rho^2_p.\tau_{nc}.\alpha_p)$$

Energy absorbed by the black-netting:

$$Q_{\text{black-netting}} = I.A_n.\tau_p.\alpha_{nc}.(1 + \tau_{nc}.\rho_p + \rho_{nc}.\rho_p + \tau^2_{nc}.\rho^2_p + 2.\tau_{nc}.\rho^2_p.\rho_{nc} + \rho^2_{nc}.\rho^2_p + \tau^2_{nc}.\rho^3_p.\rho_{nc} + \tau^3_{nc}.\rho^3_p + \tau^2_{nc}.\rho^3_p.\rho_{nc} + \tau_{nc}.\rho^3_p.\rho^2_{nc})$$

Energy absorbed by the top cover:

$$Q_{\text{top cover}} = I.A_{cts}.(\alpha_p + \tau_p.\rho_{nc}.\alpha_p + \tau_p.\tau^2_{nc}.\rho_p.\alpha_p + \tau_p.\rho^2_{nc}.\rho_p.\alpha_p + 2.\tau_p.\tau^2_{nc}.\rho^2_p.\rho_{nc}.\alpha_p + \tau_p.\rho^3_{nc}.\rho^2_p.\alpha_p + \tau_p.\rho_{nc}.\rho^2_p.\tau^2_{nc}.\alpha_p)$$

The energy absorbed by the edge cover is assumed to consist only of the primary absorption. In the calculations the values of the initial incidence angle and all subsequent reflected and transmitted radiation angles are assumed equal. (i.e. except for the edge cover, all surfaces are assumed parallel).

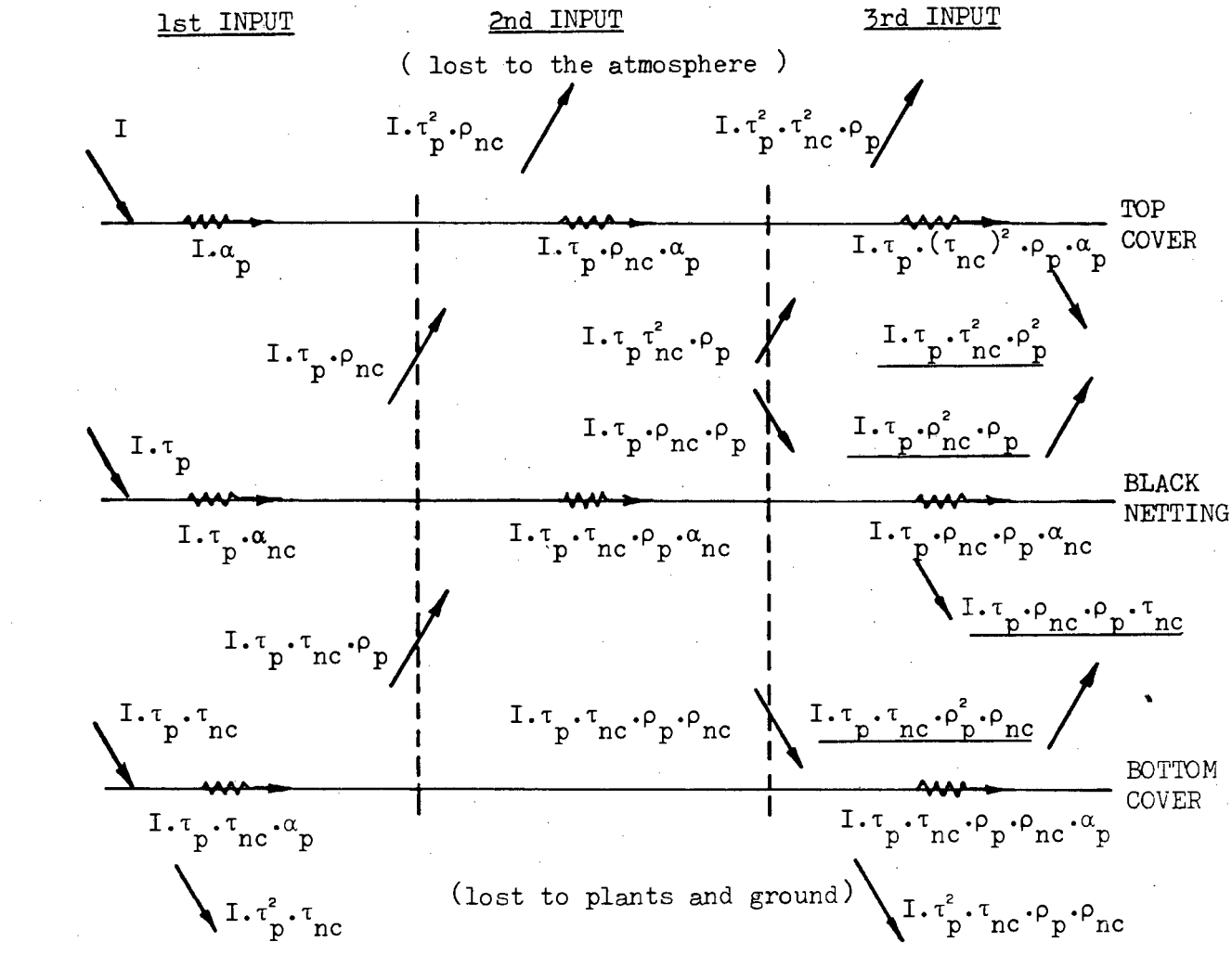

NOTE: (Underlined fractions denote inputs for the next analysis)

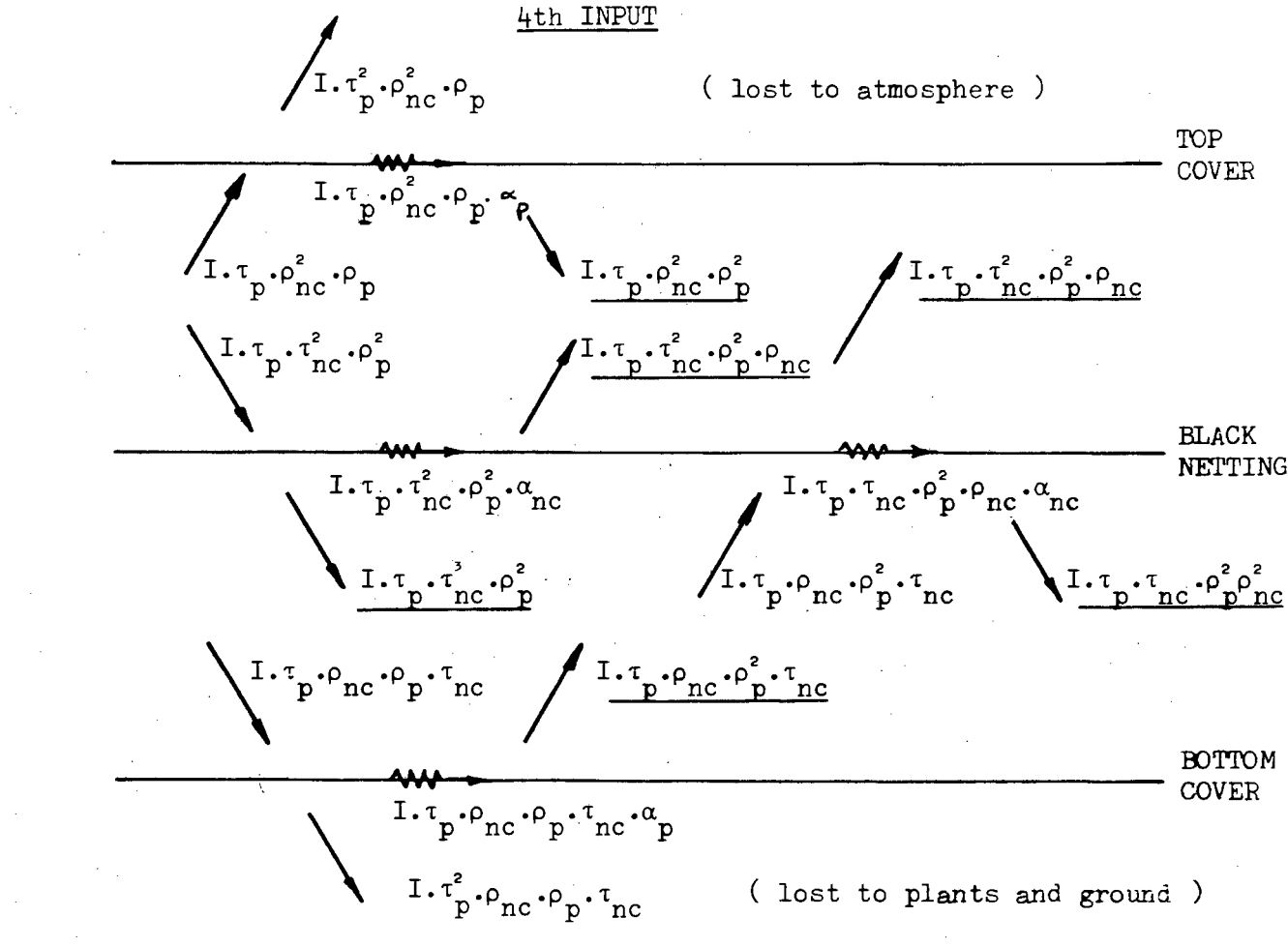

FIGURE 63: INTERNAL COLLECTOR ABSORPTIONS, TRANSMISSIONS AND REFLECTIONS

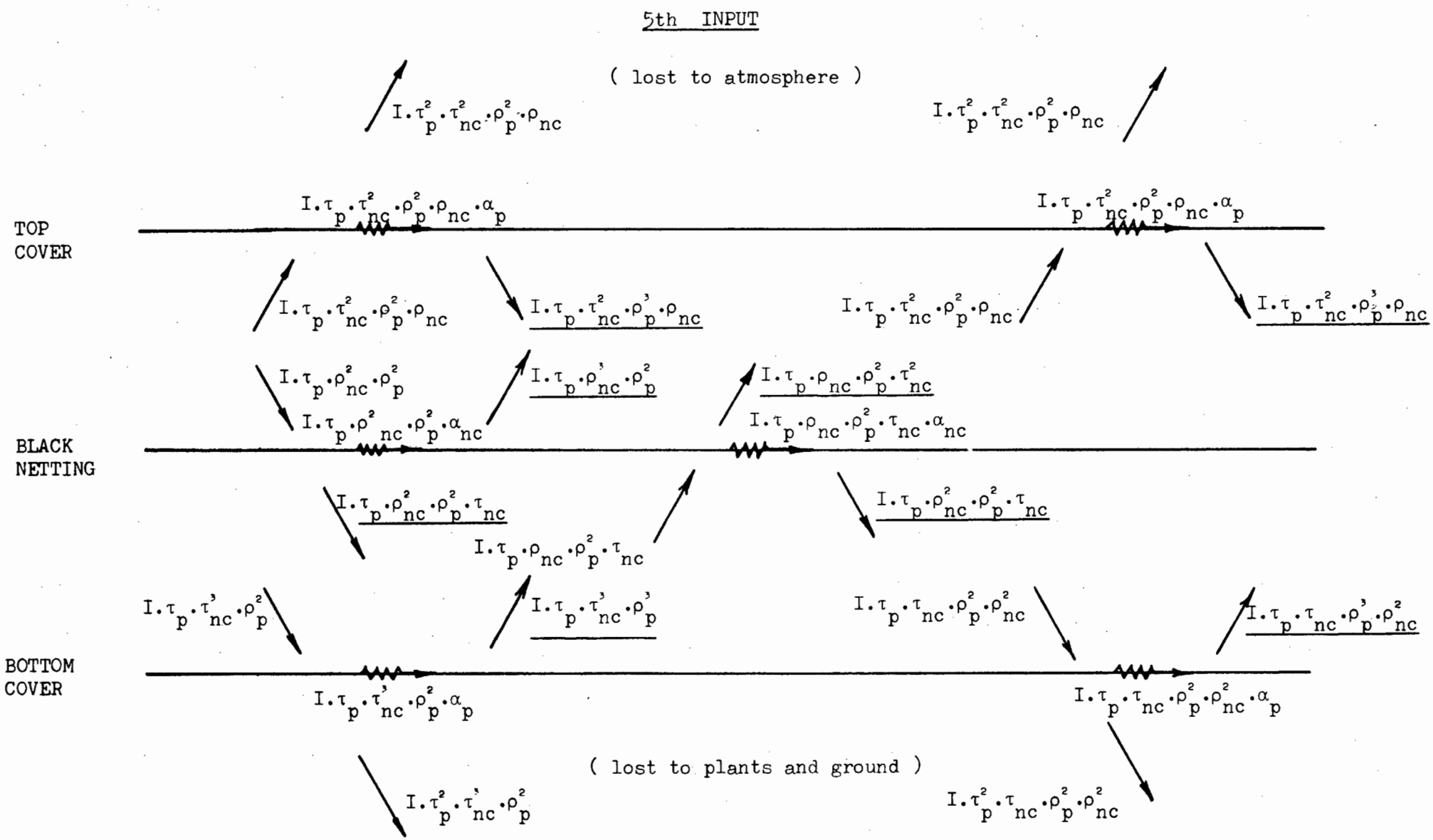

FIGURE 64: INTERNAL COLLECTOR ABSORPTIONS, TRANSMISSIONS AND REFLECTIONS Note: Underlined fractions denote inputs for the next analysis

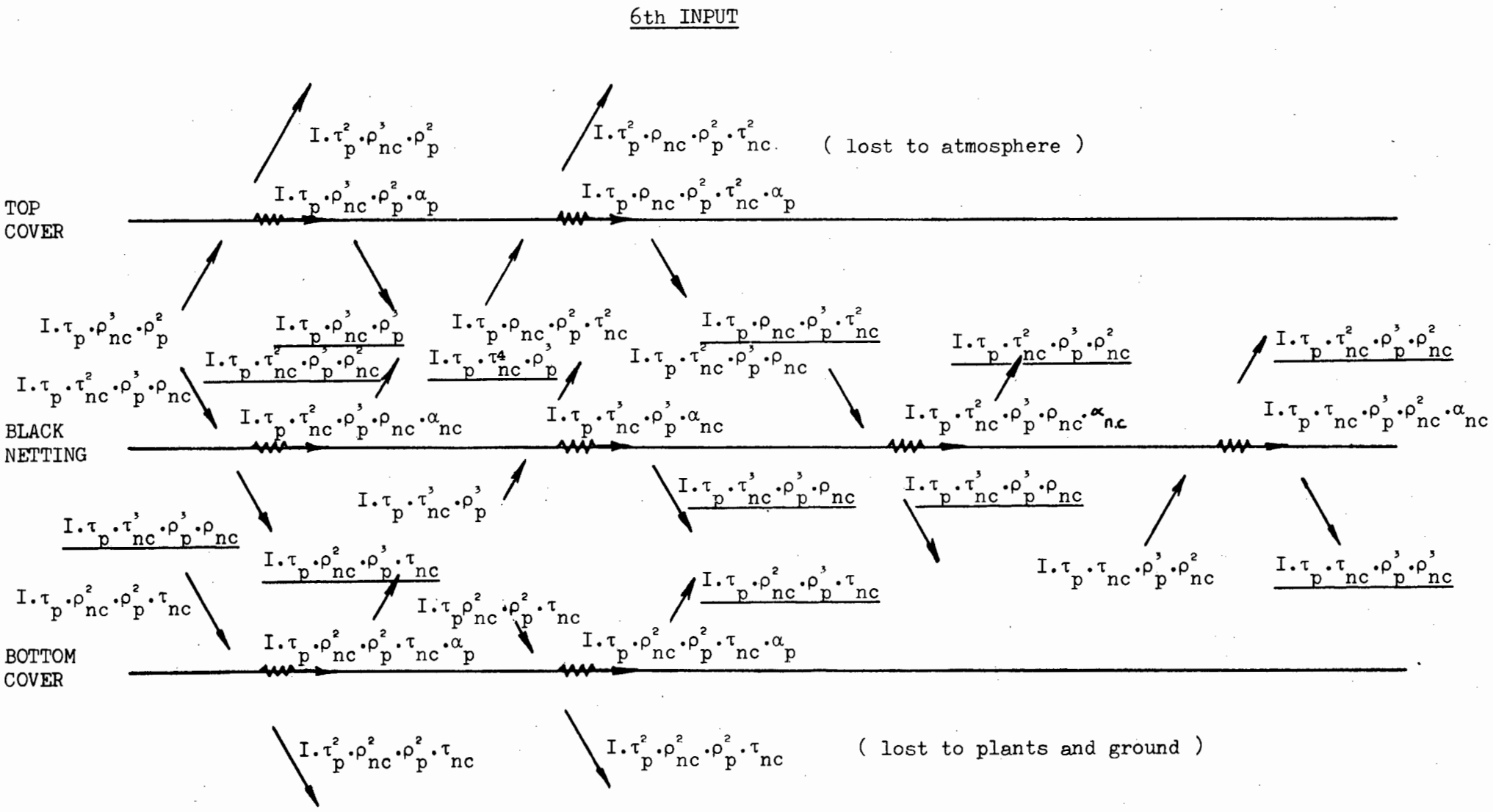

FIGURE 65 : THE INTERNAL COLLECTOR ABSORPTIONS, TRANSMISSIONS AND REFLECTIONS

Note: Underlined fractions denote inputs for the next analysis

APPENDIX 27

THE SOLUTION PROCESS FLOWCHART

(a) The Flat Plate Model

INPUT

(1) Areas ($A_n, A_{ct}, A_{cts}, A_{cb}, A_{ce}, A_{ces}$)

(2) Emittances ($\varepsilon_n, \varepsilon_{ct}, \varepsilon_{cb}, \varepsilon_{ce}, \varepsilon_s$)

(3) Radiation shape factors ($F_{n-ct}, F_{cb-ct}, F_{ce-ct}, F_{ct-s}, F_{ct-g}, F_{n-cb}$ $F_{cb-s}, F_{cb-ce}, F_{cb-g}, F_{n-ce}, F_{ce-gout}, F_{ce-gin}$ $F_{ce-sout}, F_{ce-sin}, F_{n-s}, F_{n-g}$)

(4) Collector mass flowrate ($\dot{m}$)

(5) Incident Radiation (I)

(6) Inlet air temperature ($T_{in} : T_{fst} = T_{fsb} = T_{int} = T_{inb} = T_{in}$)

(7) Ambient air temperature ($T_a : T_g = T_s = T_a$)

(8) Fractions of incident radiation absorbed by the collector surfaces ($\alpha_{cee}, \alpha_{cte}, \alpha_{cbe}, \alpha_{ne}$) at zero degrees incidence angle

GUESS

Initial values of the unknowns ($T_{ct}, T_{ce}, T_{cb}, T_n, T_{outt}, T_{outb}, T_{out}$)

CALCULATE

(1) Flowrates in the top and bottom collector sections ($\dot{m}_t, \dot{m}_b$)

(2) Length from the leading edge of the collector to the mid-point of the element under consideration (ℓ)

(3) Film temperature properties for the various surfaces of the collector ($k_f, C_{pf}, Pr_f, \mu_f, \nu_f$)

*** ⟶

(4) Internal collector surface forced convection heat transfer coefficients ($h_{ct}, h_{cb}, h_{ce}, h_{nt}, h_{nb}$)

(5) whether the external surface natural convection regimes are laminar or turbulent (i.e. evaluate $Gr_f.Pr_f$) and hence select the appropriate equations and calculate (h_{wct},h_{wce},h_{convcb})

(6) improved values of the temperatures (T_{ct},T_{ce},T_{cb},T_n,T_{outt},T_{outb},T_{out})

If, on substitution into the simultaneous equations, any residual value is more than $|0.01|$ (see Appendix 28), then repeat the calculations using the improved 'guesstimate' of the unknown temperatures i.e.
RETURN TO 'CALCULATE (3)'

If, on substitution into the simultaneous equations, the residual values are less than $|0.01|$, then use these solution values as the solution values of the element under consideration. Consider the next element along the collector length.

If there are no more elements, T_{out} becomes the predicted collector air-outlet temperature and the program stops 'running' i.e. 'END'

If there are more elements to consider, the following input conditions for the new element are transferred from the results of the old element:

$$T_{int} = T_{outt}(old) \qquad \text{and} \qquad T_{inb} = T_{outb}(old)$$

The procedure is now repeated i.e.
RETURN TO 'CALCULATE (2)'

(b) <u>The Flat-Plate/Tube Model</u>:

The flowchart for this model is the same as for the Flat-Plate model, except that the following is done at the position marked '***' :
The top and bottom section thermal entry lengths are calculated and the results of these calculations are used to decide whether the tube or flat-plate considerations are to be applied.

(c) The Life-Size Baird-type collector performance predictions:

INPUT

(1) Areas

(2) Emittances

(3) Radiation shape factors

(4) Mass flowrate

(5) Start time

(6) Incident Radiation at time 't'

(7) Inlet air temperature at time 't' ($T_{in} = T_a$: $T_s = T_a - 6$)

(8) Ground temperature at time 't' (T_g)

GUESS

Initial values of the unknowns ($T_{ct}, T_{ce}, T_{cb}, T_n, T_{outt}, T_{outb}, T_{out}$)

CALCULATE

(1) Calculate the radiation incidence angle at time 't' and use the answer to calculate the fractions of incident radiation absorbed by the collector surfaces ($\alpha_{cee}, \alpha_{cte}, \alpha_{cbe}, \alpha_{ne}$) at time 't'

(2) Top and bottom section mass-flowrates

(3) Length from leading edge to mid-point of the element under consideration

(4) Film temperature properties for the various collector surfaces

(5) Calculate the internal and external surface heat-transfer coefficients

(6) Improved values of the temperatures ($T_{ct}, T_{ce}, T_{cb}, T_n, T_{outt}, T_{outb}, T_{out}$)

If, on substitution into the simultaneous equations, any residual value is more than $|0.01|$, then repeat the calculations using the improved 'guesstimate' of the unknown temperatures i.e. RETURN TO 'CALCULATE (4)'

If, on substitution into the simultaneous equations, the residual values are less than $|0.01|$, then use these solution values as the solution values of the element under consideration. Consider the next element along the collector length.

If there are no more elements, 'T_{out}' becomes the predicted collector air-outlet temperature at time 't'. The time is advanced by one time interval (which in the case of this thesis is twelve minutes) and the program returns to the point 'INPUT (6)'. If the radiation intensity is zero the program stops 'running' i.e. END

If there are more elements to consider, the following input conditions for the new element are transferred from the results of the old element:

$$T_{int} = T_{outt}(old) \quad \text{and} \quad T_{inb} = T_{outb}(old)$$

The procedure is now repeated i.e. return to 'CALCULATE (3)'

APPENDIX 28

A SAMPLE CALCULATION AND THE VERIFICATION OF THE SOLUTION PROCESS

Consider the results of the computations done by the computer for element ten of Test 10 using the flat plate model:

Distance from the leading edge of the collector to the mid-point of element ten = 0.432 metres

Top section air-inlet temperature ..... = 30.3 degrees Centigrade

Bottom section air-inlet temperature ..... = 30.5 degrees Centigrade

Air-inlet temperature ..... = 30.4 degrees Centigrade

Top cover temperature ..... = 23.3 degrees Centigrade

Edge cover temperature ..... = 22.2 degrees Centigrade

Bottom cover temperature ..... = 23.0 degrees Centigrade

Black-netting temperature ..... = 37.4 degrees Centigrade

Top section air-outlet temperature ..... = 30.8 degrees Centigrade

Bottom section air-outlet temperature ..... = 31.1 degrees Centigrade

Outlet-air temperature ..... = 31.0 degrees Centigrade

These values were generated using the following input conditions:

Mass-flowrate through the collector = 0.002317 kg/s

Inlet-air temperature to element one of the collector = 25.0 degrees Centigrade

Ambient-air temperature ..... = 18.8 degrees Centigrade

Total radiation intensity incident on the collector = 852 W/m^2

A summary of the results listed above is included in Appendix 19. The sample calculation that follows is based on the flat-plate model solution.

Calculation of the top-side black-netting heat-transfer coefficient:

$$h_n = \frac{k_f}{\ell} \times \left(\frac{\ell}{L}\right)^{-0.22} \times \left(\frac{\dot{m}_t \times \ell}{\mu_f \times A_{xt}}\right)^{0.64} \times 0.3593 \quad \ldots\ldots (1)$$

Equation (1) is derived in Appendix 2. The properties of the air specified in (1) are all evaluated at the top-side netting film temperature, which is defined as:

$T_f = (T_n + T_{fst})/2$ substituting values from the results

$= (37.4 + 25.0)/2$

$= 31.2$ degrees Centigrade

Properties are evaluated by extrapolation of tables presented in Holman (41):

$k_{31.2\,^\circ C} = 0.02656$ W/m.°C

$\mu_{31.2\,^\circ C} = 1.991 \times 10^{-5}$ kg/m.s

$\dot{m}_t = 0.52 \times 0.002317$

$= 1.205 \times 10^{-3}$ kg/s

For element ten, $\ell = 0.432$ metres and the top section cross-sectional area is calculated in Appendix 13 as:

$A_{xt} = 1309 \times 10^{-6}$ m^2

Substituting these values into Equation (1):

$$h_{nt} = 0.3593 \times \frac{0.02656}{0.432} \times \left(\frac{0.432}{0.455}\right)^{-0.22} \times \left(\frac{1.205 \times 10^{-3} \times 0.432}{1.991 \times 10^{-5} \times 1309 \times 10^{-6}}\right)^{0.64}$$

$= 12.63$ W/m^2

Calculation of the bottom-side black-netting heat-transfer coefficient:

The bottom netting heat-transfer coefficient is also evaluated using Equation (1). Since the upper and lower collector free-stream temperatures are the same, the netting film temperature is again 31.2 degrees Centigrade.

Thus the thermal conductivity and dynamic viscosity of the air are the same as in the top collector section.

$$\dot{m}_b = 0.48 \times 0.002317 \quad \text{(see Appendix 6)}$$

$$= 0.001112 \text{ kg/s}$$

$$A_{xb} = 1202 \times 10^{-6} \text{ m}^2 \quad \text{(see Appendix 13)}$$

Substituting the appropriate values into (1):

$$h_{nb} = 0.3593 \times \frac{0.02656}{0.432} \times \left(\frac{0.432}{0.455}\right)^{-0.22} \times \left(\frac{0.001112 \times 0.432}{1.991 \times 10^{-5} \times 1202 \times 10^{-6}}\right)^{0.64}$$

$$= 12.67 \text{ W/m}^2.^{\circ}\text{C}$$

Calculation of the internal edge cover convection heat-transfer coefficient:

$$h_c = 0.453 \times \frac{k_f}{\ell} \times (Pr_f)^{\frac{1}{3}} \times \left(\frac{\dot{m} \times \ell}{\mu_f \times A_x}\right)^{0.5} \quad \ldots\ldots\ldots\ldots\ldots \quad (2)$$

The origin of Equation (2) is explained in Appendix 10.

In this case:

$$T_f = (T_{ce} + T_{fsb})/2$$

$$= (22.2 + 25.0)/2$$

$$= 23.6 \text{ degrees Centigrade}$$

The air properties at this temperature were obtained from Holman (41):

$$k_{23.6^{\circ}C} = 2.597 \times 10^{-2} \text{ W/m.}^{\circ}\text{C}$$

$$\mu_{23.6^{\circ}C} = 1.949 \times 10^{-5} \text{ kg/ms}$$

$$Pr_{23.6^{\circ}C} = 0.709$$

Substituting these values into Equation (2):

$$h_{ce} = 0.453 \times \frac{2.597 \times 10^{-2}}{0.432} \times (0.709)^{\frac{1}{3}} \times \left(\frac{1.112 \times 10^{-3} \times 0.432}{0.00001949 \times 1202 \times 10^{-6}}\right)^{0.5}$$

$$= 3.48 \text{ W/m}^2.^{\circ}\text{C}$$

Calculation of the internal top cover convection heat-transfer coefficient:

The internal top cover convection heat-transfer coefficient is also evaluated using Equation (2). The top cover film temperature is:

$$T_f = (T_{ct} + T_{fst})/2$$
$$= (23.3 + 25.0)/2$$
$$= 24.2 \text{ degrees Centigrade}$$

The air properties at this temperature were obtained from Holman (41):

$$k_{24.2\ ^oC} = 2.601 \times 10^{-2} \text{ W/m.}^oC$$

$$\mu_{24.2\ ^oC} = 1.955 \times 10^{-5} \text{ kg/m.s}$$

$$Pr_{24.2\ ^oC} = 0.709$$

Substituting these values into Equation (2):

$$h_{ct} = 0.453 \times \frac{2.601 \times 10^{-3}}{0.432} \times (0.709)^{\frac{1}{3}} \times \left(\frac{0.001205 \times 0.432}{0.00001955 \times 1309 \times 10^{-6}}\right)^{0.5}$$
$$= 3.47 \text{ W/m}^2\text{.}^oC$$

Calculation of the internal bottom cover convection heat-transfer coefficient:

The internal bottom cover forced-convection heat-transfer coefficient is also evaluated using Equation (2). The bottom cover film temperature is:

$$T_f = (T_{cb} + T_{fsb})/2$$
$$= (23.0 + 25.0)/2 = 24.0 \text{ degrees Centigrade}$$

Evaluating the air properties at this temperature:

$$k_{24.0\ ^oC} = 2.6 \times 10^{-2} \text{ W/m.}^oC$$

$$\mu_{24.0\ ^oC} = 1.953 \times 10^{-5} \text{ kg/m.s}$$

$$Pr_{24.0\ ^oC} = 0.709$$

Substituting these values into Equation (2):

$$h_{cb} = 0.453 \times \frac{0.026}{0.432} \times (0.709)^{\frac{1}{3}} \times \left(\frac{0.001112 \times 0.432}{1.953 \times 10^{-6} \times 1202 \times 10^{-6}}\right)^{0.5}$$
$$= 3.48 \text{ W/m}^2\text{.}^oC$$

The natural convection coefficients that pertain to the external collector surfaces are derived from the equations listed in Appendix 10. In order to establish the nature of the flow regime (and therefore to select the appropriate equation), it is necessary to evaluate the 'Gr.Pr' product.

Consider the top cover:

The top cover film temperature is:

$$T_f = (T_{ct} + T_a)/2$$

$$= (23.3 + 18.8)/2 = 21.05 \text{ degrees Centigrade}$$

Once again, the following properties are extracted from Holman (41):

$$\nu_{21.05\ ^oC} = 14.94 \times 10^{-6}\ m^2/s$$

$$\beta_{21.05\ ^oC} = (1/(273 + 21.05)) = 3.4 \times 10^{-3}\ {}^oK^{-1}$$

$$Pr_{21.05\ ^oC} = 0.710$$

Now $$Gr_f = \frac{g \times \beta_f \times (T_{ct} - T_a) \times L^3}{\nu_f^2}$$

$$= \frac{9.8 \times 3.4 \times 10^{-3} \times (23.3 - 18.8) \times \left(\frac{0.11 + 0.0455}{2}\right)^3}{(14.94 \times 10^{-6})^2}$$

$$= 3.16 \times 10^5$$

Thus $$Pr_f.Gr_f = 0.710 \times 3.16 \times 10^5$$

$$= 2.24 \times 10^5$$

Inspection of Appendix 10 reveals that the flow regime falls within the laminar region. Similar calculations for the edge and bottom covers establish that all the natural convection processes have laminar flow regimes.

Calculation of the top cover external convection heat-transfer coefficient:

$$h_{wct} = 1.32 \times \left(\frac{T_{ct} - T_a}{L}\right)^{0.25} \qquad \text{(from Appendix 10)}$$

Substituting appropriate values:

$$h_{wct} = 1.32 \times \left(\frac{23.3 - 18.8}{\frac{(0.11 + 0.0455)}{2}}\right)^{0.25}$$

$$= 3.64 \text{ W/m}^2.^{\circ}\text{C}$$

Calculation of the edge cover external convection heat-transfer coefficient:

$$h_{wce} = 1.42 \times \left(\frac{T_{ce} - T_a}{L}\right)^{0.25} \qquad \text{(from Appendix 10)}$$

Substituting appropriate values:

$$h_{wce} = 1.42 \times \left(\frac{22.2 - 18.8}{\frac{(0.014 + 0.0455)}{2}}\right)^{0.25}$$

$$= 4.64 \text{ W/m}^2.^{\circ}\text{C}$$

Calculation of the bottom cover external convection heat-transfer coefficient:

$$h_{convcb} = 0.61 \times \left(\frac{T_{cb} - T_a}{L^2}\right)^{0.2} \qquad \text{(from Appendix 10)}$$

Substituting appropriate values:

$$h_{convcb} = \left(\frac{23.0 - 18.8}{\left(\frac{0.12 + 0.0455}{2}\right)^2}\right)^{0.2} \times 0.61$$

$$= 2.2 \text{ W/m}^2.^{\circ}\text{C}$$

The values of the above forced and natural heat-transfer coefficients can now be used in the energy balances to confirm the validity of the solution values. The energy balance equations come from Chapter Three.

(1) The energy balance on the top section fluid:

$$h_{nt}.A_n.(T_n - T_{fst}) - h_{ct}.A_{ct}.(T_{fst} - T_{ct}) - \dot{m}_t.C_{pt}.(T_{outt} - T_{int}) = 0$$

The areas are calculated from dimensions given in Appendix 13, and are:

$$A_n = 0.00455 \text{ m}^2$$

$$A_{ct} = 0.005005 \text{ m}^2$$

$$C_{pt} = 1006 \text{ J/kg}.^{\circ}\text{C} \quad - \text{ evaluated at } (T_{outt} + T_{int})/2$$

Substituting the relevant values into the equation:

$$12.63 \times 0.00455 \times (37.4 - 25.0)$$

$$- 3.47 \times 0.005005 \times (25.0 - 23.3)$$

$$- 1.205 \times 10^{-3} \times 1006 \times (30.8 - 30.3)$$

$$= 0.08$$

(2) The energy balance on the bottom section fluid:

$$h_{nb}.A_n.(T_n - T_{fsb}) - h_{cb}.A_{cb}.(T_{fsb} - T_{cb})$$

$$- 2.h_{ce}.A_{ce}.(T_{fsb} - T_{ce}) - \dot{m}_b.C_{pb}.(Toutb - Tinb) = 0$$

Areas are calculated from the dimensions given in Appendix 13, and are:

$A_{cb} = 0.00546$

$A_{ce} = 0.000637$

$C_{pb} = 1006$ -evaluated at the mean bulk fluid temperature of element ten i.e. $((T_{outb} + T_{inb})/2)$

Substituting relevant values into the equation:

$$12.67 \times 0.00455 \times (37.4 - 25.0) - 3.48 \times 0.00546 \times (25.0 - 23.0)$$

$$- 2\times 3.48 \times 0.000637 \times (25.0 - 22.2)$$

$$- 0.001112 \times 1006 \times (31.1 - 30.5)$$

$$= 0.007$$

(3) Energy balance on the top cover:

$$h_{ct}.A_{ct}.(T_{fst} - T_{ct}) + A_{cts}.I.\alpha_{cte}$$

$$+ A_{cb}.F_{cb-ct}.\varepsilon_{cb}.\varepsilon_{ct}.(1-\varepsilon_n).\sigma.(T_{cb}^4 - T_{ct}^4)$$

$$+ A_n.F_{n-ct}.\varepsilon_n.\varepsilon_{ct}.\sigma.(T_n^4 - T_{ct}^4)$$

$$+ 2.A_{ce}.F_{ce-ct}.\varepsilon_{ce}.\varepsilon_{ct}.(1-\varepsilon_n).\sigma.(T_{ce}^4 - T_{ct}^4)$$

$$- A_{ct}.F_{ct-s}.\varepsilon_{ct}.\varepsilon_s.\sigma.(T_{ct}^4 - T_s^4)$$

$$- \frac{\sigma.(T_{ct}^4 - T_g^4)}{\frac{1}{A_{ct}.F_{ct-g}.\varepsilon_{ct}.(1-\varepsilon_n).(1-\varepsilon_{cb})} + \frac{1-\varepsilon_g}{\varepsilon_g.A_g}}$$

tends to 0 since A_g tends to infinity

$$- h_{wct}.A_{ct}.(T_{ct} - T_a)$$

$$= 0$$

Now $A_{cts} = A_n$

α_{cte} = 0.021 for an incident radiation angle of 0^o - see Appendix 27

I = 852 W/m^2 - see Appendix 16

F_{n-ct} = 0.65, F_{cb-ct} = 0.5, F_{ce-ct} = 0.24

F_{ct-s} = 1, F_{ct-g} = 1 - see Appendix 11

ε_{ce} =0.48 , ε_{cb} = 0.48 , ε_s = 1

ε_{ct} =0.48 , ε_n = 0.43 - see Appendix 3

Substituting relevant values into the equation:

$$3.47 \times 0.005005 \times (25.0 - 23.3) + 0.00455 \times 852 \times 0.021$$

$$+ 0.00546 \times 0.5 \times 0.48 \times 0.48 \times (1-0.43) \times 5.669 \times 10^{-8} \times (296^4 - 296.3^4)$$

$$+ 0.00455 \times 0.65 \times 0.43 \times 0.48 \times 5.669 \times 10^{-8} \times (310.4^4 - 296.3^4)$$

$$+ 2 \times 0.000637 \times 0.24 \times 0.48^2 \times (1-0.43) \times 5.669 \times 10^{-8} \times (295.2^4 - 296.3^4)$$

$$- 0.005005 \times 1 \times 0.48 \times 1 \times 5.669 \times 10^{-8} \times (296.3^4 - 291.8^4)$$

$$- \frac{5.669 \times 10^{-8} \times (296.3^4 - 291.8^4)}{\frac{1}{0.005005 \times 1 \times 0.48 \times (1-0.43) \times (1-0.48)}}$$

$$- 3.64 \times 0.005005 \times (23.3 - 18.8)$$

$$= + 0.0173673 + 0.0814086 - 6.3349 \times 10^{-4}$$

$$+ 0.0545112 - 2.591 \times 10^{-4} - 0.0623323$$

$$- 0.0184752 - 0.0819819$$

$$= -0.01$$

(4) Energy balance on the bottom cover:

$$h_{cb}.A_{cb}.(T_{fsb} - T_{cb}) + A_{cb}.I.\alpha_{cbe}$$

$$+ A_n.F_{n-cb}.\varepsilon_n.\varepsilon_{cb}.\sigma.(T_n^4 - T_{cb}^4)$$

$$- A_{cb}.F_{cb-ct}.\varepsilon_{cb}.\varepsilon_{ct}.(1-\varepsilon_n).\sigma.(T_{cb}^4 - T_{ct}^4)$$

$$- A_{cb}.F_{cb-s}.\varepsilon_{cb}.\varepsilon_s.(1-\varepsilon_{ct}).(1-\varepsilon_n).\sigma.(T_{cb}^4 - T_s^4)$$

$$- 2.A_{cb}.F_{cb-ce}.\varepsilon_{cb}.\varepsilon_{ce}.\sigma.(T_{cb}^4 - T_{ce}^4)$$

$$- \frac{\sigma.(T_{cb}^4 - T_g^4)}{\frac{1}{A_{cb}.F_{cb-g}.\varepsilon_{cb}} + \frac{1-\varepsilon_g}{\varepsilon_g.A_g}}$$ tends to zero since A_g tends to infinity

$$- h_{convcb}.A_{cb}.(T_{cb} - T_a)$$

$$= 0$$

Now $\alpha_{cbe} = 0.007$ - see Appendix 27

$F_{n-cb} = 0.75$, $F_{cb-ct} = 0.5$, $F_{cb-s} = 1$

$F_{cb-ce} = 0.05$, $F_{cb-g} = 1$ - see Appendix 11

Substituting relevant values into the equation:

$$
\begin{aligned}
& 3.48 \times 0.00546 \times (25.0 - 23.0) \; + \; 0.00546 \times 852 \times 0.007 \\
+ \; & 0.00455 \times 0.75 \times 0.43 \times 0.48 \times 5.669 \times 10^{-8} \times (310.4^4 - 296^4) \\
- \; & 0.00546 \times 0.5 \times 0.48^2 \times (1-0.43) \times 5.669 \times 10^{-8} \times (296^4 - 296.3^4) \\
- \; & 0.00546 \times 1 \times 0.48 \times 1 \times (1-0.48) \times (1-0.43) \times 5.669 \times 10^{-8} \times (296^4 - 291.8^4) \\
- \; & 2 \times 0.00546 \times 0.05 \times 0.48^2 \times 5.669 \times 10^{-8} \times (296^4 - 295.2^4) \\
- \; & \frac{5.669 \times 10^{-8} \times (296^4 - 291.8^4)}{\frac{1}{0.00546 \times 1 \times 0.48}} \\
- \; & 2.2 \times 0.00546 \times (23.0 - 18.8) \\
\\
= \; & + 0.0380016 \; + \; 0.0325634 \; + \; 0.0641421 \; + \; 6.3349 \times 10^{-4} \\
& - 0.0187822 \; - \; 5.89447 \times 10^{-4} \; - \; 0.063368 \; - \; 0.0504504 \\
= \; & 0.002
\end{aligned}
$$

(5) Energy balance on the edge cover:

$$
\begin{aligned}
& h_{ce}.A_{ce}.(T_{fsb} - T_{ce}) \; + \; A_{ces}.I.\alpha_{cee} \\
+ \; & A_n.F_{n-ce}.\varepsilon_n.\varepsilon_{ce}.\sigma.(T_n^4 - T_{ce}^4) \\
+ \; & A_{cb}.F_{cb-ce}.\varepsilon_{cb}.\varepsilon_{ce}.\sigma.(T_{cb}^4 - T_{ce}^4) \\
- \; & \frac{\sigma.(T_{ce}^4 - T_g^4)}{\frac{1}{A_{ce}.\varepsilon_{ce}.(F_{ce-gout} + F_{ce-gin}.(1-\varepsilon_{cb}))} + \frac{1-\varepsilon_g}{\varepsilon_g.A_g}} \quad \text{tends to 0 since } A_g \text{ large} \\
- \; & \sigma.A_{ce}.\varepsilon_{ce}.\varepsilon_s.(F_{ce-sout} + F_{ce-sin}.(1-\varepsilon_n).(1-\varepsilon_{ct})).(T_{ce}^4 - T_s^4) \\
- \; & A_{ce}.F_{ce-ct}.\varepsilon_{ce}.\varepsilon_{ct}.(1-\varepsilon_n).\sigma.(T_{ce}^4 - T_{ct}^4) \\
- \; & h_{wce}.A_{ce}.(T_{ce} - T_a) \\
= \; & 0
\end{aligned}
$$

Now $\alpha_{cee} = 0.02$ - see Appendix 27

$A_{ces} = 0.000455$

$F_{n-ce}=0.05$, $F_{ce-gout}=0.25$, $F_{ce-gin}=0.75$, $F_{ce-sout}=0.75$, $F_{ce-sin}=0.25$

Substituting relevant values into the equation:

$$
\begin{aligned}
& 3.48 \times 0.000637 \times (25.0 - 22.2) \; + \; 0.000455 \times 852 \times 0.02 \\
+ \; & 0.00455 \times 0.05 \times 0.43 \times 0.48 \times 5.669 \times 10^{-8} \times (310.4^4 - 295.2^4) \\
+ \; & 0.00546 \times 0.05 \times 0.48^2 \times 5.669 \times 10^{-8} \times (296^4 - 295.2^4) \\
- \; & \frac{5.669 \times 10^{-8} \times (295.2^4 - 291.8^4)}{\frac{1}{0.000637 \times 0.48 \times (0.25 + 0.75 \times (1 - 0.48))}} \\
- \; & 5.669 \times 10^{-8} \times 0.000637 \times 0.48 \times 1 \times (0.75 + 0.25 \times (0.57) \times (0.52)) \times (295.2^4 - 291.8^4 \\
- \; & 0.000637 \times 0.24 \times 0.48^2 \times (1 - 0.43) \times 5.669 \times 10^{-8} \times (295.2^4 - 296.3^4) \\
- \; & 4.64 \times 0.000637 \times (295.2 - 291.8)
\end{aligned}
$$

$$
\begin{aligned}
= \; & + 6.20692 \times 10^{-3} \; + \; 7.7532 \times 10^{-3} \; + \; 4.49616 \times 10^{-3} \; + \; 2.94723 \times 10^{-4} \\
& - 3.81456 \times 10^{-3} \; - \; 4.91184 \times 10^{-3} \; - \; 1.2955 \times 10^{-4} \; - \; 0.0100493
\end{aligned}
$$

$$
= \; -0.00015
$$

(6) Energy balance on the black-netting:

$$
\begin{aligned}
& h_{nt} \cdot A_n \cdot (T_n - T_{fst}) \\
+ \; & A_n \cdot F_{n-ct} \cdot \varepsilon_n \cdot \varepsilon_{ct} \cdot \sigma \cdot (T_n^4 - T_{ct}^4) \\
+ \; & A_n \cdot F_{n-s} \cdot \varepsilon_n \cdot \varepsilon_s \cdot (1 - \varepsilon_{ct}) \cdot \sigma \cdot (T_n^4 - T_s^4) \\
+ \; & h_{nb} \cdot A_n \cdot (T_n - T_{fsb}) \\
+ \; & A_n \cdot F_{n-cb} \cdot \varepsilon_n \cdot \varepsilon_{cb} \cdot \sigma \cdot (T_n^4 - T_{cb}^4) \\
+ \; & 2 A_n \cdot F_{n-ce} \cdot \varepsilon_n \cdot \varepsilon_{ce} \cdot \sigma \cdot (T_n^4 - T_{ce}^4) \\
+ \; & \frac{\sigma \cdot (T_n^4 - T_g^4)}{\frac{1}{A_n \cdot F_{n-g} \cdot \varepsilon_n \cdot (1 - \varepsilon_{cb})} + \frac{1 - \varepsilon_g}{\varepsilon_g \cdot A_g}} \quad \text{tends to zero since } A_g \text{ tends to infinity} \\
- \; & A_n \cdot I \cdot \alpha_{ne} \\
= \; & 0
\end{aligned}
$$

Now $\alpha_{ne} = 0.46$ - see Appendix 27

Substituting the relevant values into the equation:

$$12.63 \times 0.00455 \times (37.4 - 25.0)$$

$$+ \; 0.00455 \times 0.65 \times 0.43 \times 0.47 \times 5.669 \times 10^{-8} \times (310.4^4 - 296.3^4)$$

$$+ \; 0.00455 \times 1 \times 0.43 \times 1 \times (1-0.48) \times 5.669 \times 10^{-8} \times (310.4^4 - 291.8^4)$$

$$+ \; 12.67 \times 0.00455 \times (37.4 - 25.0)$$

$$+ \; 0.00455 \times 0.75 \times 0.43 \times 0.48 \times 5.669 \times 10^{-8} \times (310.4^4 - 296^4)$$

$$+ \; 2 \times 0.00455 \times 0.05 \times 0.43 \times 0.48 \times 5.669 \times 10^{-8} \times (310.4^4 - 295.2^4)$$

$$+ \; \frac{5.669 \times 10^{-8} \times (310.4^4 - 291.8^4)}{\frac{1}{0.00455 \times 1 \times 0.43 \times (1-0.48)}}$$

$$- \; 0.00455 \times 852 \times 0.46$$

$$= + 0.7125846 + 0.0533756 + 0.0908521 + 0.7148414$$

$$+ 0.0641421 + 8.99233 \times 10^{-3} + 0.1172489 - 1.783236$$

$$= -0.021$$

(7) Energy balance on the fluid(s):

$$\dot{m}_t . C_{pt} . (T_{outt} - T_{int}) + \dot{m}_b . C_{pb} . (T_{outb} - T_{inb}) - \dot{m} . C_p . (T_{out} - T_{in}) = 0$$

Substituting the relevant values into the above equation:

$$1.2505 \times 10^{-3} \times 1006 \times (30.8 - 30.3)$$

$$+ \; 0.001112 \times 1006 \times (31.1 - 30.5)$$

$$- \; 0.002317 \times 1006 \times (31.0 - 30.4)$$

$$= +0.6290015 + 0.6712032 - 1.3985412$$

$$= -0.098$$

The residuals of the seven energy balance equations were calculated on the computer as:

(1) -6.3×10^{-6}

(2) -6.4×10^{-6}

(3) 8.0×10^{-6}

(4) 2.9×10^{-6}

(5) -8.1×10^{-6}

(6) 1.28×10^{-5}

(7) 2.25×10^{-7}

These values are all smaller than those calculated above in Appendix 28. This is a result of the fact that the computer uses nine decimal places in all the calculations, leading to a smaller 'round-off' error.

Tests were conducted to establish the optimum residual value in order to minimise calculation time. The result of the tests was the selection of a maximum allowable residual value of $|0.01|$

Calculation of the percentage predicted heat-gain error:

The percentage predicted heat-gain error was calculated using the following equation:

$$100 \times \left[\frac{\dot{m} \times C_p \times (T_{out}-T_{in})_{predicted} - \dot{m} \times C_p \times (T_{out}-T_{in})_{measured}}{\dot{m} \times C_p \times (T_{out}-T_{in})_{measured}} \right]$$

Consider the calculation of the predicted heat-gain error for Test 10. Since the specific heat of air is not very temperature sensitive, it was taken as a constant. This means that the predicted heat-gain error was calculated through the temperature differences i.e.

$$100 \times \left[\frac{(31.0 - 25.0) - (31.9 - 25.0)}{(31.9 - 25.0)} \right] = -13\ \%$$

In Appendix 19, the result for Test 10 is -13.7%. The difference between the results is due to round-off errors in the temperature values.

Calculation of the collector efficiency:

The collector efficiency was calculated using the following equation:

$$\text{Efficiency} = \left[\frac{\dot{m} \times C_p \times (T_{out} - T_{in})}{I \times A_n} \right] \times 100$$

Consider the calculation of the predicted collector efficiency of Test 10:

$$\text{Predicted Efficiency} = \left[\frac{0.002317 \times 1006 \times (31.0 - 25.0)}{852 \times 0.455 \times 0.1} \right] \times 100$$

$$= 36.0\ \%$$

Again, this is slightly different from the value of 35.8 % listed for Test 10 in Appendix 19 and is the result of round-off errors in the temperature values.